7-2008

THE ROLE OF CRYSTALLOGRAPHIC RELATIONSHIPS BETWEEN ALPHA(α) AND BETA(β) PHASES ON THE ELEVATED TEMPERATURE ISOTHERMAL PHASE TRANSFORMATION KINETICS IN TIMETAL LCB (Ti-6.5Mo-4.5Fe-1.5Al)

Basak Kokuoz
Clemson University, byazgan@clemson.edu

THE ROLE OF CRYSTALLOGRAPHIC RELATIONSHIPS BETWEEN ALPHA(α) AND BETA(β) PHASES ON THE ELEVATED TEMPERATURE ISOTHERMAL PHASE TRANSFORMATION KINETICS IN TIMETAL LCB (Ti-6.5Mo-4.5Fe-1.5Al)

A Thesis
Presented to
the Graduate School of
Clemson University

In Partial Fulfillment
of the Requirements for the Degree
Master of Science
Materials Science and Engineering.

---

by
Basak Kokuoz
August 2008

Accepted by:
Dr. Stephen H. Foulger, Committee Chair
Dr. Eric Skaar
Dr. Jian Luo

ABSTRACT

This investigation has examined the mechanisms controlling the precipitation of various alpha (α) phase morphologies which form during the elevated temperature beta(β)→beta(β)+alpha(α) phase transformations in TIMETAL Low Cost Beta (TIMETAL LCB, Ti-6.8Mo-4.5Fe-1.5Al, in wt.%).

Alpha (α) phase precipitation was promoted by aging the TIMETAL LCB specimens in the α+β two phase region. The temperature range considered was between 700-745^{o}C.The specimens were isothermally aged for successively increasing times, starting at 30 seconds until the equilibrium microstructure was achieved. Solution treated and aged TIMETAL LCB specimens were investigated using x-ray diffraction (XRD), optical (OM) and scanning electron microscopy (SEM), electron backscattered diffraction (EBSD) and quantitative image analysis techniques.

EBSD analysis indicated that, the grain boundary character distribution in the single phase, solution treated TIMETAL LCB can be controlled and modified by the proper choice of solution treatment schedule. Quantitative image analysis measurements also showed that, grain boundaries within the single phase microstructure tend to reduce their overall energy by decreasing the surface area of high energy boundaries during grain growth.

During isothermal aging, the β phase decomposes into three different α morphologies. These morphologies can be classified using the system developed

by Dubė as a) grain boundary allotriomorphs (α_{GRB}), b) widmenstätten side plates (α_{WSP}) and c) widmenstätten intragranular plates (α_{WIG}).

SEM examination of the aged microstructures showed that, grain boundary alpha allotriomorphs ($_{\alpha GRB}$) are the first transformation morphology to appear, independent of the aging temperature. Precipitation of α_{GRB} does not occur simultaneously on the entire grain boundary area during the early stages of the transformation and α_{GRB} distribution is confined to select grain boundaries. EBSD analysis indicated that, the specific choice of a particular grain boundary is based on the orientations of the α_{GRB} and β grains. In each instance, α_{GRB} hold a Burger's orientation relationship (OR) with respect to one of the adjacent β grains and lower the activation energy barrier required during precipitation. Further reduction in the activation energy barrier is possible if the orientation relationship between α_{GRB} particles and the adjacent β matrix slightly deviates (typically 7-8^{o}) from an exact Burger's OR.

Quantitative image analysis measurements showed that, the uniformity of α_{GRB} precipitates increases with increasing aging time and decreasing undercooling. Untransformed grain boundary area at high undercoolings involves the low angle boundaries.

Once the orientation of α_{GRB} is established, widmenstätten side plate morphology (α_{WSP}) grows into the β matrix from α_{GRB} with the same orientation. α_{WSP} particles also maintain a Burger's OR with one of the adjacent β grains and grow into this grain. SEM examination suggests that, evolution α_{WSP} morphology

is controlled by the formation of micron sized facet along the grain boundaries with the increasing surface area of micron sized facets at lower undercoolings being associated with higher α_{WSP} volume fraction.

The final $\beta \rightarrow \beta+\alpha$ transformation involves the homogenous nucleation of widmenstätten intragranular plates (α_{WIG}) within the matrix grains. The driving force for the formation of α_{WIG} is the volume free energy change and increases with decreasing undercooling. As a result, the volume fraction of α_{WIG} particles increases with decreasing aging temperature.

Jonhson-Mehl-Avrami (JMA) analysis implied that, overall phase transformations up to 745^{o}C can be described by two stages. At temperatures below 745^{o}C, the transformation includes rapid lengthening of grain boundary alpha particles which consume the available heterogeneous nucleation sites early during the reaction. Further progression of the $\beta \rightarrow \beta+\alpha$ transformation takes place by the lengthening of the side plates into the β matrix. The first stage is terminated when $\alpha_{GRB}+\alpha_{SP}$ reaches its equilibrium state. The second stage of the transformation is controlled solely by the two dimensional thickening of the intragranular alpha plates. At 745^{o}C, $\beta \rightarrow \beta+\alpha$ transformation takes place at a single stage. Grain boundary alpha is the only transformation product available at this temperature and the transformation is controlled by the thickening of grain boundary alpha precipitates.

DEDICATION

This thesis is dedicated to my love, husband and best friend Baris Kokuoz for always encouraging me to follow my dreams and standing by me in the most difficult times.

ACKNOWLEDGEMENTS

I would like express my sincere gratitude to everyone who has guided me, encouraged me, inspired me and supported me during my graduate studies.

TABLE OF CONTENTS

Page

TITLE PAGE ..... **i**

ABSTRACT ..... **ii**

DEDICATION ..... **v**

ACKNOWLEDGEMENTS ..... **vi**

LIST OF TABLES ..... **x**

LIST OF FIGURES ..... **xv**

CHAPTER

1. INTRODUCTION **1**
References 4

2. BACKGROUND **10**
Understanding the Metastable Beta (β) Titanium Alloys 10
Understanding the Overall Transformation Kinetics of Metastable Titanium Alloys 19
Understanding the Nucleation of Alpha Phase in Metastable β Titanium Alloys 27
Volume Free Energy 29
Surface Free Energy 32
Strain Free Energy 34
Nucleation Rate 41
Homogenous (Matrix) Nucleation 43
Heterogeneous (Grain Boundary) Nucleation 44
Orientation Relationships Between α and β Phases 46
Understanding the Growth of Alpha Phase in Metastable β Titanium Alloys 51
Growth of Grain Boundary Alpha Precipitates 52
Growth of Plate-like Precipitates 57
Understanding Grain Boundary Structure 62
Low Angle Boundaries 64
High Angle Boundaries 69

Table of Contents (Continued)

Page

Understanding Electron Back Scatter Diffraction (EBSD) to Study the Crystallographic Relationships between Alpha (α) and Beta (β) Phases 75
Formation of Kikuchi Bands 80
Detecting Kikuchi Bands 84
Indexing Kikuchi Bands 88
Crystal Orientation 88
The ideal Orientation 91
The Euler Angles 92
The Angle/Axis Rotation 94
The Rodrigues Vector 96
Orientation Imaging Microscopy(OIM) 97
References 99

3. EXPERIMENTAL PROCEDURES 109
As Received Material 109
Heat Treatment 110
Metallographic Sample Preparation 115
Microstructural Characterization 117
X-Ray Diffraction (XRD) 117
Electron Backscatter Diffraction (EBSD) Analysis 117
Quantitative Metallography 120
Volume Fraction Measurements 120
Surface Area Measurements 122
Grain Size Measurement 123
References 124

4. RESULTS AND DISCUSSION 125
Designing A Solution Treatment Procedure 125
Solution Treatment Temperature 125
Solution Treatment Time 130
X-Ray Diffraction (XRD) Analysis of the Solution Heat Treated TIMETAL LCB Specimens 132
Orientation Imaging Microscopy of the Solution Heat Treated Microstructure 137
Results of the Orientation Imaging Microscopy (OIM) 137
Discussion of the Orientation Imaging Microscopy (OIM) 145
Conclusions of the Orientation Imaging Microscopy (OIM) 149
Elevated Temperature Phase Transformation Kinetics of TIMETAL LCB 153

Table of Contents (Continued)

Page

Result of the Phase Transformation Kinetics 153
Discussion of the Phase Transformation Kinetics 185
Conclusions of the Phase Transformation Kinetics 205
References 207

5. SUMMARY AND CONCLUSIONS 211

APPENDIX: Volume Fraction Data 215

LIST OF TABLES

Table Page

2.1. Effect of aging temperature on the room temperature tensile properties of TIMETAL.....18

2.2. c/a ratios for various second phae precipitate shapes; c and a are the semi axes for a given shape. 38

3.1. Chemical composition of Ti-6.5 Mo-4.5Fe-1.5Al 109

3.2. Aging Treatment Conditions 114

4.1. Angle/Axis Pair and V_m values of several CSL type boundaries.....149

4.2. Angle/Axis pairs of grain boundaries.....159

4.3. Angle/axis pairs of boundaries displaying alpha phase precipitation in TIMETAL LCB aged at 745°C for 17 minutes. 164

4.4. Angle/axis pairs of boundaries displaying alpha phase precipitation in TIMETAL LCB aged at 700°C for 6 minutes. 166

A.2. Total Volume Percent Data of TIMETAL LCB Solution Treated at 820°C for 30 minutes and aged at 745°C for subsequently increasing times. 229

A.2. Total Volume Percent Data of TIMETAL LCB Solution Treated at 820°C for 30 minutes and aged at 730°C for subsequently increasing times. 230

A.3. Total Volume Percent Data of TIMETAL LCB Solution Treated at 820°C for 30 minutes and aged at 715°C for subsequently increasing times. 231

A.4. Total Volume Percent Data of TIMETAL LCB Solution Treated at 820°C for 30 minutes and aged at 700°C for subsequently increasing times. 232

List of Tables (Continued)

Table Page

A.5. Grain Boundary Alpha Volume Percent Data of TIMETAL LCB Solution Treated at 820°C for 30 minutes and aged at 745°C for subsequently increasing times 233

A.6. Grain Boundary Alpha Volume Percent Data of TIMETAL LCB Solution Treated at 820°C for 30 minutes and aged at 730°C for subsequently increasing times 234

A.7. Grain Boundary Alpha Volume Percent Data of TIMETAL LCB Solution Treated at 820°C for 30 minutes and aged at 715°C for subsequently increasing times 235

A.8. Grain Boundary Alpha Volume Percent Data of TIMETAL LCB Solution Treated at 820°C for 30 minutes and aged at 700°C for subsequently increasing times 236

A.9. Side Plate Volume Percent Data of TIMETAL LCB Solution Treated at 820°C for 30 minutes and aged at 745°C for subsequently increasing times. 237

A.10. Side Plate Volume Percent Data of TIMETAL LCB Solution Treated at 820°C for 30 minutes and aged at 730°C for subsequently increasing times. 238

A.11. Side Plate Volume Percent Data of TIMETAL LCB Solution Treated at 820°C for 30 minutes and aged at 715°C for subsequently increasing times. 239

A.12. Side Plate Volume Percent Data of TIMETAL LCB Solution Treated at 820°C for 30 minutes and aged at 700°C for subsequently increasing times. 240

A.13. Intragranular Alpha Volume Percent Data of TIMETAL LCB Solution Treated at 820°C for 30 minutes and aged at 745°C for subsequently increasing times. 241

List of Tables (Continued)

Table Page

A.14. Intragranular Alpha Volume Percent Data of TIMETAL LCB Solution Treated at 820°C for 30 minutes and aged at 730°C for subsequently increasing times. 242

A.15. Intragranular Alpha Volume Percent Data of TIMETAL LCB Solution Treated at 820°C for 30 minutes and aged at 715°C for subsequently increasing times. 243

A.16. Intragranular Alpha Volume Percent Data of TIMETAL LCB Solution Treated at 820°C for 30 minutes and aged at 700°C for subsequently increasing times. 244

A.17. Average Total Volume Percent (P_P), Standard Deviation ($\sigma(V_V)$) and Accuracy (acc(%)) of TIMETAL LCB Solution Treated at 820°C for 30 minutes and aged at 745°C for subsequently increasing times 245

A.18. Average Total Volume Percent (P_P), Standard Deviation ($\sigma(V_V)$), and Accuracy (acc(%)) of TIMETAL LCB Solution Treated at 820°C for 30 minutes and aged at 730°C for subsequently increasing times 245

A.19. Average Total Volume Percent (P_P), Standard Deviation ($\sigma(V_V)$), and Accuracy (acc(%)) of TIMETAL LCB Solution Treated at 820°C for 30 minutes and aged at 715°C for subsequently increasing times 246

A.20. Average Total Volume Percent (P_P), Standard Deviation ($\sigma(V_V)$), and Accuracy (acc(%)) of TIMETAL LCB Solution Treated at 820°C for 30 minutes and aged at 700°C for subsequently increasing times 246

A.21. Average Grain Boundary Alpha Volume Percent (P_P), Standard Deviation ($\sigma(V_V)$) and Accuracy (acc(%)) of **T**IMETAL LCB Solution Treated at 820°C for 30 minutes and aged at 745°C for subsequently increasing times. 247

A.22. Average Grain Boundary Alpha Volume Percent (P_P), Standard Deviation ($\sigma(V_V)$) and Accuracy (acc(%)) of TIMETAL LCB Solution Treated at 820°C for 30 minutes and aged at 730°C for subsequently increasing times. 247

List of Tables (Continued)

Table Page

A.23. Average Grain Boundary Alpha Volume Percent (P_P), Standard Deviation ($\sigma(V_V)$) and Accuracy (acc(%)) of TIMETAL LCB Solution Treated at 820°C for 30 minutes and aged at 715°C for subsequently increasing times. 248

A.24. Average Grain Boundary Alpha Volume Percent (P_P), Standard Deviation ($\sigma(V_V)$) and Accuracy (acc(%)) of TIMETAL LCB Solution Treated at 820°C for 30 minutes and aged at 700°C for subsequently increasing times. 248

A.25. Average Side Plate Volume Percent (P_P), Standard Deviation ($\sigma(V_V)$) and Accuracy (acc(%)) of TIMETAL LCB Solution Treated at 820°C for 30 minutes and aged at 745°C for subsequently increasing times. 249

A.26. Average Side Plate Volume Percent (P_P), Standard Deviation ($\sigma(V_V)$) and Accuracy (acc(%)) of TIMETAL LCB Solution Treated at 820°C for 30 minutes and aged at 730°C for subsequently increasing times. 249

A.27. Average Side Plate Volume Percent (P_P), Standard Deviation ($\sigma(V_V)$) and Accuracy (acc(%)) of TIMETAL LCB Solution Treated at 820°C for 30 minutes and aged at 715°C for subsequently increasing times. 250

A.28. Average Side Plate Volume Percent (P_P), Standard Deviation ($\sigma(V_V)$) and Accuracy (acc(%)) of TIMETAL LCB Solution Treated at 820°C for 30 minutes and aged at 700°C for subsequently increasing times. 250

A.29. Average Intragranular Alpha Volume Percent (P_P), Standard Deviation ($\sigma(V_V)$) and Accuracy (acc(%)) of TIMETAL LCB Solution Treated at 820°C for 30 minutes and aged at 745°C for subsequently increasing times. 251

List of Tables (Continued)

Table Page

A.30. Average Intragranular Alpha Volume Percent (P_P), Standard Deviation ($\sigma(V_V)$) and Accuracy (acc(%)) of TIMETAL LCB Solution Treated at 820°C for 30 minutes and aged at 730°C for subsequently increasing times. 251

A.31. Average Intragranular Alpha Volume Percent (P_P), Standard Deviation ($\sigma(V_V)$) and Accuracy (acc(%)) of TIMETAL LCB Solution Treated at 820°C for 30 minutes and aged at 715°C for subsequently increasing times. 252

A.32. Average Intragranular Alpha Volume Percent (P_P), Standard Deviation ($\sigma(V_V)$) and Accuracy (acc(%)) of TIMETAL LCB Solution Treated at 820°C for 30 minutes and aged at 700°C for subsequently increasing times. 252

LIST OF FIGURES

Figure Page

2.1. Schematic illustration of β(bcc)→α(hcp) transformation in pure titanium. Tβ=882.5°C 11

2.2. Typical equilibrium binary phase diagram of titanium with a) neutral b) alpha stabilizing c) β isomorphous alloying element d) a β eutectoid alloying element. 12

2.3. Pseudo binary phase diagram of titanium and a β stabilizer. β_c and β_s are the minimum β stabilizer content for metastable and stable beta titanium alloy formation, respectively 14

2.4. Molybdenum equivalence of various metastable β titanium alloys. 14

2.5. Schematic of metastable β titanium alloy manufacturing 16

2.6. BSEI micrograph of a)α+β processed b) aged TIMETAL LCB, ... 16
work done for this project.

2.7. Evidence of high cycle fatigue crack initiation at the grain boundary α/β interface in TIMETAL LCB (work done for this project) 18

2.8. Isothermal Time-Temperature-Transformation Diagram for Ti-6.5 Mo-4.5Fe-1.5Al 19

2.9. Schematic illustration of successive steps during β→α transformation. Alpha particles grow into and through each other and nucleation happen everywhere including in regions that have already transformed 21

2.10. The equilibrium phase diagram showing the isothermal solid-solid transformation of β→β+α at T_1. c_α and c_β are equilibrium compositions of α and β phases respectively. co represents the alloy composition. 28

2.11. Schematic for the graphical determination of the free energy change associated with the precipitation of α phase 29

List of Figures (Continued)

Figure Page

2.12. A section through γ-plot illustrating the equilibrium shape of a precipitate showing a) incoherent interface at all precipitate matrix interface orientations. b) one coherent or semi coherent interface at only one precipitate/matrix interface orientation. 34

2.13. Schematic illustration of origin of coherency and volume strains during coherent and incoherent precipitation, respectively 36

2.14. The variation of $f\left(c/a\right)$ with c/a 38

2.15. Variation in the free energy of the system as function of cluster size.....40

2.16. Schematic illustration of a heterogeneous critical nucleus. 45

2.17. Schematic of illustration of a) superimposed closed packed {110} bcc and {0001} hcp planes b) parallel $<111>$ and $<11\bar{2}0>$ directions (shown with an arrow on the figure) that was brought into coincidence by a rotation of hcp crystal about $<0001>$ by 5.26^{o}.....48

2.18. Stereographic projection of Burgers Orientation Relationship. This projection is projected normal to the close packed {110} and {0001} planes in the two structures. Open circles represent the bcc pole and closed circles represent the hcp poles. 48

2.19. Schematic illustration of composition profile across an α/β interface moving under a) diffusion-control b) interface-control growth. 52

2.20. The binary phase diagram showing the bulk and the α/β interface composition. 53

2.21. Simplified composition profiles across the α/β interface 55

2.22. Balance of interfacial energies assumed at the advancing edge of a grain boundary precipitate. 57

2.23. Composition profile along the centerline of a plate-like alpha precipitate. 59

List of Figures (Continued)

Figure Page

2.24. Effect of curvature on the a) composition of the β phase infront of the α/β phase boundary b) composition profile along centerline of a plate-like precipitate 60

2.25. Schematic illustration of a a) tilt and b) twist boundary. 63

2.26. Schematic illustration of an array of dislocations along a low angle tilt boundary. 65

2.27. Variation of the grain boundary energy as a function of misorientation.....68

2.28. Schematic illustration of the island model of Mott. 70

2.29. Schematic illustration of the grain boundary model of Schomolowski. ...71

2.30 Schematic of a ∑=5 CSL boundary. 72

2.31. Schematic illustration of a grain boundary lying along a) a low index plane b) a random high index plane and c) illustration of faceting of a random grain boundary. 73

2.32. Various signals that can be detected in a scanning electron microscope. 75

2.33. Components of an EBSD system.....79

2.34. Scattering of a planar wave front from a single atom with in the material giving rise to spherical wave. 80

2.35. Schematic illustration of the diffraction from lattice planes. The geometry of diffraction leads to derivation of the Bragg's law. 81

2.36. Schematic representation of the origin of Kikuchi lines. 83

2.37. EBSD Kikuchi pattern from Ti-6.5Mo-4.5Fe-1.5Al, 20kV accelerating voltage, work done for this project. 83
List of Figures (Continued)

2.38. Schematic illustration of a Kikuchi pattern as a gnomonic projection. 85

List of Figures (Continued)

Figure Page

2.39. Variation in diffraction pattern with crystal orientation. 85

2.40. Schematic of transformation of x-y coordinates to Hough space. The numbers given do not have any physical significance. They are for illustrative purposes only.....87

2.41. Photograph of a a) hough transform and b) its corresponding EBSD pattern with the detected bands, work done for this project. 88

2.42. Schematic illustration of the relationship between the crystal and sample coordinate systems. α_1 ,β_1 and γ_1 are the angles between the crystal direction [100] and X_s, Y_s and Z_s(Normal Direction) respectively. α_2, β_2, γ_2 and α_3, β_3, γ_3 are similarly defined as the angles between the [010] and [001] crystal directions and the three sample axes. 89

2.43. Schematic illustration of the effect of rotating a crystal with its <100>, <010>, <001> directions being parallel to the specimen's x, y, z axes about the <001> by an angle φ_1 followed by a rotation about the <100> direction by an angle ϕ and finally rotating φ_2 degrees about the <001> direction on the sample orientation. 93

2.44. Schematic illustration of Euler coloring which transforms an orientation $(\varphi_1, \phi, \varphi_2)$ to an RGB (Red, Green, Blue) color (Channel 5^{TM} User Manual). 95

2.45. Schematic illustration of the angle/axis pair. 96

3.1. Schematic of salt bath set up used to heat treat TIMETAL LCB specimens.....111

3.2. Isothermal Time-Temperature-Transformation Diagram for Ti-6.5 Mo-4.5Fe-1.5Al [1]. 113

3.3. Schematic of Heat Treatment Procedure.....113

List of Figures (Continued)

Figure Page

3.4. Successive steps of sample preparation (a) cutting the as-received material parallel to transverse direction. (b) Sectioning 30 cm long bars into 10 mm long blanks. c) Removing the oxide layer due to heat treatment. (c) Coarse grinding followed by fine polishing to eliminate the deformed layer.(d) Optical or scanning electron microscopy examination. ...116

3.5. Schematic steps involved in a) automatic data collection mode during orientation imaging microscopy and b) interactive data collection mode in an HKL EBSD system. 119

4.1. BSEI micrographs of as-received Ti-6.5 Mo-4.5Fe-1.5Al a) Low magnification b) High magnification. 126

4.2. BSEI of Ti-6.5Mo-4.5Fe-1.5Al solution treated at a) 633^0C b) 715^oC c) 730^oC d) 745^oC e)760^oC f) 790^oC for 30 minutes followed by water quenching. 127

4.3. BSEI of Ti-6.5Mo-4.5Fe-1.5Al solution treated at a) 800^0C b) 810^oC c) 820^oC for 30 minutes followed by water quenching. 128

4.4. Comparison of the experimental and theoretical volume fraction of alpha phase with temperature. Samples were solution treated for 30 minutes. 129

4.5. BSEI micrograph of TIMETAL LCB Solution treated at 820^0C for 30 minutes followed indirect aging at 550^oC for 5 minutes and subsequently water quenched at room temperature. 131

4.6. X-ray diffraction spectra of TIMETAL LCB solution heat treated at a) 700^oC b)715^oC c) 730^oC and d) 745^oC. 133

4.7. Influence of solution treatment temperature on a) a_β b)a_α and c)c_α.....135

4.8. BSEI of TIMETAL LCB solution treated for 30 minutes at 820^oC and water quenched. 138

4.9. a)Crystal orientation map of solution treated TIMETAL LCB b) All Euler Key. c)Image Quality (IQ) Map. 138

List of Figures (Continued)

Figure Page

4.10. OIM map of TIMETAL LCB solution treated for 30 minutes a)grain boundary map (red $5 \leq \theta \leq 22.5^{o}$, black $22.5 < \theta < 52.5^{o}$, blue $52.5 < \theta < 62.5^{o}$) and b) grain boundary map key representing grain boundary misorientations. 141

4.11. OIM map of TIMETAL LCB solution treated for 5 minutes a)grain boundary map (green $5 \leq \theta \leq 22.5^{o}$, aqua $22.5 < \theta < 52.5^{o}$, red $52.5 < \theta < 62.5^{o}$) and b) grain boundary map key representing grain boundary misorientations. 142

4.12. Effect of solution treatment time on the grain size of TIMETAL LCB. ... 142

4.13. Effect of solution treatment time on the grain boundary surface area per unit volume. 144

4.14. Predicted grain boundary energy as a function of tilt angle 147

4.15. Distribution of CSL type boundaries in TIMETAL LCB solution heat treated for 30 minutes. 149

4.16. Frequency of CSL boundary distribution. 150

4.17 Grain boundary map illustrating the distribution of grain boundaries with in the misorientation range 52.5-62.5^{o} (black lines). 150

4.18. SEM micrographs of TIMETAL LCB a) Solution treated at 820^{0}C for 30 minutes followed by water quenching b) Solution treated at 820^{0}C for 30 minutes and subsequently aged at 700^{0}C for 60 seconds followed by water quenching..... 154

4.19 BSEI micrographs illustrating a)Grain boundary α precipitation at a triple point junction b) grain boundary α precipitation on a grain boundary surface c) grain boundary alpha film formation of TIMETAL LCB aged at 745^{o}C for three minutes.. 155

4.20. BSEI micrograph showing three β grains meeting at a triple point junction in TIMETAL LCB aged at 700^{o}C for 3 minutes.. 156

List of Figures (Continued)

Figure Page

4.21. Pole figures of the a) β_1 b) β_2 and c) β_3 grains. The common (102) direction in β_1 and β_2 grains is shown with an arrow. 156

4.22. BSEI images demonstrating grain boundary α precipitation in TIMETAL LCB specimens aged at a-b) 700°C c-d) 715°C e-f)745°C and g-h)745°C for 3 minutes.. 158

4.23. Variation in the transformed grain boundary area with aging time and temperature. 161

4.24. Low magnification BSEI micrograph of TIMETAL LCB aged at 745°C for 17 minutes. Alpha (α) phase precipitation is confined to select grain boundaries. 161

4.25. High magnification BSEI micrographs demonstrating α phase precipitation on different regions of the same grain boundary between β_1 and β_2 grains...162

4.26. Results of the EBSD analysis. a) $\{0001\}_\alpha$ b) $\{11\bar{2}0\}_\alpha$ c) $\{110\}_{\beta_1}$ d) $\{111\}_{\beta_2}$ e) $\{110\}_{\beta_2}$ and f) $\{111\}_{\beta_2}$ pole figures.....162

4.27. Low magnification BSEI micrograph of TIMETAL LCB aged at 700°C for 6 minutes.. 166

4.28. BSEI micrograph showing a triple point junction at the intersection of grains β_1, β_2 and β_3.....169

4.29. The pole figures of a) β_1 b) β_2 and c) β_3 grains. Common axes between grains are indicated by arrows. 169

4.30. BSEI micrograph illustrating alpha phase precipitation on a low angle boundary between β_1 and β_2 grains. 170

4.31. The pole figures of a) β_1 and c) β_3 grains. Common $\{0\bar{2}\bar{1}\}$ axis between these grains is indicated by an arrow. 170

4.32. FE-SEM micrograph illustrating a) the onset of side plate growth from grain boundary alpha precipitates in TIMETAL LCB aged at 700°C for 25 minutes.. 172

List of Figures (Continued)

Figure Page

4.33. BSEI micrographs demonstrating side plate growth on a) single side b) both sides of the grain boundary in aged TIMETAL LCB..... 172

4.34. High magnification BSEI micrograph illustrating two different grain boundary alpha morphologies (α_1 and α_2) precipitating on a grain boundary between β_1 and β_2 in TIMETAL LCB aged at 700°C for 30 minutes 173

4.35. Results of the EBSD analysis. a) $\{0001\}$ b) $\{11\bar{2}0\}$ pole figures α_1 precipitates. Superimposed c) $\{0001\}$ d) $\{11\bar{2}0\}$ pole figures α_2 and α_3 precipitates.. e) $\{110\}$ and f) $\{111\}$ pole figures of the β1 grain. g) $\{110\}$ and h) $\{111\}$ pole figures of the β_2 grain..... 174

4.36. FE-SEM micrograph illustrating oriented side plate growth into β matrix in TIMETAL LCB aged at 700°C for 200 minutes..... 176

4.37. Evolution of alpha precipitates in TIMETAL LCB specimens aged at a) 700°C for 40 min. b)715°C for 50 min c)730°C for 40 min d)745°C for 50 min..... 177

4.38. Influence of aging temperature on the side plate volume fraction at 40 minutes. The data point presented at 745°C correspond to 60 minutes aging..... 178

4.39. Variation in the volume fraction of α phase with aging time and corresponding BSEI micrographs at a) 700°C b)715°C c)730°C and d)745°C..... 180

4.40. Equilibrium volume percent of α phase as a function of aging temperature..... 183

4.41. Equilibrium microstructures of TIMETAL LCB samples aged a) 700°C b)715°C c) 730°C and d)745°C..... 183

.

4.42. Equilibrium volume percent of a)Grain boundary α b) Side plates c) Intragranular α plate..... 184

4.43. Effect of a) Grain boundary energy b) undercooling on α phase precipitation..... 189

List of Figures (Continued)

Figure Page

4.44. Schematic representation of α phase precipitation on a) a pure tilt boundary b) a boundary deviating from pure tilt character [48]. 191

4.45. Variation in the a) percentage of transformed grain boundary area b) grain boundary alpha thickness with aging temperature.. 191

4.46. BSEI micrograph illustrating a)non uniform grain boundary α distribution in TIMETAL LCB aged at 745^{o}C. Arrows indicate untransformed grain boundary area b) uniform grain boundary α distribution in TIMETAL LCB aged at 700^{o}C.. 193

4.47. BSEI micrograph illustrating a) α phase precipitation at a triple point junction in TIMETAL LCB aged for 3 minutes b) rapid lengthening of alpha phase precipitates along the grain boundaries with increasing aging time to 10 minutes. 195

4.48. Schematic illustration of the relationship between the closed packed β planes and the grain boundary plane along a a) flat boundary b) faceted boundary. 195
.
4.49. Effect of aging temperature on the percentage of equilibrium faceted grain boundary area per unit volume $\%S_v$(faceted) 197

4.50. Application of JMA law to isothermal phase transformation kinetics at a)700^{o}C b)715^{o}C c)730^{o}C and d)745^{o}C.. 200

4.51. Time-Temperature-Transformation(TTT) curve of TIMETAL LCB obtained by a) Electron microscopy and image analysis b) Optical microscopy and –X-ray diffraction techniques as reported by Azimzadeh [5]. 204

CHAPTER I

INTRODUCTION

Metastable beta (β) titanium alloys are receiving ever-increasing attention for possible incorporation in automotive suspension systems [1-10]. Their high strength to density ratio, high toughness and low modulus make them attractive candidates for these applications [11, 12].In general, metastable β titanium alloys exhibit relatively low strengths in the un-aged condition which limits their use in structural applications[12,13]. However, these alloys are age hardenable; their strengthening being achieved through the precipitation of secondary phases [14-20].

Essentially precipitation behavior of the alpha (α) phase in metastable β titanium alloys can be characterized by two distinct temperature regimes: a) low temperature regime, where β phase may transform first into a metastable "transition" phase followed by the precipitation of equilibrium α phase and b) high temperature regime, in which the β phase directly decomposes into various α phase morphologies resulting in the equilibrium α+β microstructure. A typical morphological development sequence within the high temperature regime includes heterogeneous precipitation of α phase on the grain boundaries followed by side plate growth in the vicinity of the aforementioned grain boundary α and intragranular alpha precipitation within the β matrix [21].

The low temperature phase transformations of metastable β titanium alloys have been studied extensively [22-28]. There are also numerous studies

reporting the direct decomposition of metastable β phase into equilibrium α at elevated temperatures with the primary emphasis being the effect of thermo-mechanical processing variables, impurities and solute elements on the α phase volume fraction and morphology [29-35]. Only a few of these studies have focused on the global β to α phase transformation kinetics [30-35].

Morphological development of precipitates is not only governed by kinetic factors such as time and temperature but also by the grain boundary structure and the crystallographic relationships between the precipitate and matrix. Effect of grain boundaries on the precipitation of second phases has been the subject of several investigations in Al- and Fe- based alloys [36-45]. However, there have been relatively few attempts to relate the grain boundary structure to the nucleation and growth of alpha particles in titanium alloys [46-52]. In general, the main focus of these studies has been the precipitation of the α phase in the α/β titanium systems [48-52].

The objective of this study was to bring an understanding to the mechanisms controlling the precipitation of various α phase morphologies which form during the elevated temperature β→β+α phase transformations in TIMETAL LCB by investigating the:

1) effect of solution treatment conditions on the grain and grain boundary structure;

2) decomposition sequence of β phase into various α phase morphologies at temperatures close to T_β;

3) contribution of various alpha phase morphologies on the overall transformation kinetics;

4) role of crystallographic relationships between these morphologies and the β phase on the progression of phase transformations.

Such an understanding is of primary importance to predict the final microstructure and achieve a wide variety of microstructure/property combinations through altering the thermo mechanical processing conditions.

References

1) Ferrari Stradale First to Use All-Titanium Springs, *Auto Technology*, 4, 2004, p.34.

2) Faller, K., Ferrari First to Ride on all Titanium Springs, *Springs,*43, 2004, p.39-41.

3) Ponticel, P., TIMET titanium for Ferrari springs, *Automotive Engineering International*, 112, 2004, pp.83-85.

4) Kosaka, Y., Fox, S. P., Faller, K., Reichman, S. H., Tilly, D., Low cost processes for automotive titanium materials, Cost Affordable Titanium: A Symposium Dedicated to Harvey Flower, TMS Annual Meeting, Charlotte, USA, 14-18 March 2004, pp.77-84,.

5) Titanium cuts weigth, raises performance in auto springs, *Advanced Materials and Processes*, 161 (6), 2003, pp. 11.

6) Wringley, A., TIMET wins Japanese auto spring deal: Nippon Steel marketing titanium as substitute, *American Metal Market* (USA), 109 (203), 2001, pp. 5.

7) Wringley, A., Hope 'springs' for automotive applications, *American Metal Market* (USA), 109,2001, pp.8A.

8) Haflich, F., VW's Lupo FSI to rise on titanium springs, *American Metal Market* (USA), 109 (10), 2001, pp. 8.

9) Timet announces introduction of titanium suspension springs, *Light Metals News*, 2, 2001, pp. 7.

10) Allen, P, G., Bania, P. J., Hutt, A. J., Combres, Y., TIMETAL LCB: a low cost beta alloy for automotive and other industrial applications, *Titanium '95,* Birmingham, UK, 22-26 October 1995, 2, 1996, pp.1680-1687.

11) P. J. Bania, Beta Titanium Alloys and Their Role in the Titanium Industry, *Beta Titanium Alloys of the 1990s*, 1st ed., D. Eylon, R. R. Boyer and D. A. Koss, Eds., Feb. 22-24, 1993 (Denver), Titanium Committee of TMS, TMS Waarendale, PA, 1993, p.211 – 226.

12) Metals Handbook, 9th ed., Vol. 1-3, American Society for Metals, Metals Park, OH, 1980, pp. 422-448 (Vol. 1), 115-136 (Vol. 2), 378-405 (Vol. 3).

13) Wagner, L. and Gregory, J. K., "Fatigue and Fracture Properties of Titanium Alloys", *ASM Handbook,* Vol. 19, ASM International, p. 829-853.

14) J. C. Fanning, Fatigue Data for TIMETAL 15-3, *Beta Titanium Alloys of the 1990s*, 1st ed., D. Eylon, R. R. Boyer and D. A. Koss, Eds., Feb. 22-24, 1993 (Denver), Titanium Committee of TMS, TMS Waarendale, PA, 1993, p. 439-798

15) Morgan, G. C., The Ageing Characteristics of Two Metastable Beta Titanium Alloys, *Modern Metallography Conference and Exhibition*, Birmingham, England, 1978, pp. 27.

16) Rosenberg, H. W., Ti 15-3 Property Data, *Beta Titanium Alloys in the 1980's*; Atlanta, GA, USA, 8 March 1983, 1984, pp. 409-432.

17) Boyer, R. R., Rosenberg, H. W., Ti-10V-2Fe-3Al Properties, *Beta Titanium Alloys in the 1980's*, Atlanta, GA, USA, 8 March 1983, 1984, pp. 441-456.

18) Rosenberg, H. W. Beta Titanium Alloys for Structural Efficiency, *Materials and Processes-Continuing Innovations*, Anaheim, CA, 12-14 April, 1983, 1983, pp. 1223-1230.

19) Fanning, J. C., TIMETAL 15-3 Property Data, *Beta Titanium Alloys in the 1990's*, Denver, Colarado, USA, 22-24 February, 1993, 1993, 411-43

20) Bania, P. J., *Beta Titanium Alloys and Their Role in Titanium Industry, JOM*(USA), 46(7), 1994, pp.16-19.

21) Azimzadeh, S. and Rack, H.J., Phase transformations in Ti-6.8Mo-4.5Fe-1.5Al, *Metall. and Mater. Trans.A*, Vol. 29A (10), 1998, pp. 2455-2467.

22) Parris, W. M. and Rosenberg, H. W., *Producing Ti-13V-11Cr-3Al Mill Product at TMCA Historical Note II,* Beta Titanium Alloys 1980s, R. R. Boyer and H. W. Rosenberg eds. , Warrandale, P.A., The Metallurgical Society, 1984, pp.9-15.

23) Krugmann, H. E. and Gregory, J. K., *Microstructure and Crack Propogation in Ti-3Al-8V-6Cr-4Mo-4Zr*, Microstructure/Property Relationships in Titanium Aluminides and Alloys, Kim, Y. W. and Boyer, R.R. eds., Warrandale, P.A., The Metallurgical Society, 1991, pp.549-561.

24) Okada, M. *Strengthening of Ti-15V-3Al-3Sn-3Cr- by Two Step Aging*, Sixth World Conference on Titanium, P. Lacombe, R. Tricot and G. Beranger (eds.), 1989, pp. 1625-1628.

25) L. Wagner and J.K. Gregory, Improvement of Mechanical Behavior in Ti-3Al-8V-6Cr-4Mo-4Zr by Dupex Aging, *Beta Titanium Alloys of the 1990s*, 1st ed., D. Eylon, R. R. Boyer and D. A. Koss, Eds., Feb. 22-24, 1993 (Denver), Titanium Committee of TMS, TMS Waarendale, PA, 1993, p.199-210.

26) M. A. Imam, P. K. Poulose and B. B. Rath, Modification of Alpha Phase Precipitation by Cold Work of the Ti 15-5-3 Alloy, *Beta Titanium Alloys in the 1990's*; Denver, Colorado; USA; 22-24 Feb. 1993. pp. 261-271.

27) Furuhara, T., Maki, T. and Makino, T., *Microstructure control by thermomechanical processing in β-Ti–15–3 alloy*, Journal of Materials Processing Technology, Vol. 117, no 3, 2001, pp.318-323.

28) Makino, T., Chikaizumi, R., Nagaoka, T., Furuhara, T. and Makino, T., *Microstructure development in a thermomechanically processed Ti-15V-3Cr-3Sn-3Al alloy*, Materials Science and Engineering A213, 1996, pp.51-60.

29) Lenain A, Clement, N. Veron, N. Jacques, P. J., Characterization of the α phase nucleation in a two phase metastable β Ti alloy, Journal of Materials Engineering and Performance, V. 114(6), 2005, pp.722-727.

30) Bein, S., Comparative approach of phase transformations in titanium alloys Ti—6246, beta Cez, Ti-1023 using dilatometric analysis and electrical resistivity measurements, Titanium 95, V.3, Birmingham, UK, 1996, pp.2353-2360.

31) Imam, M. A. and Feng, C. R., Study of transformation kinetics in TIMETAL 021S Titanium Alloy, Titanium 95, V.3, Birmingham, UK, 1996, pp.2361-2368.

32) Hanada, S. and Izumi, O., The Decomposition of Metastable β Phase in Titanium Alloys, Trans. Jpn. Ins. Met., Vol. 21 (4), 1980, pp.201-210.

33) Costa Teixeri, J. C., Appolaire, B., Gautier, E. A., Denis, S., Callietaud, G., Spath, N., Transformation kinetics and microstructure of Ti17 titanium alloy during continuous cooling, Materials Science and Engineering A, 448, 2007, pp. 135-145.

34) Laude, E., Gautier, E. and Denis, S., Calculation of Transformation Kinetics of Titanium Alloys during Continuous Cooling. Application to the β-Cez alloy, Titanium 95, V.3, Birmingham, UK, 1996, pp.2330-2337.

35) Bein, S. and Bechet, J., Phase Transformation Kinetics and Mechanism in Titanium alloys Ti-6246, β-Cez and Ti-1023, Journal de Physique IV, 6, 1996, pp.C1-99-108.

36) S. Toney and H. I. Aaronson, “Effects of Grain Boundary Structure on Precipitate Morphology in an Fe-1.55 Pct Si Alloy“ , Trans. metal. Soc. AIME, 221, pp.909 (1961).

37)H. I. Aaronson, in Decomposition of Austenite by Diffusional Processes, Zackay and H. I. Aaronson (eds.), Interscience, pp.387- (1962).

38) J. B. Clark, “Effects of Grain Boundary Structure on Precipitate Morphology in Al-18w/o Ag-an Application of High Temperature Electron Microscopy“ in High Temperature High Resolution Metallography, H. I. Aaronson and G. S. Ansell (eds.), Gordon and Breach, Science Publishers, New York, pp. 347-375 (1967).

39) D. Vaughan, “Grain boundary precipitation in an Al-Cu Alloy”, Acta Metall. 16, pp.563-577 (1968).

40) J. K. Park and A. J. Ardell, “ Precipitation at Grain Boundaries in the Commercial Alloy Al 7075”, Acta metal., 34, pp.2399-2409 (1986)

41) P. N. T. Unwin and R. B. Nicholson, “Nucleation and Initial Stages of Growth of Grain Boundary Precipitates in Al-Zn-Mg and Al-Zn Alloys“ Acta Metall, 17., pp. 1379-1393 (1969).

42) D. A. Vaughan, “The precipitation of θ' at high-angle boundaries in an Al-Cu”, alloy, Acta Met., 18, pp. 183-187 (1970).

43) J. K. Park and A. J. Ardell, “Effect of Retroregression and Reaging Treatments on the Microstructure of Al-7075-T651”, Metall. Trans. A, 15, pp.1531- 1543 (1984).

44) J. K. Park and A. J. Ardell, “Microstructures of Commercial 7075 Al Alloy in the T651 and T7 Tempers’, Metall. Trans. A, 14, pp.1957- 1965 (1983).

45) E. P. Butler and P. R. Swann, “In-situ observation of the nucleation and initial growth of grain boundary precipitate in Al-Zn-Mg Alloys”, Acta Metall, 24, pp.343-352 (1976).

46) T. Furuhara, S. Takagi, H. Watanabe and T. Maki, “Crystallography of Grain Boundary Alpha Precipitates in a β Titanium Alloy”, Metallurgical and Materials Transactions A, 27, pp.1635-1646 (1996)

47) T. Furuhara and T. Maki, “Variant Selection in Heterogeneous Nucleation on Defects in Diffusional Phase Transformation and Precipitation”, Mater. Sci. and Eng. A, 312, pp.145-154 (2001).

48) R. Banarjee, P. C. Collins, D. Bhattacharyya, S. Banerjee and H.L. Fraser, “Microstructural evolution in laser deposited compositionally graded α/β titanium –vanadium alloys”, Acta Materialia, 51, pp.3277-3292 (2003).

49) D. Bhattacharyya, G. B. Viswananthan, R. Denkenberger, D. Furrer, H. L. Fraser, “The role of crystallographic and geometrical relationships beteen α and β phases in an α/β titanium alloy”, Acta Materialia, 51, pp. 4679-4691 (2003).

50) R. Banarjee, D. Bhattacharyya, P. C. Collins, G. B. Viswanathan and H. L. Fraser, “Precipitation of grain boundary alpha in a laser deposited compositionally graded Ti-8Al-xV alloy-an orientation microscopy study.”, Acta Mater., 52, pp. 377-385 (2004).

51) D. Bhattacharyya, G. B. Viswanathan and H. L. Fraser, “Crystallographic and morphological relationships between β phase and the Widmenstätten and allotriomorphic α phase at special β grain boundaries in an α/β titanium alloys”. , Acta Mater. , 55 , pp. 6765-6778 (2007).

52) E. Lee, R. Banarjee, S. Kar, D. Bhattacharyya, H. L. Fraser, “Selection of α variants during microstructural evolution in α/β titanium alloys” , Philosophical Magazine, 87, pp.3615-3627 (2007).

CHAPTER II

BACKGROUND

2.1. Understanding the Metastable β Titanium Alloys

In researching titanium for use in the automotive industry, a complete explanation of how titanium is processed to yield usable alloys is necessary. Titanium is abundant in the earth's crust and is extracted from its ore minerals, rutile (TiO_2) and ilmenite ($FeTiO_3$), through Kroll's Process [1]. This process involves treatment of the ore with chlorine gas (Cl_2) to produce titanium tetrachloride ($TiCl_4$), which is then purified and reduced to a metallic titanium sponge by reacting with magnesium or sodium. The chemical process involving the reduction of rutile through magnesium can be described as follows:

$$TiO_2 + 2Cl_2 + 2C \rightarrow TiCl_4 + 2CO \qquad 2.1a$$

$$TiCl_4 + 2Mg \rightarrow 2MgCl_2(l) + Ti \qquad 2.1b$$

At room temperature, unalloyed titanium has a hexagonal closed packed structure (hcp) and is referred to as the (α) phase. Upon exceeding the 'β-transus' temperature (T_β=882.5^{o}C), α titanium transforms into a body centered cubic (bcc) structure [2]. This transformation is depicted in Figure 2.1.

Pure titanium can be blended with other metallic elements to obtain a titanium alloy. The primary reasons for alloying titanium is to alter the α→β transformation temperature and to introduce a two phase range where α- and β-

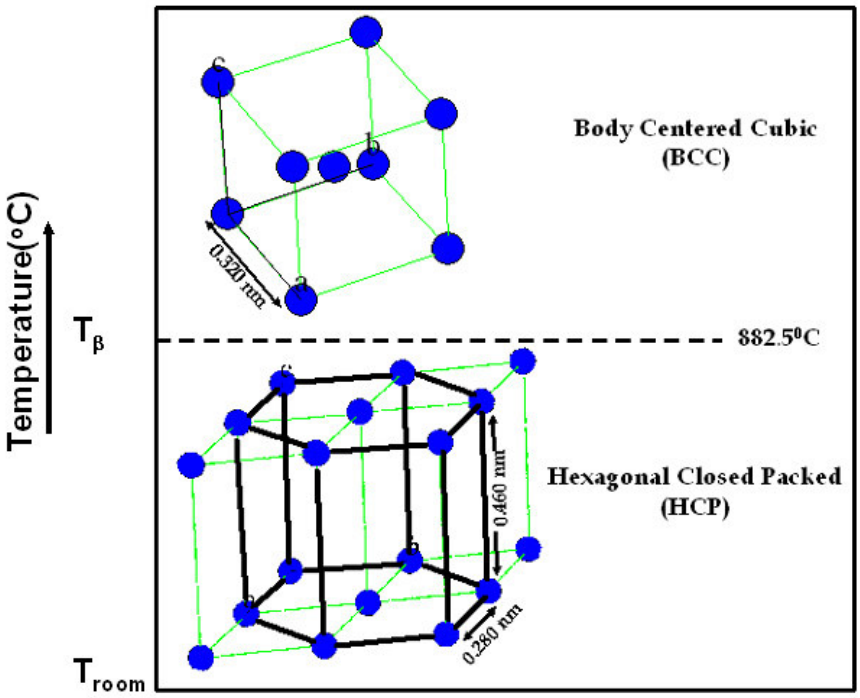

Figure 2.1. Schematic illustration of β (bcc)→α (hcp) transformation in pure titanium. T_β=882.5°C

phases coexist. Depending on their influence on the β-transus temperature, these alloying elements can be sub-divided in three categories: a) *neutral elements, b)alpha stabilizing elements* and b) *beta stabilizing elements* [3].

Alloying elements, that have only a minor influence on the β-transus temperature, are called the neutral elements (Figure 2.2a). Alpha stabilizing elements increase the β-transus temperature and widen the α phase stability range (Figure 2.2b). In contrast the β stabilizing elements lower the β-transus temperature restricting α phase field and can be separated into two: a) *β-isomorphous* and b) *β-eutectoid elements*. While β-isomorphous elements exhibit complete solubility with β titanium (Figure 2.2c), the β-eutectoid stabilizing

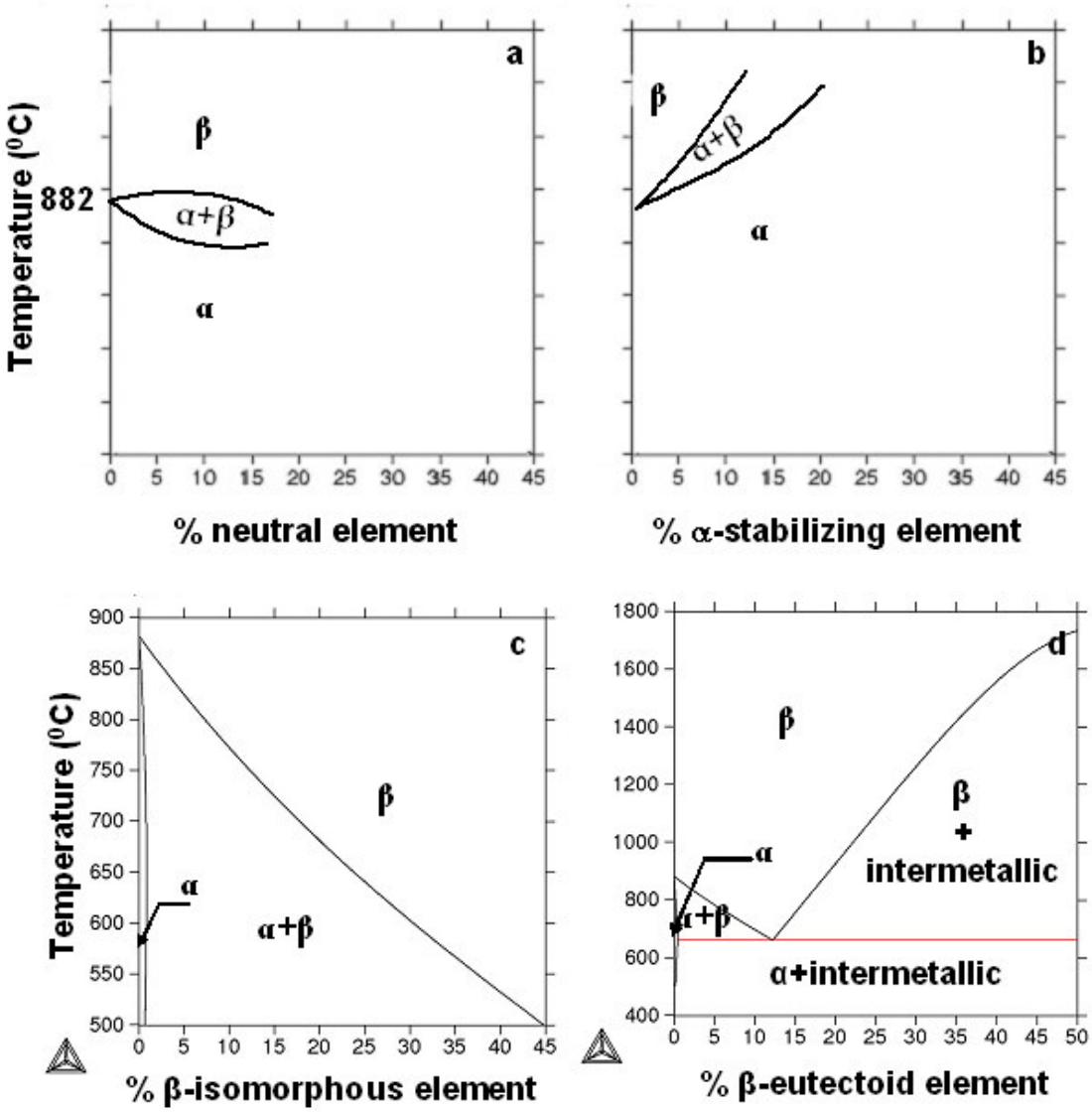

Figure 2.2. Typical equilibrium binary phase diagram of titanium with a) neutral b) alpha stabilizing c) β isomorphous alloying element and d) a β eutectoid alloying element

elements have restricted solid solubility in β titanium and form a two phase α+intermetallic compound region through a eutectoid decomposition of the β phase (Figure 2.2 d).

Insufficient amounts of β stabilizing elements result in a martensitic transformation of the β phase upon quenching from the β phase field. However, by adding sufficient amount of β stabilizing elements, it is possible to lower the martensitic transformation temperature (M_s) to below room temperature and retain the β phase structure upon quenching, shown in Figure 2.3. A "metastable beta (β) titanium alloy" can be defined as any titanium composition with enough β stabilizer content to retain the β phase, without decomposing into martensite, upon quenching to room temperature from elevated temperatures within the single phase β field [4].

This phase stability of alloyed titanium alloys is generally defined by "molybdenum equivalent (MoEq.)" and "aluminum equivalent (AlEq.)" and is calculated in the following manner [5,6] :

$$\begin{aligned} MoEq = {} & 1.0(wt.\%Mo) + 0.67(wt.\%V) + 0.44wt\%W) + (0.28wt.\%Nb) \\ & + 0.22(wt.Ta) + 2.9(wt.\%)Fe + 1.6(wt.\%Cr) - 1.0(wt.\%Al) \end{aligned} \quad 2.2a$$

$$\begin{aligned} AlEq. = {} & 1.0(wt.Al) + 10.0(wt.\%O) + 20.0(wt.\%N) + 10.0(wt.\%C) \\ & + 0.17(wt.\%Zr) + 0.33(wt.\%Sn) \end{aligned} \quad 2.2b$$

In general, metastable β titanium alloys have a MoEq. higher than 10, as quantified in Figure 2.4 [4]. For example the MoEq. of TIMETAL LCB is given by:

$$MoEq = 1.0(6.465) + 2.9(4.646) - 1.0(1.444) \approx 18 \quad 2.3a$$

After blending with various alloying elements titanium is typically vacuum-melted. Several melting operations may be required to achieve a homogeneous

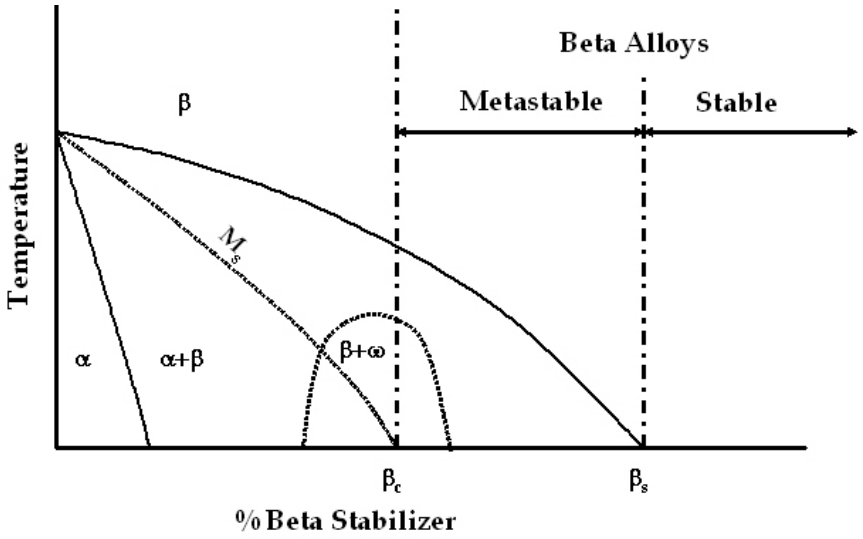

Figure 2.3. Pseudo binary phase diagram of titanium and a β stabilizer. β_c and β_s are the minimum β stabilizer content for metastable and stable beta titanium alloy formation, respectively [4].

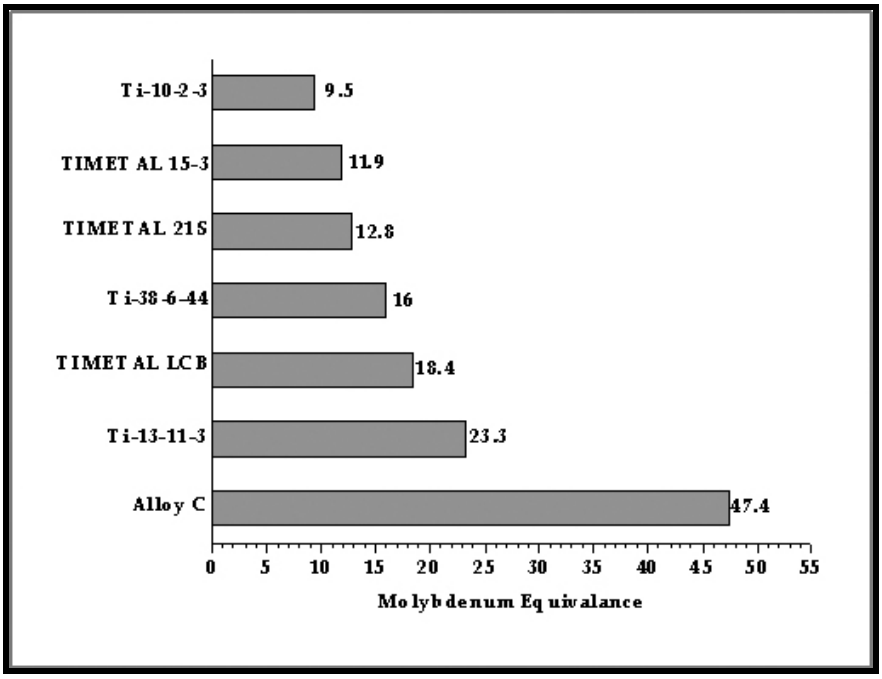

Figure 2.4. Molybdenum equivalence of various metastable β titanium alloys.

ingot which is then processed into useful shapes [7-9]. Processing of metastable β titanium alloys typically involves a hot working operation, which is then followed by an aging treatment [10]. A brief manufacturing process of metastable β titanium alloys is shown in Figure 2.5 [12].

The bcc crystal structure of the β phase offers excellent deformability; therefore, processing (forging, extrusion or rolling) of richer β titanium alloys include working within the β-phase field (β-processing). Alternatively, β processing followed by α+β processing can be preferred for leaner alloys such as TIMETAL LCB [11]. The β processing results in a single phase microstructure, whereas the α+β processing route establishes a two phase microstructure. The primary purpose of the aging treatment, preceding hot working operation, is to strengthen the metastable β matrix. In Figure 2.6a, primary alpha, α_p (the first transformation product that forms when the temperature drops below the β-transus [11]) and super saturated β phase of hot worked TIMETAL LCB is shown. Figure 2.6b demonstrates the resultant fine, needle-like precipitates of secondary alpha, α_s (the transformation product that forms during aging) of aged metastable β titanium alloy.

Precipitation of α_p has two major influences on the properties of metastable β titanium alloys [4]. First, it increases the stability of the β matrix and reduces the driving force for the martensitic decomposition of the β phase, both during quenching and aging. Second, α_p particles limit the mobility of β grain boundaries during recrystallization and grain growth.

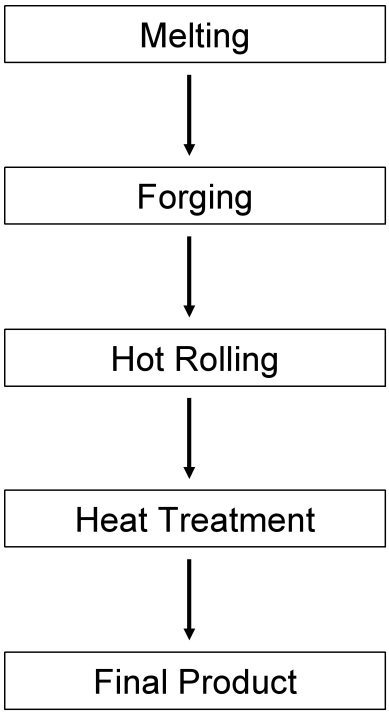

Figure 2.5. Schematic of metastable β titanium alloy manufacturing.

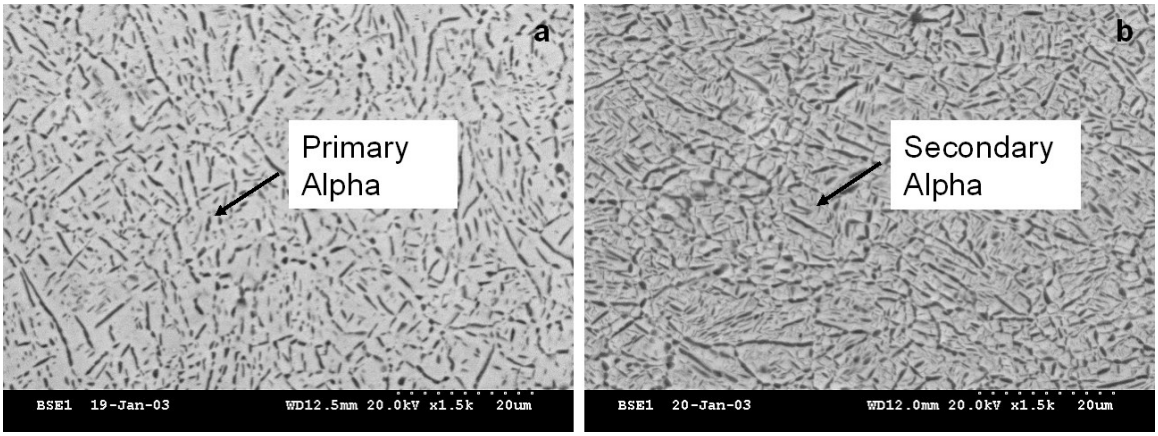

Figure 2.6.BSEI micrograph of a) α+β processed b) aged TIMETAL LCB, work done for this project.

The α_p particles were thought to have an indirect influence on the strengthening of metastable β titanium, however, a recent work has shown that, under equivalent tensile properties, α phase volume fraction, and prior beta grain size the high cycle fatigue (HCF) behavior of metastable beta titanium alloys is controlled by the contiguity of grain boundary alpha phase, a higher contiguity ratio being associated with a decreased crack initiation resistance. The evidence of HCF crack initiation at the α/β interface in TIMETAL LCB is shown in Figure 2.7 [13-15].

In general, the strengthening of the metastable β matrix is achieved by the precipitation of extremely fine size and uniform distribution of secondary alpha particles (α_s) because α_s precipitates increases the number of α/β interfaces available and act as slip barriers.

The morphology and the volume fraction of α_s, has a direct effect on the mechanical properties of the metastable β titanium alloys. Among the factors that influence the morphology and the volume fraction of α_s particles are the solution treatment [16, 17] and aging conditions [18-20], the amount of α stabilizing elements [19,20] and hot working history [22-34]. As an example, the influence of aging temperature on the room temperature tensile properties of TIMETAL LCB is given in Table 2.1 [12].

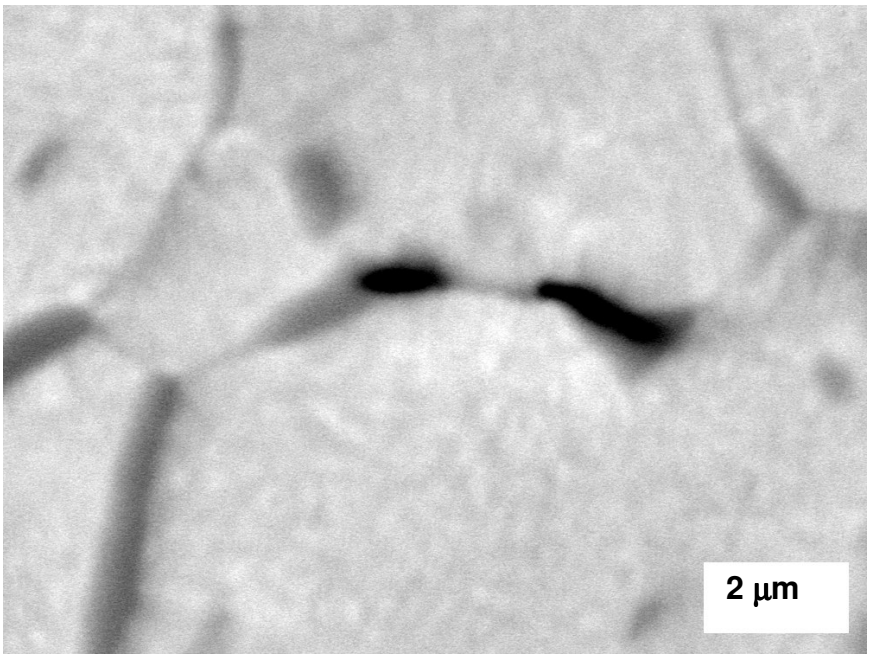

Figure 2.7. Evidence of high cycle fatigue crack initiation at the grain boundary α/β interface in TIMETAL LCB (work done for this project)

Table 2.1.Effect of aging temperature on the room temperature tensile properties of TIMETAL LCB[33].

Aging Temperature (°C)	UTS*(MPa)	0.2 YS** (MPa)	Elongation(%)	Reduction in Area(%)
520	1502	1469	9	30.5
550	1382	1338	12	45.1
580	1296	1269	15	54.4

*UTS:Ultimate tensile streght
**YS: Yield Streght

2.2. Understanding the Overall Transformation Kinetics of Metastable β Titanium Alloys

In metastable β titanium alloys, decomposition of the β phase starts when the temperature of the alloy decreases below the critical temperature of β phase stability, T_β. Depending on the holding temperature, β phase may decompose into α or ω phases. The kinetics of phase transformation below T_β can be quantitatively described by a Time-Temperature-Transformation (TTT) curve, as shown in Figure 2.8 [35].

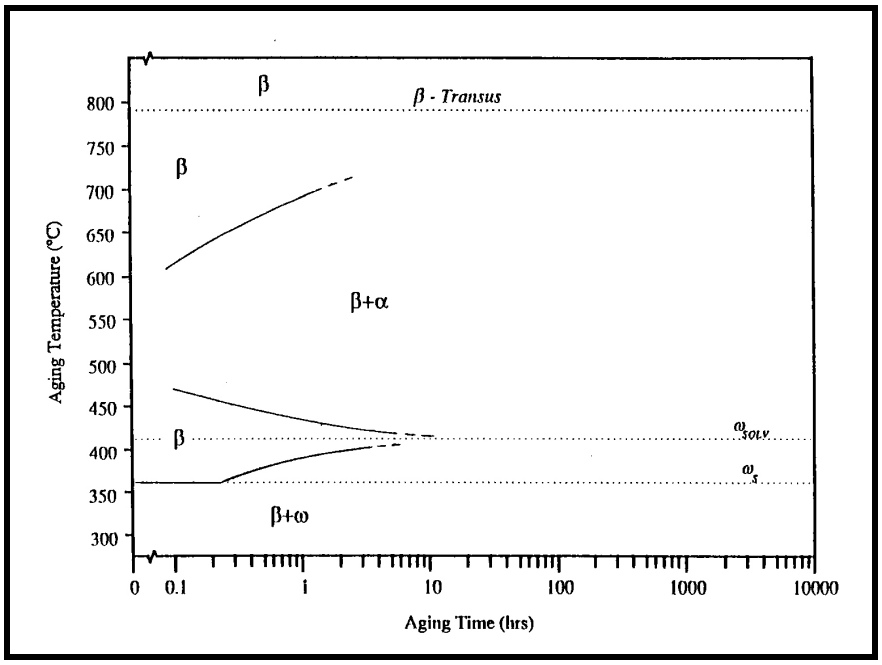

Figure 2.8. Isothermal Time-Temperature-Transformation Diagram for Ti-6.5 Mo-4.5Fe-1.5Al [35]

This curve is defined by the locus of points which represent the time required to nucleate a detectable degree of transformation (typically 1%), at constant temperature. In other words, the progress of an isothermal phase

transformation is plotted on a TTT curve to depict the relationship between the temperature(plotted linearly) and the reaction time (plotted logarithmically) for fixed fractional amounts of transformation.

In the past, Johnson-Mehl Avrami (JMA) equation [41-44] has been successfully used to describe the progress of a large number of diffusion controlled reactions that occur in metastable β titanium alloys [36-40], therefore the JMA equation will be derived next.

Upon deriving the JMA equation, the first reaction to be considered includes β→α transformation where the entire β matrix is consumed by the product phase α. In general, formation of α from β phase starts only after a critical incubation period, τ. If G is the growth rate of alpha particles, the volume v_α of a single α particle at any given reaction time, t is given by:

$$v_\alpha = \begin{cases} 0 & \text{if } t<\tau \\ K_V G^m (t-\tau)^m & \text{if } t>\tau \end{cases} \qquad 2.4$$

where K_V is the volume shape factor and m is related to the dimensionality of growth. For example, when three dimensional spherical particles evolve under isotropic, interface controlled growth conditions; $m=3$ and $K_V = \frac{4}{3}\pi$, whereas $m = 3/2$ when the α/β interface migrates under diffusion-controlled growth. The

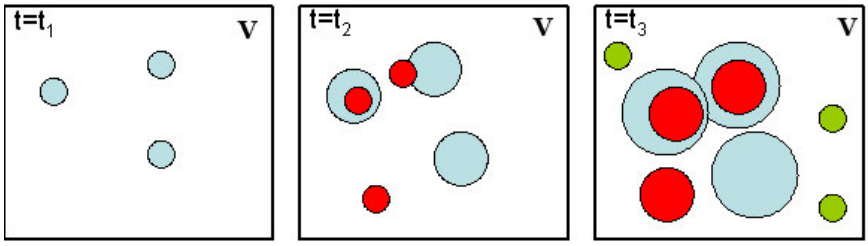

Figure 2.9. Schematic illustration of successive steps during β→α transformation. Alpha particles grow into and through each other and nucleation happen everywhere including in regions that have already transformed.

β→α transformation will terminate by the impingement of the adjacent growing particles. However, in deriving the JMA equation, the possibility of the impingement is at first ignored, allowing the α particles to grow into and through each other and for nucleation to happen everywhere, including the regions that have already transformed, shown in Figure 2.9.

An extended volume (V_α^e) can then be defined which includes particles that have formed in the un-transformed as well as in the already transformed regions. The increase in the extended volume due to these new particles nucleating in any given time interval between τ and $\tau + d\tau$ can be given as:

$$dV_\alpha^e = v_\alpha I V d\tau \qquad 2.5$$

Substituting equation 2.4 into 2.5 gives:

$$V_\alpha^e = (K_V V) \int_{\tau=0}^{t} G^m I (t-\tau)^m d\tau \qquad 2.6$$

where I is the nucleation rate per unit volume and V is the total volume.

It should be noted that, not all the increase in the extended volume is real. To find the actual transformed volume, contributions from particles that have formed in the regions that have transformed earlier during the reaction must be excluded. Of the new elements which make up dV_α^e, a fraction $\left(1-\frac{V_\alpha}{V}\right)$ on the average will lie in the untransformed volume and contribute to the increase the real volume dV_α. If it is assumed that nucleation occurs randomly throughout the volume, increase in the actual transformed volume, dV_α, at any given time interval can be given as:

$$dV_\alpha = \left(1-\frac{V_\alpha}{V}\right)dV_\alpha^e \qquad 2.7a$$

$$V_\alpha^e = -V\ln\left(1-\frac{V_\alpha}{V}\right) \qquad 2.7b$$

Substituting in to equation 2.6 into 2.7b gives:

$$-\ln\left(1-\frac{V_\alpha}{V}\right) = K_V\int_0^t G^m I(t-\tau)^m d\tau \qquad 2.8$$

Equation 2.8 may be integrated by making specific assumptions about the variation of nucleation rate with time [45]. These assumptions are as follows:

1) Nucleation is assumed to take place randomly in the β matrix

2) The number of nucleation sites per unit volume of the β phase is N_o at the beginning of the transformation.

3) As the α phase nucleates and grows these sites are gradually exhausted.

If the number of sites remaining after time t is N, and the frequency at which an available site becomes a nucleus is v, then the number of disappearing sites (dN) in a further time interval $d\tau$ may be given as:

$$dN = -Nvd\tau \qquad 2.9a$$

$$N = -N_o \exp(-v\tau) \qquad 2.9b$$

The nucleation rate per unit volume can then be given as:

$$I = \frac{dN}{dt} = N_o v \exp(-v\tau) \qquad 2.10$$

Substituting equation 2.10 into 2.8 and integrating by parts gives:

$$f^{\alpha} = \frac{V^{\alpha}}{V} = 1 - \exp\left[\frac{K_V G^m N_o}{v^m}\left\{\exp(-vt) - 1 + vt - \frac{v^2t^2}{2} .... \frac{v^m t^m}{m!}\right\}\right] \qquad 2.11$$

The two limiting forms of equation 2.11 correspond to very small or very large vt. Very small vt values imply a constant nucleation rate and equation 2.11 can be evaluated by expanding $\exp(-vt)$. This operation gives f^{α} as:

$$f^{\alpha} = \frac{V^{\alpha}}{V} = 1 - \exp\left[K_V G^m N_o t^{m+1}\right] \qquad 2.12$$

Very large vt values, correspond to a situation where all the available nucleation sites are consumed at the very early stages of transformation. The nucleation rate for the entire transformation is then assumed to be zero. This limiting case gives f^{α} as:

$$f^{\alpha} = \frac{V^{\alpha}}{V} = 1 - \exp(-K_V N_o G^m t^m) \qquad 2.13$$

In general, the time exponent can be replaced with a generalized constant n which is referred as the Avrami constant and the $\left(K_V N_o G^m\right)$ term in equation 2.13 can be expressed as a single rate constant, k. As a result, a generalized form for the JMA equation is obtained and given as.

$$f^{\alpha} = \frac{V^{\alpha}}{V} = 1 - \exp(-kt^n) \qquad 2.14$$

The values of k and n can be determined from the plots of $\ln\ln\left(\frac{1}{1-f^{\alpha}}\right)$ versus $\ln t$.

Reaction kinetics considered so far took into account the transformation of the entire starting volume into the second phase α. For precipitation reactions occurring in TIMETAL LCB, however, only a given fraction of the β phase

assembly transforms into α phase and the amount of the transformed volume is found by considering the conservation of solute atoms [45]:

$$\frac{V_{\alpha}^{eqm}}{V} = \frac{C_{Mo}^{\beta} - C_{Mo}^{bulk}}{C_{Mo}^{\beta} - C_{Mo}^{\alpha}} \qquad 2.15$$

where C_{Mo}^{β} and C_{Mo}^{α} are the solute concentrations in the matrix adjacent to the α phase and in the precipitate, respectively, whereas C_{Mo}^{bulk} defines the bulk, concentration. The volume of α at a given time during the β→β+α transformation is given as $V^{\alpha}(t)$, and the α phase volume fraction may be expressed as:

$$\frac{V^{\alpha}(t)}{V_{eqm}^{\alpha}} = \left\{ V^{\alpha}(t) \Big/ V \right\} \left[c^{\beta} - c^{\alpha} \Big/ c^{\beta} - c^{m} \right] \qquad 2.16$$

Re-writing the extended volume for diffusion controlled reactions gives:

$$dV_{\alpha}(t) = \left(1 - \frac{V^{\alpha}(t)}{V_{eam}^{\alpha}} \right) dV_{\alpha}^{e} \qquad 2.17a$$

$$V_{\alpha}^{e} = -V_{eqm}^{\alpha} \ln \left(1 - \frac{V_{\alpha}(t)}{V_{eqm}^{\alpha}} \right) \qquad 2.17b$$

Substituting equation 2.6 into 2.18b and re-arranging gives:

$$\frac{V^{\alpha}(t)}{V^{eqm}} = 1 - \exp\left(- \left[\frac{c^{\beta} - c^{\alpha}}{c^{\beta} - c^{m}} \right] K_V V G \int_{\tau=0}^{t} (t - \tau)^m d\tau \right) \qquad 2.18$$

Equation 2.18 leads to the usual form of the JMA equation with $n = \frac{5}{2}$ for constant nucleation rate and $n = \frac{3}{2}$ for early site saturation.

2.3. Understanding the Nucleation of Alpha Phase in Metastable β Titanium Alloys

Majority of phase transformations occurring in the solid state are accompanied by rearrangement of atomic structure. In addition to a structure change, a phase transformation may alter the bulk composition or introduce strain [45].

Consider a binary Ti-Mo metastable β titanium alloy as a model system. If this alloy, with a specific composition c_o, is solution treated above the β-transus temperature ,cooled rapidly to T_1 and held at this temperature for a given amount of time α phase particles, lean in Mo, will begin to precipitate enriching the β matrix in Mo, as illustrated in the phase diagram given in Figure 2.10.

However, the β→β+α transformation does not proceed spontaneously upon reaching the temperature T_1. Initially, thermal agitation results in unstable compositional fluctuations within the system. Typically, below a critical size entire fluctuations tend to decay. Occasionally, however, a fluctuation becomes large enough that, addition of another atom decreases the free energy of the system. The fluctuation is then said to be stable and grows into macroscopic dimensions. These fluctuations, through which the smallest stable aggregate of a more stable phase develops from the matrix phase, are known as nucleation. The fluctuation with the same probability of growing or decaying is called a critical nucleus. A fluctuation of any size, on the other hand, is referred as a cluster [46].

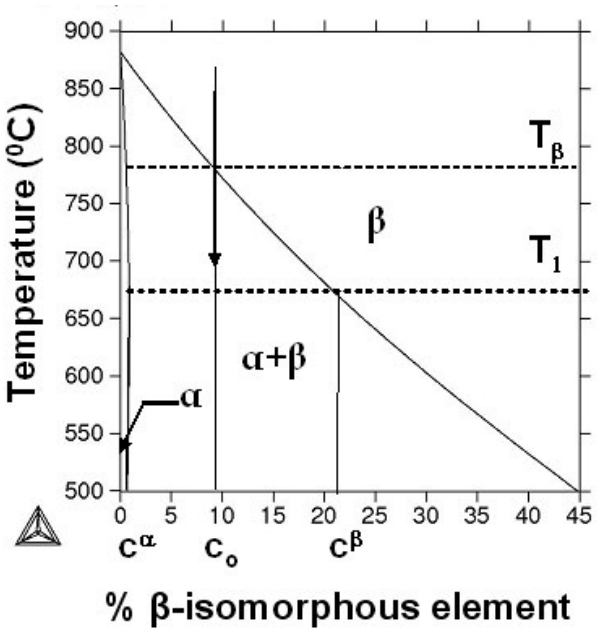

Figure 2.10. The equilibrium phase diagram showing the isothermal solid-solid transformation of β→β+α at T_1. c_α and c_β are equilibrium compositions of α and β phases respectively. co represents the alloy composition.

The free energy change, ΔG°, accompanying the β→β+α transformation will have the following contributions [47]:

1) At temperatures where the α phase is stable, creation of an α phase volume V will cause a volume free energy reduction of $V\Delta G_V$.

2) The barrier to nucleation, *i.e.* the reason why fluctuations under a critical size tend to decay is the extra free energy, γ, associated with the α/β interface.

3) In solid-solid phase transformations volume or shape changes, due to precipitation of a second phase, may result in misfit strain energy, ΔG_S, proportional to the volume of the precipitate.

2.3.1. Volume Free Energy

Consider a single phase metastable β titanium alloy with a bulk of composition c_o, and quenched to a temperature T_1 below the β-transus temperature. The free energy composition diagram of the β phase is given in Figure 2.11.

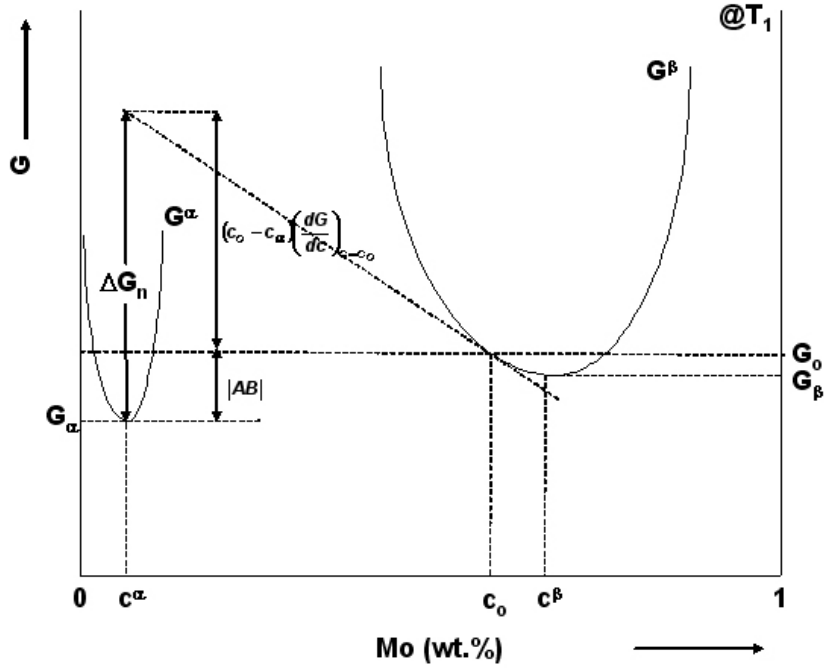

Figure 2.11. Schematic for the graphical determinations of the free energy change associated with the precipitation of α phase.

The free energy per mole of the β phase with a bulk composition of c_o is equal to G_o and precipitation of a small amount of α precipitate with a composition of c_α, increases the composition of the β phase to c_β. The curve representing the free energy of the α phase as a function of composition is also

given in Figure 2.11. The free energies of the alloy system before ($G_{initial}$) and after (G_{final}) the α phase precipitation can be given as [48]:

$$G(initial) = (n_1 + n_2)G_o \qquad 2.19a$$

$$G(final) = n_1G_1 + n_2G_2 \qquad 2.19b$$

where n_1 and n_2 are the number of moles of β and α phases in the two phase α+β mixture. The relationship between n_1 and n_2 can be given as:

$$\frac{n_1}{n_2} = \frac{c_o - c_\alpha}{c_\beta - c_o} \qquad 2.20$$

The free energy change associated with the formation of the α precipitate is the difference between the free energies of the system before and after precipitation and can be given as:

$$\Delta G = G(final) - G(initial) \qquad 2.21$$

Combining equation 2.18, 2.19 and 2.20 and substituting into 2.21 gives:

$$\Delta G = n_2\left[G_2 - G_o - \left(\frac{c_o - c_\alpha}{c_\beta - c_o}\right)(G_o - G_1)\right] \qquad 2.22$$

Typically, the first α nuclei to form will not significantly alter the bulk composition of the β matrix and it can be assumed that $c_o \approx c_\beta$. Re-writing equation 2.22 gives:

$$\Delta G_n = \frac{\Delta G}{n_2} = \left[G_2 - G_o - (c_o - c_\alpha)\left(\frac{dG}{dc}\right)_{c=c_o} \right] \quad 2.23$$

and the volume free energy decrease associated with nucleation is given by:

$$\Delta G_v = \frac{\Delta G_n}{V_m} \quad 2.24$$

where V_m is the molar volume of α phase.

The term $G_2 - G_o$ can be found directly from the G versus composition graph given in Figure 2.11. The term $\left(\frac{dG}{dc}\right)_{c=c_o}$ is the slope of the tangent to the curve G_β at c_o and $(c_o - c_\alpha)\left(\frac{dG}{dc}\right)_{c=c_o}$ is the distance given as $|AB|$. For dilute solutions $\Delta G_v \propto \Delta C$ [47]. ΔC and may be given as:

$$\Delta C = C_\beta - C_o \quad 2.25$$

Further, ΔC is directly proportional to the undercooling, ΔT. As a result, the driving force for precipitation of alpha phase increases with increasing undercooling below the β-transus temperature.

2.3.2. Surface Free Energy

Surface free energy may be defined as the change in the free energy of a system when a unit area of the precipitate/matrix interface is generated [49]. In other words, it is the energy associated with the chemical bonds that are broken

to generate a new surface. Interphase boundaries in solids can be divided in three based on their atomic structure. These are coherent, semicoherent and incoherent interfaces [50]

A coherent interface forms when the two crystals match perfectly at the interface plane and the lattice sites are conserved in the region of the precipitate/matrix interface. Fully coherent interfaces are associated with very low surface energies. For example, in Cu-Si alloys precipitate/matrix interfacial energies as low as 1erg/cm^2 has been reported [51]. This value can be compared to several hundreds ergs/cm^2 for a random precipitate matrix interface.

From an energy stand point, it is very favorable for a precipitate to be surrounded by low energy coherent interfaces, however, when the precipitate and the matrix have different crystal structures, it may be difficult to find a lattice plane that is common to both phases. For certain phase combinations there may be one plane that is more or less identical in each crystal and by choosing the correct orientation relationship it is possible to form a low energy coherent or semi coherent interface. Usually, the number of planes of good matching is limited and the remaining precipitate/matrix interfaces have relatively higher energies [47].

When the two phases have completely different crystal structures or when the two lattices are in a random orientation it is very difficult to form a coherent or semicoherent interface and the precipitate/matrix interface adopts an incoherent structure. The surface energy of an incoherent interface is expected to be very

high and similar to that of a high angle boundary, which approaches to 500 ergs/cm^2 [52].

When the precipitate and the matrix are strain free, the optimum precipitate shape may be found by minimizing the total interfacial energy, $\sum A_i\gamma_i$ and the equilibrium shape of a precipitate can be predicted from a γ-plot [53]. A γ-plot is a graphical method to represent the variation in surface energy with crystal orientation. On a γ-plot the free energy of any plane within the crystal may be depicted with a radial vector and has the direction of the plane normal and the magnitude equal to the surface energy of that plane [50]. As an example, the equilibrium shape of an incoherent precipitate is shown in Figure 2.12a.

Precipitate/matrix interfaces bounding an incoherent precipitate are expected to have the same energy (γ_i) at every orientation. As a result, the equilibrium shape of an incoherent α precipitate approaches to a sphere, whereas, the γ-plot of a semi-coherent α precipitate may have two deep cusps normal to the low energy semi-coherent interfaces. The precipitate/matrix interface energy at this orientation is relatively low and is depicted as γ_c in Figure 2.12b. The precipitate/matrix interface at every other orientation of a semi

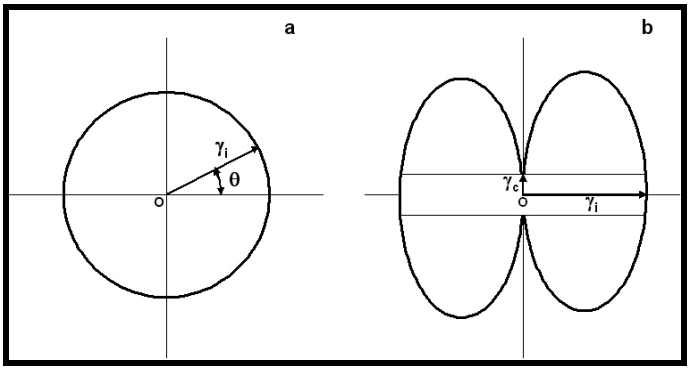

Figure 2.12 A section through γ-plot illustrating the equilibrium shape of a precipitate showing a) incoherent interface at all precipitate matrix interface orientations. b) one coherent or semi coherent interface at only one precipitate/matrix interface orientation.

coherent precipitate exhibit poor matching and have higher energies(γ_i.). As a result, the precipitate shape approaches to a disc as shown in Figure 2.12b

2.3.3. Strain Free Energy

During solid-solid phase transformations two types of misfit strains may arise upon precipitation of a second phase. These are coherency and volume misfit strains. [47]. The coherency misfit strains are expected to arise along a coherent or semi-coherent precipitate/matrix interface, whereas volume misfit strains are the only misfit strains present when the precipitate/matrix interface is incoherent. The origin of coherency and volume misfit strains are demonstrated in Figures 2.13.a and b.

Consider a spherical region being removed from the β phase and transformed into the α phase as shown in Figure 2.13a. If the volume of the α sphere is different then the original volume of the β sphere, the volume misfit

strains (Δ) may arise when the α sphere is inserted back into the β matrix and Δ can be given as [47]:

$$\Delta = \frac{V_\beta - V_\alpha}{V_\beta} \qquad 2.26$$

where V_β is the volume of the unconstrained hole in the matrix and V_α is the volume of the unconstrained precipitate. The unconstraint linear lattice misfit δ is given as:

$$\delta = \frac{a_\alpha - a_\beta}{a_\beta} \qquad 2.27$$

where a_α and a_β are the lattice parameters of the unconstrained α precipitate and β matrix. The volume misfit strain is three times the linear misfit strain for a coherent precipitate, whereas it is independent of the linear lattice misfit for an incoherent precipitate.

The elastic strain fields may arise, if the β matrix hole and the second phase α are constraint to occupy the same volume. In the case of coherent precipitation the lattice sites are conserved at the α/β interface and the total elastic energy due to the precipitation of the α phase may be given as:

$$\Delta G_s = 4\mu\delta^2 V \qquad 2.28$$

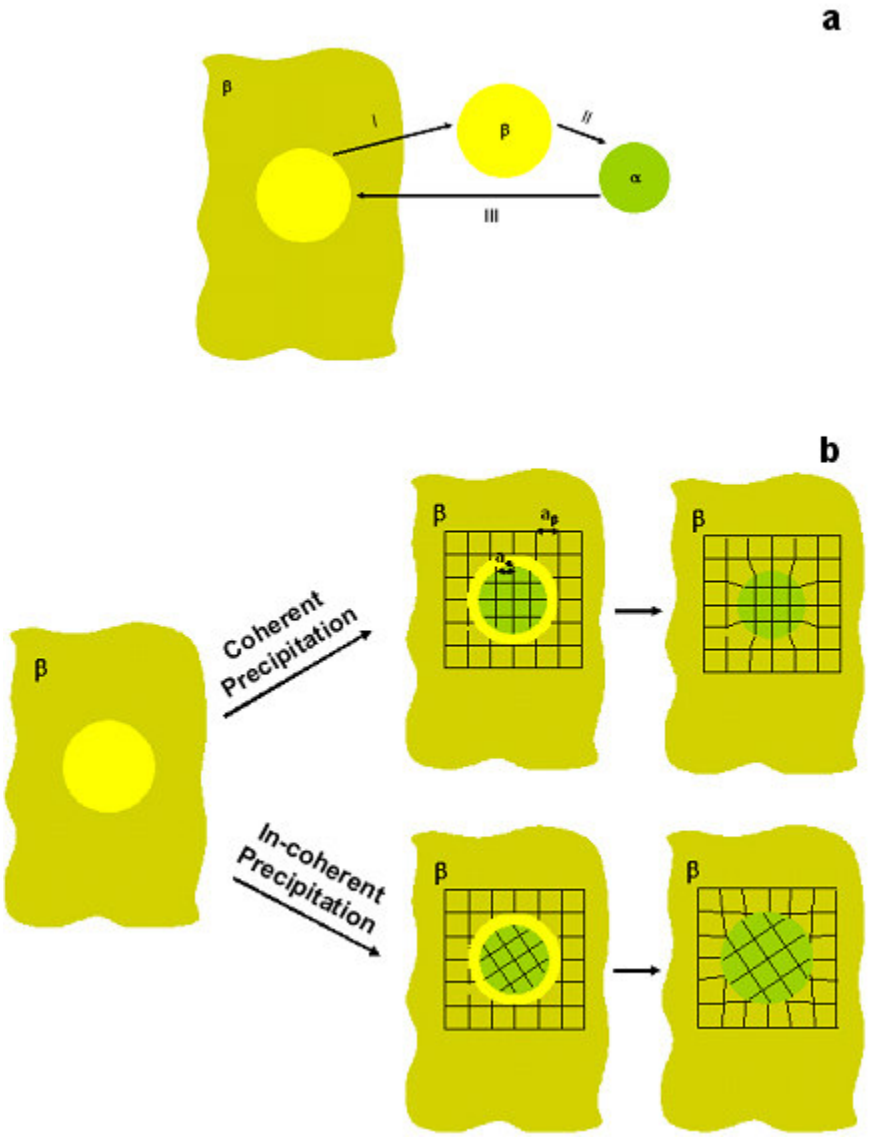

Figure 2.13. Schematic illustration of origin of coherency and volume strains during coherent and incoherent precipitation, respectively.

where μ is the shear modulus, V is the volume of the unconstrained hole in the matrix and δ I the unconstrained lattice misfit. Equation 2.28 assumes that the β matrix is elastically isotropic and the elastic moduli for the precipitate and matrix are equal. As a result, the total elastic energy arising from the precipitation of the

α phase is independent of its shape. The elastic strain is shape dependent when the precipitate and matrix have different elastic moduli. If the matrix is softer, all strain is accommodated by the matrix and a spherical precipitate shape will give the minimum elastic energy, whereas all the strain is accommodated by the precipitate if the precipitate is softer and the optimum precipitate shape is a disc [54]. Finally, if the matrix is elastically anisotropic and softer along certain crystallographic directions, α will have a disc shape and lie parallel to the softer directions.

The elastic strain energy for a homogenous, incompressible and incoherent precipitate in an isotropic matrix was calculated by Nabarro as [55]:

$$\Delta G_s = \frac{2}{3}\mu\Delta^2 Vf\left(c/a\right) \qquad 2.29$$

Equation 2.29 states that elastic strain energy of an incoherent precipitate is proportional to the square of the volume misfit. $f\left(c/a\right)$ takes into account the precipitate shape effects where c and a are the semi axes of an ellipsoid of revolution. An ellipsoid of revolution may be described by the following equation:

$$\frac{x^2}{a^2}+\frac{y^2}{a^2}+\frac{z^2}{c^2}=1 \qquad 2.30$$

Various shapes that can be observed for different c/a ratios are tabulated in Table 2.2.

Table 2.2. c/a ratios for various second phase precipitate shapes; c and a are the semi axes for a given shape.

Shape	c/a ratio
Sphere	$c/a = 1$
Needle	$c/a >> 1$
Disk or Plate	$c/a \approx 0$

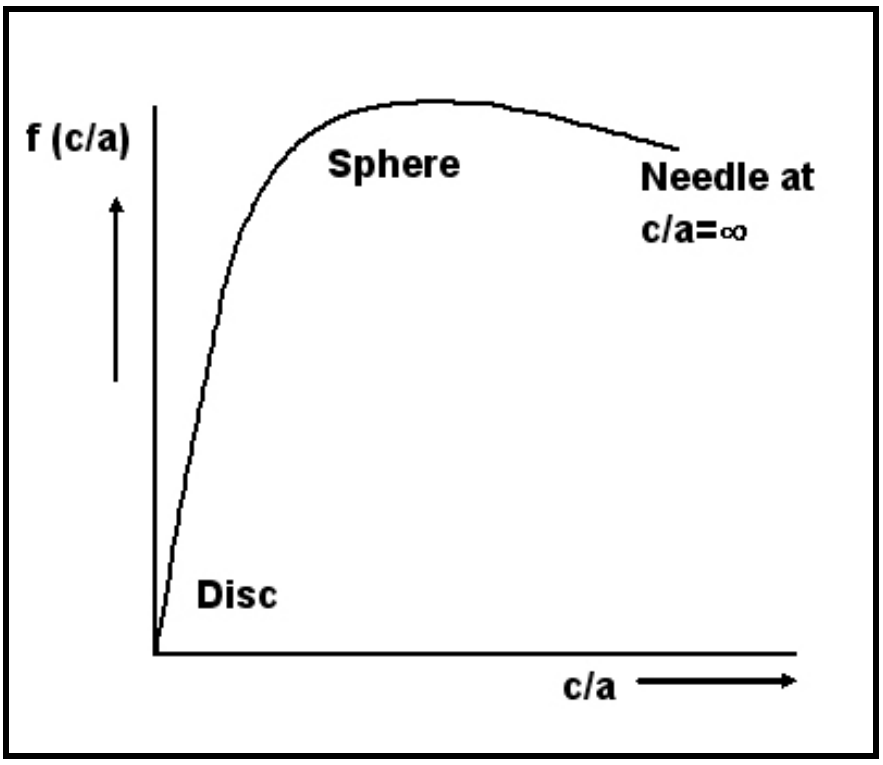

Figure 2.14 The variation of $f(c/a)$ with c/a.

The variation of $f\left(c/a\right)$ with c/a is shown in Figure 2.14. This figure suggests that for a given precipitate volume, a sphere has the highest strain energy, whereas a disc has the minimum and a needle lies in between.

Upon specifying the different free energy contributions to the formation of critical nucleus, ΔG° may be given as:

$$\Delta G^{o} = -V(\Delta G_V - \Delta G_S) + A\gamma \qquad 2.31$$

Equation 2.31 is plotted in Figure 2.15 and the general result can be summarized as follows:

1) The driving force for nucleation is the volume free energy change attending the nucleation plus the volume strain energy arising from the size and/or shape misfit between the cluster and the matrix.

2) The strain energy reduces the driving force for nucleation.

3) The barrier to nucleation is the interfacial free energy of the cluster/matrix interface.

4) There is a critical activation energy barrier, ΔG^{*}, to nucleation and the critical nucleus size required to exceed ΔG^{*} corresponds r^{*}

5) Upon exceeding this critical size, r^{*}, the growth of the nucleus continuously reduces the free energy of the system.

After discussing the effects of surface and strain energy on the equilibrium shapes of second phase precipitates, it can be concluded that

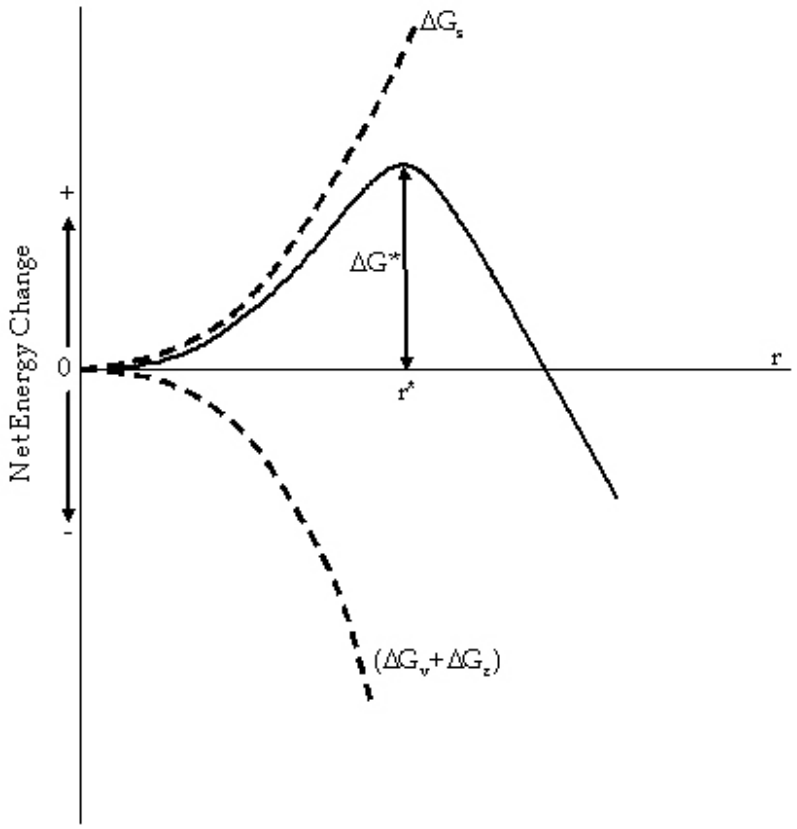

Figure 2.15 Variation in the free energy of the system as function of cluster size.

ΔG^* and r^* can be determined by simultaneous minimization of strain and surface energy terms, however when some portion of critical nucleus is a part of sphere ΔG_S and $\Delta G_V + \Delta G_\varepsilon$ are proportional to r^2 and r^3, respectively. As a result, ΔG_S increases more rapidly than $\Delta G_V + \Delta G_\varepsilon$ decreases and for small values of r failure to minimize interfacial and strain energies simultaneously does not introduce a significant error in deriving ΔG^* and r^* [56].

2.3.4. Nucleation Rate

Nucleation of a new phase generally takes place at discontinuities with in the matrix such as grain boundaries or dislocations, however, under suitable conditions such as very large under-coolings, it may also occur uniformly within the matrix. The former is called the heterogeneous nucleation, whereas the latter is referred as the homogenous nucleation. Nucleation rate of second phase particles are strongly influenced by the choice of a specific site.

Nucleation rate (N) can be defined as the rate at which new nuclei appear in a system [48]:

$$N = fC^* \tag{2.32}$$

where f and C^* are defined as the frequency of atoms joining the critical nucleus and the number of clusters that have the critical size, respectively. Two factors that influence f are the vibrational frequency (ω) of the atoms and the activation energy for migration, ΔG_m. Within a system, the fraction of atoms with energy greater than ΔG_m may be given as:

$$\exp(-\Delta G_m / kT) \tag{2.33}$$

and f may be given as:

$$f = \omega \exp(-\Delta G_m / kT) \tag{2.34}$$

Whereas C^* is equal to:

$$C^* = C_o \exp(-\Delta G^* / kT) \qquad 2.35$$

where C_o is the number of atoms per unit volume in the β matrix, ΔG^* is the critical activation energy, k and T are the Boltzman constant and temperature, respectively. Equation 2.35 is valid only for clusters with a radius $r < r^*$ because clusters greater than the critical size are stable nuclei of α and are not a part of β phase.

Combining equation 2.34 and 2.35 and substituting in 2.32 gives the nucleation rate as:

$$N = C_o \varpi \exp(-\Delta G_m / kT) \exp(-\Delta G^* / kT) \qquad 2.36$$

Equation 2.36 can be used to express both the heterogeneous (N_{het}) and the homogenous (N_{hom}) nucleation rate. The ratio of (N_{het}) to that of (N_{hom}) can be given as:

$$\frac{N_{het}}{N_{hom}} = \frac{C_{het}}{C_{hom}} \exp -\left(\frac{\Delta G^*_{het} - \Delta G^*_{hom}}{kT}\right) \qquad 2.37$$

In equation 2.37, the differences in f for heterogeneous and homogenous nucleation were ignored. Normally, f is expected to be higher during heterogeneous nucleation due to the high diffusivity paths, however, the number of nucleation sites for heterogonous, C_{het}, and homogenous, C_{hom}, nucleation over rides the influence of f on N. C_{hom} is always greater than C_{het}. As a

result, the dominating effect of heterogonous nucleation comes from its effectiveness in decreasing ΔG^*. The following section will derive the ΔG^* for homogenous and heterogeneous nucleation

2.3.5. Homogenous (Matrix) Nucleation

When the precipitate/matrix boundary is incoherent and interfacial free energy is independent of boundary orientation, γ plot predicts the equilibrium shape of the nucleus as a sphere. Re-writing equation 2.18 gives the free energy change associated with the homogenous precipitation of a spherical particle as:

$$\Delta G^{\circ}_{hom} = -\frac{4}{3}\pi r^3 \Delta G_V + 4\pi r^2 \gamma \qquad 2.38$$

In equation 2.38, the strain energy contribution to ΔG°_{hom} was ignored because precipitate/matrix interface is incoherent. The critical fluctuation size above which the clusters can grow into stable nuclei is found by differentiating equation 2.38 with respect to r and given as:

$$r^* = -\frac{2\gamma_{\alpha\beta}}{\Delta G_V} \qquad 2.39$$

Upon substituting equation 2.39 into 2.38 ΔG^* is found as:

$$\Delta G^* = \frac{16\pi\gamma^3_{\alpha\beta}}{3\Delta G_V} \qquad 2.40$$

2.3.6. Heterogenous (Grain Boundary) Nucleation

The equilibrium nucleus shape on a disordered and planar, β/β grain boundary between β_1 and β_2 grains will be two abutted spherical caps provided that the matrix/precipitate interface energy is isotropic (Figure 2.16). In Figure 2.16, the boundary area destroyed due to the formation of α phase is represented by a dashed line. The free energy change accompanying the heterogeneous nucleation of a particle is given as:

$$\Delta G^{\circ}_{het} = -V\Delta G_V + A_{\alpha\beta}\gamma_{\alpha\beta} - A_{\beta\beta}\gamma_{\beta\beta} \qquad 2.41$$

where $A_{\beta\beta}$ is the grain boundary area destroyed as a result of the formation of the α precipitate and $\gamma_{\beta\beta}$ is the free energy of β/β grain boundary. Letting $S = \cos\theta$, where θ is the contact angle, the volume, V_α, and the surface area , A_α, of the nucleus is given by:

$$V_\alpha = 2\pi r_\alpha^3\left[\frac{2-3S+S^3}{3}\right] \qquad 2.42a$$

$$A_\alpha = 4\pi r_\alpha^2[1-S] \qquad 2.42b$$

$$r_\beta = r_\alpha \sin\theta \qquad 2.42c$$

The surface tension force balance at the junction of α, β_1 and β_2 may be expressed as the following :

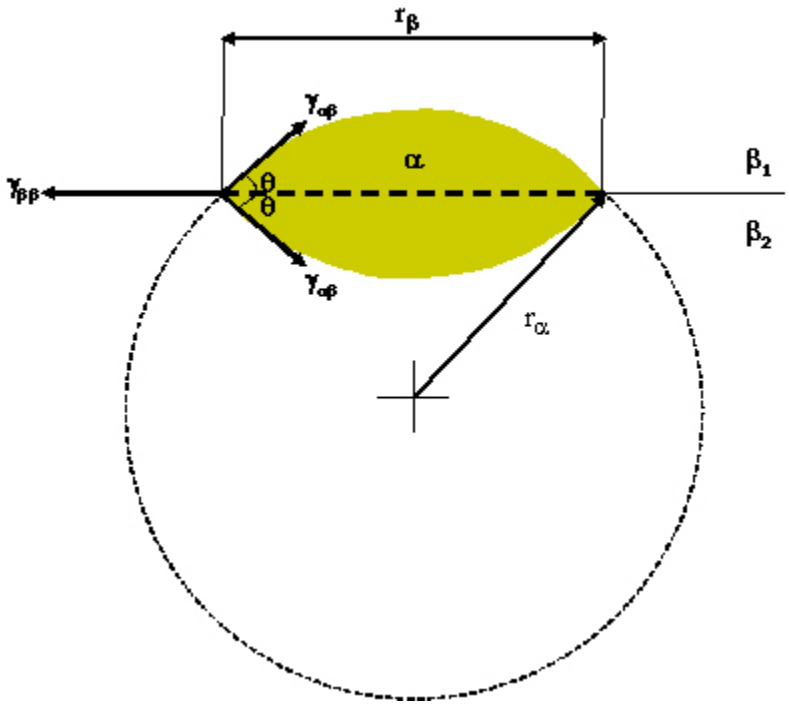

Figure 2.16 Schematic illustration of a heterogeneous critical nucleus.

$$\gamma_{\beta\beta} = 2\gamma_{\alpha\beta}\cos\theta \qquad 2.43$$

Combining equation 2.42a-c and 2.43 and substituting into 2.41 gives ΔG_{het} as:

$$\Delta G_{het} = \pi r_\alpha^3\left[\frac{2-3S+S^3}{3}\right]\Delta G_V + \left[2\pi r_\alpha^2(1-S) - \pi r_\alpha^2 \sin^2\theta S\right]\gamma_{\alpha\beta} \qquad 2.44$$

Rearranging equation 2.44 gives:

$$\Delta G_{het} = \left[\frac{4}{3}\pi r_\alpha^3 \Delta G_V + 4\pi r_\alpha^2 \gamma_{\alpha\beta}\right]\left[\frac{2-3S+S^3}{4}\right] \qquad 2.45$$

As a result the critical value for r^* is may be given as:

$$r^* = -\frac{2\gamma_{\alpha\beta}}{\Delta G_V} \qquad 2.46$$

Upon comparing of equations 2.39 and 2.46, it was concluded that, the critical nuclei radii for homogenous and heterogeneous nucleation are identical. As a result, the free energy for formation of a critical nucleus during heterogeneous nucleation is reduced by an amount equal to $\left[\frac{2-3S+S^3}{4}\right]$ from that of homogenous nucleation.

Quite often, the need to minimize ΔG^* and achieve maximum nucleation rate, results in a tendency to match the pattern and spacing of the matrix phase atoms as closely as possible at one or more precipitate/matrix boundary orientations. Such boundaries have relatively low interfacial energies and Lee and Aaronson showed that, formation of these low γ interfaces reduces ΔG^* [56].

2.3.7. Orientation Relationship Between α and β Phases

The orientation relationship (OR) between α(hcp) and β(bcc) phases is important because it has a strong influence on the microstructure property relationships. In general, an orientation relationship between a precipitate/matrix system may be determined by selected area diffraction in transmission electron microscopy [57]. Spots in a diffraction pattern correspond to sets of

crystallographic planes that give rise to reflections with non-zero structure factor [57]. A typical spot pattern analysis includes obtaining simultaneous diffraction patterns from the precipitate and the matrix phases. Upon determining the zone axes of the spot patterns (the direction parallel to the electron beam), this information is plotted on a stereographic projection. Using either the stereographic projection or the diffraction pattern one can look for poles or reflections which are close together. A stereographic projection displays only angular relationships between the crystallographic planes, whereas a diffraction spot pattern shows both angles and spacings between planes. Thus, if a precipitate spot is close to a matrix spot the corresponding crystal planes are nearly parallel and have a small mismatch in spacing.

For example, in a spot pattern obtained from a bcc/hcp system, the closed packed {110} planes of the bcc phase are expected to lie parallel to the closed {0001} planes of the alpha phase. The atomic arrangements of the {110} and {0001} closed packed planes are superimposed and shown in Figure 2.17a. Open circles represent the atoms of the in {110} bcc plane, whereas the solid circles show the {0001} hexagonal arrangement of the hcp plane. The symmetries of these two-dimensional arrangements are two fold and sixfold rotations. In spite of their different symmetries the two atomic arrangements are very similar and two orthogonal strains along $<001>$ and $<110>$ bcc directions are sufficient to produce one lattice from the other. As a result, the close packed $<111>$ and $<11\bar{2}0>$ directions in the two lattices are misaligned by an angle

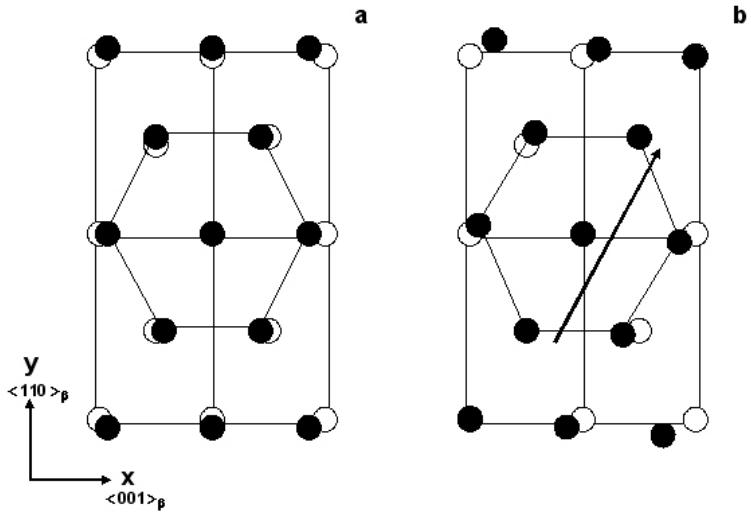

Figure 2.17 Schematic of illustration of a) superimposed closed packed {110} bcc and {0001} hcp planes b) parallel $<111>$ and $<11\bar{2}0>$ directions (shown with an arrow on the figure) that was brought into coincidence by a rotation of hcp crystal about $<0001>$ by 5.26^{o}.

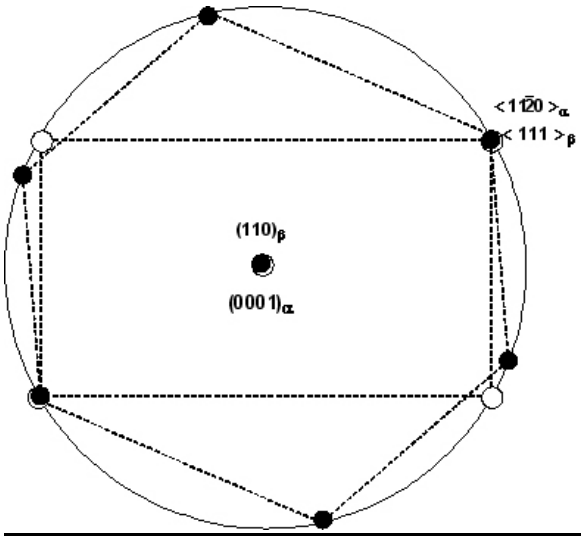

Figure 2.18 Stereographic projection of Burgers Orientation Relationship. This projection is projected normal to the close packed {110} and {0001} planes in the two structures. Open circles represent the bcc pole and closed circles represent the hcp poles.

5.26°. Upon rotating one of the lattices through this angle of 5.26°, the closed packed $<111>$ and $<11\bar{2}0>$ directions in beta and alpha phases may be brought into coincidence as shown in Figure 2.17b. This is the Burgers orientation relationship between bcc and hcp phases commonly observed in titanium alloys and can be described by a set of parallel planes and directions as [58]:

$$\{0001\}_{\alpha} \| \{110\}_{\alpha}$$

$$\langle 11\bar{2}0 \rangle_{\alpha} \| \langle 111 \rangle_{\beta}$$

The Burgers orientation relationship is also illustrated on a stereographic projection and shown in Figure 2.18. This projection is projected normal to the close packed {110} and {0001} planes in the two structures and matched to Figure 2.17b. Open circles represent the {111} bcc poles and the solid circles depict the $\{11\bar{2}0\}$ hcp poles. The rectangle and a hexagon, outline the closed packed planes in bcc and hcp crystals, respectively.

A given orientation relationship may have several variants [26]. For example, in the bcc/hcp case, there are three close packed $\langle 11\bar{2}0 \rangle_{\alpha}$ directions on the $\{0001\}_{\alpha}$ plane of the α phase. However, due to the six fold symmetry along $\{0001\}_{\alpha}$, three $\langle 11\bar{2}0 \rangle_{\alpha}$ directions are indistinguishable from one another. Furthermore, there are six $\{110\}_{\beta}$ planes in a bcc crystal structure and each

$\{110\}_\beta$ β plane has two $\langle 111\rangle_\beta$ directions. As a result, 12 variants of the Burgers orientation relationship can be identified in a given bcc/hcp system.

2.4. Understanding the Growth of α Phase in Metastable β Titanium Alloys

In metastable β titanium alloys α first appears at certain sites as nuclei within the parent β phase during nucleation [61].Once stable, these nuclei grow into the matrix [61]. In diffusional phase transformations, growth of a new product is governed by two processes: a) migration of the precipitate/matrix interface and b) diffusion of solute atoms across the interface when a composition difference exists between the parent and precipitate phases [45, 47]. During precipitate growth, these two processes occur simultaneously and the slower process controls the overall growth rate. For example, slower diffusion of atoms compared to that of the interface migration rate implies diffusion controlled growth and the α/β interface will migrate as fast as the lattice diffusion removes the solute atoms into or away from the interface, whereas, interface controlled growth occurs if the mobility of interface is the rate limiting step. The solute concentration profiles ahead of a migrating α/β interface depends on the growth conditions and are illustrated in Figures 2.19a and b for diffusion- and interface-controlled growth, respectively.

In metastable β titanium alloys, the α phase can grow in two products. These are grain boundary alpha particles and plate like precipitates. In the following sections, mechanisms governing the growth of these two transformation products will be established.

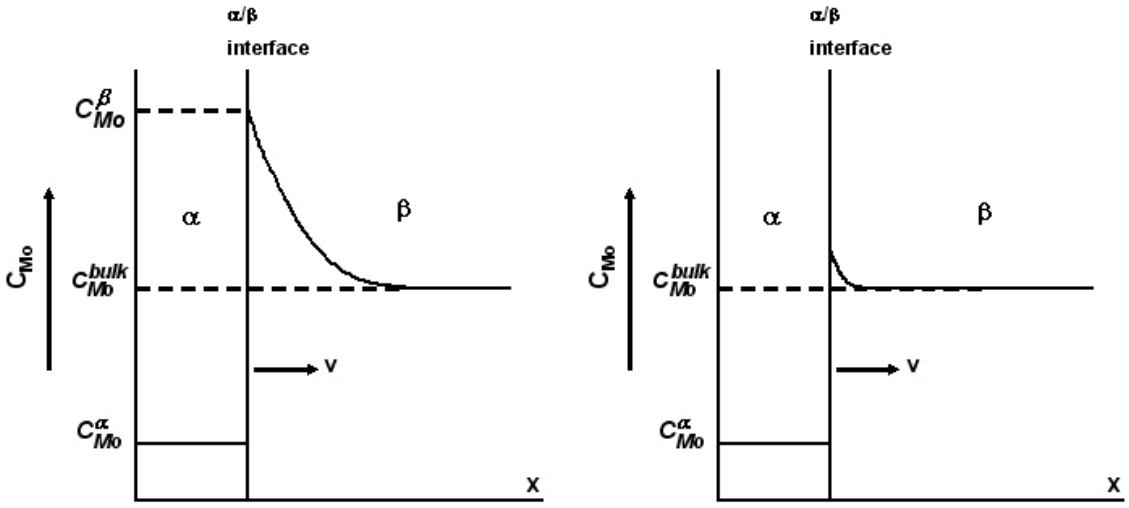

Figure 2.19. Schematic illustration of composition profile across an α/β interface moving under a) diffusion-control b) interface-control growth.

2.4.1. Growth of Grain Boundary Alpha Precipitates

2.4.1.1. Thickening of Grain Boundary Alpha Precipitates

In titanium alloys, diffusion of molybdenum (Mo) atoms is a possible mechanism controlling the growth of α phase into the metastable β matrix [38] Consider the formation a grain boundary alpha precipitate with in the β matrix when a metastable β titanium alloy with an initial composition C^{bulk}_{Mo} is quenched in to a temperature T_1, as illustrated in Figure 2.20 The composition of alpha phase at temperature, T_1, will be C^{α}_{Mo}. Assuming that local equilibrium conditions are achieved, composition of the β at the α/β interface will be C^{β}_{Mo}. The concentration difference in the α and β phases will create a driving force for the flux of the solute atoms and the flux of these atoms with respect to the interface

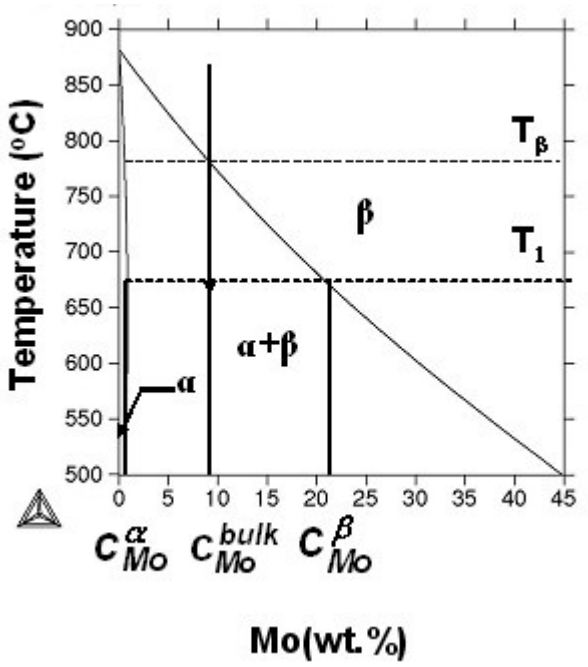

Figure 2.20. The binary phase diagram showing the bulk and the α/β interface composition.

may be written as:

$$J_1 = VC_{Mo}^{\alpha} \qquad 2.47a$$

$$J_2 = VC_{Mo}^{\beta} - D^{\beta}\left[\frac{dC}{dx}\right] \qquad 2.47b$$

where J_1 and J_2 are the flux of Mo atoms into and away from the interface, respectively.

Under steady state conditions J_1 and J_2 will remain balanced and the velocity of the interface (V) may be written as:

$$V = -\frac{D^{\beta}}{(C_{Mo}^{\alpha} - C_{Mo}^{\beta})}\left[\frac{dC}{dx}\right] \qquad 2.48$$

The concentration profile in front of a moving interface can be simplified considering an approach due to Zener [62]:

$$\frac{dC_{Mo}}{dx} = \frac{\Delta C_o}{L} \qquad 2.49$$

where $\Delta C_o = C_{Mo}^{\beta} - C_{Mo}^{bulk}$ and L is the width of the diffusion zone, shown in Figure 2.21. L can be obtained by considering the overall conservation of mass such that the solute ejected from the grain boundary α phase must be equal to the solute piling up ahead of the interface. As a result the overall mass is conserved which can be expressed in the following manner:

$$\left(C_{Mo}^{bulk} - C_{Mo}^{\alpha}\right)x = L\,\Delta C_o/2 \qquad 2.50$$

where x is the thickness of the alpha precipitate.

Re-arranging equation 2.50 gives:

$$L = \frac{2x(C_{Mo}^{bulk} - C_{Mo}^{\alpha})}{\Delta C_o} \qquad 2.51$$

Combining equation 2.49 and 2.50 to find the composition profile gives:

$$\frac{dC_{Mo}}{dx} = \frac{(\Delta C_o)^2}{2x(C_{Mo}^{bulk} - C_{Mo}^{\alpha})} \qquad 2.51$$

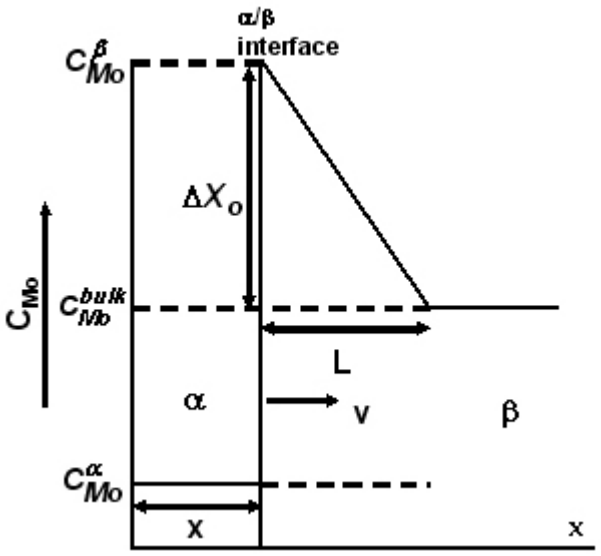

Figure 2.21 Simplified composition profiles across the α/β interface

Noting that $V = \frac{dx}{dt}$ and substituting into equation 2.52 into 2.47 gives:

$$\frac{dx}{dt} = \frac{D(\Delta C_o)^2}{2x\left(C_{Mo}^{\beta} - C_{Mo}^{\alpha}\right)\left(C_{Mo}^{bulk} - C_{Mo}^{\alpha}\right)} \qquad 2.53$$

Assuming $C_{Mo}^{bulk} \approx C_{Mo}^{\beta}$ and re-writing equation 2.53 gives:

$$\frac{dx}{dt} = \frac{D(\Delta C_o)^2}{2x\left(C_{Mo}^{\beta} - C_{Mo}^{\alpha}\right)^2} \qquad 2.54$$

Integrating equation 2.53 to find the thickness of the α precipitate gives:

$$x = \frac{\Delta X_0}{\left(X_{Mo}^{\beta} - X_{Mo}^{\alpha}\right)} \sqrt{Dt} \qquad 2.55$$

Differentiating 2.55 to find the velocity gives:

$$V = \frac{\Delta X_0}{2\left(X_{Mo}^{\beta} - X_{Mo}^{\alpha}\right)} \sqrt{\frac{D}{t}} \qquad 2.56$$

In conclusion; Equations2.55 and 2.56 mathematically substantiate the following [47, 48]:

- Thickening of grain boundary α precipitate is time dependent and obeys a parabolic law.

- For a given time, growth rate is a function of supersaturation and decreases with increasing time.

2.4.1.2. Lengthening of Grain Boundary Alpha Precipitates

Upon forming, grain boundary precipitates may quickly lengthen along the boundary on which they precipitated and form a thin film. In his studies on plain carbon steels Dube showed that lengthening rates of grain boundary ferrite precipitates are independent of time [63] and his approach will be used to understand the lengthening kinetics of grain boundary α precipitates in metastable β titanium alloys. The lengthening of a grain boundary α particle is considered to be essentially the same as that of a plate and can be given as [64]:

$$V = \frac{D^{\beta}}{4r' \sin\theta} \frac{\left(C_{Mo}^{\beta}(r) - C_{Mo}^{bulk}\right)}{\left(C_{Mo}^{\beta}(r) - C_{Mo}^{\alpha}(r)\right)} \qquad 2.57$$

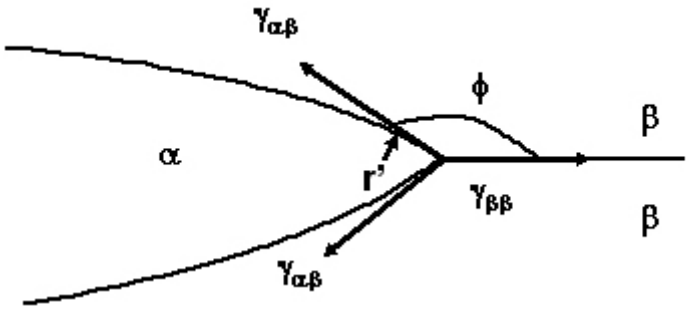

Figure2.22. Balance of interfacial energies assumed at the advancing edge of a grain boundary precipitate.

Where r' is the radius of the curvature of a grain boundary precipitate in the area immediately adjacent to the junction with the grain boundary and ϕ is defined as the supplement of the contact angle, θ, depicted in Figure 2.22. Upon replacing $r'\sin\phi$ with r' (the radius of curvature of the edge of a plate) the elementary form of Zener-Hillert equation for plate lengthening is obtained as discussed in the following section.

2.4.2. Growth of Plate-like Precipitates

As a result of grain boundary growth of the α phase, a secondary phase forms of out of the grain boundary itself from grain boundary precipitates or within the grains. Dubė's morphological classification system identifies two different plate-like precipitates which can be used to describe this secondary phase and are known as a) Widmenstätten sideplates b) Intragranular widmenstätten plates [65]. Sideplates are needle tipped plates growing directly out of a grain boundary or from grain boundary precipitates, whereas intragranular plates form within the

grains. The composition profile across an α/β interface, as a plate-like precipitate grows into a matrix of composition C_{Mo}^{bulk} is illustrated in Figure 2.23.

As the α precipitate grows, solute ejected from the tip of the precipitate diffuse to the sides and the amount of solute piling up at the tip of the α/β interface is not equal to the solute ejected from the α precipitate. As a result, the concentration gradient ($\frac{dC}{dx}$) at the tip will be much steeper when compared to a growing grain boundary precipitate. Assuming that diffusion distance, L, is linearly proportional to the tip radius, r as:

$$L = ar \tag{2.58}$$

Upon substituting equation 2.58 into 2.49 , the concentration gradient can be found as:

$$\frac{dC_{Mo}}{dx} = \frac{\Delta C_o}{ar} \tag{2.59}$$

The velocity of the α/β interface of a plate-like precipitate can be found by combining 2.48 and 2.59 to give:

$$V = -\frac{D^{\beta}}{ar}\frac{(C_{Mo}^{\beta} - C_{Mo}^{bulk})}{(C_{Mo}^{\alpha} - C_{Mo}^{\beta})} \tag{2.60}$$

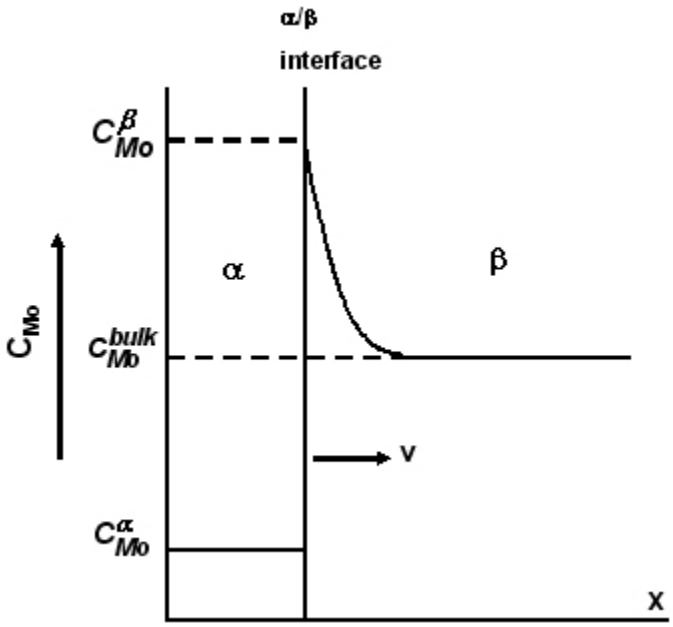

Figure 2.23. Composition profile along the centerline of a plate-like alpha precipitate.

Growth kinetics of plate-like precipitate differ from the thickening of grain boundary α in three main ways [48]:

1) The growth rate of the plate-like precipitates is much higher due to the very small tip radius.

2) Diffusion distance is proportional to the tip radius of a plate-like precipitate. As a result diffusion occurs over much shorter distances.

3) Solute profile at the centerline of the tip of a plate-like precipitate is independent of time, thus growth velocity will be time independent.

Upon deriving equation 2.60, the effect of interface curvature on the on the equilibrium phase diagram has not been taken into account. The interface curvature is expected to shift the phase boundaries and the solute concentration

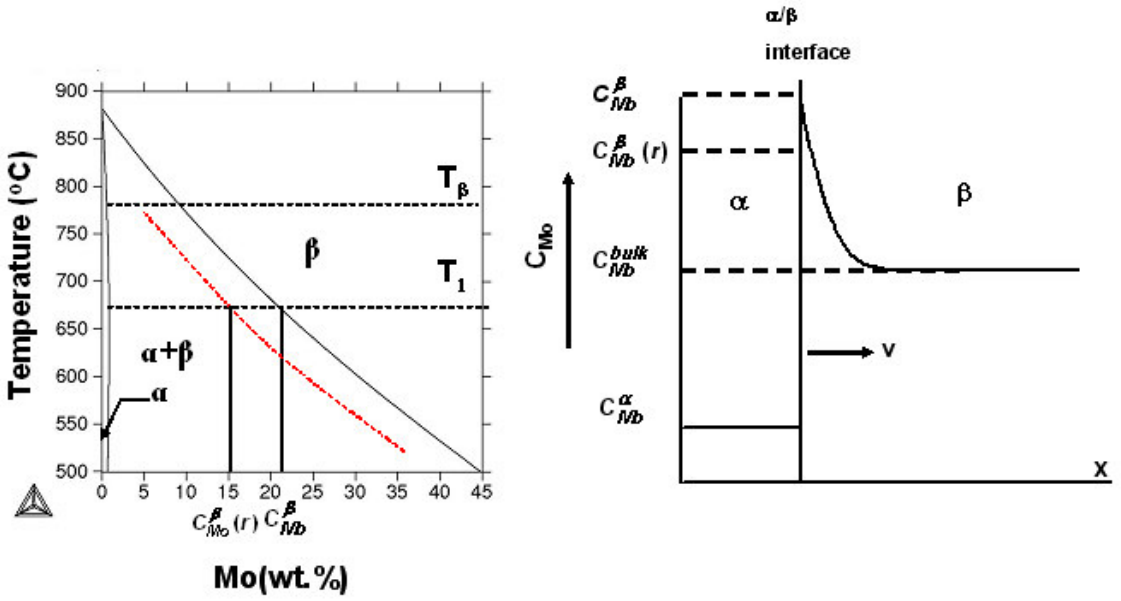

Figure 2.24. Effect of curvature on the a) composition of the β phase infront of the α/β phase boundary b) composition profile along centerline of a plate-like precipitate

at tip is reduced from X^{β}_{Mo} to $X^{\beta}_{Mo}(r)$, as shown in Figure 2.24. As a result of the smaller concentration gradient at the interface, tip migration rate will decrease. Under these conditions equation 2.59 may be re-written as:

$$V = \frac{D^{\beta}}{ar}\frac{\left(C^{\beta}_{Mo}(r) - C^{bulk}_{Mo}\right)}{\left(C^{\beta}_{Mo}(r) - C^{\alpha}_{Mo}(r)\right)} \qquad 2.61$$

As $C^{\beta}_{Mo}(r) \rightarrow \mathbf{C^{bulk}_{Mo}}$ the gradient will be zero and growth will cease. Therefore a critical tip radius (r_C) may be defined where $C^{\beta}_{Mo}(r_C) = C^{bulk}_{Mo}$.

Recognizing that:

$$C^{\beta}_{Mo}(r) - C^{bulk}_{Mo} = \left(C^{\beta}_{Mo} - C^{bulk}_{Mo}\right)\left[1 - \frac{r_c}{r}\right] \qquad 2.62$$

The variation of the plate velocity with the tip radius can be given as:

$$V = \frac{D^{\beta}}{ar}\frac{\left(C^{\beta}_{Mo} - C^{bulk}_{Mo}\right)}{\left(C^{\beta}_{Mo}(r) - C^{\alpha}_{Mo}(r)\right)}\left[1 - \frac{r_c}{r}\right] \qquad 2.63$$

Equation 2.63 implies that $V \to 0$ as $r \to r_C$.

Assuming that $X^{\beta}_{Mo}(r) - X^{\alpha}_{Mo}(r)$ is constant and differentiating equation 2.61 with respect to r gives a maximum rate at $r = 2r_C$. Substituting this into equation 2.61 gives the well known Zener-Hillert equation for plate like precipitate growth as [64, 66]:

$$V = \frac{D^{\beta}}{2ar_c}\frac{\left(C^{\beta}_{Mo} - C^{bulk}_{Mo}\right)}{\left(C^{\beta}_{Mo}(r) - C^{\alpha}_{Mo}(r)\right)} \qquad 2.62$$

2.5. Understanding the Grain Boundary Structure

Polycrystalline materials are made up of small crystalline units that differ in orientation. These crystalline units are called grains and separated by interfaces called grain boundaries. Similar to other metal systems, grains and grain boundaries have important influences on the properties of metastable β titanium alloys. For example, morphology and distribution of alpha phase particles, consequently the mechanical properties can be improved by modifying the grain and grain boundary structure [67]. Since the properties of metastable β titanium alloys depend on the physical properties of grains and grain boundaries an understanding of the nature of these microstructural features provides a useful background in studying phase transformations.

In three dimensions, a grain boundary can be described by the orientation of two crystals with respect to each other and the orientation of the boundary plane relative to one of these crystals. In general three degrees are required to specify the orientation of one grain relative to the other and two degrees to specify the orientation of the boundary relative to one of the grains [68].

A common notation, that has been adopted to describe the relative orientations of two crystals, includes defining a single rotation θ about an axis, l which is common to the coordinate systems of the two crystals [69, 70]. Two simple boundaries arise when the rotation axis is oriented in a special way to the two crystals [71]. These are tilt and twist boundaries. A tilt boundary occurs when the rotation axis is parallel to the grain boundary plane and a twist boundary is

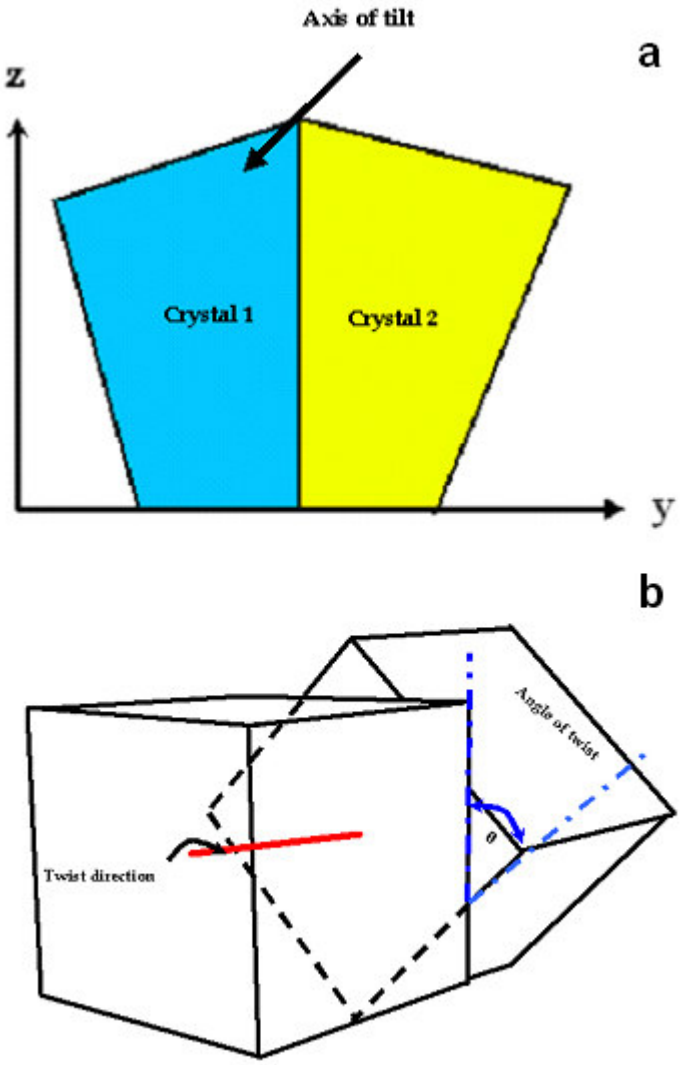

Figure 2.25. Schematic illustration of a a) tilt and b) twist boundary.

formed when the rotation axis is perpendicular to the boundary plane as shown in Figure 2.25.

Further, grain boundaries can be examined under two categories based on the amount of rotation of the two crystals with respect to each other: low- and high- angle boundaries. If the amount of rotation is low, the boundary between

two crystals is defined as a low angle boundary, whereas a high angle boundary forms at relatively large rotations.

2.5.1. Low Angle Boundaries

Low angle boundaries are described by a dislocation model and defined as an array of edge dislocations [72, 73]. The cores of these dislocations are located D distance apart from one another as depicted in Figure 2.26. The total energy associated with the grain boundary $\mathbf{E_B}$ depends on D and thought to be made up of two parts. These are elastic strain energy and dislocation core energy.

The elastic strain energy defines the energy of the elastically distorted crystal region in the vicinity of the dislocations and can be calculated from the of elastic theory, whereas the dislocation core energy is associated with the energy of atoms that are located within the dislocation core. These atoms are displaced so severely from their equilibrium positions that elastic theory is not applicable in this region.

When calculating the energy of grain boundaries, it is assumed that no interaction occurs between the individual dislocations and the total energy is directly proportional to density of dislocations, 1/D, which can be given as:

$$\frac{1}{D} = \frac{2\sin(\theta/2)}{b} \qquad 2.65$$

For small θ values equation 2.65 can be re-arranged and given as:

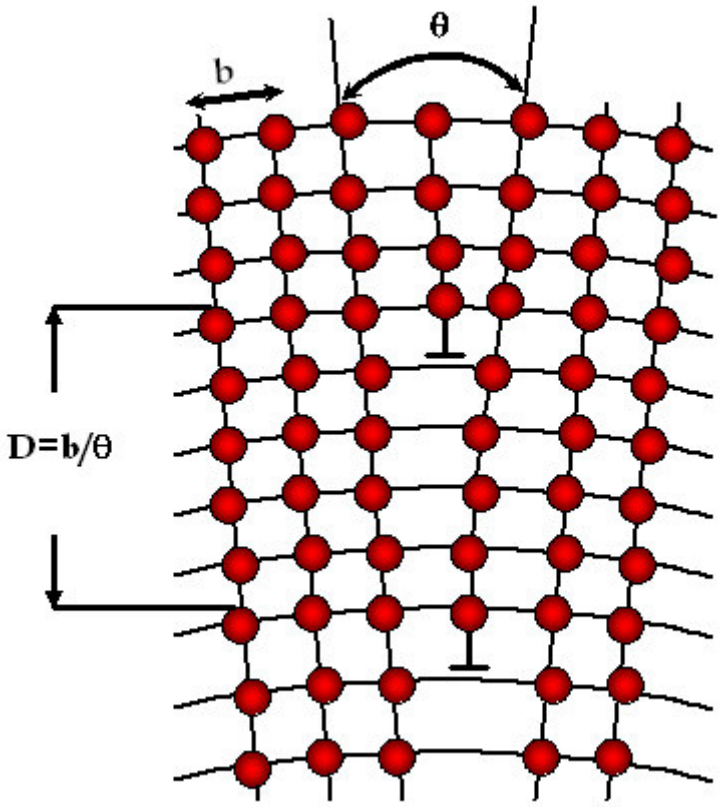

Figure 2.26. Schematic illustration of an array of dislocations along a low angle tilt boundary.

$$\frac{1}{D} = \frac{\theta}{b} \qquad 2.66$$

If the energy of a single edge dislocation per unit length is equal to E, then the total grain boundary energy E_B can be given as (13):

$$E_B = E\frac{1}{D} \qquad 2.67$$

and E is expressed as:

$$E = \frac{Gb^2}{4\pi(1-\nu)} \ln \frac{r}{b} + E_c \qquad 2.68$$

where G is the shear modulus, b is the Burger's vector of the dislocation, ν is Poisson's ratio, r is the distance to which the elastic distortion produced by the dislocations reaches, and E_c is the energy in the core of the edge dislocation where the distortion becomes non-linear.

Combining equations 2.66 and 2.68 and substituting into 2.67 gives:

$$E_B = \left(\frac{Gb^2}{4\pi(1-\nu)} \ln \frac{r}{b} + E_c\right) \frac{\theta}{b} \qquad 2.69$$

Re arranging equation 2.69 gives:

$$E_B \frac{Gb}{4\pi(1-\nu)} \ln \frac{r}{b} + E_c \frac{\theta}{b} \qquad 2.70$$

The elastic strain of an array of dislocation forming the boundary vanishes at distances greater than D, therefore r may be assumed to be equal to D. Recognizing that $D = r = \frac{b}{\theta}$ and substituting in to equation 2.70 gives:

$$E_B = \theta \frac{Gb}{4\pi(1-\nu)} \left(E_c \frac{4\pi(1-\nu)}{Gb^2} - \ln \theta\right) \qquad 2.71$$

Re-arranging equation 2.71 and grouping the material related constants together gives:

$$E_B = A\theta(B - \ln\theta) \qquad 2.72$$

where

$$A = \frac{\mu b}{4\pi(1-\nu)} \qquad 2.73a$$

$$B = \frac{E_c 4\pi(1-\nu)}{Gb^2} \qquad 2.73b$$

The dislocation spacing (D) decreases with increasing the amount of rotation (θ) between two crystals and results in an increase in the atomic disorder at the grain boundary. As a result, the strain field associated with the dislocation spreads out to very large distance in the crystal and the grain boundary energy increases sharply from negative infinitive at zero tilt angles as shown in Figure 2.27. Upon decreasing the distance between dislocations, their strain fields start to overlap and cancel each other. This reduces the total strain energy associated with dislocations and the slope of the E_B versus θ curve becomes less steep at increasing tilt angles. At relatively high θ the grain boundary energy becomes independent of the amount of rotation. This transition occurs at the angles of (15-20^o) for tilt boundaries and defines the transition from a low to a high angle boundary.

Equation 2.72 can also be applied to predict the energy of twist boundaries.

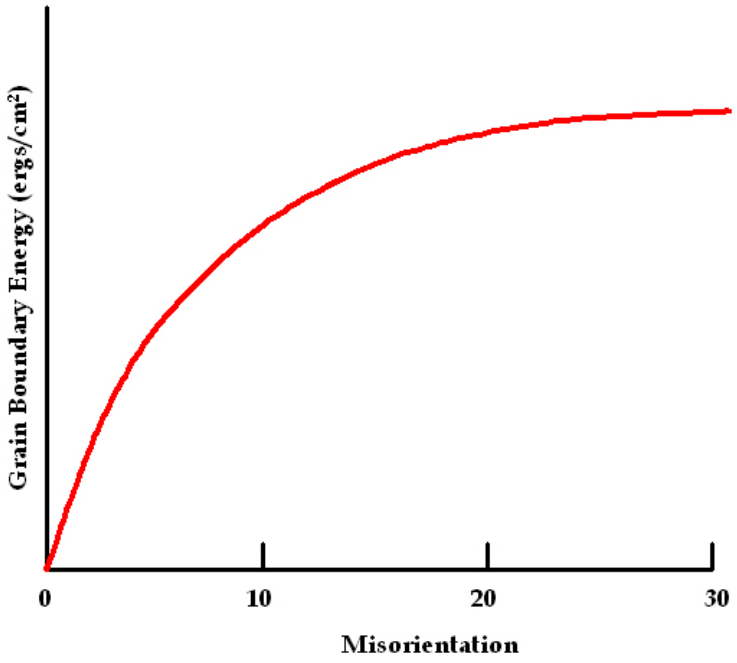

Figure 2.27. Variation of the grain boundary energy as a function of misorientation.

In this case the constants A and B are replaced with $A = \frac{Gb}{2\pi}$ and $B = \frac{E_c 2\pi}{Gb^2}$, respectively. The grain boundary energy varies in a similar manner with the twist angle, however twist boundaries are made up of a crossed grid of screw dislocations and have lower dislocation density when compared to the tilt boundaries [74]. A lower dislocation density is expected to shift the E_B versus θ curve and E_B becomes independent of twist angle at higher θ [75].

2.5.2. High Angle Boundaries

According to the dislocation model a high angle grain boundary form between two crystals that are rotated with respect to each other at angles greater than 15-20^0. These boundaries are disordered and have constant energies [76]. However, experimental evidence suggests that high angle boundaries are not completely disordered and may display cusps at specific misorientations of the E_B versus θ curve [77]. These cusps were associated to boundaries with relatively low energies and several theories were proposed to explain the structure of these *'special'* high angle boundaries.

In general, these models are divided in two based on their areas of applicability [73]. The first group attempts to bring an explanation to the mechanical behavior of the boundaries. For example, Mott [78] proposed an 'island' model to explain the sliding behavior of the boundaries. In this model the structure of the boundary between the two crystal lattices is described in terms of islands good fit separated by islands of bad fit as illustrated in Figure 2.28

The second group deals with the atomic structure of the boundaries. One of these models is due to Smoluchowski [79] who correlates the structure of the boundary to the angle of tilt. In his model, Smoluchowski describes grain boundaries with tilt angles smaller than 15^o as an array of dislocation which are separated by undistorted regions. Upon exceeding 15^o, he suggests that, these dislocations approach each other and form regions of misfit with large Burger's vectors. These misfit regions are separated by relatively undistorted areas and a

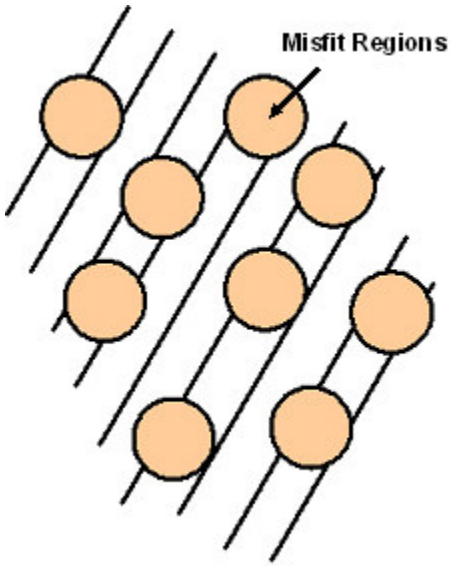

Figure 2.28. Schematic illustration of the island model of Mott.

continuous misfit region along the boundary area can be observed when the tilt angle exceeds 35^{o} , shown in Figure 2.29.

The theories proposed by Mott and Schmolowski have been largely suppressed by the introduction of the coincident site lattice (CSL) model. These boundaries are referred as coincident site lattice (CSL) boundaries because they form at boundary planes which allow the two adjoining lattices to fit together with relatively little distortion of the inter-atomic bonds [80]. The CSL boundaries may form only at exact rotation angles about specific rotation axes and the density of common lattice sites varies with the specific choice of angle/axis pair. The density of common lattice sites are described by a sigma ($\sum$) value and the density of coincident sites decreases with increasing the sigma value. For example $\sum$=5 ,shown in Figure 2.30, defines a CSL boundary where 1 out of 5

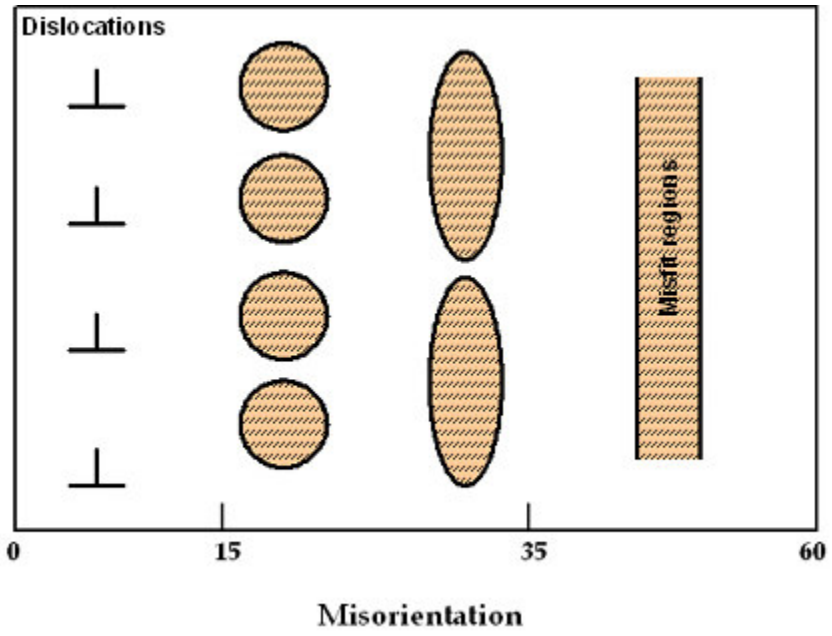

Figure 2.29. Schematic illustration of the grain boundary model of Schomolowski.

lattice sites is common to both grains, whereas 1 out of every 3 lattice points is common to both crystals along a $\sum$=3 CSL boundary.

In theory, the $\sum$ value of a CSL boundary can take up any value, however, only low sigma values were associated with unique properties. For example, Aust and Rutter [81] showed impurity segregation to the boundaries is related to the grain boundary structure and CSL type boundaries are associated with very little impurity segregation due their ordered structures.

In general, exact CSL orientations are not observed in actual systems. Brandon et. al. [82] have examined the atomic structure along the grain boundaries of tungsten and tungsten-rhenium alloys by field ion microscopy and

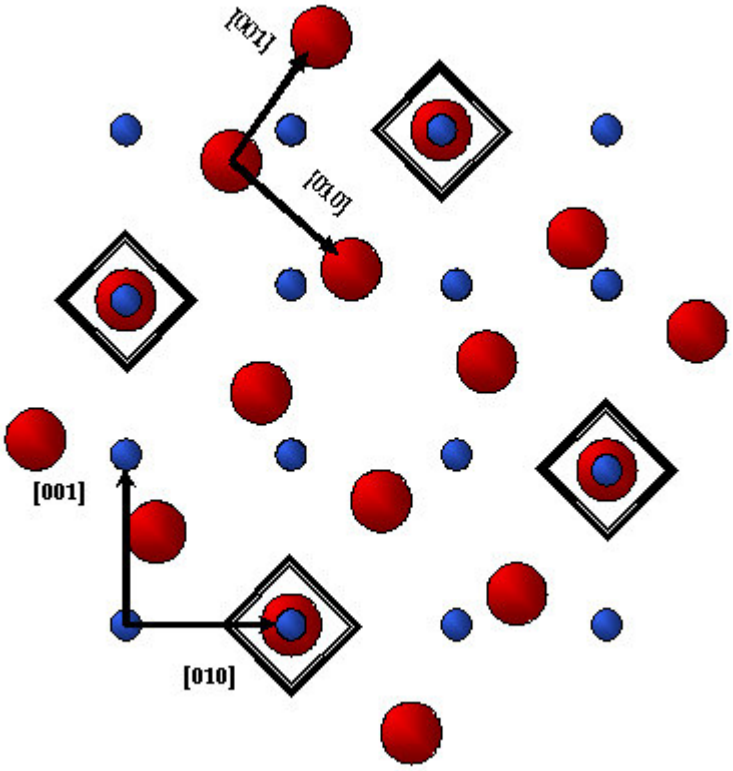

Figure 2.30. Schematic of a ∑=5 CSL boundary.

showed that an angular deviation of the boundary plane from the most densely packed plane of the coincident site lattice is associated with the formation ledges along the boundary. They proposed that these boundaries can described as regions of good fit where the boundary follows the most densely packed planes of the coincidence lattice and a superimposed dislocation sub-boundary where misfit occurs. They concluded that, the density of dislocations that can be introduced into a coincidence boundary is limited by the density of coincident sites at the boundary and a maximum deviation from an exact CSL orientation

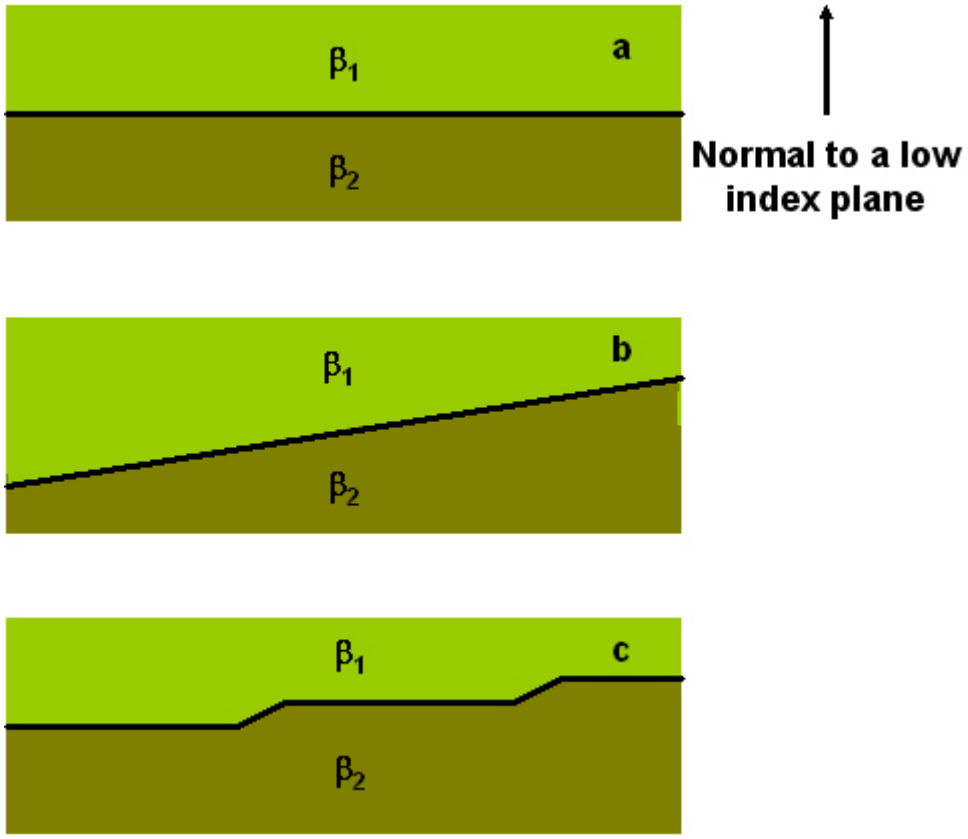

Figure 2.31 Schematic illustration of a grain boundary lying along a) a low index plane b) a random high index plane and c) illustration of faceting of a random grain boundary.

, V_m, can be defined through Brandon criterion where V_m is proportional to the highest density of dislocations that can be accommodated by the boundary [83]:

$$V_m = V_o \Sigma^{-1/2} \qquad 2.74$$

where V_o is proportionality constant. Substituting $\Sigma=1$ into equation 2.74 gives V_m as 15^o, this angle being the limit for the low angle boundaries. Therefore the

low angle boundaries correspond to $\sum=1$ CSL type boundaries.

The grain boundaries that can not be described by a CSL relationship are referred as random high angle boundaries and increase the total energy of the system. Whenever possible, a given system is expected to reduce its total energy. Two mechanisms that may reduce the energy of a system include grain growth and faceting. Upon grain growth, the grain boundaries migrate and increase the mean grain size [84], whereas by faceting the grain boundary plane deviates from its original direction and form facet parts [85]. These facet parts lie along the low index planes, as shown in Figure 2.31. In conclusion, both grain growth and faceting reduce the energy of a system at the expense of increasing the total grain boundary area.

2.6. Understanding Electron Back Scatter Diffraction (EBSD) to Study the Crystallographic Relationships between α and β Phases

In a scanning electron microscope (SEM) chamber, interaction of an electron beam with specimen surface results in different scattering events (elastic and inelastic) which in turn give rise to a variety of signals including secondary electrons, characteristic x-rays, and back scattered electrons, illustrated in Figure 2.32 [86].

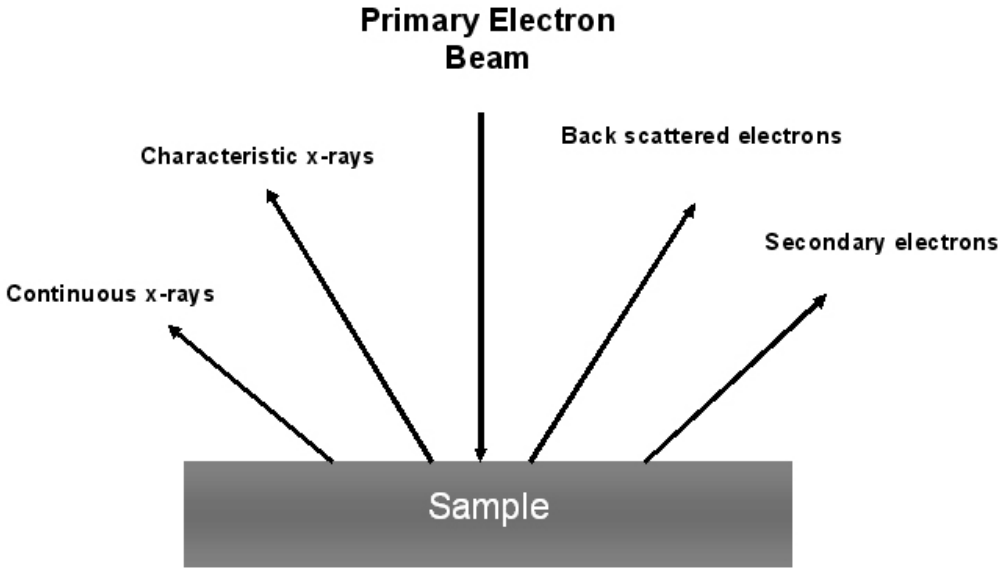

Figure 2.32. Various signals that can be detected in a scanning electron microscope.

Secondary electrons can be defined as all the electrons emitted from the specimen with energy less than 50eV [86]. These electrons are ejected from the loosely bound outer shell electron of the specimen atoms during inelastic scattering of the primary beam. Secondary electrons can be captured by a

secondary electron detector providing signals for sample navigation, focusing, beam optimization and topographic studies.

Inelastic scattering of the primary beam may also form x-ray signal which are useful for chemical analysis. Two processes that form x rays are: a) Continuous x-ray process (Bremstrahlung)and b) Inner shell ionization process. The continuous x-ray process is a radiation event that occurs when the electron of the primary beam lose their energy due to the interaction with the Coulombic field of an atom. The energy difference is then emitted as a photon electromagnetic energy given as:

$$\Delta E = h\nu \qquad 2.75$$

where ΔE is the energy lost by the electron, h is the Planck constant and ν is the electromagnetic radiation frequency. Bremstrahlung radiation creates a background limiting the characterization of the chemical composition.

The inner shell ionization process arises from the interaction of the electron beam with tightly bound inner shell electrons. This interaction may eject an electron, resulting in a vacancy in the atom's inner shell (K-shell) and leave the atom, as an ion, in an excited state. Other electrons in the outer shells (L- ,M- .shells) immediately fill the inner vacancy. The difference between the electron shells has a characteristic value for each element. This excess energy may be released in one of the two ways: Auger or characteristic x-ray process [86].During Auger processes the difference in the shell energies can be transmitted to another outer shell electron in the form of kinetic energy and ejects

the electron from its atom. During characteristic x-ray processes the difference in energy is expressed as a photon electromagnetic radiation with a sharply defined energy. Detection of the characteristic x-ray is done by a wavelength dispersive spectrometer (WDS) or an energy dispersive spectrometer (EDS) detector.

Finally, backscattered electron signals arise from elastic scattering. These signals consist of high-energy electrons originating from the electron beam that are reflected or backscattered out of the same surface that they entered into the specimen. A backscattered electron detector may be used to collect these signals for imaging purposes. This technique may be used to detect contrast between areas with different chemical compositions in multi phase materials or between areas with different crystallographic orientations in single phase materials [86].

Nevertheless, backscattered electrons can also be used to form electron backscatter diffraction (EBSD) for quantitative analysis of crystallographic orientation of the sampled volume. Since fewer backscattered electrons are emitted (only 30% of the incident beam) from a sample than secondary electrons, the number of backscattered electrons leaving the sample perpendicular to the surface might be significantly lower than those that other follow trajectories toward the sides. EBSD technique relies on enhancing the proportion of the backscattered electrons that are able to undergo diffraction and escape from the specimen surface

The backscattered fraction can be quantified using the backscatter coefficient, η which is defined as [86]:

$$\eta = \frac{\eta_{BSE}}{\eta_B} \qquad 2.76$$

where η_{BSE} and η_B are the number of backscattered electrons and beam electrons incident on the specimen surface, respectively.

The backscatter coefficient is a function of tilt angle, θ (the complement of the angle between the beam and the surface plane) and may be expressed as [87]:

$$\eta(\theta) = \frac{1}{(1+\cos\theta)^p} \qquad 2.77$$

Where p is a function of the atomic number Z and given as:

$$p = {}^{9}\!/_{Z^{1/2}} \qquad 2.78$$

Substituting equation 2.76 into 2.77 gives:

$$\frac{\eta_{BSE}}{\eta_B} = \frac{1}{(1+\cos\theta)^p} \qquad 2.79$$

Equation 2.79 suggests that the backscattered electron fraction increases with increasing tilt angle, approaching unity at very high values of θ.For this purpose, a typical EBSD experiment includes tilting the sample to large angles, typically 70^o from the horizontal [87].

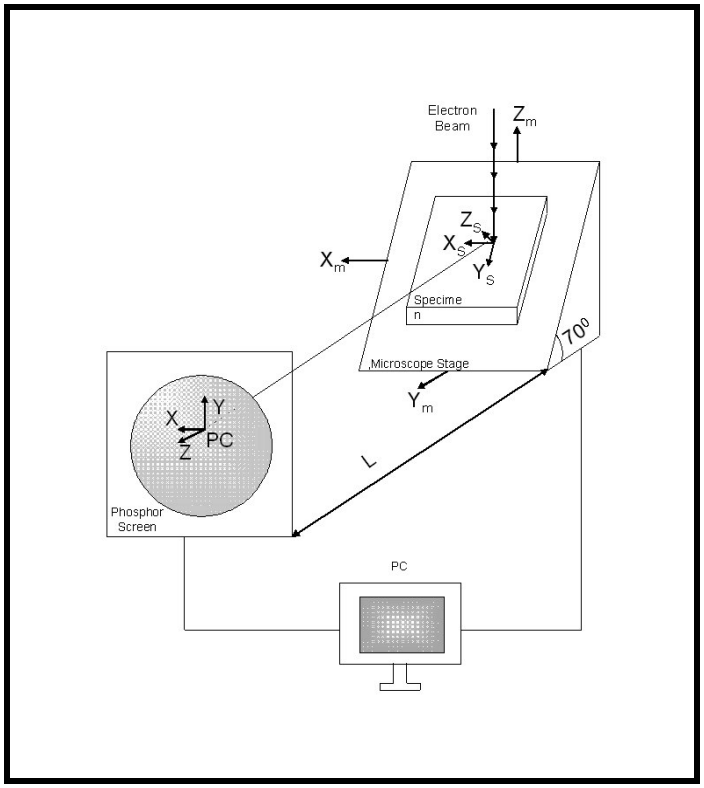

Figure 2.33 Components of an EBSD system.

The backscattered electrons escaping from a tilted sample surface may be detected by an EBSD detector for orientation analysis. Major components of an EBSD system are shown in Figure 2.33.

This system consists of a phosphorus screen which is placed in front of a sensitive charged coupled device (CCD) video, mounted parallel to microscope's Y_m axis, for capturing a diffraction pattern. Both the phosphor screen and the camera are mounted in one of the SEM ports and held under vacuum. The backscattered electrons reflected onto this phosphorus screen and form a diffraction pattern The resulting diffraction pattern is then recorded and analyzed

by means of computer algorithms to obtain orientation information of the sampled volume.

Over the last decade, EBSD has become one of the most widely used experimental techniques for micro-texture analysis. The introduction of high speed cameras for pattern capturing and algorithms for fully automatic pattern recognition and indexing provide additional methods for analysis.

2.6.1. Formation of Kikuchi Bands

An electron beam entering a crystalline solid is scattered diffusely and elastically in all directions [88]. Interaction of electrons with atoms within the material results in radiation of waves with the same wavelength, λ, depicted in Figure 2.34.

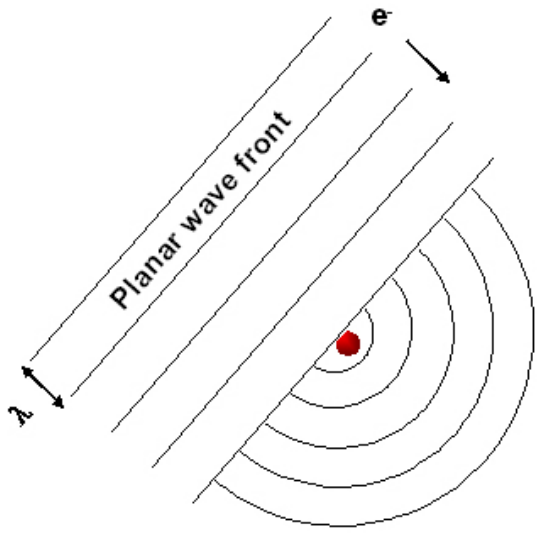

Figure 2.34. Scattering of a planar wave front from a single atom with in the material giving rise to spherical wave.

Radiated fields from all atoms within a given volume interfere with each other either constructively or destructively. The constructive interference occurs if

the atomic arrangement in the material is ordered, radiation is monochromatic and the wavelength is on the same order of magnitude (or smaller) than the diffracting feature [88].

The condition for constructive interference is given by Bragg's Law [89]. Consider atoms in an ordered material that lie on a set of lattice planes {hkl} separated by a distance d, Figure 2.35. The rays of the incident beam are always in phase and parallel up to the point at which the top beam strikes the atom X lying on the first layer of the lattice planes. The second beam continues to the next layer where it is scattered by atom Y. The second beam must travel the extra distance $|AY| + |YB|$ if the two beams are to continue traveling adjacent and parallel.

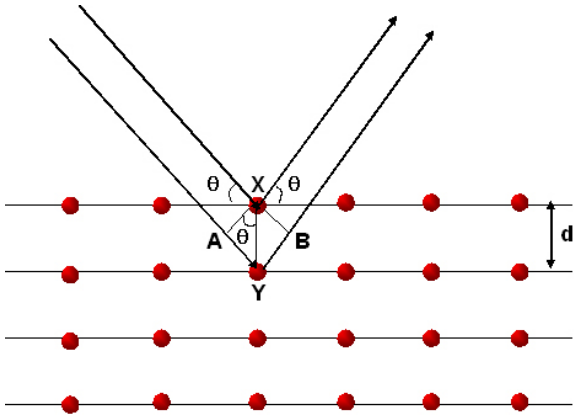

Figure 2.35. Schematic illustration of the diffraction from lattice planes. The geometry of diffraction leads to derivation of the Bragg's law.

These two beams will be constructive if the extra distance is an integral, n, multiple of the wavelength:

$$|AY| + |YB| = n\lambda \qquad 2.80$$

where

$$|AY| = d\sin\theta \qquad 2.81$$

and

$$|AY| = |YB| \qquad 2.82$$

Substituting equation 2.80 and2.81 into 2.79 gives:

$$n\lambda = 2d\sin\theta \qquad 2.83$$

This constructive wave interference can be observed as a diffraction pattern on an EBSD detector.

Since the electrons entering into a specimen in an SEM travel in all directions, the Bragg condition is satisfied for all sets of planes. These electrons may then inelastically scatter resulting in constructive interference. Since electrons are diffracted from a given set of planes in all directions, the diffracted beams will lie on the surface of a cone with the cone axis being normal to the diffracting planes, see Figure 2.36. In an EBSD experiment these cones will intersect a phosphor screen placed in front of the camera within in the SEM. Due to the large apex angle (~180^{o}) of the diffraction cones, their intersections with

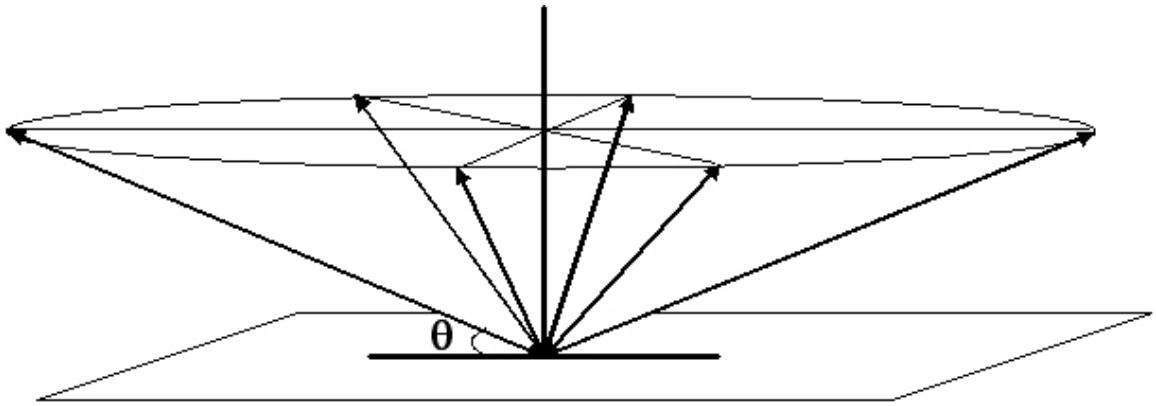

Figure 2.36. Schematic representation of the origin of Kikuchi lines.

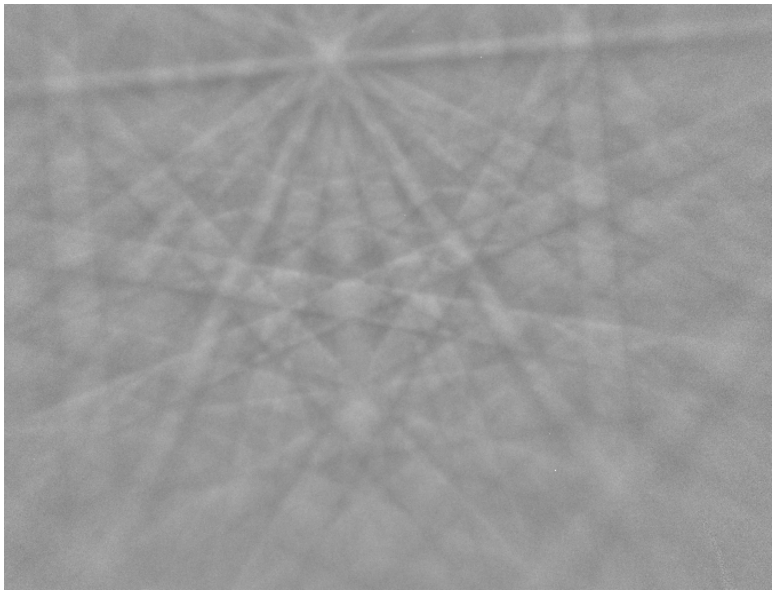

Figure 2.37. EBSD Kikuchi pattern from Ti-6.5Mo-4.5Fe-1.5Al, 20kV accelerating voltage, work done for this project.

the phosphor screen appear as two parallel, straight lines, separated at a distance proportional to the interplanar spacing between the diffraction planes [88]. The whole EBSD Kikuchi pattern consists of pairs of parallel lines where each pair is known as a Kikuchi band, shown in Figure 2.37 [90]. The intersection

of several bands corresponds to a zone axis (pole) representing the normal to a plane in the sample.

EBSD Kikuchi diffraction patterns are a gnomonic projection onto a flat surface, shown in Figure 2.38 [91].This concept can be understood by considering the sampled volume of crystal lying at the center of a sphere with a radius , $|ON|$, where $|ON|$ is the distance between the specimen and the projection plane, i.e. the phosphor screen. The point N is referred to as the pattern center. The coordinates of N and ON are defined during the calibration process. Diffracted rays intersecting the sphere are projected on the phosphor screen. The relationship between the distance from the pattern center to a given point on the projection plane, $|NP|$, and the sample to screen distance, $|ON|$, is given as:

$$|NP| = |ON| \tan \tau \qquad 2.83$$

where τ defines the angular displacement of P from the pattern center.

Since a given diffraction pattern obtained from the crystal is a function of orientation, the positions of Kikuchi bands can be used to calculate the orientation of a diffracting crystal, as demonstrated in Figure 2.39

2.6.2. Detecting Kikuchi Bands

The first step in automated indexing of EBSD patterns is to extract bands from the pattern. The method of choice was developed by Kreiger Lansen *et. al*

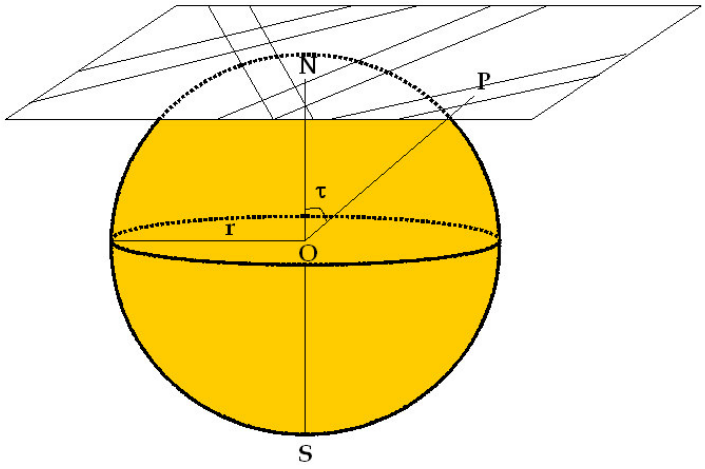

Figure 2.38. Schematic illustration of a Kikuchi pattern as a gnomonic projection.

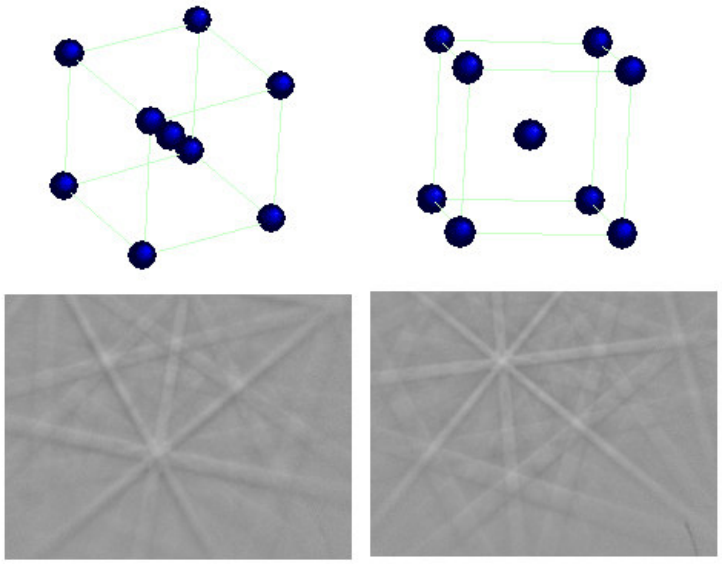

Figure 2.39. Variation in diffraction pattern with crystal orientation.

[92]. This technique applies Hough transform to a diffraction pattern image. The equation governing the Hough transform is given as:

$$\rho = x\cos\theta + y\sin\theta \qquad 2.84$$

with x and y defining a set of pixel coordinates on the image. The transition from the pixel coordinate system (x,y) to the Hough space (p,θ) is possible by plotting a number of collinear lines going through each pixel in the image. The normal to these lines intersecting the origin is then generated. The length of each normal line and angle that they make with the x axis is measured .This process is repeated for each pixel on the image and a graph of length (p) against angle (θ), known as the Hough space graph, is created, Figure 2.40.

Hough space may be divided into discrete bins (e.g. 1^{o} step in θ and 100 steps in p from $-p_{min}$ to $+p_{max}$) and the intensity at each x,y pixel in the image can be added into all corresponding bins [93]. A band in a diffraction pattern is then represented by a peak of high intensity in the Hough space. The peaks in the Hough space have a characteristic shape with the peak being surrounded by two valleys in the p direction. In order to draw out peaks of this characteristic shape the Hough transform is convoluted with a butterfly mask. Figure 2.41 shows an EBSD pattern, corresponding Hough transform and the bands detected.

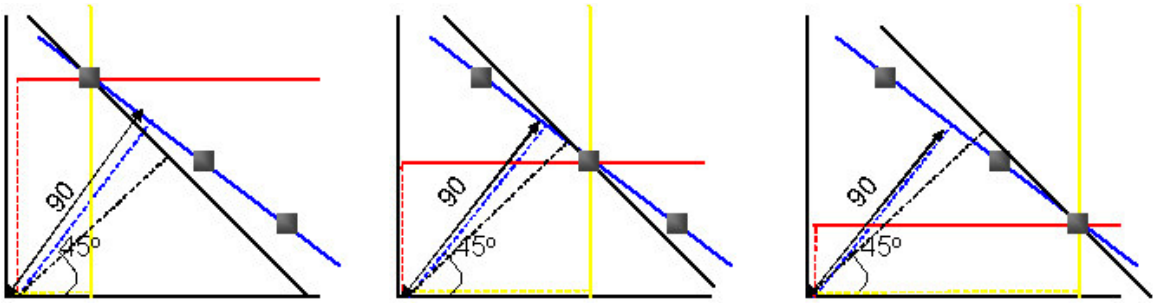

Angle	Distance
0	40
30	80
45	90
90	65

Angle	Distance
0	55
30	100
45	90
90	30

Angle	Distance
0	70
30	130
45	90
90	10

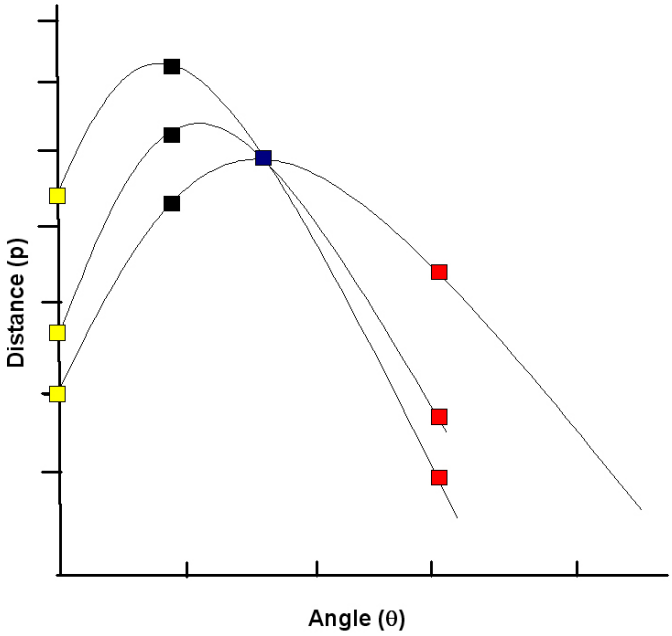

Figure 2.40 Schematic of transformation of x-y coordinates to Hough space. The numbers given do not have any physical significance. They are for illustrative purposes only.

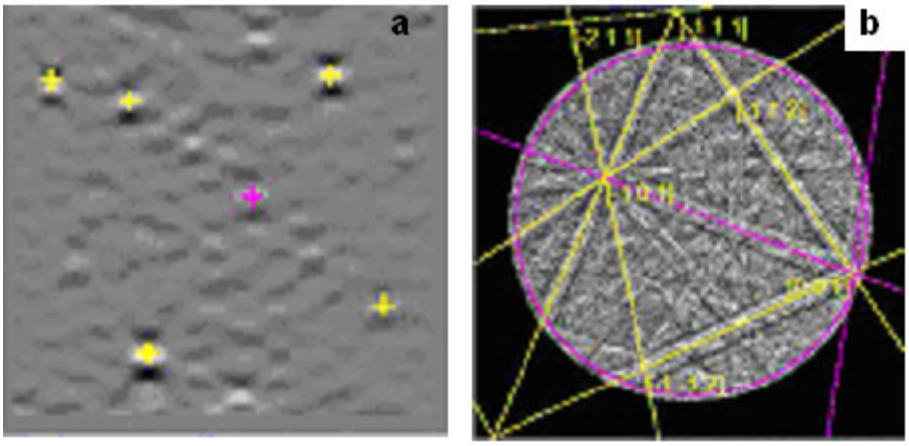

Figure 2.41 Photograph of a a) hough transform and b) its corresponding EBSD pattern with the detected bands, work done for this project..

2.6.3. Indexing Kikuchi Bands

In automated EBSD systems the detected bands can be indexed using a voting scheme [93-95]. This procedure involves first creating the all possible sets of three bands from the detected bands. Next, angles between the bands in each set are compared to a table containing all possible interplanar angles between the diffracting planes. Each band in a band set is associated with a Miller index. However, more than one solution can be found for any set. The number of solutions is a function of tolerance allowed between the measured and theoretical interplanar angles. The solutions found for all the sets are used in a voting scheme to identify the most probable indexing of the pattern. The final solution is the one receiving the most votes.

2.6.4. Crystal Orientation

A crystal lattice orientation can be defined with respect to a coordinate system fixed in the sample, Figure 2.42. For this purpose, it is necessary to

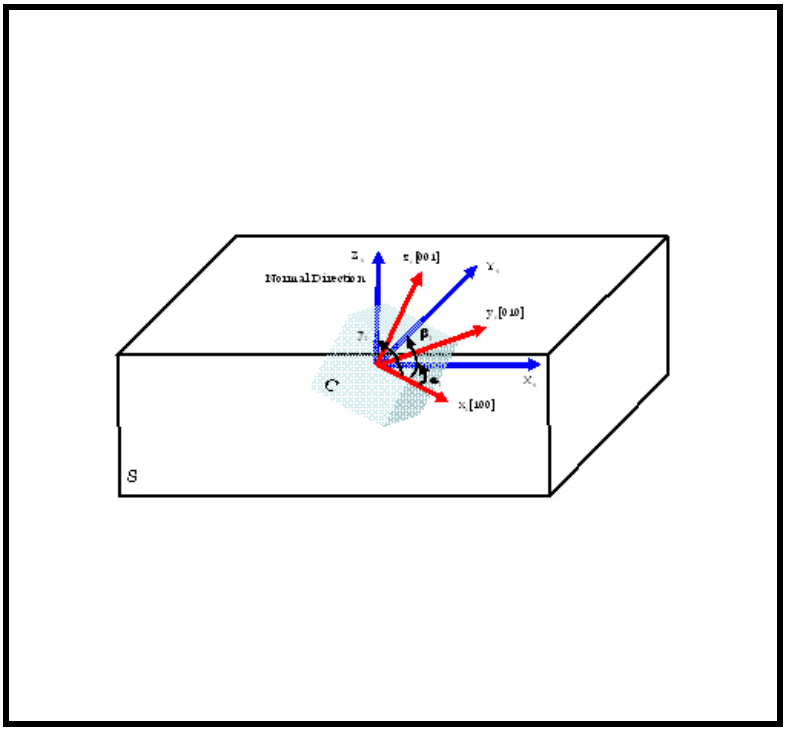

Figure 2.42. Schematic illustration of the relationship between the crystal and sample coordinate systems. α_1 ,β_1 and γ_1 are the angles between the crystal direction [100] and X_s, Y_s and Z_s(Normal Direction) respectively. α_2, β_2, γ_2 and α_3, β_3, γ_3 are similarly defined as the angles between the [010] and [001] crystal directions and the three sample axes.

.

define two sets of reference axes, known as coordinate systems, one within the specimen, C_S, and the other one in the crystal lattice, $\mathbf{C_C}$ [96] .These systems are Cartesian and right-handed. Typically, the axes of the specimen coordinate system (X_s, Y_s and Z_s) are respectively parallel to the rolling, transverse and normal directions if they exist otherwise defined arbitrarily. The second set of coordinate system is specified by the by the orthogonal [100], [010], [001] directions in the crystal

The two coordinate systems can be related through an orientation matrix, A. which bring them into coincidence.

$$C_c = A \cdot C_s \tag{2.86}$$

An orientation matrix is a 3X3 matrix given as:

$$A = \begin{matrix} a_{11} & a_{12} & a_{13} \\ a_{21} & a_{22} & a_{23} \\ a_{31} & a_{23} & a_{33} \end{matrix} \tag{2.87}$$

The elements of the orientation matrix (a_{ij}) are described by considering a relationship between the sample and crystal coordinates:

$$a_{11} = \cos\alpha_1 \tag{2.88a}$$

$$a_{12} = \cos\beta_1 \tag{2.88b}$$

$$a_{13} = \cos\gamma_1 \tag{2.88c}$$

$$a_{21} = \cos\alpha_2 \tag{2.88d}$$

$$a_{22} = \cos\beta_2 \tag{2.88e}$$

$$a_{23} = \cos\gamma_2 \tag{2.88f}$$

$$a_{31} = \cos\alpha_3 \tag{2.88g}$$

$$a_{32} = \cos\beta_3 \tag{2.88h}$$

$$a_{33}=\gamma_3 \qquad 2.88i$$

where- α_1, β_1 and γ_1- define the angles between the [100] direction of the crystal and the X_s, Y_s, Z_s directions of the specimen, respectively. Similarly, α_2, β_2, γ_2 and α_3, β_3, γ_3, define the angles between the [010] and [001] crystal directions and the three specimen axes

Various orientation descriptors that can be extracted from the orientation matrix include: the ideal orientation, the Euler angles, the angle/axis pair and Rodrigues vector. These descriptors are used to define orientations of the grains and misorientation between two grains

2.6.5. The Ideal Orientation

A practical way of describing the orientation of a sampled volume includes defining two Miller indices to represent the crystallographic directions, [hkl] that are parallel to the sample normal (Z_s) and transverse direction (X_s). The first and last column of the orientation matrix expresses the specimen's X and Z directions in the crystal coordinate system. Direction cosines in these columns can be multiplied by a suitable factor to bring them into whole numbers and subsequently divided by their lowest common denominator. This operation defines the ideal orientation (or Miller indices) which may be represented as

$$(hkl)[hkl] \qquad 2.89$$

It should be noted that extracting the ideal orientation directly from the orientation matrix is valid only for cubic crystals as indices for a plane and a direction are identical solely for cubic systems. For non cubic systems, on the other hand, determining ideal orientation is less straight forward and includes associating an orthogonal frame with the crystal axes [97].

2.6.6. The Euler Angles

According to Euler's rotation theorem, any orientation can be described using three angles (98, 99). The Euler angles refer to the three rotations which brings the specimen coordinate system into coincidence with the crystal coordinate system when performed in the ideal sequence. The three angles giving the rotation matrices are called the Euler angles. To define these angles consider a crystal with its [100], [010], [001] directions being parallel to the specimen's X, Y, Z axes. It is first rotated about the [001] by an angle φ_1 followed by a rotation about the [100] direction by an angle $\tilde{\phi}$ and finally, it is rotated φ_2 degrees about the [001] direction, as shown in Figure 2.43.

The relationship between the elements of the orientation matrix and the Euler angles can be given as:

$$a_{11} = \cos\varphi_1 \cos\varphi_2 - \sin\varphi_1 \sin\varphi_2 \cos\phi \qquad 2.90a$$

$$a_{12} = \sin\varphi_1 \cos\varphi_2 - \cos\varphi_1 \sin\varphi_2 \cos\phi \qquad 2.90b$$

$$a_{13} = \sin\varphi_2 \sin\phi \qquad 2.90c$$

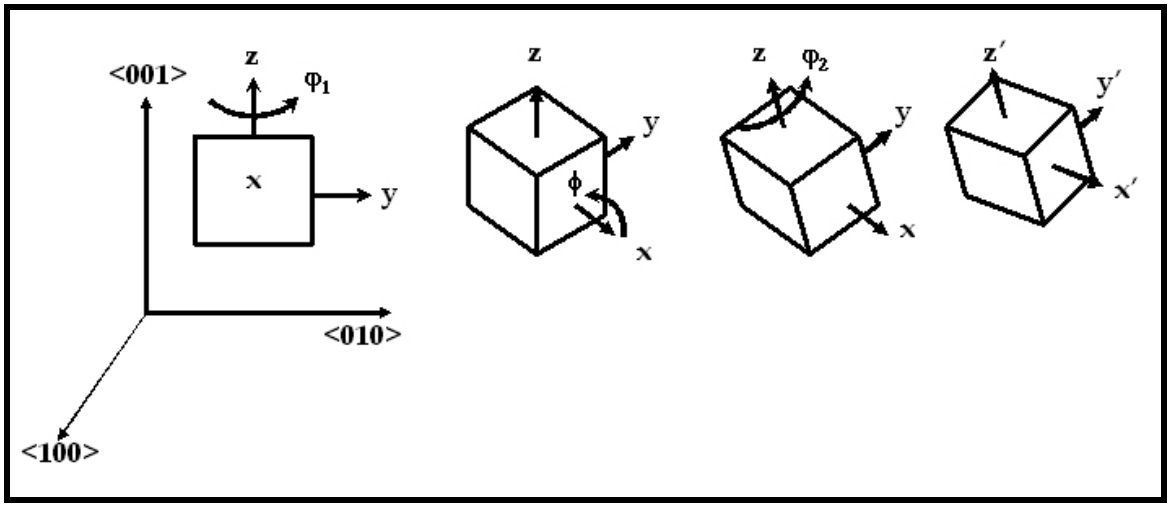

Figure 2.43. Schematic illustration of the effect of rotating a crystal with its <100>, <010>, <001> directions being parallel to the specimen's x, y, z axes about the <001> by an angle φ_1 followed by a rotation about the <100> direction by an angle ϕ and finally rotating φ_2 degrees about the <001> direction on the sample orientation.

$$a_{21} = -\cos\varphi_1 \sin\varphi_2 - \sin\varphi_1 \sin\varphi_2 \cos\phi \qquad 2.90d$$

$$a_{22} = \sin\varphi_1 \sin\varphi_2 - \cos\varphi_1 \cos\varphi_2 \cos\phi \qquad 2.90e$$

$$a_{23} = \cos\varphi_2 \sin\phi \qquad 2.90f$$

$$a_{31} = \sin\varphi_1 \sin\phi \qquad 2.90g$$

$$a_{32} = -\cos\varphi_1 \sin\phi \qquad 2.90h$$

$$a_{33} = \cos\phi \qquad 2.90i$$

A crystal orientation map may be colored by Euler coloring which transforms an orientation $(\varphi_1, \phi, \varphi_2)$ to an RGB (Red, Green, Blue) color through the following formula (Figure 2.44):

$$\text{Red} = 255.\frac{\varphi_1}{360} \tag{2.91a}$$

$$\text{Green} = 255.\frac{\phi}{360} \tag{2.91b}$$

$$\text{Blue} = 255.\frac{\varphi_2}{360} \tag{2.91c}$$

2.6.7. The Angle/Axis Rotation

The crystal coordinate system can be transformed onto the specimen coordinate system by a rotation through a single angle provided that rotation is performed about a specific axis or the angle axis/pair (Figure 2.45) [88]. Three variables, required to specify the orientation comprise one variable for rotation angle, θ and two variables, r_1 and r_2 for the rotation axis, r. The third index, r_3 is related to, r_1 and r_2 in the following manner:

$$r = r_1^2 + r_2^2 + r_3^2 \tag{2.92}$$

The relationship between the angle/axis pair and the orientation matrix is given as:

$$\cos\theta = (a_{11} + a_{22} + a_{33} - 1)/2 \tag{2.93a}$$

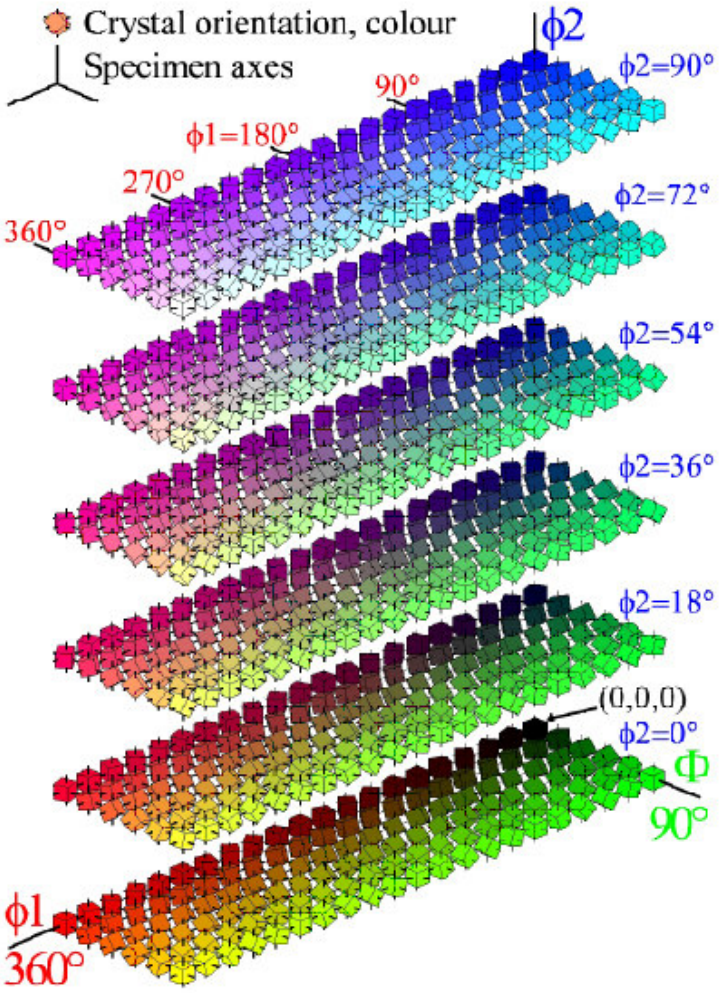

Figure 2.44. Schematic illustration of Euler coloring which transforms an orientation ($\varphi_1, \phi, \varphi_2$) to an RGB (Red, Green, Blue) color (Channel 5^{TM} User Manual).

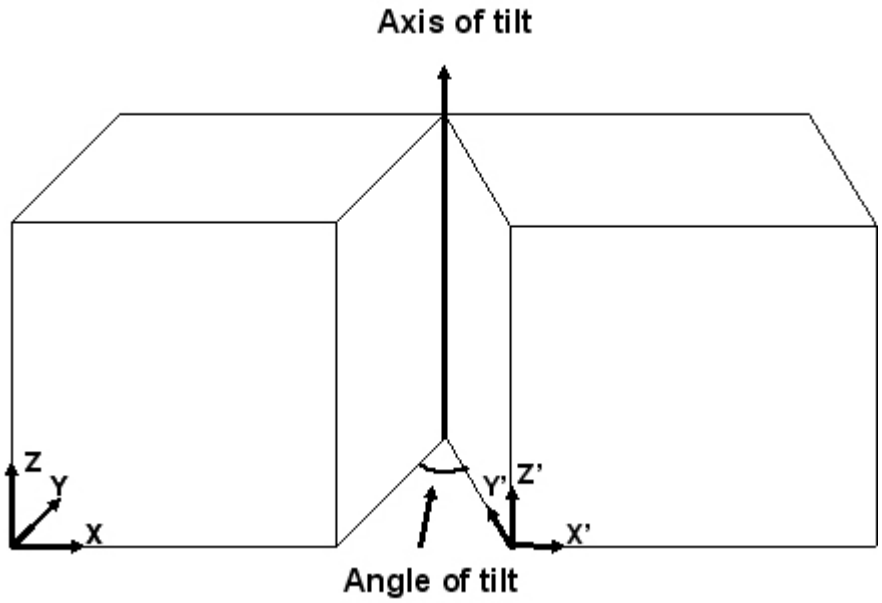

Figure 2.45. Schematic illustration of the angle/axis pair.

$$r_1 = a_{23} - a_{32} \qquad 2.93b$$

$$r_2 = a_{31} - a_{13} \qquad 2.93c$$

$$r_3 = a_{12} - a_{21} \qquad 2.93d$$

Alternatively the angle/axis rotation can be used to bring the coordinate system of one crystal into coincidence with another crystal which can then be related to the misorientation between these two crystals.

If the orientations (A_1 and A_2) of two grains are known a misorientation matrix , $M_{1\rightarrow 2,}$ can be calculated as:

$$M_{1\rightarrow 2} = A_1^{-1} A_2 \qquad 2.94$$

The angle/axis (θ/l) pair of the boundary can then be expressed utilizing the elements, m_{ij} of the misorientation matrix as follows :

$$l_1 = m_{23'} - m_{32} \quad 2.95a$$

$$l_2 = m_{31} - m_{13} \quad 2.95b$$

$$l_3 = m_{12} - m_{21} \quad 2.95c$$

$$\cos\theta = (m_{11} + m_{22} + m_{33} - 1)/2 \quad 2.95d$$

2.6.8. The Rodrigues Vector

Orientation of a sampled volume may be expressed by a three dimensional orientation vector that is extracted from the angle/axis descriptor with the rotation axis being the direction of the vector and the rotation angle being its magnitude. The angle/axis pair can then be combined into a single mathematical entity to express Rodrigues vector is given by [88]:

$$R = \tan\left(\theta/2\right)r \quad 2.96$$

2.6.9. Orientation Imaging Microscopy (OIM)

Orientation imaging microscopy (OIM) refers to the automated measurement and storage of orientations according to a pre-defined pattern coordinates on the sampling plane of the specimen. During this procedure, a diffraction pattern is obtained and the crystal orientation is determined at each

point. The resulting data can then be displayed as a crystal orientation map (COM). The sample points of the grains in a crystal orientation map are marked with colors specific to their lattice orientations [100], with a single grain being defined by the collection of neighboring pixels in the map having a misorientation less than user a defined angle [101, 102].

References

1) H. Sibum, *"Titanium and Titanium Alloy From Raw Material to Semi-finished Products*", Advanced Engineering Materials, 5, pp.393-398 (2003).

2) M. Peters, J. Hemptenmacher, J. Kumpfert and C. Leyens, *"Structure and Properties of Titanium Alloys"*, in Titanium and Titanium Alloys, C. Leyens and M. Peters (Eds.), Wiley-VCH GmbH&Co. KGaA, Weinheim, pp.1-35 (2003).

3)S. Ankem and S. R. Seagle, " Heat Treatment of Beta Titanium Alloys", Beta Titanium Alloys in the 1980s, R. R. Boyer and H. W. Rosenberg, eds. The Minerals, Metals and Materials Society, Warrendale, PA, 1984, pp. 107-128.

4) T. W. Duerig and J. C. Williams, "*Overview: Microstructure and Properties of Beta Titanium Alloys*", in Beta Titanium Alloys in the 1980's, R. R. Boyer and H. W. Rosenberg (Eds.), The Minerals, Metals and Materials Society, Warrendale, PA, pp.19-67 (1984).

5) J.J. Polmear, "*Titanium Alloys*", in Light Alloys, Halsted Press, New York, pp.248-314 (1996).

6) P. J. Bania, *"Beta Titanium Alloys and Their Role in the Titanium Industry",* in Beta Titanium Alloys of the 1990s, D. Eylon, R. R. Boyer and D. A. Koss (Eds.), The Minerals, Metals and Materials Society, Warrendale, PA, p.211 – 226 (1993).

7) A. Choudhury and E. Weingartner, *"Vacuum Arc Remelting (VAR)"*, in Metals Handbook, ASM International, Metals Park, OH, 15, pp.406-408 (1998).

8) F. Muller and E Weingartner " Vacuum Arc Skull Melting and Skull", in Metals Handbook, ASM International, Metals Park, OH, 15, pp. (1998).

9) W. Dietrich and H. Stephan "*Electron Beam Melting and Casting*", in Metals Handbook, ASM International, Metals Park, OH, 15, pp. (1998).

10) I Weiss and S. L. Semiatin, *"Thermomechanical of Beta Titanium Alloys-An Overwiew"*, Materials Science and Engineering A, 243, pp.46-68 (1998).

11) G. Terlinde and G. Fischer, *"Beta Titanium Alloys"*, in Titanium and Titanium Alloys, in Titanium and Titanium Alloys, C. Leyens and M. Peters (Eds.), Wiley-VCH GmbH&Co. KGaA, Weinheim, pp.37-55 (2003).

12) Y. Kosaka, S. P. Fox, K. Fuller and S. H. Reichmann, "Properties and Processing of TIMETAL LCB", Journal of Materials Engineering and Processing, pp. 792-798 (2005).

13) R. R. Boyer, W. J. Porter, E. R. Barta and D. Eylon, Microstructure/Properties Relationships inTi-15V-3Cr-3Al-3Sn High Strength Castings, *Microstructure/ Property Relationships in Titanium Aluminides and Alloys*, 1st ed., Y. W. Kim and R. R. Boyer, Eds., Oct. 7-11, 1990 (Michigan), Titanium Committee of The Minerals, Metals and Materials Society, TMS Warrandale, PA, 1991, p. 511- 520

14) J. G. Ferrero, J. R. Wood, P. A. Russo, Microstructural/Mechanical Property Relationships in Bar Products of Beta-C (Ti-3Al-8V-6Cr-4Mo-4Zr), *Beta Titanium Alloys of the 1990s*, 1st ed., D. Eylon, R. R. Boyer and D. A. Koss, Eds., Feb. 22-24, 1993 (Denver), Titanium Committee of TMS, TMS Waarendale, PA, 1993, p.211 – 226.

15) B. Y. Kokuoz, Y. Kosaka, H. J. Rack, High-Cycle Fatigue Crack Initiation and Growth in TIMETAL LCB, Journal of Materials Engineering and Performance. Vol. 14 (6), 2005, pp. 773-777.

16) H. Ohyama, Y. Ashida, T. Nishimura and T. Maki, *"Effects of Deformation Temperature on Deformed and Aged Microstructures and Tensile Properties in Ti-15V-3Cr-3Sn3Al"*, ISIJ International, 33, pp.889-897 (1993).

17) H. Fujii, and H. G. Suzuki, *"Effect of Solution Treatment Conditions on Aging Response in Ti-15V-3Cr-3Al"*, in Beta Titanium alloys in the 1990s, D. Eylon, R. R. Boyer, and D. A. Koss (Eds.), The Minerals Metals and Materials Society, pp.249-259 (1993).

18) N. Niwa, A. Arai, H. Takatori, K Ito, *"Mechanical Properties of Cold-Worked and High--Low Temperature Duplex-Aged Ti--15V--3Cr--3Sn--3Al Alloy"*, ISIJ International. 31, pp. 856-862. (1991).

19) M. Okada, *"Strengthening of Ti--15V--3Cr--3Sn--3Al by Thermomechanical Treatments"*, ISIJ International, 31, pp. 834-839. (1991).

20) S. Kamachi, N. Niwa, and K. Goto, *"Effect of Aging After Cold Working on the Mechanical Properties of Ti-3Al- 8V-6Cr-4Mo-4Zr (Beta C)"*, in Metallurgy and Technology of Practical Titanium Alloy, S. Fujishiro, D. Eylon and T. Kishi, (Eds.) The Mineral, Metals and Materials Society, pp. 159-165 (1994).

21) J. Ma and Q. Wang, *"Aging characterization and application of Ti-15-3 alloy",* Materials Science and Engineering A, 243, pp.150-154 (1998).

22) C. Ouchi, H. Suenaga and Y. Kohsaka,*."Strengthening Mechanism of Ultra High Strength Achieved by New Processing Ti-15%V-3%Cr-3%Sn-3%Al Alloy",* in Sixth World Conference on Titanium, France pp. 819-823 (1988).

23) B. Wang, Z. Liu, Y. Gao, S. Zhang, and X. Wang, *"Microstructural Evolution During Aging of Ti-10V-2Fe-3Al"*, Journal of University of Science and Technology, 14, pp.335-340 (2007).

24) O. M. Ivasishin, P.E. Markovsky, Y. V. Matviychuk, S. L. Semiatin, C. H. Ward and S. Fox, *"A Comparative Study of Mechanical Properties of High Strength β-titanium Alloys",* Journal of Alloys and Compounds, In press (2007).

25) O. M. Ivasishin, P. E. Markovsky, S. L. Semiatin and C. H. Ward, *"Aging Response of Coarse and Fine Beta Titanium Alloys"*, Materials Science and Engineering A., 405, pp. 296-305 (2005).

26) T. Furuhara, T. Maki and T. Makino, *"Microstructure Control by Thermo mechanical Processing in β-Ti-15-3 alloy"*, Journal of Materials Processing and Technology, 117, pp.318-323 (2001).

27) T. Makino, R. Chikaizumi, T. Nagaoka, T. Furuhara, and T. Makino, *"Microstructure Development in the Thermo mechanically Processed Ti-15V-3Cr-3Sn-3Al alloy"*, Materials Science and Engineering A, 213, pp.51-60 (1996).

28) R. R. Boyer and G. W. Kuhlman, *"Processing Properties Relationships of Ti--10V--2Fe--3Al"*, Metall. Trans. A, pp. 2095-2103 (1987).

29) G. Terlinde, H. J. Rathjen, K. H. Schwalbe and G. W. Kuhlmann, *"Microstructure and Fracture Toughness of the Aged Beta -Ti Alloy Ti--10V--2Fe--3Al"*, Metall. Trans., 19, pp. 1037-1049 (1988).

30) G. T. Terlinde, T. W. Duerig, and J. C. Williams, *"Microstructure, Tensile Deformation and Fracture in Aged Ti--10V--2Fe--3Al"*, Metall. Trans. A, 14, pp. 2102-2115 (1983).

31) T. Inaba, K. Ameyama, and M. Tokizane, *"Formation of (alpha + beta) Microduplex Structure in a Ti--15V--3Cr--3Sn--3Al Alloy*", ISIJ International, 31, pp. 792-798 (1991)

32) M, Ninomi, T. Kobayashi and H. Honda, *"Mechanical Properties of Microstructurally Controlled β Type Titanium Alloys",* in Science and Engineering of Light Metals, K. H. Oikawa and I. Hirano (Eds.), Japan Institute of Light Metals, pp.85-90 (1991).

33)S. Komatrsu, M. Ikeda, T. Sugimoto, and K. Kiyoshi, *"Influence of Rolling Bi phased α+β Temperature Range on Aging Behaviour of Ti-15V-3-Cr-3Sn-3Al Alloy",* in Metallurgy and Technology of Practical Titanium Alloys, S. Fujishiro, D. Eylon and T. Kishi (Eds.), The Minerals, Metals and Materials Society, Warrendale, PA, pp.259-266 (1993).

34) J. G. Ferrero, J. R. Wood, and P. A. Russo, *"Microstructure and Mechanical Property Relationship in Bar Products of Beta C (Ti-3Al-8V-6Cr-4Mo-4Zr)",* in Beta Titanium Alloys in the 1990s, D. Eylon, R. R. Boyer, and D. A. Koss (Eds.), The Minerals, Metals and Materials Society, Warrendale, PA, pp.211-226 (1993).

35) S. Azimzadeh, “Phase Transformations in Metastable β Titanium Alloy TIMET LCB (Ti-6.8Mo-4.5Fe-1.5Al)”, Master of Science Thesis, Clemson University, Clemson, SC, December, 1995.

36) C. Angelier, S. Bein and J. Bechet, “ Building a Continuous Cooking Transformation Diagram of β-CEZ Alloy by Metallography and Electrical Resistivity Measurements”, Metallurgical and Materials Transactions A, 28, pp.2467-2474(1997).

37)S. Malinov, W. Sha and P. Markovsky, ”Experimental Study and Computer Modeling of β→β+α Phase Transformation in β21 Alloy at Isothermal Conditions”, Journal of Alloys and Compounds, 348, pp.110-118 (2003).

38) S. Bein and J. Bechet, “Phase Transformation Kinetics and Mechanisms in Titanium Alloys”, Journal De Physique IV, 6, pp.C1-99 (1996).

39) J. D. C. Teixeira, B. Appolaire, E. A. Gautier, S. Denis, G. Cailetaud and N. Spath, “ Transformation Kinetics and Microstructure of Ti17 Titanium Alloy During Continuous Cooling” , Materials Science and Engineering, 448, pp. 135-145 (2007).

40) E. Laude, E. Gautier and S. Denis, “Calculation of Transformation Kinetics of Titanium Alloys during Continuous Cooling. Application to the β CEZ Alloy”, Titanium 95: Science and Technology, 3, pp.2330- 2337 (1996).

41) W. A. Johnson and K. E. Mehl, Trans. Am. Inst. Min. Met. Eng., 135, pp.416- (1939).

42) M. Avrami, “Kinetics of Phase Change. I General Theory”, J. Chem. Phys., 7, pp.1103 (1939).

43) M. Avrami, “Kinetics of Phase Change. II Transformation Time Relations for Random Distribution of Nuclei”, J. Chem. Phys., 8, pp. 212 (1940).

44) M. Avrami, “Granulation, Phase Change and Microstructure Kinetics of Phase Chage. III”, J. Chem. Phys., 9, pp.177 (1941).

45) J.W. Christian, “The Theory of Transformations in Metals and Alloys”, Pergamon Press, London, (1965).

46) H. I. Aaronson and J. K. Lee, “ The Kinetic Equations of Solid-Solid Nucleation Theory”, in Lectures on the Theory of Phase Transformations, H. I. Aaronson (Eds.), American Institue of Mining, Metallurgical and Petroleum Engineers, New York , pp.83-111 (1975).

47) D. A. Porter and K. E. Easterling, “Phase Transformations in Metals and Alloys”, Nelson Thornes Ltd., UK (2001).

48) J. D. Verhoeven, “Fundamentals of Physical Metallurgy”, John Wiley and Sons, New York (1975).

49)F. C. Frank, “ Metal Surface”, W.D. Robertson and N. A. Gjostein (eds.), American Society for Metals (1963).

50) K. C. Russel, “ Nucleation in Solids”, in Phase Transformations, American Society for Metals, Metals Park, Ohio, pp. 219-264 (1970).

51) K. R. Kinsman, H. I. Aaronson and E. Eichen, "The Kinetics and Mechanism of the Thickening of kappa Plates in a Cu-Si Alloy," Met. Trans., 2, pp. 1041 (1971)..

52) H. B. Aaron and H. I. Aaronson, "Comparison of Relative Interfacial Energies of Disordered Interphase (alpha:theta) and Grain (alpha:alpha) Boundaries at Grain Boundary Precipitates in Al-4% Cu During Growth and at Equilibrium," Acta Met., 18, pp. 699 (1970).

53) C. J. Mullins, “Metal Surface”, W.D. Robertson and N. A. Gjostein (eds.), American Society for Metals (1963).

54) K. C. Russel,” Nucleation in Solids”, in Phase Transformations, American Society for Metals, Metals Park, Ohio, pp. 219-268 (1970).

55) F.R. N. Nabarro, “The Influence of Elastic Strain on the Shape of Particles Segregating in an Alloy”, Proc. Phys.Soc. 52, pp.90-93 (1940).

56)J. K. Lee and H. I. Aaronson, “ Influence of Faceting Upon the Equilibrium Shape of Nuclei at Grain Boundaries-I Two-Dimensions”, Acta Metallurgica, 23, pp.799-808 (1975).

57) U. Dahmen, “Orientation Relationships in Precipitation Systems”, Acta. Met., 30, pp.63 (1982).

58) W. G.Burgers, “ The process of transition of the cubic body centered modification into the hexagonal close packed modification of zirconium”, Physica, 1, pp.561- (1934).

59) T. Furuhara, S. Takagi, H. Watanabe and T. Maki, “Crystallography of Grain Boundary Alpha Precipitates in a β Titanium Alloy”, Metallurgical and Materials Transactions A, 27, pp.1635-1646 (1996)

60) D. Bhattacharyya, G. B. Viswananthan, R. Denkenberger, D. Furrer, H. L. Fraser, “The role of crystallographic and geometrical relationships beteen α and β phases in an α/β titanium alloy”, Acta Materialia, 51, pp. 4679-4691 (2003).

61) B. Appolaire, L. Hericher and E. A. Gautier, “Modeling Phase Transformation Kinetics in Ti-Alloys- Isothermal Treatments”, Acta Materialia, 53, pp.3001-3011(2005).

62) C. J. Zener, “Theory of Growth of Spherical Precipitates from Solid Solution”, J. Appl. Phys., 20, pp.950 (1949).

63) H. I. Aaroson, C. Laird, and K. R. Kinsman, “ Mechanisms of Diffusional Growth of Preciptiate Crystals”, in Phase Transformations, American Society for Metals, Metals Park, Ohio,pp.313-390 (1970).

64) M. Hillert, Jernkontorets Ann, 141, pp.757-764 (1957).

65) H. I. Aaronson, in Decomposition of Austenite by Diffusional Processes, V. F. Zackay and H. I. Aaronson (Eds.), Interscience, New York pp.387-546 (1962).

66) C. J. Zener, Trans. AIME, 167, pp.500- (1946).

67) Makino, T., Chikaizumi, R., Nagaoka, T., Furuhara, T. and Makino, T., *Microstructure development in a thermomechanically processed Ti-15V-3Cr-3Sn-3Al alloy*, Materials Science and Engineering A213, 1996, pp.51-60.

68) J. Pospiech and K. Lucke, “Rolling Textures of Cu and Alpha-Brasses Discussed in Terms of the Orientation-Distribution Function “, Acta Met, 23, 8 (1975), 997-1007.

69) H. J. Bunge, Prefered Orientation in Deformed Metals and Rocks: an Introduction to Modern Texture Analysis (ed. H. –R Wenk), Academic Press, London, 1985, 73.

70) H. Grimmer, W. Bollmann and D. H. Warrington, “Coincidence-site lattices and complete pattern-shift in cubic crystals”, Acta Crystallographica, 30A, 1974, 197-207.

71) H. Mykura, Grain Boundary Structure and Kinetics, eds. R. W. Ballufi, ASM International, Ohio, USA, 1980, 445.

72) W. T. Read and W. Shockley, " Dislocation Models of Crystal Boundaries", Physical Rev. 78 (1950), 275-289.

73) D. Mclean, Grain boundaries in Metals, Clarendon, Oxford, p. 116 (1957).

74) N. A. Gjostein and F. N. Rhines, " Absolute Interfacial Energies of [001] Tilt and Twist Grain Boundaries in Copper, Acta Met., 7 (1959), pp.319-330.

75) D. Vaughan, " Grain Boundary Precipitation in an Al-Cu Alloy", Acta Met, 16, pp. 563-577 (1968)

76) D. H. Warrington, in Grain Boundary Structure and Kinetics, ASM International, Ohio, 1980, 1.

77) P. J. Goodhew, "The Relationship Between Grain Boundary Structure and Energy", in Grain Boundary Structure and Kinetics, ASM, Metals Park Ohio, pp.155-176 (1979).

78) N. F. Mott, "Slip at the Grain Boundaries and Grain Growth in Metals", Proceedings of the Physical Society of London, 60 (1948), pp. 391-394.

79) R. Smoluchovski, "Theory of Grain Boundary Diffusion", Physical Review, 87 (1952), pp. 482-487.

80) H. Grimmer, W. Bollmann and D. H. Warrington, "Coincident site lattices and complete pattern shift lattices in cubic crystals", Acta Cryst. 30, pp.197-207 (1974).

81) K. T. Aust and J. W. Rutter , "Temperature Dependence of Grain Migration in High Purity Lead Containing Small Additions of Tin", Transactions of Metallurgical Society A.I.M.E., 215 (1959), pp. 820-831.

82. D. G. Brandon, "The Structure of High Angle Grain Boundaries", Acta Met., 14 (1966), pp.1479-1484.

83.) D G. Brandon, "The Structure of High Angle Boundaries" Acta. Met. 14, pp.1479-1484(1966).

84) R. D. Doherty, D. A. Hughes, F. J. Humphreys, D. Juul Jensen, M. E. Kassner, W. E. King, T. R. McNelley, H. J. McQueen and A. D. Rollet, "Current Issues in Recrystallization: A review", Materials Science and Engineering A, 238, pp.219-274 (1997).

85) P. Virtanen, T. Tiainen, T. Lepisto, "Precipitation at faceting grain boundaries of Cu-Ni-Sn alloys", Materials Science and Engineering, 251, pp.269-275 (1998).

86) J. I. Goldstein, D. E. Newbury, P. Echlin, D. C. Joy, A. D. Roming Jr., C. E. Lyman, C. Fiori, and E. Lifshin, " Scanning Electron Microscopy and X-Ray Microanalysis", Plenum Press, New York, pp. 69-146 (1992).

87) J. A. Venables and C. J. Harland, "Electron Back-Scattering Patterns--A New Technique for Obtaining Crystallographic Information in the Scanning Electron Microscope", Philosophical Magazine, 27, pp.1193-1200 (1973)

88) V. Randle and O. Engler, Introduction to Texture Analysis: Macrotexture, Microtexture and Orientation Mapping", CRC Press (2000).

89) W. L. Bragg, "Diffraction of Short Electromagnetic Waves by a Crystal", Proceedings of the Cambridge. Philosophical Society, 17, 43–57 (1913).

90) S. Kikuchi, "Diffraction of cathode rays by mica", Jap. J. Phys., 5, pp.83- (1928).

91) V. Randle, " Theoretical Framework for Electron Back Scatter Diffraction", in Electron Backscatter Diffraction in Materials Science, A. J. Schwarts, M. Kumar and B. L. Adams (Eds.), Kluwer Academic-Plenum Publishers, New York, pp.19-30 (2000).

92) N. C. Krieger Lassen, D. Juul Jensen and K. Conradsen, "Automatic recognition of deformed and recrystallized regions in partly recrystallized samples using electron back scattering patterns" Mater. Sci. Forum, 194, pp.157-162 (1994).

93) S. I. Wright, " Fundamentals of Automated EBSD", in in Electron Backscatter Diffraction in Materials Science, A. J. Schwarts, M. Kumar and B. L. Adams (Eds.), Kluwer Academic-Plenum Publishers, New York, pp.51-61 (2000).

94) S. I. Wright and B. L. Adams, "Automatic Analysis of EBSD Diffraction Patterns", Met. Trans, 35, pp. 1317- , (1992).

95) D. J. Dingley and V. Randle, "Microtexture Determination by Electron Back-Scatter Diffraction ", Journal of Marerials Science, 27, pp.4545-4566 (1992).

96) Bollman, W., Crystal Defects and Crystalline Interfaces, Springer, Berlin (1970).

97) P. G. Partridge, Met. Rev., 118, pp.169 (1969).

98) H. J. Bunge, “Zur Darstellung allgemeiner Texturen “ Z. Metallk., 56, pp.872-874 (1965).

99) H. J. Bunge, “ An Introduction to Modern Texture Analaysis”, in Preferred Orientation in Deformed Metals and Rocks, H. R. Wenk (Ed.), Academic Press Inc, UK, pp. 73- (1985).

100) D. Gerth and R. A. Schwartzer, “Graphical Representation of Grain and Hillcock Orientations in Annealed Al-1%Si films”, Textures and Microtextures, 21, pp.177-1993 (1993).

101) D.J. Prior, “Problems in determining the misorientation axes for small angular misorientation using electron back scattered diffraction in the SEM”, J. Microscopy, 195, pp.217-225 (1999).

102) K. S. Raju, M. G. Krishna, K. A. Padmanabhan, K. Muralledharan, N. P. Gurao, G. Wilde, “ Grain size and grain boundary character distribution in ultrafinegrained (ECAP) nickel”, Materials Science and Engineering A, *In press* (2008).

CHAPTER III

EXPERIMENTAL PROCEDURES

3.1. As Received Material

This investigation has examined Ti-6.5 Mo-4.5Fe-1.5Al, provided by TIMET Corp., Henderson, Nevada in the form of rods with a diameter 10mm and 493.2 cm long that had been vacuum arc melted, forged and hot rolled. The average chemical composition (wt %) of the material is shown in Table 3.1.

Table 3.1. Chemical composition of Ti-6.5 Mo-4.5Fe-1.5Al

Elements	Wt.(%)	Standard Deviation
Al	1.444	0.002
C	0.015	0.001
Cr	0.065	0.000
Fe	4.646	0.0419
Mo	6.465	0.0242
N	0.003	0.002
Nb	0.018	0.000
Ni	0.024	0.000
O	0.126	0.002
Si	0.083	0.000
H (ppm)	124.5	5.5
Ti	87.10	0.05

3.2. Heat Treatment

All the heat treatments considered in this study were carried out in neutral salt baths. A plain carbon steel salt bath pot with carbonate based neutral salt called Universal Thermics EU 9418 was used for this purpose. The EU 9418 has lithium, sodium and potassium carbonate as its main components and melting temperature of 432^0C. Temperature of the molten salt bath was measured by a 0.635 cm diameter, 45.72 cm long ungrounded Inconel K type thermocouple equipped with dual channel. This configuration allowed independent monitoring of the temperature with a high temperature digital controller and a digital reader simultaneously. The temperatures were controlled within ± 3^0C. During heat treatments, all the specimens were wrapped around 0.635 cm diameter, 43.18 cm long 304 grade stainless steel bars and placed 5 cm away from the thermocouples. Finally, a 0.635 cm diameter, 45.72 cm long ceramic type K thermocouple was placed in close contact with the heating elements and monitored by a digital high temperature indicator. A schematic representation of the salt bath configuration is given in Figure 3.1

Since the primary goal of this investigation was to examine the role of crystallographic relationships between the α and β phases on kinetics of phase transformations, several preliminary studies were performed to (a) confirm the β transus temperature for Ti-6.5 Mo-4.5Fe-1.5Al previously obtained [1] and (b) establish the solution treatment time necessary to avoid intra-granular dislocation assisted heterogeneous α phase nucleation and growth. The first was performed

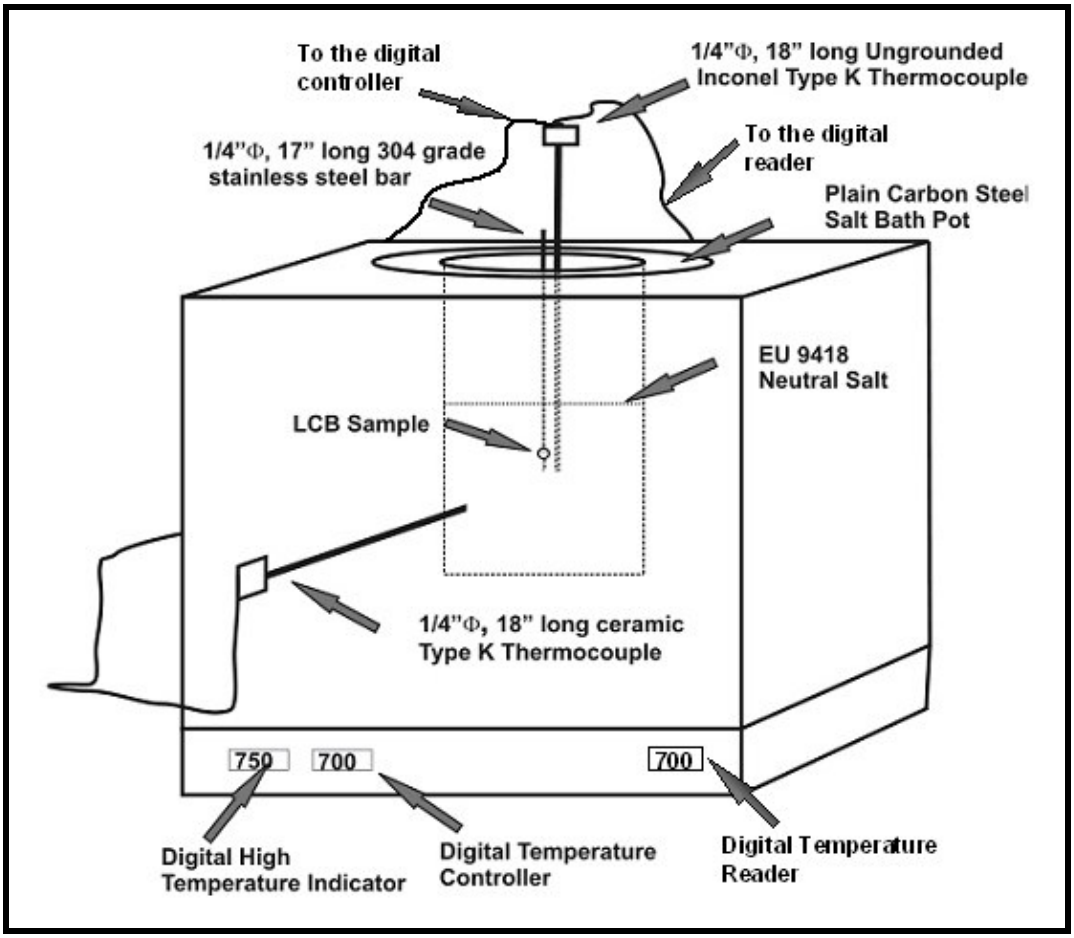

Figure 3.1. Schematic of salt bath set up used to heat treat TIMETAL LCB specimens.

by monitoring the α phase volume fraction following solution treatment in neutral salt baths at temperatures between 633 and 820^0C for 30 minutes. The second study used decoration heat treatment which involved solution treating at 820^0C for 30 minutes, followed by direct aging at 550^0C for five minutes. This was used to verify if heterogeneous nucleation of α on any remnant dislocation substructure occurred.

In order to study the phase transformation kinetics, TIMETAL LCB specimens were isothermally heat treated within the temperature range 700-745^{o}C for successively increasing aging times. The isothermal aging temperatures and times were limited to those above the nose of Ti-6.5 Mo-4.5Fe-1.5Al Time-Temperature-Transformation (TTT) curves [1], thereby avoiding intra-granular alpha precipitation at the early stages of reaction, shown in Figure 3.2. A typical heat treatment schedule is given in Figure 3.3. All aging treatments were terminated by water quenching.

Azimzadeh et. al. [1] demonstrated that the time required to reach the appropriate aging temperatures, after solution treatment, is 24 seconds and the time to reach room temperature from the highest aging temperature via water quenching is 12 seconds. These short times are expected to have only a minor influence on the precipitation phenomena studied.

Finally, the heat treatment matrix illustrating all the aging treatment conditions considered during this study is given in Table 3.2 and the aging treatments that were performed was marked with an X.

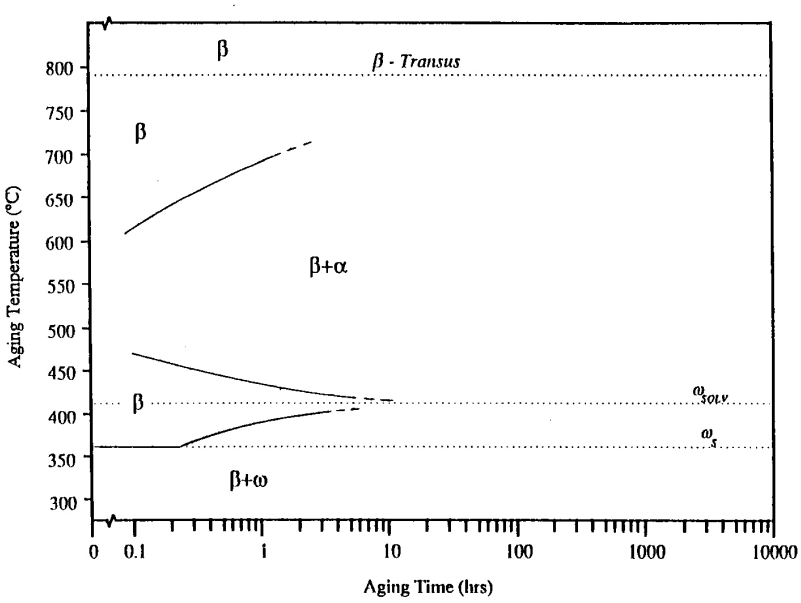

Figure 3.2. Isothermal Time-Temperature-Transformation Diagram for Ti-6.5 Mo-4.5Fe-1.5Al [1].

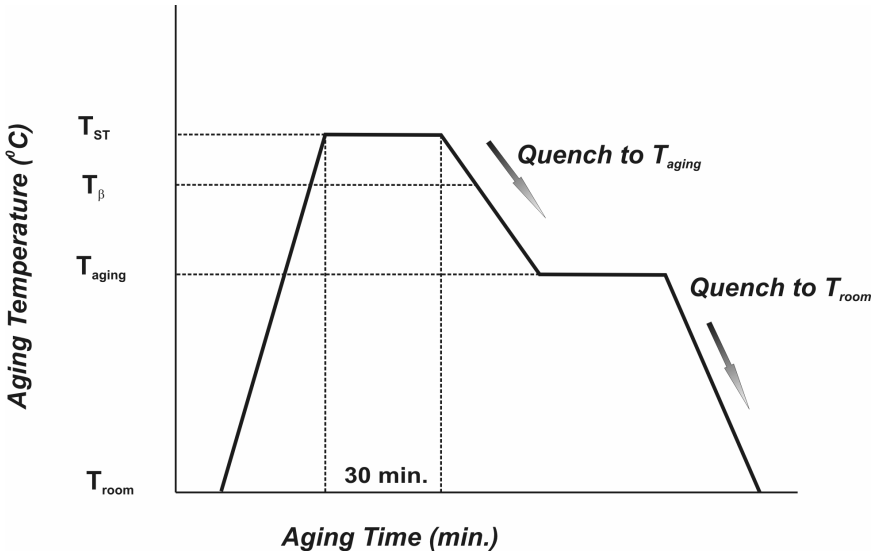

Figure 3.3. Schematic of Heat Treatment Procedure

Table 3.2. Aging Treatment Conditions

.

time(min)	Temperature(°C)			
	700	715	730	745
0.5	X	X	X	X
1	X	X	X	X
5	X	X		
7	X		X	X
10	X	X	X	X
12	X	X	X	X
15	X	X	X	X
17				X
20	X		X	
25	X	X		
30	X			X
35		X	X	
40	X	X	X	
45	X			
50	X	X	X	
55	X			
60	X	X	X	X
70			X	
80	X		X	
91		X		
100			X	
120				X
125	X			
126		X		
133		X		
182				X
195			X	
200	X	X		
210			X	
220			X	
250			X	
285			X	
315			X	
330			X	
430		X		
1333				X
1980				X

3.3. Metallographic Sample Preparation

Metallographic preparation of the solution treated and aged Ti-6.5 Mo-4.5Fe-1.5Al samples included standard grinding procedures. Sample preparation for optical and scanning electron microscopy initially involved cutting the supplied 4.5 m long by 10 mm diameter bars into 30 cm long bars utilizing a vertical band saw. These were sectioned into 10 mm long blanks with a Buehler Isomet 4000 diamond saw, at 1500 rpm blade speed and 0.127 mm/min feed rate with Struers cut off wheel lubricating fluid. Following heat treatment, 3 mm lengths from both end surfaces of each specimen was removed with the Buehler Isomet 4000 to ensure complete removal of any possible α-case or oxidized layer that may have formed during heat treatment. The remaining 4 mm thick specimen surfaces were ground using 120, 320, 600 SiC grit paper, final polishing employing 0.3 and 0.05 µm aqueous Al_2O_3 and colloidal SiO_2 solutions. A schematic of a standard metallographic sample preparation sequence is given in Figure 3.4.

Two-phase specimens were etched using Kroll's Solution (1.5 vol% (HF) – 3.5 vol% (HNO3) – bal. (H2O)) for 15 seconds for optical microscope examination; un-etched specimens were used for scanning electron microscopy examination under back scattering electron (BSE) diffraction conditions.

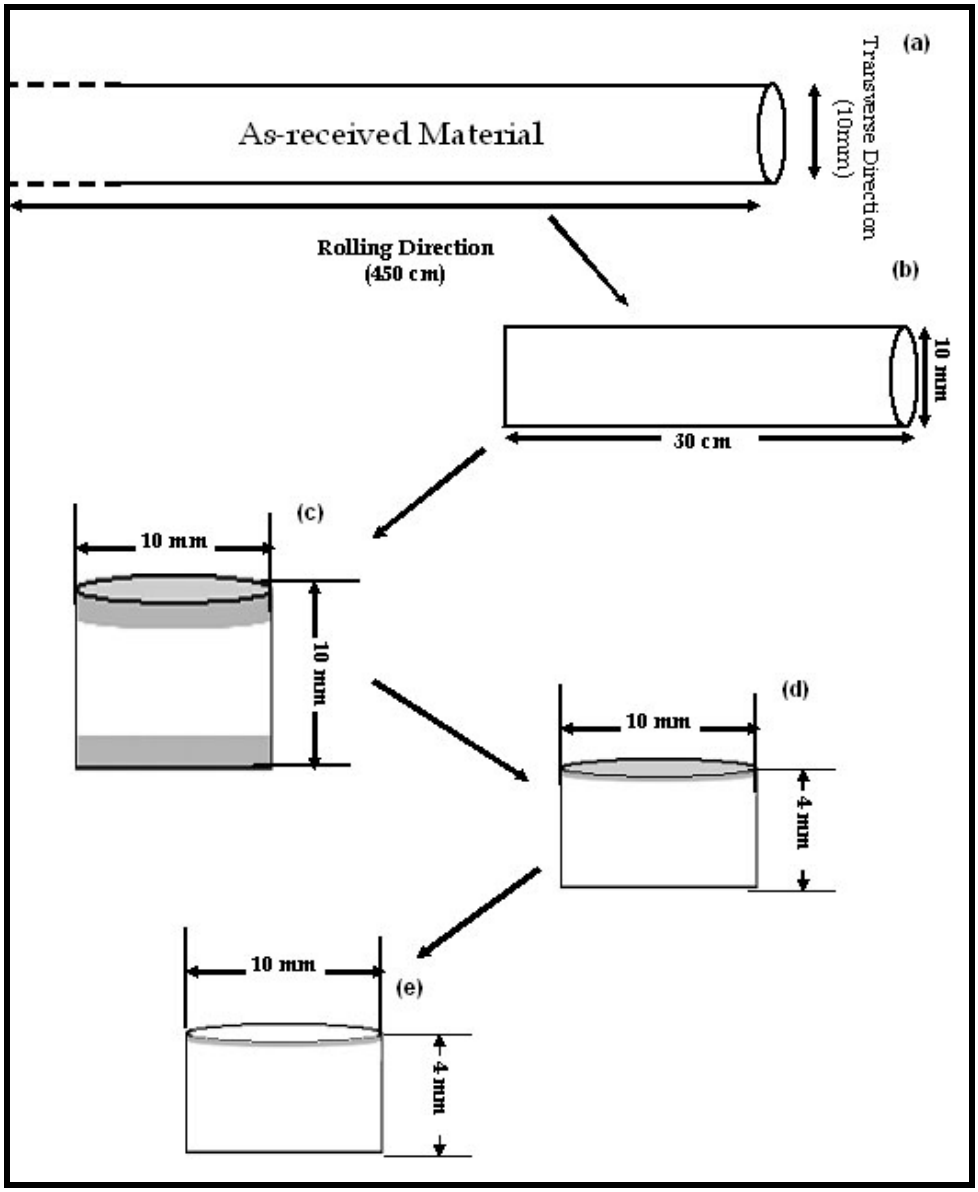

Figure 3.4. Successive steps of sample preparation (a) cutting the as-received material parallel to transverse direction. (b) Sectioning 30 cm long bars into 10 mm long blanks. c) Removing the oxide layer due to heat treatment. (c) Coarse grinding followed by fine polishing to eliminate the deformed layer.(d) Optical or scanning electron microscopy examination.

3.4. Microstructural Characterization

Microstructural characterization of solution treated and aged specimens included optical and electron microscopy. Two-phase etched specimens were examined using a Nikon Epiphot 300® optical microscope. Un-etched samples were examined with a Hitachi 3500, Hitachi 3400N, a LEO 1450 or a Hitachi 4800 field emission scanning electron microscopy (FE-SEM) under backscattering electron imaging (BSEI) conditions. Operating conditions for Hitachi 3500, Hitachi 3400N and LEO 1450 were 20 kV and 10 mm working distance and for the Hitachi 4800 it was 10 kV and 8 mm when performing BSEI analysis.

3.5. X-Ray Diffraction (XRD)

Effect of temperature on the lattice parameters of α and β phase were investigated by x-ray diffraction (XRD). These measurements were performed on a Scintag XDS-2000 θ- 2θ diffractometer operated at 40 kV and 30 mA. A Li doped Si detector utilizing CuKα radiation was used to obtain XRD diffraction patterns of the solution treated samples.

For XRD measurements, 2 mm thick samples were cut from solution treated TIMETAL LCB samples and mechanically polished with SiC polishing paper to a 600 grit.

3.6. Electron Backscatter Diffraction (EBSD) Analysis

Electron backscatter diffraction (EBSD) analysis was performed to examine crystallographic relationships between α and β phases. EBSD was

performed at 20 kV, a 80 mA beam current and a 15 – 20 mm working distance, a holder pre-tilted to an angle of 70.5 degrees being used with the Hitachi 3400N while samples examined with the LEO 1450 were manually tilted to an angle of 70 degrees.

EBSD samples were prepared according to the standard sample preparation technique described previously with the exception that the final 20 nm colloidal SiO_2 polishing step was conducted for at least 8 hours to remove any deformation or contamination from the expected 20 nm backscattered electron penetration depth [2]. All samples were ultrasonically cleaned, rinsed with pure ethanol and stored under vacuum until examination.

Automatic EBSD pattern acquisition and post acquisition of the orientation data utilized either HKL Channel 5 or INCA Crystal software packages [3, 4]. Before each run, the operating geometry was calibrated using an appended silicon wafer, the surface normal being the [001] direction. This routine minimized errors in orientation determination [2]. Pattern acquisition included automated orientation imaging microscopy when examining solution treated microstructure, whereas interactive data collection mode was used to establish the local orientation of the grains bounding grain boundary segment. Schematics of the steps involved in orientation imaging microscope and interactive data collection mode are given in Figures 3.5a and b.

The determination of the misorientation between two grains involved a selection of the minimum misorientation angle and its corresponding axis from all

24 possible symmetric bcc β phase variants [5]. Orientation relationships between two phases was be found by plotting the pole figures showing the $\{110\}_{\beta}$, $\{111\}_{\beta}$,$\{0001\}_{\alpha}$ and $\{1\bar{1}20\}_{\alpha}$ poles of individual crystals using a subroutine incorporated in to the Channel 5^{TM} software and determine the parallel poles. Alternatively, crystallography software such as Carine Crystallography 3.1 was used to plot a pole figure comprising any given pole.

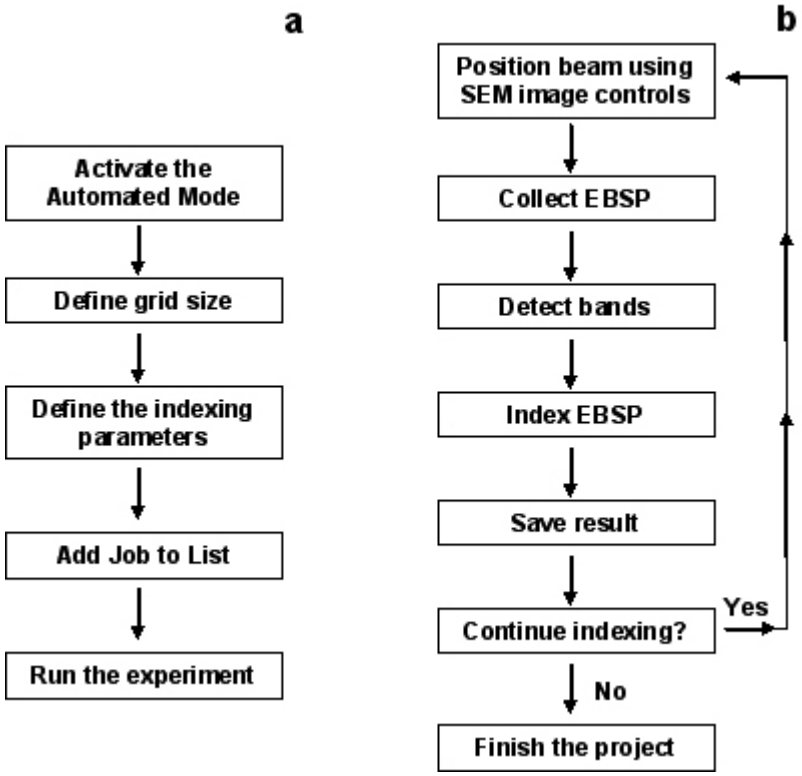

Figure 3.5. Schematic steps involved in a) automatic data collection mode during orientation imaging microscopy and b) interactive data collection mode in an HKL EBSD system.

EBSD pattern analysis included averaging 5 Kikuchi patterns arising from a single area of interest, with further indexing of the orientation including 6-7 Kikuchi bands.

The accuracy of determination of absolute orientation by means of EBSD in a conventional SEM was approximately 1^{o} and the spatial resolution was of around 1μm.

3.7. Quantitative Metallography

3.7.1. Volume Fraction Measurements

The volume fraction of α precipitation in the β matrix was determined utilizing systematic point counting. This analysis involved superimposing a two dimensional lattice on the optical or electron microscope images and measuring the fraction of points falling on the α phase [6]. Points that fell entirely within an α particle was counted as 1, those lying on an α/β phase boundary being counted as ½. A The volume fraction analysis employed in this study included fixing the total number of grid points to a certain value, P_T and estimating the standard deviation experimentally. 12X16 rectangular grid was applied to the optical microscope images at a magnification of 200X by means of Image Processing Tool Kit™. Ten optical microscope images per heat treatment condition were considered.

In order to avoid bias; special attention was paid to non-subjective imaging of the examined areas. This was established by placing a representative area of the specimen, i.e. the center, under the area of illumination in the optical

microscope, without looking through eye-piece. Further imaging was performed by advancing the stage in the x and y directions without the prior knowledge of the microstructure to be imaged.

Determination of the α volume fraction transformed in Ti-6.5Mo-4.5Fe-1.5Al aged for less than 60 sec or less utilized one dimensional point counting [7]. This method involved sequentially advancing the stage of the field emission microscope in the x and y directions in 100μm constant increments. Five hundred areas for each aging time at a magnification of 10,000X were examined for this purpose.

Volume fraction data obtained utilizing systematic point counting procedure is tabulated in Appendix A for the aging times and temperatures considered.

Accuracy of the measurements, %acc were calculated according to the following equation [8]:

$$\%acc = \frac{200}{\sqrt{P_T}} \frac{\sigma(P_P)}{P_P} \qquad 3.1$$

where P_P and $\sigma(V_V)$ are the experimentally determined values for point fraction and standard deviation; respectively. $\sigma(V_V)$ is given by:

$$\sigma(V_V) = \sqrt{\frac{1}{(n-1)} \sum_{i=1}^{n} \left(x_i - \bar{x}\right)^2} \qquad 3.2$$

Where n is the total number of observations, X_{ii} is the value of the random variable for a given measurement and $\overline{X}$ is the arithmetic mean of the sample. The f P_P, $\sigma(V_V)$ and %accuracy values are reported in Appendix A.

3.7.2. Surface Area Measurements

The surface area per unit volume of interfaces was quantified by counting the number of interfaces intersecting with test lines and expressed as [8]:

$$S_V = 2P_L \qquad mm^2/mm^3 \qquad 3.3$$

where P_L is defined as the number of interceptions generated per unit length of a test line. A typical experiment of P_L count involves randomly applying a linear test array to the microstructure on the plane of polish. The total length of the test lines may be fixed in advance. Further, the number of interceptions made by the test lines and the traces of surfaces are counted. An intersection is counted as $1/2$ if a test line appears to make a tangent hit with the trace of a surface. Similarly, if a triple point junction is intersected the count is equal to $1\,1/2$. This process may be repeated for a number of different test lines traversing different areas and an average is calculated over all locations. In this study, five parallel test lines were superimposed on electron or optical micrograph images utilizing Image Processing Tool Kit$^{TM.}$ and S_V.

3.7.3. Grain Size Measurements

Grain size measurements involved mean lineal intercept method. Mean lineal intercept length, L, can be defined as the average length of the test line along the chord that passes through the outline of the feature on the two dimensional section [9]. It is determined by averaging over a number of test lines and may be expressed as:

$$L = \frac{1}{P_L} \qquad 3.4$$

where P_L is the number of interceptions generated per unit length of a test line. The grain size, G can be estimated from L in the following manner [9]:

$$G = (-6.6457 \log_{10} L) - 3.298 \qquad 3.4$$

In order to measure L an array parallel lines were place on an electron or optical micrograph with the total number of intersections, i.e., the point where the test line cuts a grain boundary, being equal to at least 50.Upon counting, the end points of a test line that appeared to touch the grain boundary was counted as a ½ intersection. Test lines cutting across, or tangent to the grain boundaries are counted as 1 intersection, whereas triple point intersections are considered as 1-½.

References

1) S. Azimzadeh, “Phase Transformations in Metastable β Titanium Alloy TIMET LCB (Ti-6.8Mo-4.5Fe-1.5Al)”, Master of Science Thesis, Clemson University, Clemson, SC, December, 1995.

2) V. Randle, “Microtexture Determination and its Applications”, Institute of Metals, London (1992).

3) “HKL Channel 5 Acquisition and Processing Software”, Oxford Instruments, Oxfordshire, England.

4) ”Inca Crystal, Oxford Instruments”, Oxfordshire, England.

5) V. Randle and O. Engler, “Introduction to Texture Analysis Macrotexture, Microtexture and Orientation Mapping”, CRC Press, London (2000).

6) E. Thomson, “Quantitative Microscopic Analysis”, J. Geol., 38:193 (1930)

7) A. A. Glagolev, “ Quantitative Analysis with the Microscope by the Point Method”, Eng. Min. J., 135 (1934), pp. 135.

8) E. Underwood, “Quantitative Stereology”, Adison-Wesley, Reading, MA(1970), pp. 1-46.

9) John C. Russ, “ Practical Stereology”, Plenum Press, New York (1986).

CHAPTER IV

RESULTS AND DISCUSSIONS

4.1. Designing a Solution Treatment Procedure

Distribution of second phase α precipitates during decomposition of a supersaturated solid solution of β phase, is neither uniform nor random through out the matrix. In titanium alloys, β→β+α transformation typically starts on defects such as dislocations or slip bands within deformed materials [1]. In contrast, the β/β grain boundaries are preferred precipitation sites at relatively low under-coolings (T_β-200^{o}C) in un-deformed materials [2]. Since the primary goal of this study was to examine the heterogeneous grain boundary nucleation and growth of α phase during aging of TIMETAL LCB, a solution treatment procedure was designed to establish a single phase structure and to eliminate the prior sub-structure (a possible intragranular nucleation site for α phase during aging).

4.1.1. Solution Treatment Temperature

Disappearing phase technique [3] was used to determine the β-transus temperature of Ti-6.5Mo-4.5Fe-1.5. For this purpose, as-received TIMETAL LCB specimens were solution treated between 633-820^{o}C for 30 minutes and examined by a scanning electron microscope (SEM).

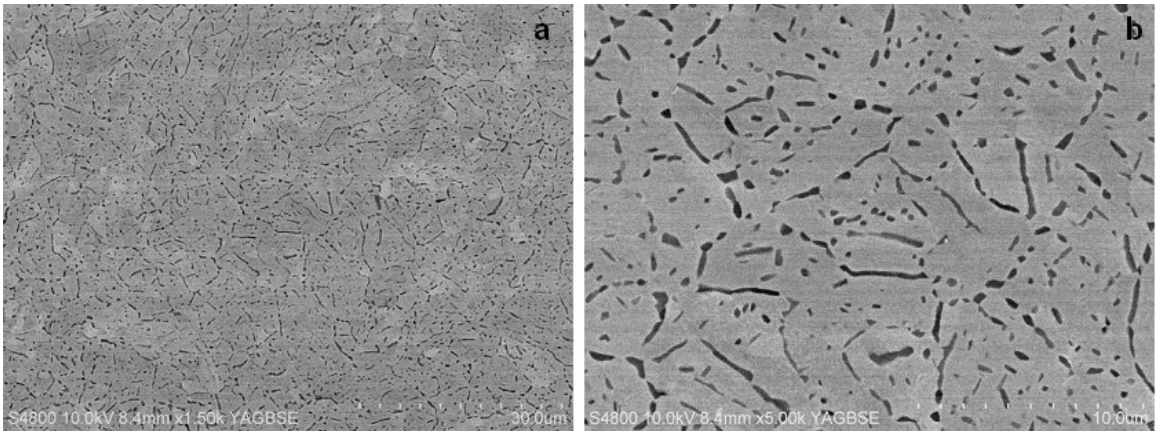

Figure 4.1. BSEI micrographs of as-received Ti-6.5 Mo-4.5Fe-1.5Al a) Low magnification b) High magnification.

Examination of the as-received condition through SEM indicated a two-phase ($\alpha+\beta$) microstructure with the primary α phase (black phase) located at the prior triple point junctions and on the grain boundaries as seen in Figure 4.1 a. High magnification backscattered electron microcopy of the same specimen did not show any evidence of intragranular α_s precipitation (Figure 4.1 b).The grain size and α phase volume percent, as determined by lineal intercept method and systematic point counting methods, were 2.19±0.39 μm and 12 ± 4 v/o, respectively.

Upon SEM examination, it was shown that, solution treating the as-received TIMETAL LCB at 633^{o}C promoted precipitation of very fine α needles with in the β matrix (Figure 4.2a). Increasing the solution treatment temperature to 715^{o}C decreased the aspect ratio (L/d) of fine α needles resulting in a spheroidized intragranular alpha morphology (Figure 4.2b). The driving force for this process -*spheroidization* - is the reduction in the overall surface area [4].

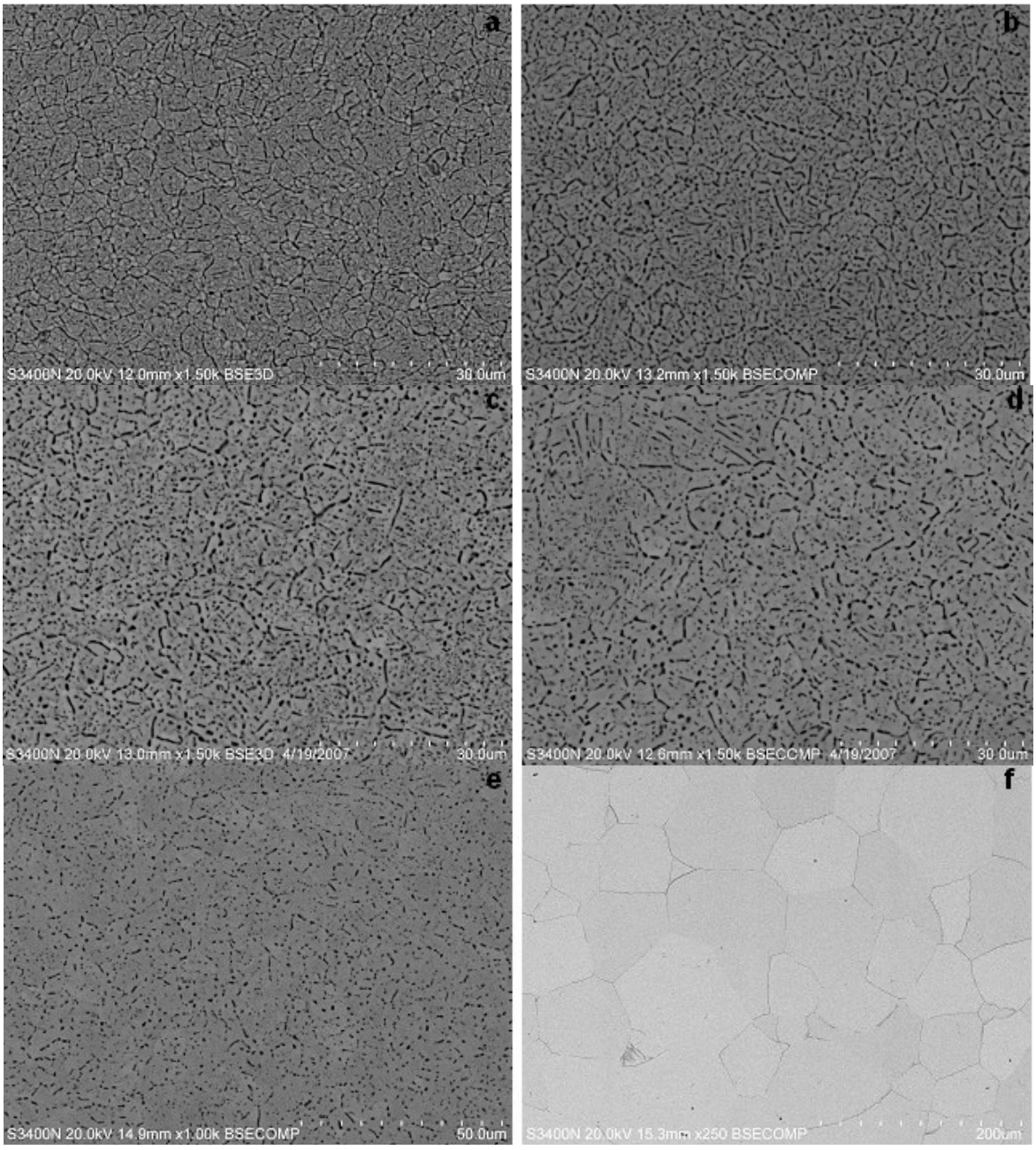

Figure 4.2. BSEI of Ti-6.5Mo-4.5Fe-1.5Al solution treated at a) 633^{0}C b) 715^{o}C c) 730^{o}C d) 745^{o}C e)760^{o}C f) 790^{o}C for 30 minutes followed by water quenching.

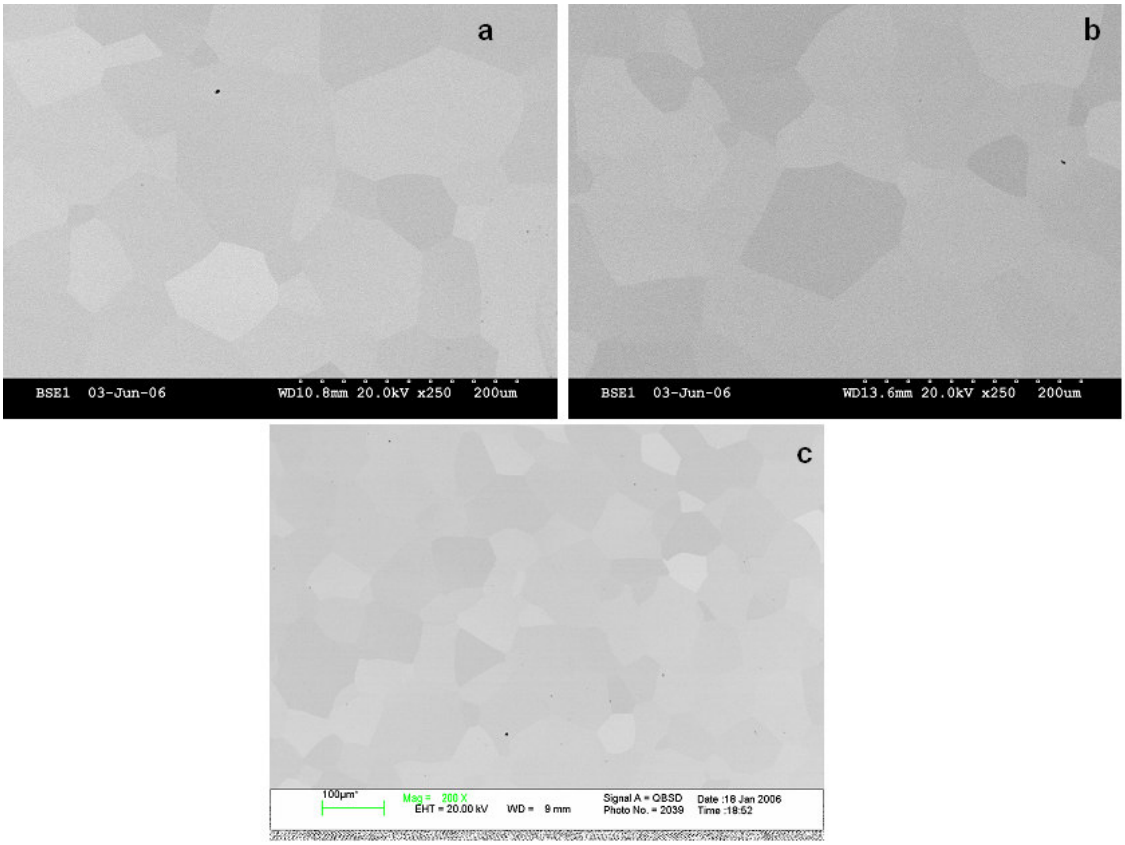

Figure 4.3. BSEI of Ti-6.5Mo-4.5Fe-1.5Al solution treated at a) 800^{0}C b) 810^{o}C c) 820^{o}C for 30 minutes followed by water quenching.

Grain boundary α phase was found to begin spheroidizing at 730^{o}C (Figure 4.2c). Further, an increase in solution treatment temperature gradually reduced the amount of grain boundary α and intragranular needle-like precipitates (Figures 4.3d and 4.2e). Since globular grain boundary α particles pin grain boundaries and inhibit grain growth , β grain size increased, with decreasing grain boundary alpha volume fraction[36]. Larger β grain size (51.78±12.35µm) at 790^{o}C assisted in thin grain boundary α film formation (Figure 4.2f). Finally, α phase precipitation, above 800^{o}C was not detected

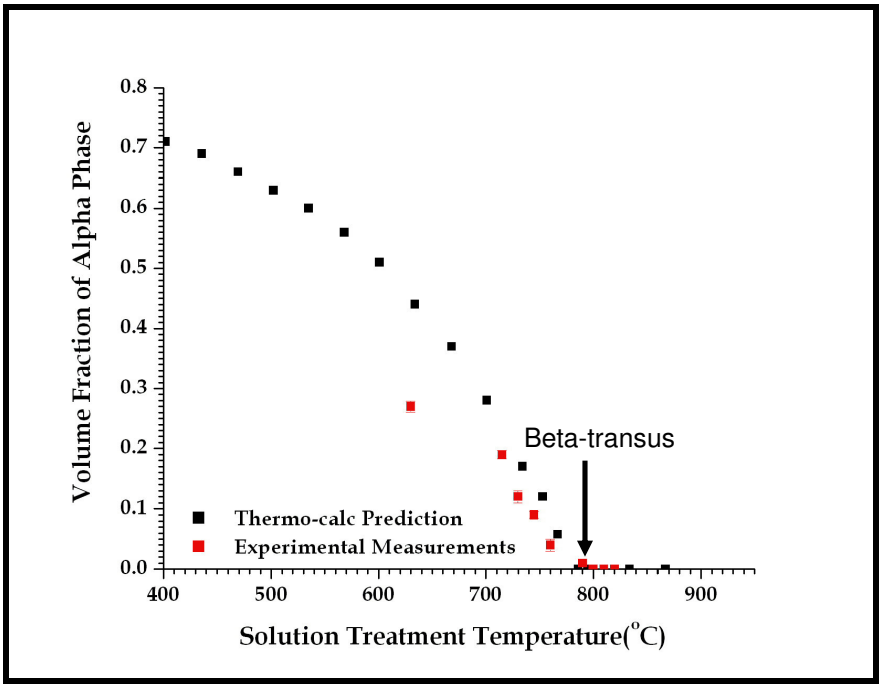

Figure 4.4. Comparison of the experimental and theoretical volume fraction of alpha phase with temperature. Samples were solution treated for 30 minutes.

through SEM examination (Figures 4.3a –c).

The variation in the α phase volume fraction with solution treatment temperature, as observed through SEM, was quantified by image analysis measurements and Thermo Calc™ predictions and is plotted in Figure 4.4. The black squares on this plot display the results of the Thermo Calc prediction and the red squares correspond to the data points of the experimental measurements. Upon comparing the two data sets, it was found that, the calculated and measured β-transus temperature and equilibrium α phase volume fractions at relatively high solution treatment temperatures are in good agreement and the volume fraction of α phase systematically decreases with increasing solution treatment temperature. Using this data, the β transus

temperature of TIMETAL LCB is calculated to be 795 ± 5°C. However, experimentally determined α phase volume fraction disagreed with the theoretical prediction at 633°C, with the measured volume fraction being lower than the theoretical calculation. Deviation of experimental volume fraction from theoretical calculations may result from in-accurate measurements of the very fine intragranular alpha needles due to the relatively poor resolution of the scanning electron microscope.

4.1.2. Solution Treatment Time

In order to determine the effect of solution treatment time on the prior hot worked sub-structure, TIMETAL LCB specimens, solution treated at 820°C for 30 minutes, were decoration heat treated at 550°C for 5 minutes to promote heterogeneous nucleation of α on any remnant dislocation substructure.

Decoration treatment technique is based on accelerating the kinetics of second phase formation in the presence of plastic deformation [5]. In β titanium alloys, relatively small amounts of deformation (<5%) reduces the minimum time for the onset of α phase precipitation, from several minutes to less than 15 seconds. As a result, α phase precipitation within the plastically deformed regions can be observed if a sample is aged for a short amount time, that is between the onset α phase precipitation in deformed and un-deformed materials. The time required for α phase precipitation in an un-deformed TIMETAL LCB specimen is 6 minutes at 550°C [6]. Therefore, aging TIMETAL LCB for 5 minutes at this

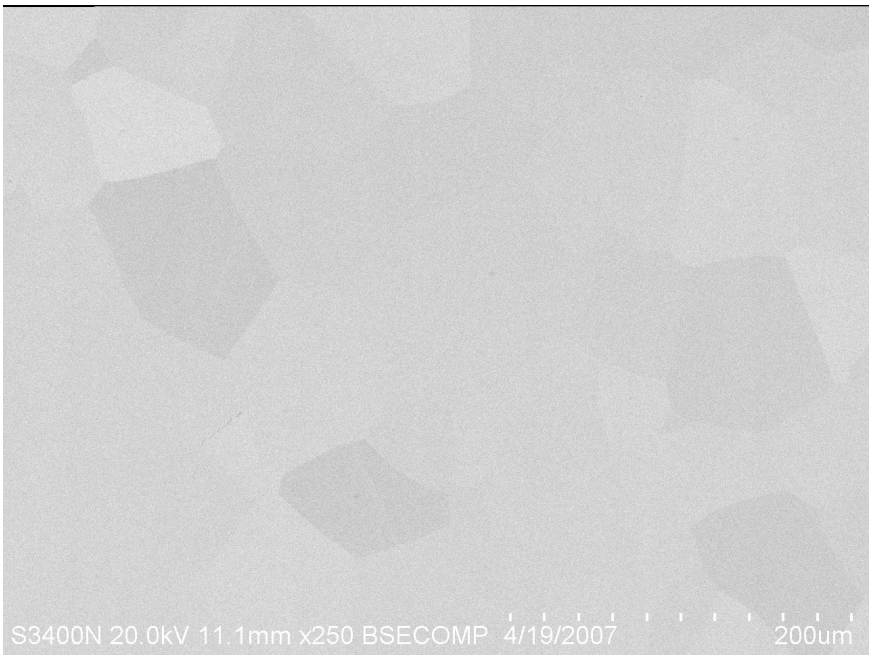

Figure 4.5. BSEI micrograph of TIMETAL LCB Solution treated at 820^{0}C for 30 minutes followed indirect aging at 550^{o}C for 5 minutes and subsequently water quenched at room temperature.

temperature were deemed to be sufficient to relieve any plastically deformed region present in the sample. Evidence of α phase precipitation was not found upon examination of the SEM micrograph of the solution treated (820^{o}C/20min.) and aged (550^{o}C/5min.) TIMETAL LCB (Figure 4.5) and it was concluded that ,30 minutes is sufficient to eliminate the entire hot-worked structure.

4.2. X-ray Diffraction (XRD) Analysis of the Solution Heat Treated TIMETAL LCB Specimens

In an electron backscatter diffraction (EBSD) experiment, diffraction patterns obtained from various phases can be analyzed if the crystal structures and lattice parameters of these phases are known. Therefore, x-ray diffraction (XRD) analysis was performed to determine the lattice parameters of the β (bcc) and α (hcp) phases prior to electron backscatter diffraction (EBSD) analysis. In order to examine the effect of temperature on the lattice parameters, TIMETAL LCB specimens solution treated for 30 minutes between 700-745^{o}C at 15^{o}C intervals were examined.

The x-ray diffraction spectra of the solution treated samples are shown in Figures 4.6a through d. These spectra were indexed using an analytical method outlined in Cullity [3].Once indexed, the lattice parameters of β (a_β) and α (a_α and c_α) phases were calculated from these spectra using the Bragg's law and plotted in Figures 4.7.a through c as a function of temperature. Upon comparing the lattice parameters of β and α phases in the solution treated samples it was found that, a_β, a_α and c_α are relatively insensitive to variations in solution treatment temperature.

The lattice parameter data obtained during this study was input into the EBSD data acquisition and processing software in order to correctly index the diffraction patterns and determine the orientation of α and β phases in the solution treated and aged specimens.

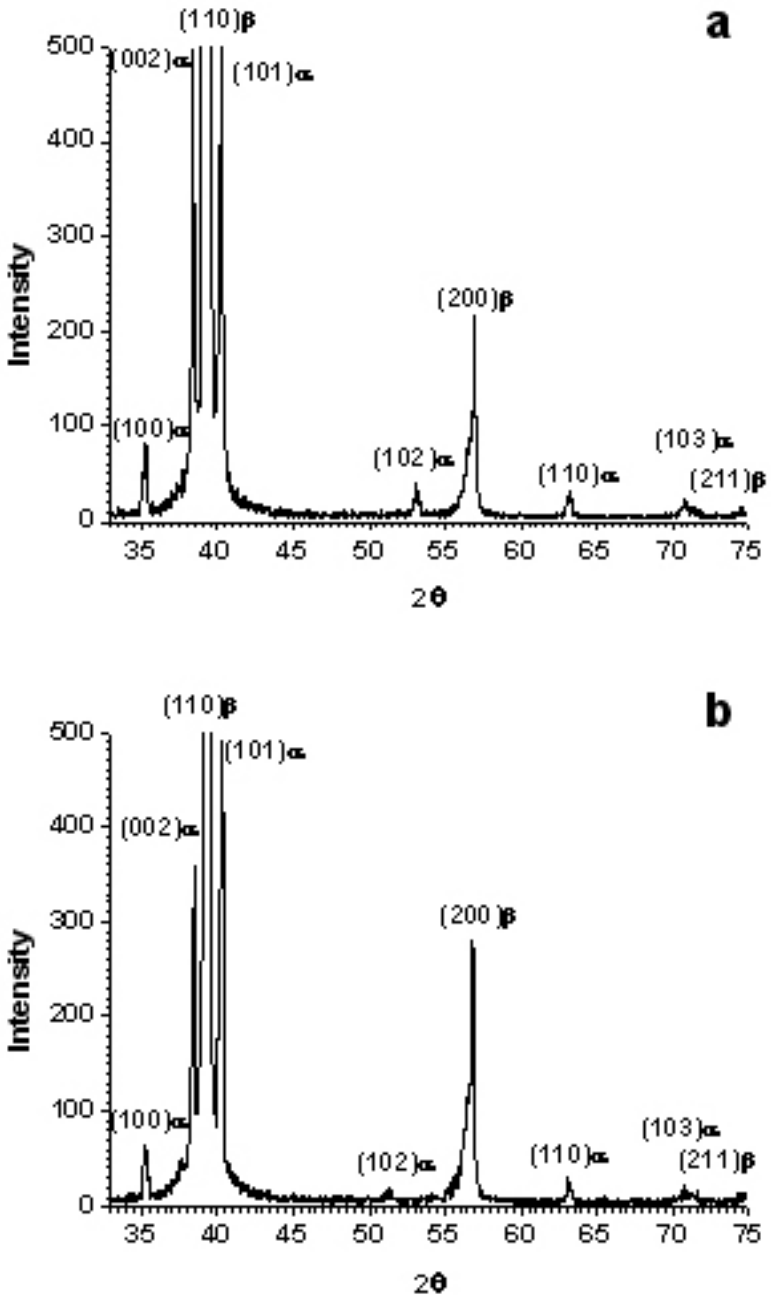

Figure 4.6. X-ray diffraction spectra of TIMETAL LCB solution heat treated at a) 700°C b)715°C c) 730°C and d) 745°C.

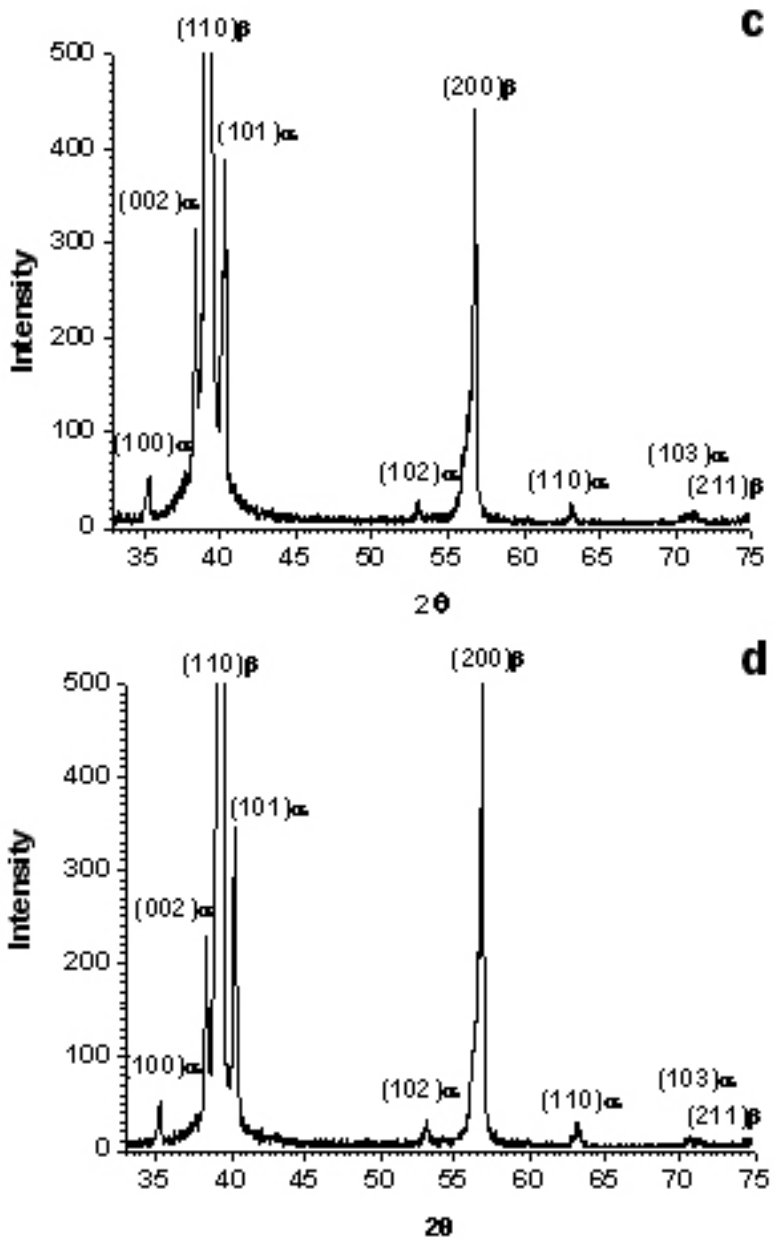

Figure 4.6. Continued.

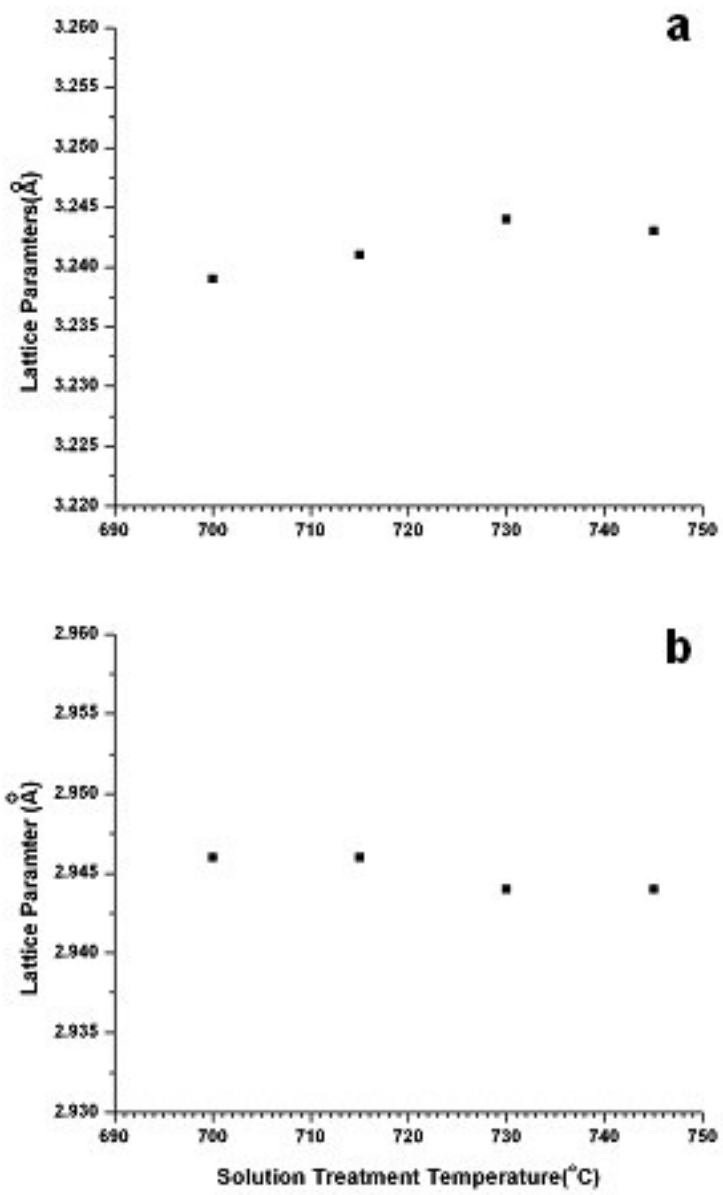

Figure 4.7. Influence of solution treatment temperature on a) a_β b)a_α and c)c_α.

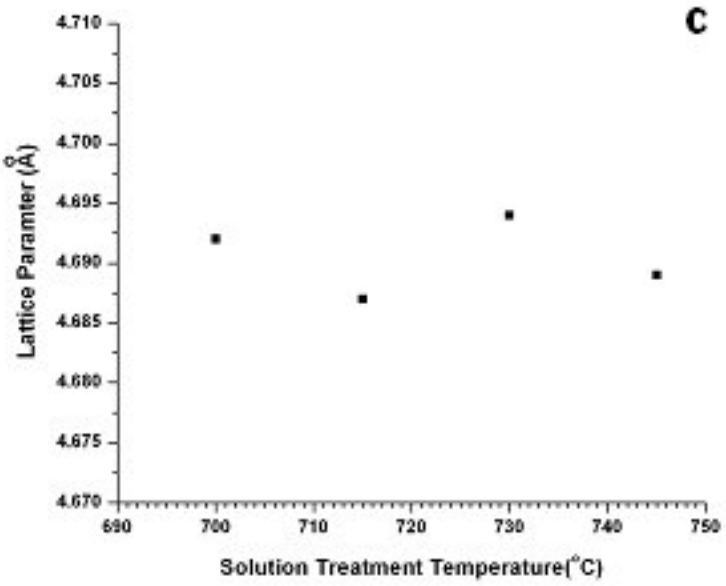

Figure 4.7. Continued.

4.3. Orientation Imaging Microscopy (OIM) of the Solution Heat Treated Microstructure

4.3.1. Results of the Orientation Imaging Microscopy (OIM) Analysis

Grain boundaries in polycrystalline aggregates are preferential nucleation sites for second phase particles during solid state phase transformations. Phase transformation studies on iron (Fe) and aluminum (Al) based alloys have shown that, morphology and quantity of second phase precipitates are strongly influenced by the structure of the grain boundaries [7-15]. These observations suggest that, in studying α phase precipitation in metastable β titanium alloys, an understanding of grain and grain boundary structure of the untransformed microstructure is essential. Such an understanding is also necessary to modify and control the grain boundary character distribution in TIMETAL LCB by the proper choice of solution treatment schedule.

Upon inquiring it was found that, current TIMETAL LCB is lacking information regarding to micro-texture of the grain boundaries in the single phase structure.

In this section, grain and grain boundary structure of TIMETAL LCB, solution treated at 820^{o}C for 30 minutes, was surveyed using SEM, OIM and quantitative image analysis techniques. In order to understand the effect of solution treatment time on the single phase microstructure, an additional specimen, solution treated at 820^{o}C for 5 minutes, was also examined.

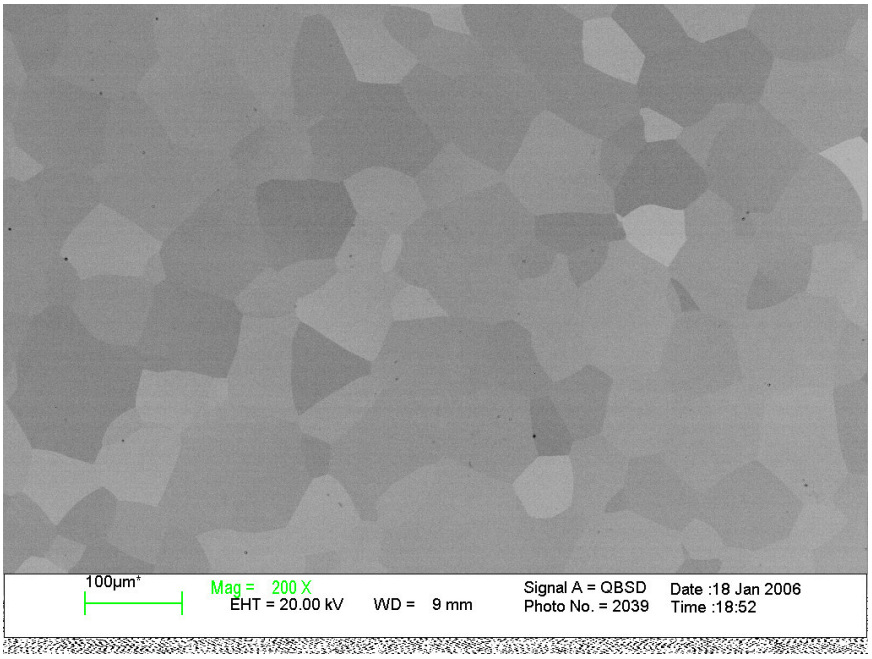

Figure 4.8. BSEI of TIMETAL LCB solution treated for 30 minutes at 820°C and water quenched.

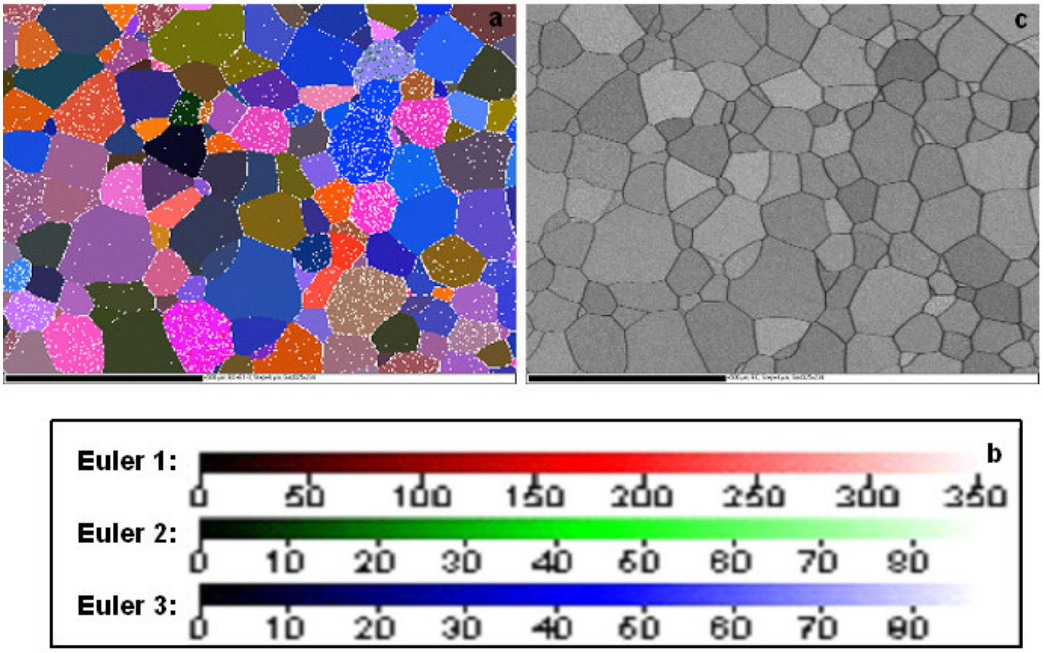

Figure 4.9. a)Crystal orientation map of solution treated TIMETAL LCB b) All Euler Key. c)Image Quality (IQ) Map.

Figure 4.8 shows a typical low magnification, backscattered electron micrograph of TIMETAL LCB, solution heat treated at 820°C for 30 minutes. The low magnification is used to identify the β grains and different gray contrasts, observed in Figure 4.8, are indicative of the interior section of these grains. Solution treated TIMETAL LCB has a single phase structure, therefore, these contrast differences are related to differences in the grain orientations.

An orientation map (OM) of the single phase microstructure was collected and is given in Figure 4.9a. This map covers an area of approximately 1 mm^2 and was obtained with a grid size of 4 μm resulting 62,500 orientations. Points on the map were colored such that grains with the same orientation share the same color (Figure 4.9a). Euler coloring was used to transform an orientation ($\varphi_1, \phi, \varphi_2$) to an RGB (Red, Green, Blue) color. The corresponding Euler angle color key is given in Figure 4.9b.

An image quality (IQ) map, representative of the sharpness or quality of the patterns, is shown in Figure 4.9c [16]. A lighter color on this map indicates a better electron backscattered pattern (EBSP) quality. Upon comparing the IQ map with the OIM map it was found that, regions of low IQ (darker areas) coincide with the un-indexed points on the OIM map (white points). The un-indexed points within the grains may be due to a) polishing induced surface deformation b) athermal omega (ω) phase of TIMETAL LCB. Typically, omega phase can form during quenching the solution treated TIMETAL LCB from above the β-transus temperature and has a hexagonal closed packed structure [17].

EBSD data processing software used in this study assumed a body centered cubic (bcc) crystal structure when indexing the diffraction patterns. As a result, the hexagonal closed packed (hcp) crystal structure of the omega phase may cause un-correct indexing.

A grain boundary map, extracted from the OM map of the solution heat treated TIMETAL LCB, is shown in Figure 4.10. The grain boundaries within the microstructure were highlighted using three different pen colors: blue, black and red, where blue corresponds to boundaries within 5-22.5^o and red corresponds to 52.5-62.5^o. For the boundaries within the $22.5^o < \theta < 52.5^o$ interval, black color was used.

The choice of misorientation interval for coloring was based on the grain boundary misorientation distribution presented in Figure 4.10b. This graph shows the proportion of the length (or projected area) of grain boundaries within a given misorientation range to the total grain boundary length. The lower and upper threshold values are 5 and 62.5^o, respectively. The two data sets shown in this graph correspond to the experimental and theoretical distribution of grain boundaries. The first set (shown as red bars) displays the actual misorientation distribution measured between the neighboring grains. The black line represents the theoretical misorientation distribution for a randomly oriented set of grains [18]. Upon comparing the two data sets it was found that, solution treated TIMETAL LCB displays a misorientation distribution with two distinct maxima at low (<22.5^o) and high angles (>52.5^o) angles.

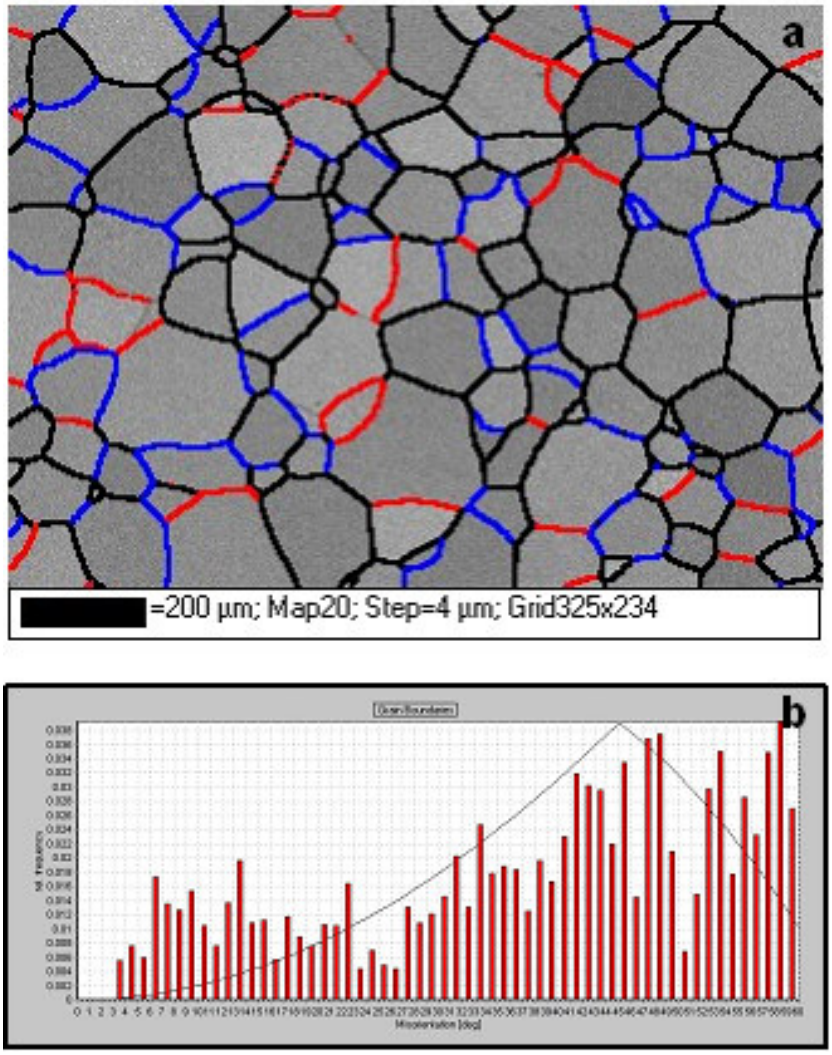

Figure 4.10. OIM map of TIMETAL LCB solution treated for 30 minutes a)grain boundary map (red $5 \leq \theta \leq 22.5^{o}$, black $22.5 < \theta < 52.5^{o}$, blue $52.5 < \theta < 62.5^{o}$) and b) grain boundary map key representing grain boundary misorientations.

In order to understand the effect of solution treatment time on the single phase microstructure, OIM analysis was performed on a sample solution treated at 820°C for 5 minutes (Figure 4.11). Next, grain size and grain boundary misorientation distribution of samples solution treated for 5 and 30 minutes were

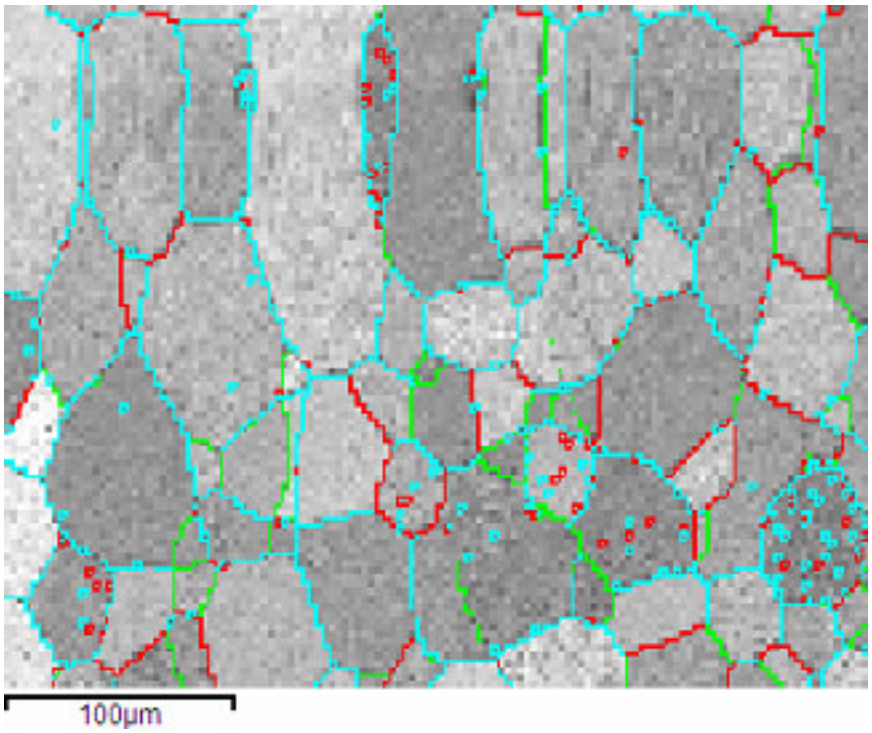

Figure 4.11 OIM map of TIMETAL LCB solution treated for 5 minutes a)grain boundary map (green $5 \leq \theta \leq 22.5^{o}$, aqua $22.5 < \theta < 52.5^{o}$, red $52.5 < \theta < 62.5^{o}$) and b) grain boundary map key representing grain boundary misorientations.

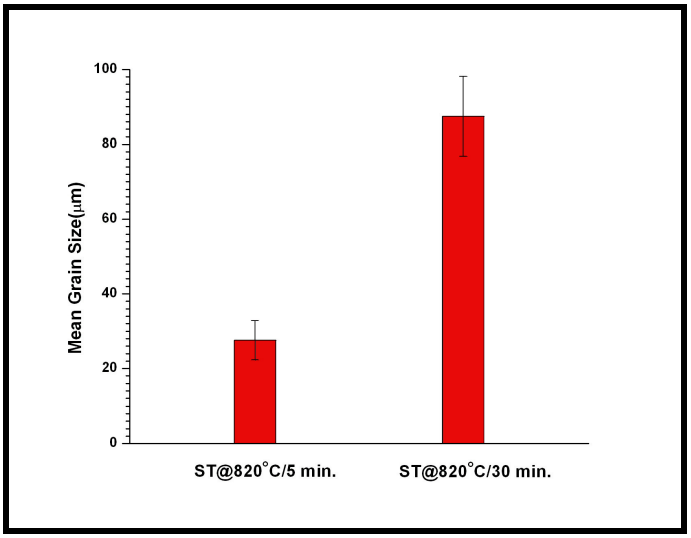

Figure 4.12 Effect of solution treatment time on the grain size of TIMETAL LCB.

explored through image analysis measurements. The grain size measurements included the mean lineal intercept method, with the grain size being determined from the number of grain boundaries intersecting a unit length of randomly distributed test lines. Comparing the quantitative image analysis results showed that, the grain size of single phase TIMETAL LCB increased from 27.54±5.25μm to 87.49±10.67μm which correlates to an increase in the solution treatment time from 5 to 30 minutes (Figure 4.12).

The effect of solution treatment time on the grain boundary misorientation distribution was characterized by measuring the fraction grain boundary surface area per unit volume ($\%S_V$) within a given misorientation range. For this purpose, three types of grain boundary areas were identified based on their misorientation. The first group involved grain boundaries within the misorientation range of $5 \le \theta \le 22.5^o$. The second and the third group involved boundaries with misorientations $22.5 < \theta < 52.5^o$ and $52.5 < \theta < 62.5^o$, respectively. The surface area per unit volume of a particular interface ($S_V^{i<\theta<j}$) was measured by counting the number of each type of grain boundary area intersected with a randomly distributed set of five test lines, (i and j standing for the lower and upper misorientation angle limit within a given interval). Upon analysis it was found that, increasing solution treatment time from 5 to 30 minutes resulted in a variation in $S_V^{5-22.5^o}$ from $0.0078\mu m^{-1}\pm0.0041$ to $0.0034\mu m^{-1}\pm0.00166$ and in $S_V^{52.5-62.5^o}$

from $0.0064\mu m^{-1}\pm0.0040$ to $0.0041\mu m_{-1}\pm0.0018$. $S_v^{22.5-52.5^o}$, in the TIMETAL LCB specimen solution heat treated for 5 minutes was $0.053\mu m^{-1}\pm0.010$. Upon increasing solution treatment time to 30 minutes $S_v^{22.5-52.5^o}$ decreased to $0.015\mu m^{-1}\pm0.0028$. These results are presented in Figure 4.13.

These observations suggest that, $S_v^{5-22.5^o}$ and $S_v^{52.5-62.5^o}$ are insensitive to variations in solution treatment time, whereas $S_v^{22.5-52.5^o}$ is a strong function of the solution treatment time and decreases significantly with increasing solution treatment time.

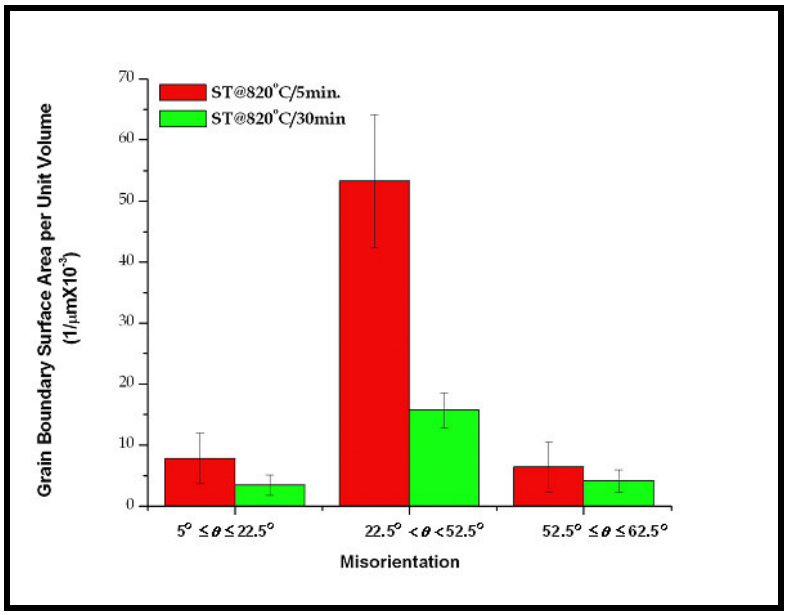

Figure 4.13. Effect of solution treatment time on the grain boundary surface area per unit volume.

4.3.2. Discussion of the Orientation Imaging Microscopy (OIM) Analysis

This study has examined the grain and grain boundary structure of the single phase TIMETAL LCB that has been solution treated according to a schedule determined previously in the section 4.1. According to this procedure a TIMETAL LCB specimen was solution treated at 820^{o}C for 30 minutes and examined through SEM and OIM. In order to understand the effect of solution treatment time on the single phase microstructure, another specimen, solution treated for 5 minutes, was also examined.

It was shown through quantitative image analysis measurements that, normal grain growth occurred with increasing solution treatment time from 5 to 30 minutes. Grain growth may be defined as a process involving the increase of the mean grain size by migration of grain boundaries. The driving force for the migration is solely the reduction of grain boundary surface area [19]. The mobility of boundaries during grain growth is directly proportional to their energy [20]. As a result, the boundaries with higher energies can be expected to be more mobile during grain growth and reduce their total surface area, whereas those that are less energetic are relatively immobile and are not expected to show a significant decrease in their surface area as a result of grain growth.

It was shown in this study that, during grain growth, the surface area of boundaries within the misorientation range of $22.5 < \theta < 52.5^{o}$ decreased with increasing solution treatment time. In contrast, surface area of the grain boundaries within the 5-22.5^{o} and 52-62.5^{o} interval was insensitive to varying

solution treatment time. These observations suggest that grain boundaries within the misorientation range $22.5^o < \theta \leq 62.5^o$ are mobile during grain growth and may be expected to have high energies, whereas those within the misorientation range $5 \leq \theta \leq 22.5^o$ and $52.5 < \theta < 62.5^o$ tend to be immobile. The low energy of these may be accounted for their constant overall surface area of during grain growth.

The low energy of grain boundaries within the misorientation range of $5^o < \theta \leq 22.5^o$ can be understood by considering the Read-Shockley relationship [21] which correlates of the grain boundary energy (E_B) in polycrystalline materials to the angular misorientation (θ)

$$E_B = A\theta[B - \ln\theta] \qquad 4.1$$

where A and B are material related constants that depend on shear modulus, Burgers vector and Possion's ratio.

Equation 4.1 states that, grain boundary energy is a function of misorientation. E_B continuously increases with increasing misorientation up to 15-20^o and remain constant at higher angles (Figure 4.14).This range is typically taken as the limit for the transition from low- to high- angle boundaries.

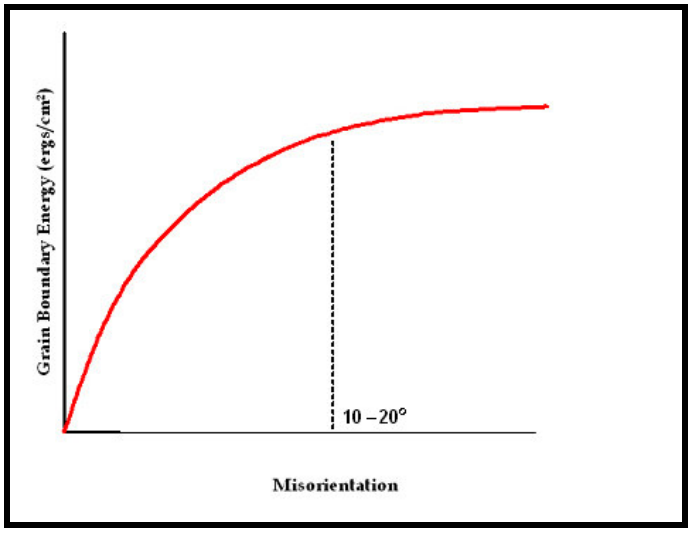

Figure 4.14. Predicted grain boundary energy as a function of tilt angle.

In order to determine the source of invariance in the surface area of grain boundaries with in the misorientation range $52.5^{o} < \theta \leq 62.5^{o}$, the solution treated microstructure was explored for the presence of coincident site lattice (CSL) boundaries. These boundaries are referred to as coincident site lattice (CSL) boundaries because they form at boundary planes which allow the two adjoining lattices to fit together with relatively little distortion of the inter-atomic bonds [22]. As a result of the good fit along the boundary plane, these boundaries have low energies and display cusps at specific misorientations of energy versus angle curves [23].

The degree of fit between two lattices that are separated by a CSL boundary can be characterized by its sigma value ($\sum$), which corresponds to the reciprocal density of the coinciding sites. Typically, the energy of the CSL boundaries is inversely proportional to their $\sum$ value.

In general, exact CSL orientations are not observed in actual systems. However, a maximum deviation from an exact CSL orientation (V_m) can be defined through Brandon criterion which corresponds to the highest density of dislocations that can be accommodated by the boundary [24]:

$$V_m = V_o \sum^{-1/2} \qquad 4.2$$

where V_o is proportionality constant. Substituting $\sum=1$ into equation 4.2 gives V_m as 15^o and defines the limit for low angle boundaries. Therefore, the low angle boundaries also correspond to $\sum=1$ CSL type boundaries.

The distribution of CSL type boundaries in the solution treated TIMETAL LCB microstructure is shown in Figure 4.15. The angle/axis pair list and V_m values for the CSL type boundaries observed in the solution treated TIMETAL LCB along with a map key is given in Table 4.1. The absence of a specific $\sum$ value means a particular CSL boundary was not observed. Although, sigma values ranged from 1 to 45, the lowest energy $\sum=1$ (aqua) and $\sum=3$ (red) boundaries dominate the total CSL population (Figure 4.16). Note that $\sum=1$ boundaries are not plotted on this histogram. However, as shown in Figure 4.15, they have the highest occurrence among all CSL type boundaries.

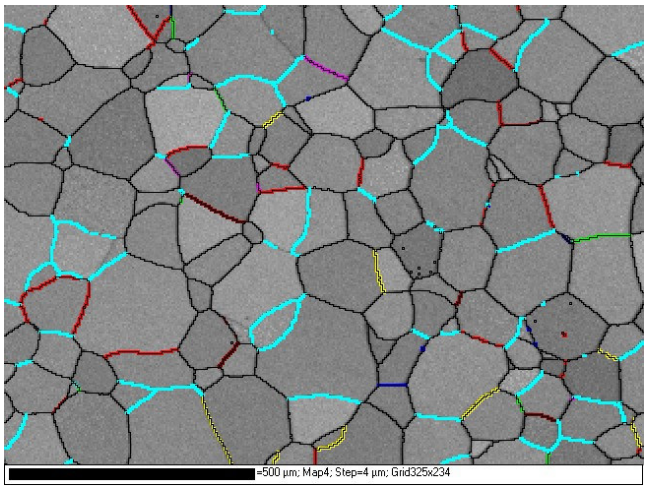

Figure 4.15 Distribution of CSL type boundaries in TIMETAL LCB solution heat treated for 30 minutes.

Table 4.1 Angle/Axis Pair and V_m values of several CSL type boundaries.

∑	Axis	Angle	V_m	Map Key
1	N/A	0	15	
3	111	60	8.66	
5	100	36	6.71	
7	111	38.21	5.67	
9	110	38.94	5	
11	110	50.48	4.92	
15	210	48.19	3.87	
17a	100	28.07	3.64	
21a	111	21.79	3.27	
21b	211	44.4	3.27	
23	311	40.45	3.13	
29a	100	43.61	2.79	
39b	321	50.3	2.4	
45c	221	53.13	2.24	

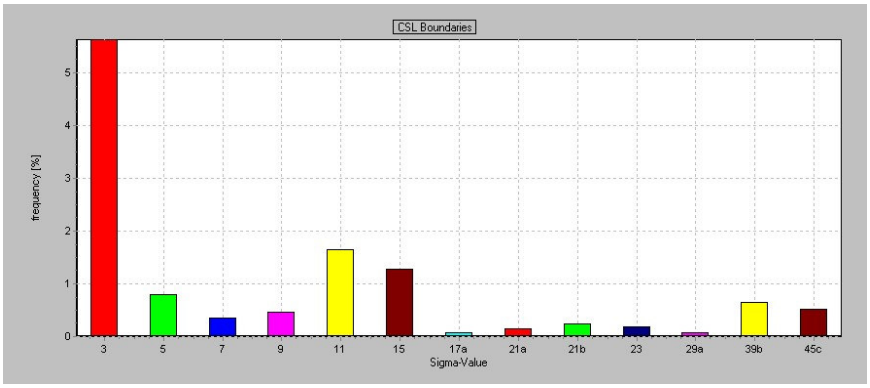

Figure 4.16. Frequency of CSL boundary distribution.

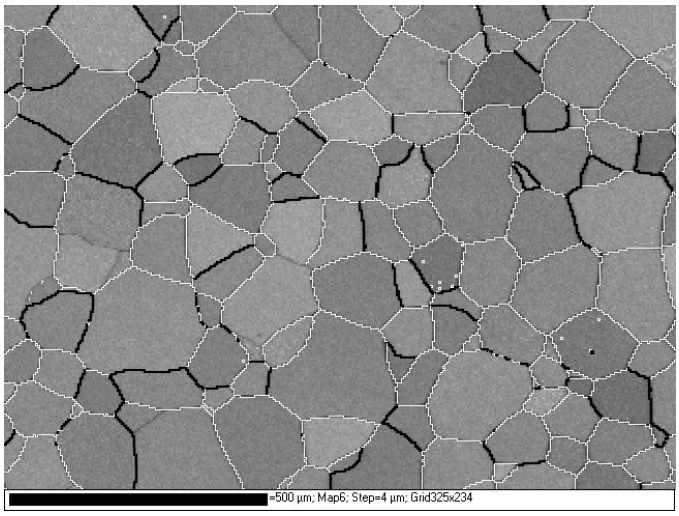

Figure 4.17 Grain boundary map illustrating the distribution of grain boundaries with in the misorientation range 52.5-62.5^{o} (black lines).

Figure 4.17 delineates the grain boundaries within the misorientation range 52.5-62.5°. Upon comparing Figure 4.17 to the CSL map to it was found that 34% of all the boundaries within the misorientation range $52.5 < \theta < 62.5$ were $\sum 3$ type, therefore have low energies. Although the majority of boundaries within the misorientation range $52.5 < \theta < 62.5$ is not $\sum 3$, the influence of non-$\sum 3$ type grain boundaries on the overall change in the grain boundary area during grain growth appears to be insignificant. However, it should be noted that these random boundaries are expected to have a higher energy than the $\sum 3$ CSL type boundaries.

These observations indicate that distribution of grain boundaries within the solution heat treated microstructure is a function of their energy, higher grain boundary energy being associated with a higher mobility. As a result, frequency of high mobility grain boundaries decreases during grain growth.

4.3.3. Conclusions of the Orientation Imaging Microscopy (OIM) Analysis

This analysis has shown that grain boundaries in solution treated TIMETAL LCB can be classified based on their energy as: a) type A and b) type B. Type A boundaries consists of grain boundaries within the misorientation range of $\mathbf{5 \leq \theta \leq 22.5^o}$ and $\mathbf{52.5 < \theta < 62.5^o}$. These boundaries have relatively low energies and they tend to be immobile during grain growth. Type B boundaries consist of grain boundaries within the misorientation range of $\mathbf{22.5 < \theta < 52.5^o}$ and have higher energies. As a result, Type B boundaries tend to reduce their total area by grain boundary migration. In conclusion, the system is trying to reduce its total energy by increasing the surface area of low energy boundaries as suggested by Mishin et. al. [25].

4.4. Elevated Temperature Phase Transformation Kinetics of TIMETAL LCB

4.4.1. Results of the Phase Transformation Kinetics

An understanding of the mechanisms, controlling the formation of various alpha morphologies and phase transformations kinetics in TIMETAL LCB, is important to predict the final microstructure and achieve a wide variety of microstructure/property combinations the alloy has to offer. This study examines the evolution of the morphological sequence of alpha phase during isothermal aging, at four different temperatures between 700-745^{o}C, as well as the $\beta \rightarrow \beta+\alpha$ phase transformation kinetics using scanning electron microscopy (SEM), electron backscatter diffraction (EBSD) and quantitative image analysis.

4.4.1.1. Incubation Period

SEM images of TIMETAL LCB samples, aged for thirty and sixty seconds, did not exhibit any evidence of α phase precipitation when examined under the field emission scanning electron microscope (FE-SEM) at a magnification of 10000X, indicating that, β to α transformation in TIMETAL LCB does not proceed spontaneously upon quenching the samples to the appropriate aging temperature. Upon comparing the SEM micrographs it was observed that, the microstructure of the samples aged for thirty and sixty seconds was indistinguishable from the solution treated and quenched TIMETAL LCB, as shown in Figures 4.18 a-b. However, α phase precipitation was observed in the FE-SEM micrographs with increasing aging time to three minutes.

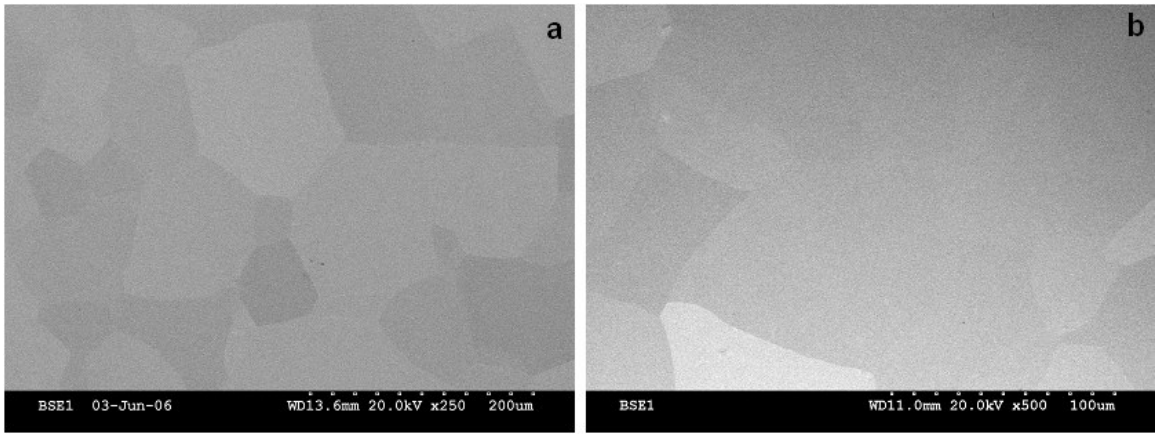

Figure 4.18. SEM micrographs of TIMETAL LCB a) Solution treated at 820^0C for 30 minutes followed by water quenching b) Solution treated at 820^0C for 30 minutes and subsequently aged at 700^0C for 60 seconds followed by water quenching.

This observation was independent of the aging temperature and suggests that the onset of α phase precipitation in TIMETAL LCB is between one and three minutes, when aged at temperatures greater than 700^oC.

4.4.1.2. Grain Boundary Alpha (α_{GRB}) Precipitation

Upon examination of the BSEI micrographs of TIMETAL LCB specimens it was found that, the α phase nucleated on triple point junctions and grain boundary surfaces when aged for three minutes. However, it was also observed that, transformation rate shows variation from boundary to boundary. For example, a series of BSEI micrographs, given in Figure 4.19, indicate that, amount of grain boundary alpha precipitates is not uniform along the grain boundaries and the early stages of the transformation may be associated solely with triple point junctions, as illustrated in Figure 4.19a, or grain boundary α

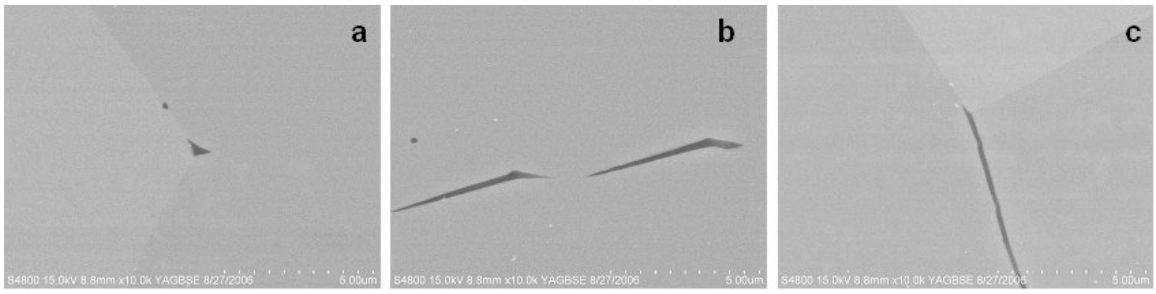

Figure 4.19. BSEI micrographs illustrating a)Grain boundary α precipitation at a triple point junction b) grain boundary α precipitation on a grain boundary surface c) grain boundary alpha film formation of TIMETAL LCB aged at 745°C for three minutes.

precipitates may be observed on the surfaces of certain boundaries, Figure 4.19b.In some instances, these precipitates may grow along some of the boundaries and form a continuous film while transformation along the neighboring boundaries remains incomplete, Figure 4.19c.

The microstructures given in Figure 4.19a through c correspond to a specimen aged at 745°C for 3 minutes; however similar observations were made, through SEM investigation, for the specimens aged at lower temperatures. For example, a BSEI image, given in Figure 4.20, illustrates three β grain boundaries meeting at a triple point junction in a TIMETAL LCB specimen aged at 700°C for 3 minutes. Grain boundary α precipitation was observed solely on the grain boundary between the β_2 and β_3 grains, $GB_{2\rightarrow3}$. EBSD analysis was performed to investigate the influence of the grain boundary structure on the precipitation of the α phase, however, orientation of grain boundary α crystals could not be examined due to the low resolution of the microscope.

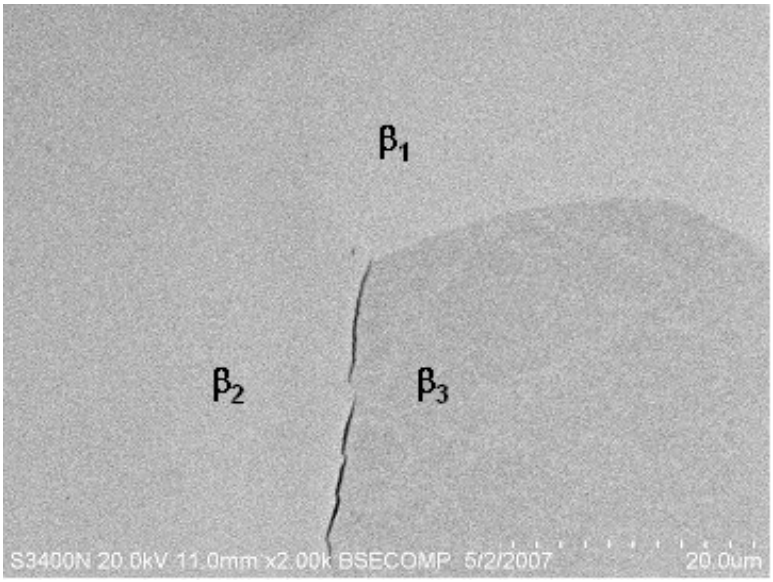

Figure 4.20 BSEI micrograph showing three β grains meeting at a triple point junction in TIMETAL LCB aged at 700°C for 3 minutes.

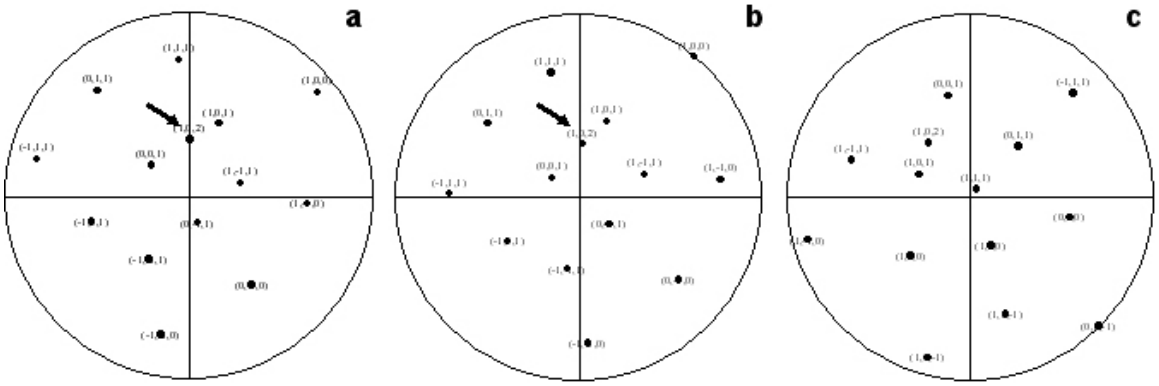

Figure 4.21. Pole figures of the a) β_1 b) β_2 and c) β_3 grains. The common (102) direction in β_1 and β_2 grains is shown with an arrow.

Average orientation of the β grains was determined through the interactive data collection mode of EBSD system. The pole figures corresponding to each grain are reconstructed using Carine Crystallography 3.1™ software and given in Figures 4.21a-c. This analysis indicated that β_1 and β_2 grains share a common $\{102\}_\beta$ pole (marked as X). A rotation of approximately 16°, about the common

$\{102\}_\beta$ pole, is required to bring β_1 into coincidence with β_2, indicating that $GB_{1\rightarrow2}$ is a low angle boundary. The grain boundary misorientations of $GB_{1\rightarrow3}$ and $GB_{2\rightarrow3}$, as determined by the Oxford Crystal Software^{TM}, were 34^o and 42^o respectively. These observations indicated that α phase precipitation takes place preferentially on the high angle boundary, $GB_{2\rightarrow3}$.

In order to verify that α precipitation is correlated with a high angle boundary during the early stages of β→β+α transformation, twenty four grain boundaries, in TIMETAL LCB specimens aged at different temperatures for 3 minutes, were examined by means of BSEI (Figures 4.22a through h). The angle/axis pairs of these grain boundaries were determined by EBSD analysis and listed in Table 4.2. The boundaries that were associated with α phase precipitation were highlighted with gray color. EBSD analysis helped to demonstrate that, grain boundary α precipitation at 3 minutes preferentially occurred on high angle boundaries (θ>15-20^o). However, probability of α_{GRB} precipitation was not the same for all the high angle boundaries and only specific high angle boundaries were selected. The selection criteria will be examined in the following pages by considering the structure of transformed boundaries with varying aging time and temperature.

SEM micrographs of the aged specimens demonstrated that, the extent of transformation on the prior β grain boundaries is a function of both aging time

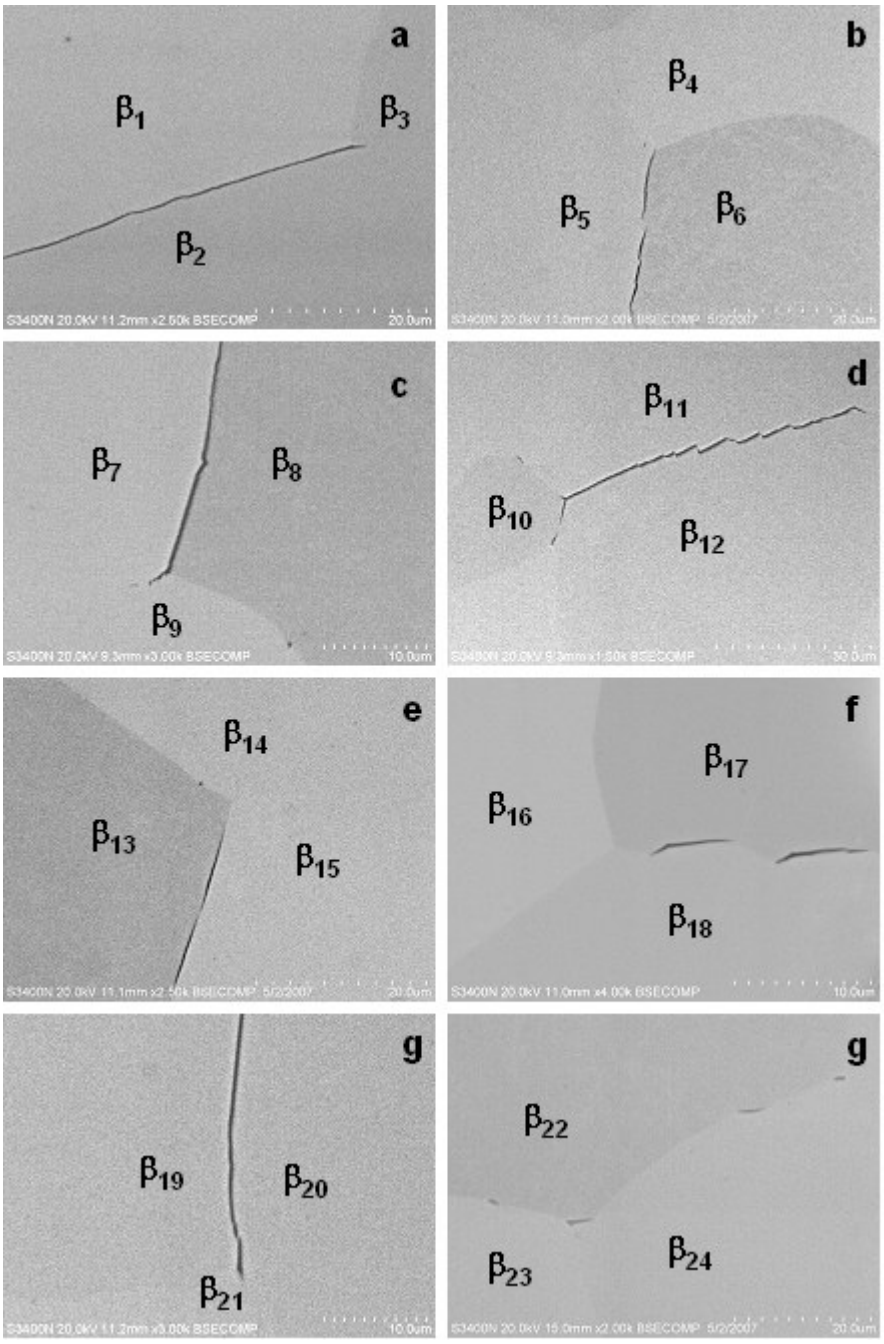

Figure 4.22 BSEI images demonstrating grain boundary α precipitation in TIMETAL LCB specimens aged at a-b) 700°C c-d) 715°C e-f)745°C and g-h)745°C for 3 minutes.

Table 4.2 Angle/Axis pairs of grain boundaries.

T (^{O}C)	GRAIN BOUNDARY	MISORIENTATION ANGLE	MISORIENTATION AXIS		
			u	w	v
700^{0}C	$GB_{1\rightarrow2}$	59.81	0.52	0.48	0.71
	$GB_{1\rightarrow3}$	45.69	0.54	0.36	-0.77
	$GB_{2\rightarrow3}$	35.22	0.45	0.51	0.73
	$GB_{4\rightarrow5}$	16.35	-0.79	-0.13	-0.6
	$GB_{4\rightarrow6}$	34.26	-0.81	-0.59	-0.05
	$GB_{5\rightarrow6}$	42.86	-0.19	0.35	-0.92
715^{0}C	$GB_{7\rightarrow8}$	45.78	-0.71	0.07	0.54
	$GB_{7\rightarrow9}$	36.77	0.19	-.081	-0.55
	$GB_{8\rightarrow9}$	13	0.78	-0.32	0.54
	$GB_{10\rightarrow11}$	43.59	0.18	-0.85	0.49
	$GB_{10\rightarrow12}$	16.27	0.68	0.73	-0.03
	$GB_{11\rightarrow12}$	34.07	-0.83	-0.17	-0.54
730^{0}C	$GB_{13\rightarrow14}$	57.34	0.31	-0.72	-0.62
	$GB_{13\rightarrow15}$	58.83	0.69	-0.2	0.7
	$GB_{14\rightarrow15}$	12.77	-0.22	0.33	0.92
	$GB_{16\rightarrow17}$	54.66	-0.29	-0.56	0.78
	$GB_{16\rightarrow18}$	56.88	0.65	0.62	0.44
	$GB_{17\rightarrow18}$	28.22	-0.51	-0.51	0.69
745^{0}C	$GB_{19\rightarrow20}$	60.42	0.71	0.42	-0.56
	$GB_{19\rightarrow21}$	5.85	0.89	-0.41	0.22
	$GB_{20\rightarrow21}$	57.94	0.64	0.44	-0.63
	$GB_{22\rightarrow23}$	26.26	0.49	-0.28	0.82
	$GB_{22\rightarrow24}$	37.57	-0.17	0.97	0.18
	$GB_{23\rightarrow24}$	37.88	-0.55	-0.81	0.19

and temperature. Image analysis measurements on the SEM micrographs of the aged specimens have aided to quantify the influence of increasing aging time and varying temperature on the extend of grain boundary surface area that has transformed into α phase. The low magnification BSEI micrographs of samples aged for ten, twenty and forty minutes, as well as the equilibrium microstructures

were used for these measurements. In these BSEI images, two types of grain boundary areas were identified: a) transformed and b) untransformed. Transformed grain boundary area corresponds to the portion of the grain boundary covered with α precipitates, and untransformed area correspond to precipitate free regions. The surface area per unit volume of a particular interface (S_V^i) was measured by counting the number of each type of grain boundary areas intersecting with five test lines (i=transformed or untransformed). The transformed grain boundary surface area per unit volume was normalized to a fraction $\%S_V^{transformed}$ and may expressed in the following manner:

$$\%S_V^{transformed} = \frac{S_V^{transformed}}{S_V^{total}} \times 100 \qquad 4.2$$

where S_V^{total} is the sum of transformed and untransformed grain boundary areas per unit volume.

Quantitative image analysis measurements showed that, at a given aging temperature the amount of transformed grain boundary area increased with increasing aging time, shown in Figure 4.23. However, increasing aging time at low undercoolings was found to have only minor influence on the grain boundary assisted nucleation of α phase. For example, increasing aging time from 30 to 600 seconds increased the percentage of the transformed grain boundary area

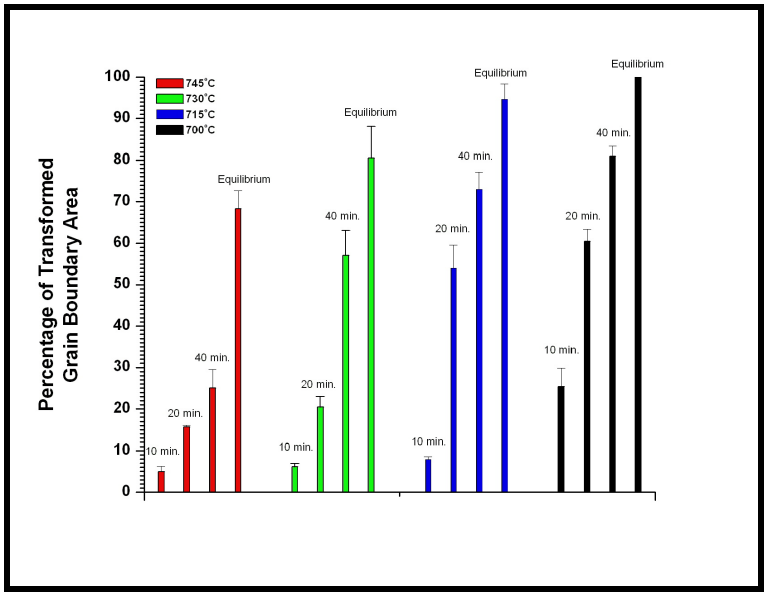

Figure 4.23. Variation in the transformed grain boundary area with aging time and temperature.

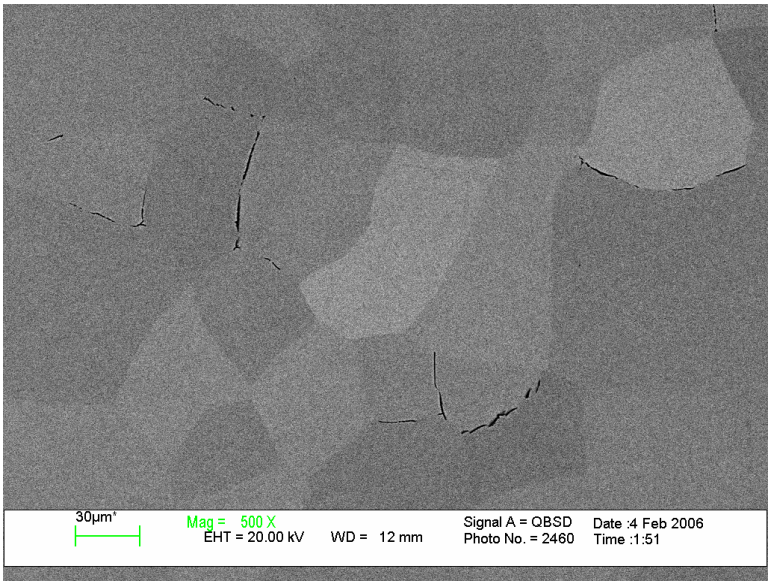

Figure 4.24. Low magnification BSEI micrograph of TIMETAL LCB aged at 745°C for 17 minutes. Alpha(α) phase precipitation is confined to select grain boundaries.

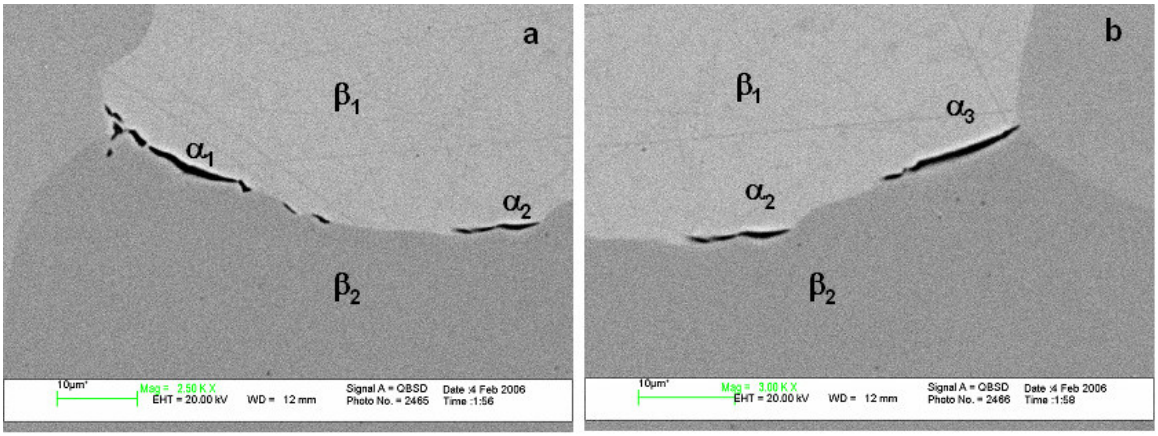

Figure 4.25 High magnification BSEI micrographs demonstrating α phase precipitation on different regions of the same grain boundary between β_1 and β_2 grains.

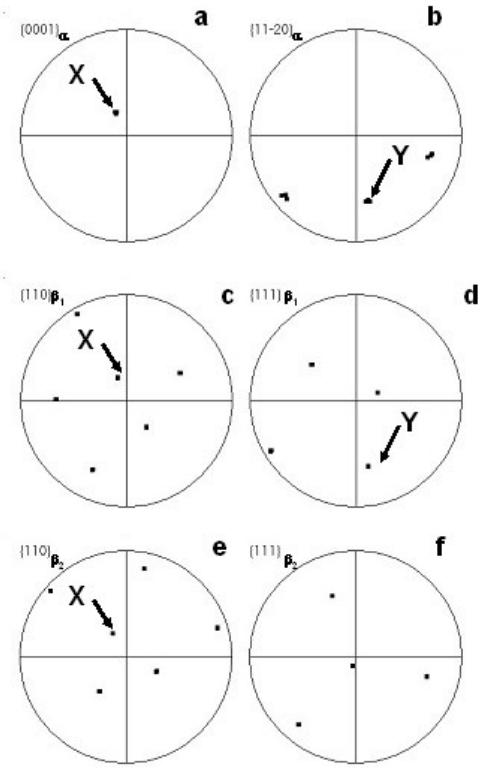

Figure 4.26. Results of the EBSD analysis. a) $\{0001\}_\alpha$ b) $\{11\bar{2}0\}_\alpha$ c) $\{110\}_{\beta_1}$ d) $\{111\}_{\beta_2}$ e) $\{110\}_{\beta_2}$ and f) $\{111\}_{\beta_2}$ pole figures.

from zero to only 4.94±1.33%. As a result, α_{GRB} distribution remained in-homogenous at low undercoolings. For instance, a typical low magnification backscattered electron micrograph of TIMETAL LCB alloy aged at 745°C for 17 minutes is given in Figure 4.24. This micrograph shows non homogenous grain boundary alpha distribution with α_{GRB} precipitation being confined to '*select'* grain boundaries. The BSEI examination of a transformed boundary in the same specimen indicates that, the grain boundary is slightly curved with α precipitates exhibiting disconnected structure (Figure 4.25 a and b). EBSD analysis was performed on this area, to investigate the grain boundary selection criteria for alpha phase precipitation. Crystallographic orientations of microstructural features of interest (α and β phases) was determined through interactive data collection mode of the EBSD system. The $\{0001\}$ and $\{1\bar{1}20\}$ pole figures of each α precipitate (α_1, α_2 and α_3) were plotted using the Channel 5 software and superimposed (Figure 4.26a and b). Upon further examination of these pole figures it was found that, α_1, α_2 and α_3 precipitates have similar orientations. Further examination the of β_1 and β_2 $\{110\}$ pole figures demonstrated that, these grains share a common $\{110\}$ pole and this pole is marked with X, shown in Figures 4.26c and e. Additionally, upon comparing the $\{0001\}$ pole figures of α precipitates to the $\{110\}$ pole figures of β grains it was found that, the grain boundary alpha precipitates have their $\{0001\}$ basal plane pole close to parallel to the common $\{110\}$ pole of the β grains. Finally, it was found that the upper β

Table 4.3. Angle/axis pairs of boundaries displaying alpha phase precipitation in TIMETAL LCB aged at 745°C for 17 minutes.

Misorientation Angle	Misorientation Axes	Common {110} pole
33.82	21-4	No
32.15	-1-20	No
56.58	4-3-8	Yes
51.28	10-1	Yes
55.36	011	Yes
49.48	-101	Yes
46.65	-110	Yes
32.20	-4-1-2	Yes
27.79	-4-21	Yes

grain has one of its $\{111\}$ pole aligned parallel to a $\{1\bar{1}20\}$ pole of the grain boundary alpha precipitates and these parallel pole are marked with Y in Figures 4.26b and d. As a result, the crystallographic pole figures of β_1, β_2 and α, are shown in Figure 4.41a through f, where β_1 is the grain on upper part of the grain boundary alpha and β_2 is the one below it. The relationship between the α_{GRB} precipitates and the upper β grain can be represented with a pair of parallel planes and directions as:

$$\{0001\}_\alpha \| \{110\}_\beta \text{ and } \langle 1\bar{1}20\rangle_\alpha \| \langle 111\rangle_\beta$$

The above relations imply that α precipitates are related to the β_1 grain through Burgers OR. In contrast, α precipitates do not hold a Burgers OR with the lower β grain because none of the $\{111\}$ poles of the lower β grain are parallel to a $\{1\bar{1}20\}$ pole of the α precipitates. However, it was determined through Carine Crystallography 3.1.™ software that, a rotation of approximately 8 degrees

around the common $\{110\}$ pole brings the β_2 grain into a Burgers OR with the α precipitates.

Additionally, nine grain boundaries, displaying α_{GRB} precipitation, in a specimen aged at 745°C for 17 minutes, was examined by BSEI and their crystallographic information was determined through EBSD analysis. Upon examining all the 24 crystallographically related solutions of the angle/axis pairs of these grain boundaries it was found that ,7 out of 9 boundaries, were between β grains that share a common $\{110\}$ pole (Table 4.3). Grain boundary alpha precipitates were found to have a Burgers OR with one of the adjacent β grains and it required only a few degrees rotation (typically less than 7-8°) about the common $\{110\}$ to bring the adjacent matrix grain into Burgers OR with the α precipitates.

In order to understand the effect of undercooling on grain boundary alpha phase precipitation TIMETAL LCB specimens, aged at lower temperatures and at comparable transformation amounts, were examined by SEM. A typical low magnification BSEI micrograph of TIMETAL LCB aged at 700°C for 6 minutes is shown in Figure 4.27. The microstructures investigated through SEM at 700°C showed similarities to those investigated at 745°C: 1) only certain grain boundaries were selected for alpha phase precipitation and 2) it was verified through EBSD examination that selective precipitation of alpha phase occurred on high grain boundaries located between β grains that share a common a $\{110\}$ pole (Table 4.4).

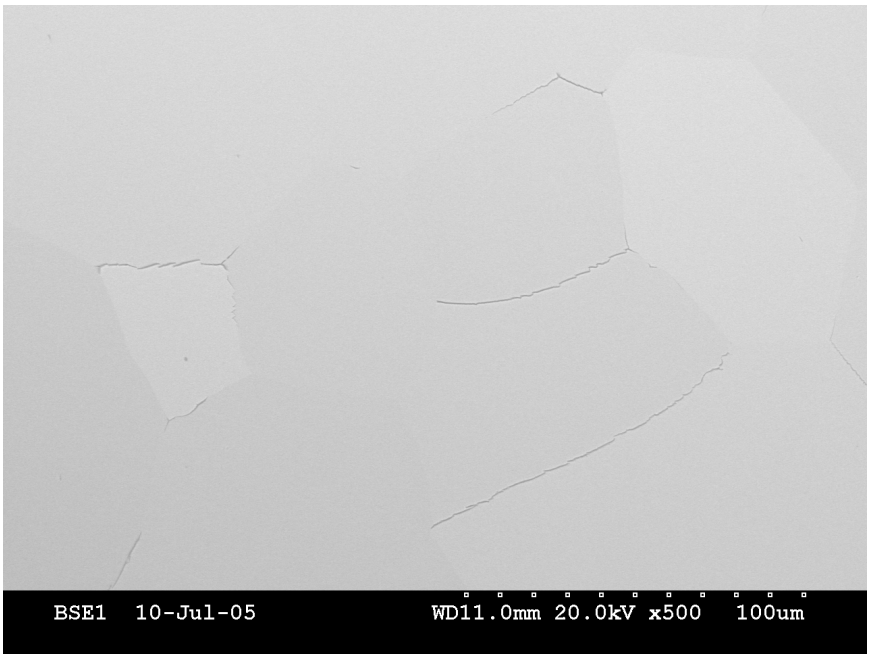

Figure 4.27 Low magnification BSEI micrograph of TIMETAL LCB aged at 700°C for 6 minutes.

Table 4.4. Angle/axis pairs of boundaries displaying alpha phase precipitation in TIMETAL LCB aged at 700°C for 6 minutes.

Misorientation Angle	Misorientation Axes	Common {110} pole	Boundary Type
35.95	-23-2	No	B
30.09	4-13	Yes	B
54.21	-1-10	Yes	A
29.49	21-3	Yes	B
30.21	4-13	Yes	B
30.96	012	Yes	B

Quantitative image analysis measurements, shown in Figure 4.23, and SEM investigation indicated that, α_{GRB} distribution becomes more homogenous with increasing aging time. However, the amount of transformed grain boundary

area is a function of aging temperature and tends to decrease with increasing aging temperature. For example, while the entire grain boundary area in TIMETAL LCB transforms into α phase when aged at 700°C at equilibrium, only 68.34%±4.32 of the entire grain boundary area transforms into alpha phase at 745°C. As a result, grain boundary alpha particles are distributed in-homogenously within the equilibrium microstructure at higher aging temperatures. The EBSD investigation presented in the following pages aims to bring an understanding to the effect of aging temperature on the transformation of the prior β grain boundaries by comparing the structure of transformed and un-transformed boundaries in specimens aged at different temperatures for long aging times.

A high magnification micrograph of a triple point junction at the intersection of three grains β_1, β_2 and β_3, in a specimen aged at 745°C for 22 h, is shown in Figure 4.28. The boundaries between β_1 and β_2 ($GB_{1\rightarrow2}$) and β_1 and β_3($GB_{1\rightarrow3}$) have a relatively flat structure. A single alpha precipitate can be identified on $GB_{1\rightarrow3}$, however the remaining grain boundary area appears to be precipitate free and α_{GRB} precipitation is not observed on $GB_{1\rightarrow2}$. SEM examination has aided in associating, $GB_{2\rightarrow3}$ to perturbations in the form of a hill and valley structure and two thick α phase particles is found to grow into the β_3 grain from the tips of these perturbations. Upon examining the pole figures of the β_1, β_2 and β_3 grains it was found that, β_1 and β_2 grains share a common (410) direction, marked with X in Figures 4.31a and b. A rotation of about 10 degrees is

sufficient to bring β_1 into exact coincidence with β_2 and it was concluded that $GB_{1\rightarrow2}$ is a low angle boundary. Similarly, examining the pole figures of β_1 and β_3 grains showed that $GB_{1\rightarrow3}$ is a low angle grain boundary where a 9.76 degrees rotation about the common $(\bar{1}\bar{1}2)$axis (marked with Y in Figures 4.29 a and c) brings β_1 into coincidence with β_3. After examining the β_2 and β_3 pole figures, $GB_{2\rightarrow3}$ was found to be a high angle boundary whose angle/axis pair is $(21\bar{1})$ /28.74^o, marked with Z in Figures 4.29 b and c. Grain boundary misorientation across six other precipitate free grain boundaries in a TIMETAL LCB specimen aged at 745^{o}C for 22 hours was measured through EBSD and it was found that low angle boundaries are not preferred precipitation sites at low undercoolings. However, increasing undercooling promotes α phase precipitation on low angle boundaries. For example, Figure 4.29 shows grain boundary precipitate formation on a low angle grain boundary (θ=6.92) in a TIMETAL LCB sample aged at 700^{o}C for 200 minutes, shown in Figure 4.30. After examining the β_1 and β_2 pole figures, a common $\{0\bar{2}\bar{1}\}$ was found and marked with X on their corresponding pole figures (Figures 4.31 a and b).

4.4.1.3. Plate-Like Alpha Precipitation

The β phase decomposes into plate-like α precipitates with increasing aging time. These alpha plates initially start growing from grain boundary regions and are referred as widmenstätten side plates, α_{wSP}. Examination of grain

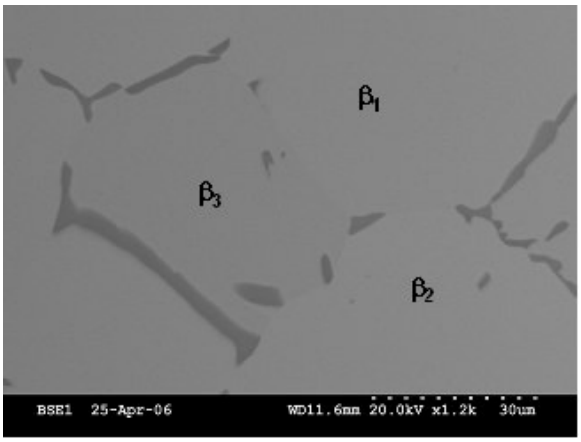

Figure 4.28. BSEI micrograph showing a triple point junction at the intersection of grains β_1, β_2 and β_3.

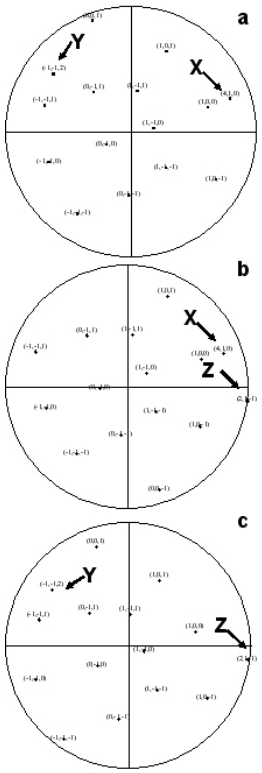

Figure 4.29. The pole figures of a) β_1 b) β_2 and c) β_3 grains. Common axes between grains are indicated by arrows.

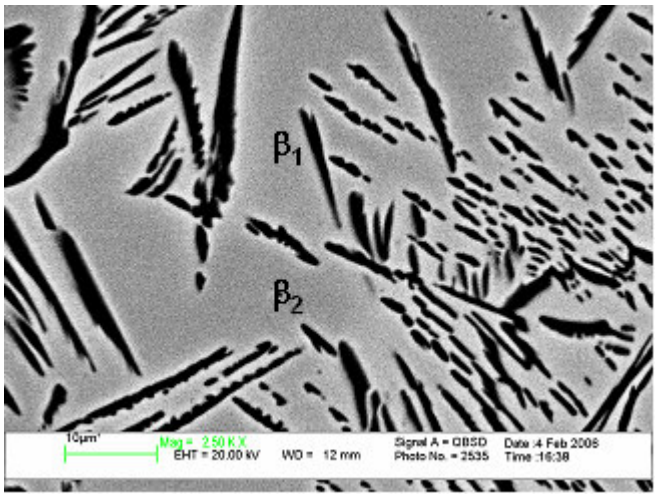

Figure 4.30 BSEI micrograph illustrating alpha phase precipitation on a low angle boundary between β_1 and β_2 grains.

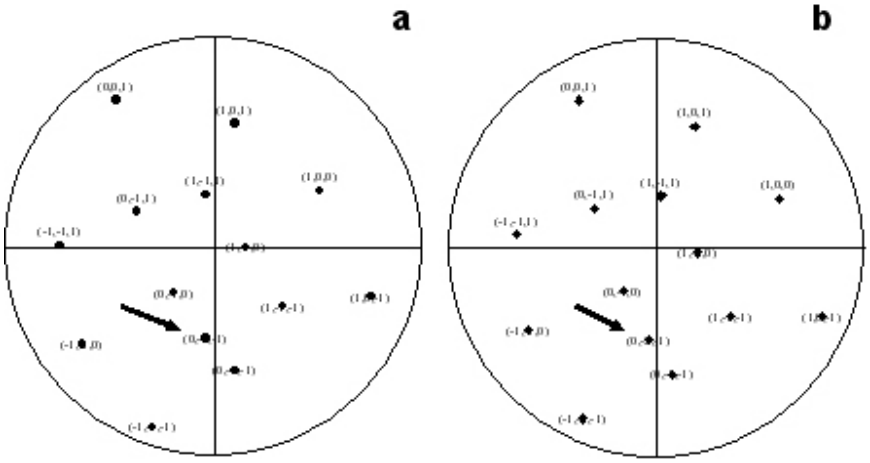

Figure 4.31. The pole figures of a) β_1 and c) β_3 grains. Common $\{0\bar{2}\bar{1}\}$ axis between these grains is indicated by an arrow.

boundary regions with high magnification FE-SEM microscopy has shown that the α_{WSP} morphology grows directly from the grain boundary α precipitates. For

example, Figure 4.32a shows the onset of α_{wSP} growth from α_{GRB} precipitates in a specimen aged at 700^{o}C for 25 minutes.

Upon SEM examination it was found that, α_{WSP} precipitates grow exclusively from grain boundary precipitates located on faceted boundaries. It appears that, the faceted nature of the grain boundary can be linked to the formation of a group morphology where several side plates evolve from the same grain boundary and align parallel to a crystallographic direction (Figure 4.33b). Typically, α_{WSP} were located on only one side of a grain boundary as demonstrated in Figure 4.33a. However, in a few rare instances, α_{WSP} growth on both sides of a grain boundary was observed with increasing aging time, illustrated in Figure 4.33b.

After examining SEM micrographs of the aged specimens it was found that, in some instances, the grain boundary facets were not distributed homogenously along the entire grain boundary but localized to specific regions (Figure 4.34). As a result of the effect of facet formation on the morphological evolution of α phase, different grain boundary α morphologies grew from a single grain boundary. For example, the grain boundary, shown in Figure 4.34, can be divided into two distinct regions, defined as faceted and non-faceted regions. The upper part of the grain boundary region has a relatively smooth structure and appears to be covered by a single alpha precipitate that has developed a film like structure (marked α_1 in Figure 4.34). The lower part of the boundary has

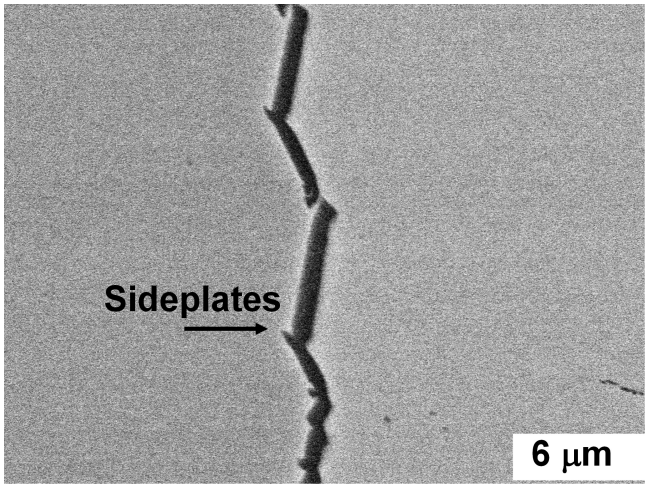

Figure 4.32. FE-SEM micrograph illustrating a) the onset of side plate growth from grain boundary alpha precipitates in TIMETAL LCB aged at 700°C for 25 minutes.

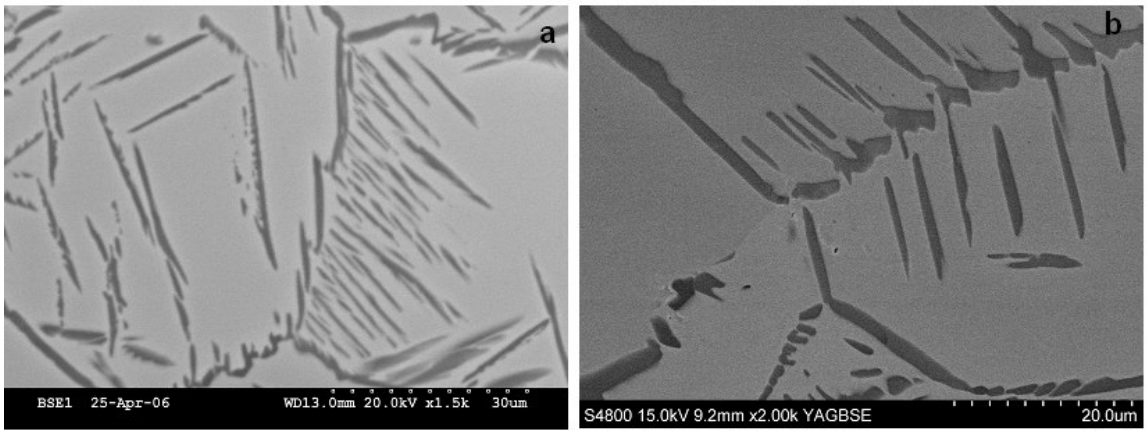

Figure 4.33. BSEI micrographs demonstrating side plate growth on a) single side b) both sides of the grain boundary in aged TIMETAL LCB.

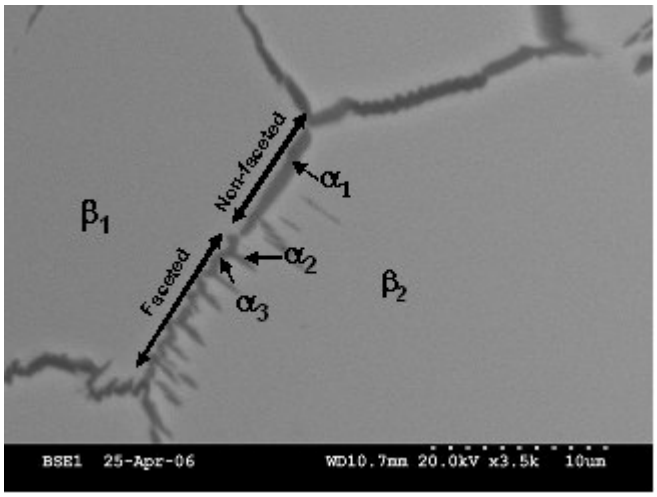

Figure 4.34. High magnification BSEI micrograph illustrating two different grain boundary alpha morphologies (α_1 and α_2) precipitating on a grain boundary between β_1 and β_2 in TIMETAL LCB aged at 700°C for 30 minutes.

dissociated into facets and single α_{GRB} particles have formed on each facet (marked as α_2). Further, α_{WSP} originated solely from the α_{GRB} that has formed on the faceted region of the boundary and grew into the β_2 grain (marked as α_3). The orientations of the α_{GRB} precipitates, α_{WSP} and adjacent β grains were determined by EBSD analysis and the crystallographic relationships between these phases were found by plotting their orientations on pole figures (Figure 4.35 a through h). By examining these pole figures it was found that, grain boundary precipitate α_1 and β_2 grain are related to each other through Burgers OR. The parallel planes and directions of the Burgers OR are indicated by X and Y on their corresponding pole figures. On the other hand, α_2 precipitates appear maintain a Burger's OR with the β_2 grain (marked as U and V). Through further examination of the pole figures, it was found that, grain boundary precipitate α_2 and α_3 plates

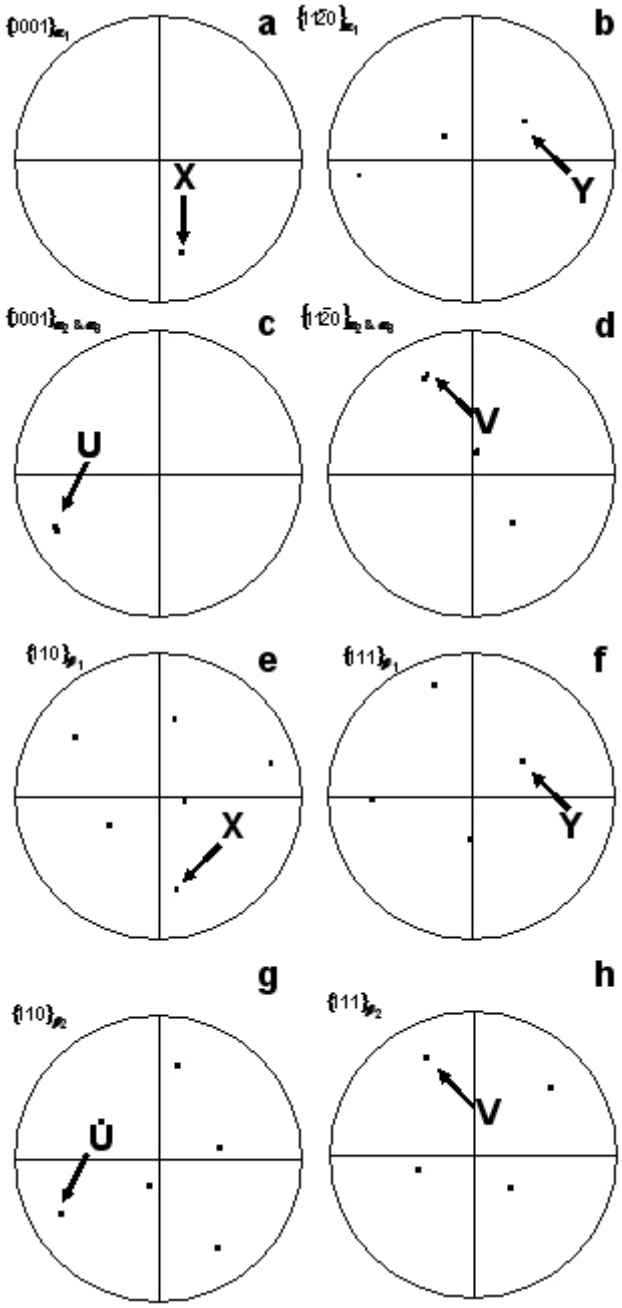

Figure 4.35. Results of the EBSD analysis. a) {0001} b) $\{11\bar{2}0\}$ pole figures α_1 precipitates. Superimposed c) {0001} d) $\{11\bar{2}0\}$ pole figures α_2 and α_3 precipitates.. e) {110} and f) {111} pole figures of the β1 grain. g) {110} and h) {111} pole figures of the β_2 grain.

originating from α_2 precipitate are similarly oriented. As a result, there is a Burgers OR between the α_3 plates and the β_2 and α_3 plates grow into this grain, with which they are crystallographically related.

The advancement of side plates were limited to only a few microns at temperatures less than 730^{o}C. This observation was attributed precipitation of alpha precipitates within the matrix. These alpha plates, which precipitate homogenously inside the β grains, are called widmenstätten intragranular plates (α_{WIG}) and they are the final morphology to form during $\beta \rightarrow \beta+\alpha$ transformation. Upon examining the high magnification SEM micrographs of the aged specimens, it was found that α_{WIG} particles tend to precipitate in front of the growing α_{WSP} and inhibit α_{WSP} growth (Figure 4.36).An α_{WIG} precipitate that has inhibited the lengthening of α_{wSP} precipitates is marked as X in Figure 4.36b. In the same figure, an α_{wSP} precipitate (marked as Y in Figure 4.36) was identified to advance further into the β matrix when compared to the remaining α_{wSP} colony that have formed on the same grain boundary. The enhanced lengthening of this particular α_{wSP} precipitate was correlated to the absence of α_{WIG} particles in front of the advancing α_{WSP}/β interface.

At a fixed transformation time, the extent of plate like alpha formation is a function of aging temperature. Figures 4.37 a through d are BSEI micrographs illustrating the effect of aging temperature on the evolution of plate-like α precipitates. All the specimens presented in these figures were aged for comparable amounts of times (i.e. between 40 and 50 minutes). At 50 minutes,

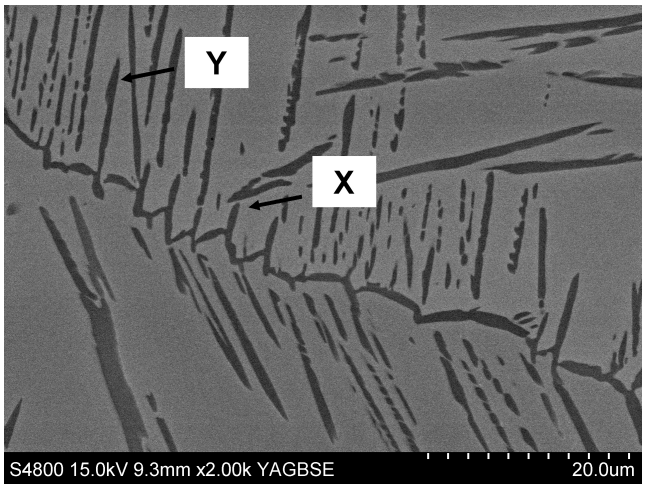

Figure 4.36. FE-SEM micrograph illustrating oriented side plate growth into β matrix in TIMETAL LCB aged at 700°C for 200 minutes.

evidence of plate like alpha precipitates could not be found upon examining the BSEI micrographs of the specimen aged at 745°C and it was concluded that the nucleation sites are limited solely to grain boundaries at this stage. Plate-like α formation was observed after decreasing the aging temperature to 730°C with the precipitation sites being limited to grain boundary regions. At 700°C and 715°C, side plate formation was more pronounced when compared to 730°C. The variation in the side plate volume fraction as a function of aging temperature was quantified at 40 minutes by systematic point counting and shown in Figure 4.38. The average volume fraction value given at 745°C was obtained at 60 minutes and is presented for solely comparison purposes. The systematic point counting has helped to demonstrate that, α_{SP} volume fraction is a function of aging temperature and decreases with increasing aging temperature.

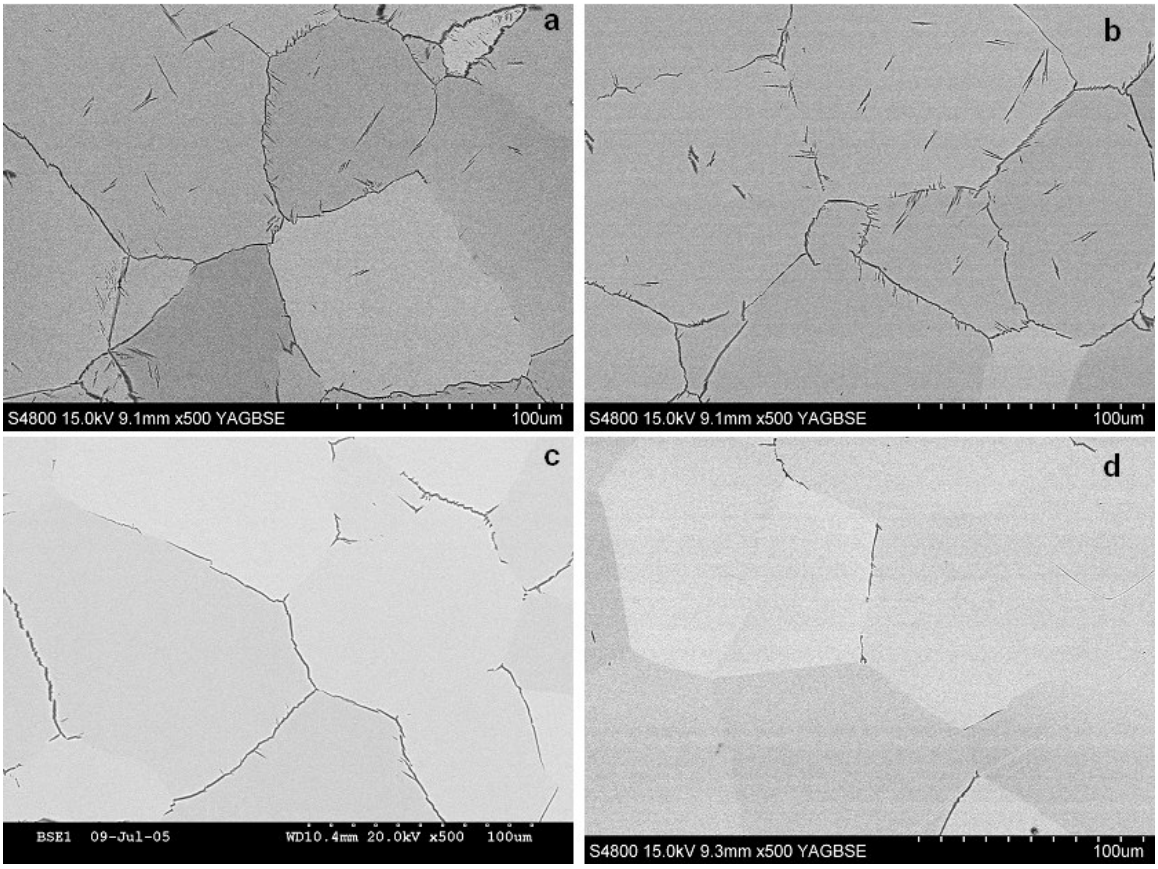

Figure 4.37 Evolution of alpha precipitates in TIMETAL LCB specimens aged at a) 700°C for 40 min. b)715°C for 50 min c)730°C for 40 min d)745°C for 50 min.

Additionally, decreasing aging temperature to 715°C at 40 minutes introduced new nucleation sites promoting intragranular alpha, α_{WI}, formation within the β matrix grains. Increasing amounts of α_{SP} and α_{WI} with decreasing aging temperature, at a fixed aging time, indicates that the kinetics of α_{wSP} and α_{WI} formation depends markedly on aging temperature and the isothermal aging times required for the plates to grow into detectable sizes increases with decreasing under cooling.

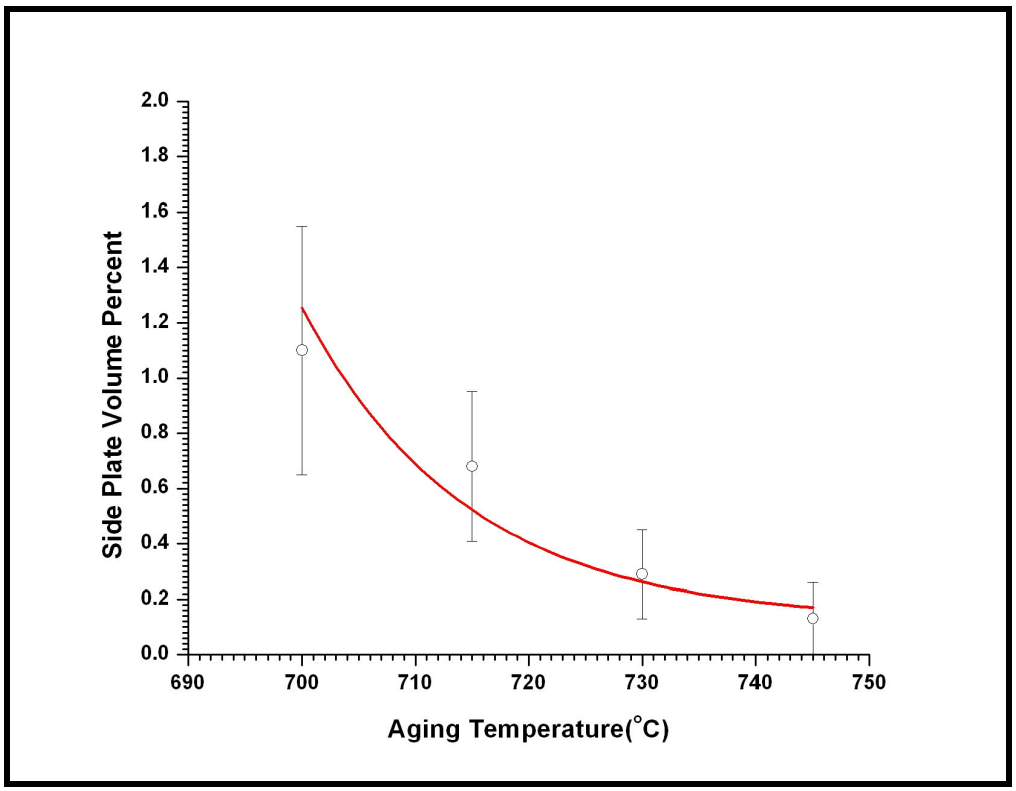

Figure 4.38. Influence of aging temperature on the side plate volume fraction at 40 minutes. The data point presented at 745°C correspond to 60 minutes aging.

4.4.1.4. Global Phase Transformation Kinetics

The overall variation in the alpha phase volume fraction at successively increasing aging times have been quantified by systematic point counting and is shown in Figures 4.39 a though b, as well as typical BSEI micrographs corresponding to different transformation stages. The SEM observations and the results of quantitative image analysis measurements can be summarized as follows:

1) β phase decomposes into three different alpha phase morphologies when aged within the temperature range of 700-745°C.

2) The sequence of morphological evolution of alpha phase can be described in the following manner:

- Independent of the aging temperature, the alpha phase forms heterogeneously on the β grain boundaries (α_{GRB}).
- Widmenstätten side plates (α_{WSP}) appear along the α_{GRB} and grow into the β matrix grains.
- Intragranular alpha plates (α_{WI}) are produced during isothermal aging of TIMETAL LCB.

As a result of these events the α phase volume fraction increases continuously with increasing aging time and reaches an equilibrium state at relatively long aging times. Equilibrium defines the state during which volume fractions of α and β phases are insensitive to variations in aging time. The influence of temperature on the equilibrium volume fraction of α phase was determined through systematic point counting (Figure 4.40). Upon examining the volume fraction data it was found that, at 700^{o}C, the equilibrium volume fraction of α phase is approximately 20% and continuously decreases with increasing aging temperature. These observations are in agreement with previous studies on metastable β titanium alloys [1].

A series of back scattered electron micrographs, demonstrating the equilibrium microstructures of TIMETAL LCB specimens aged at various temperatures, imply that equilibrium microstructure at any given temperature is a result of contribution from various transformation products, consisting of grain

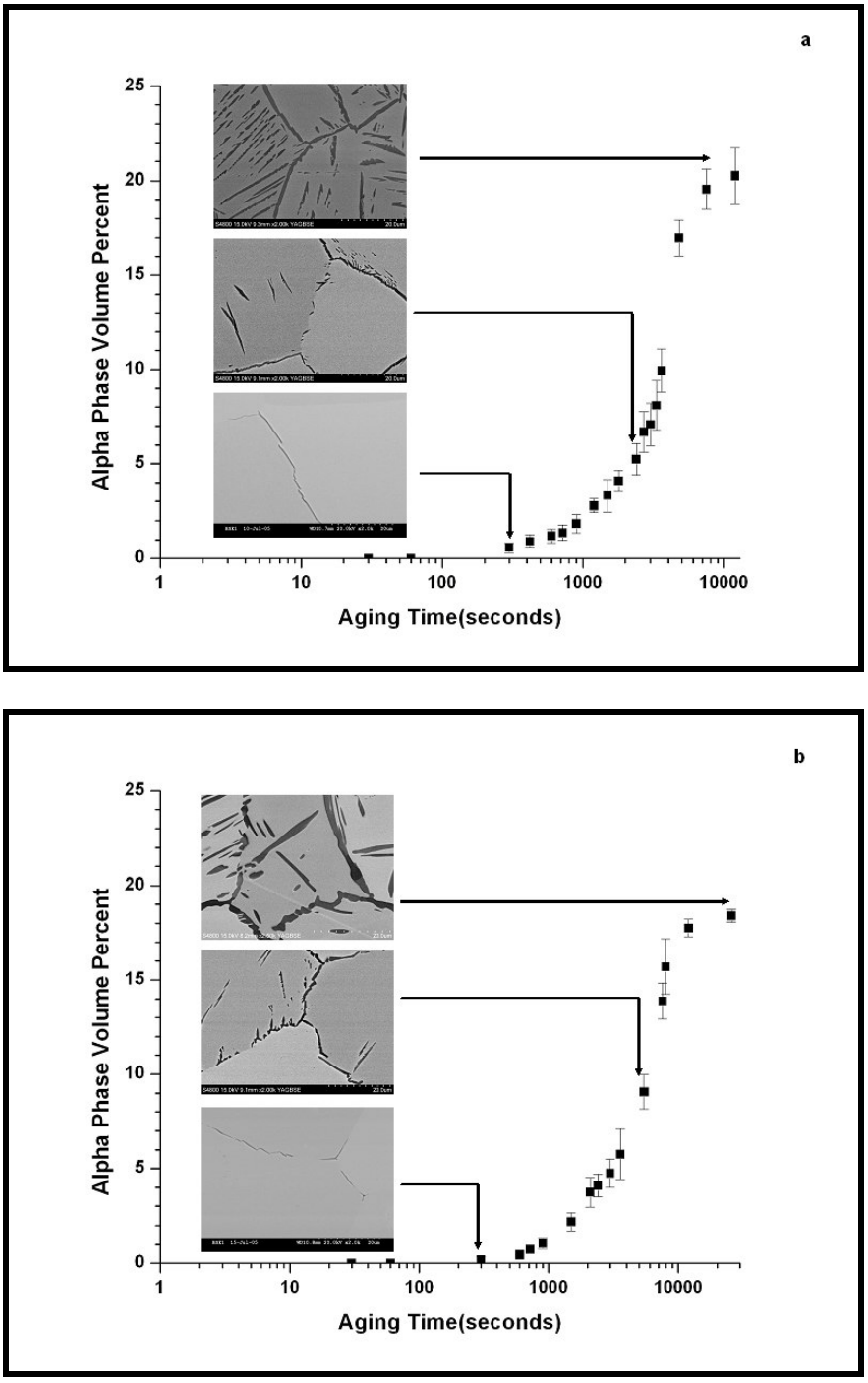

Figure 4.39 Variation in the volume fraction of α phase with aging time and corresponding BSEI micrographs at a) 700^{o}C b)715^{o}C c)730^{o}C and d)745^{o}C.

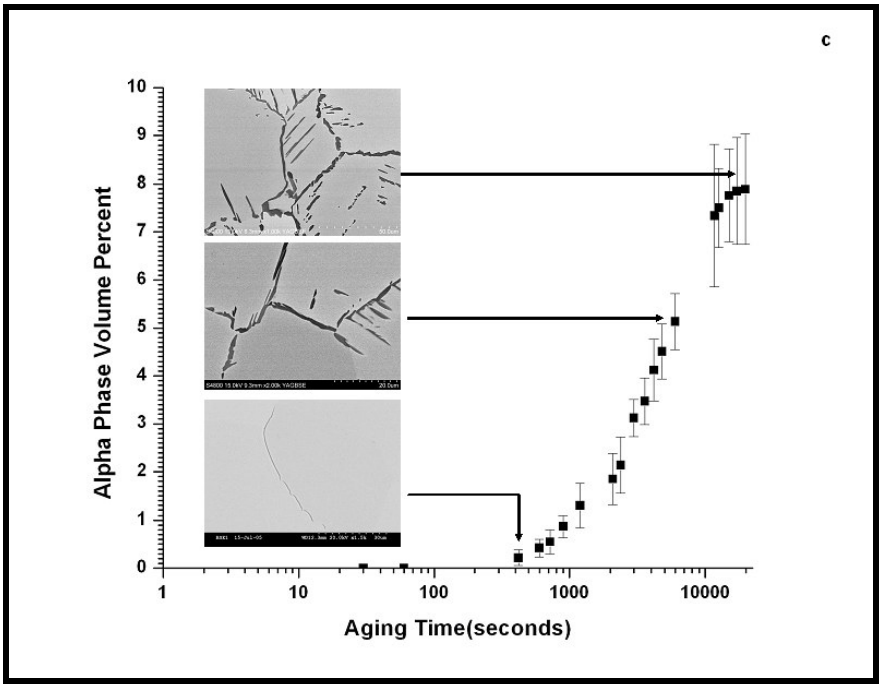

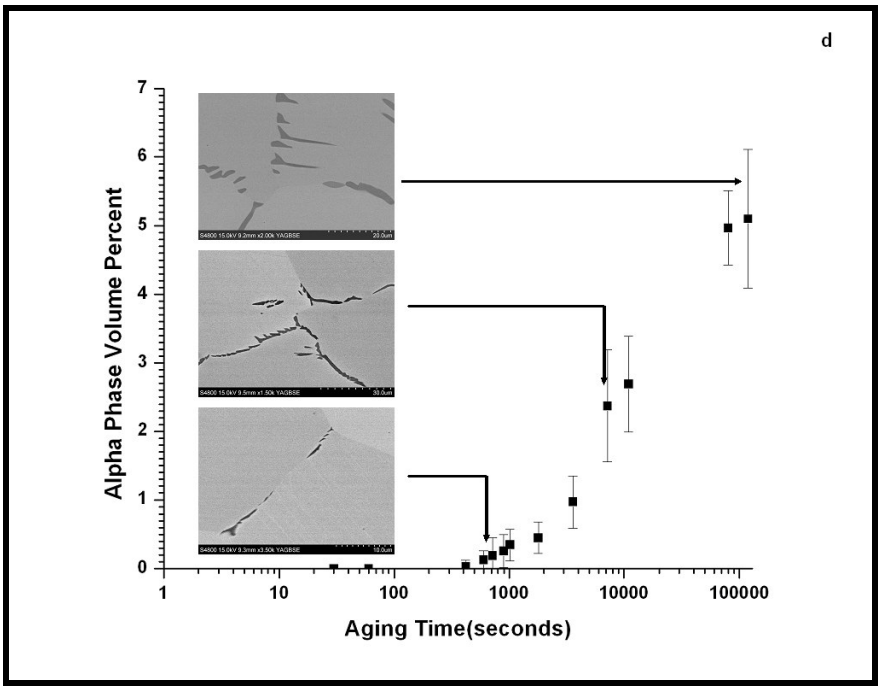

Figure 4.39 Continued.

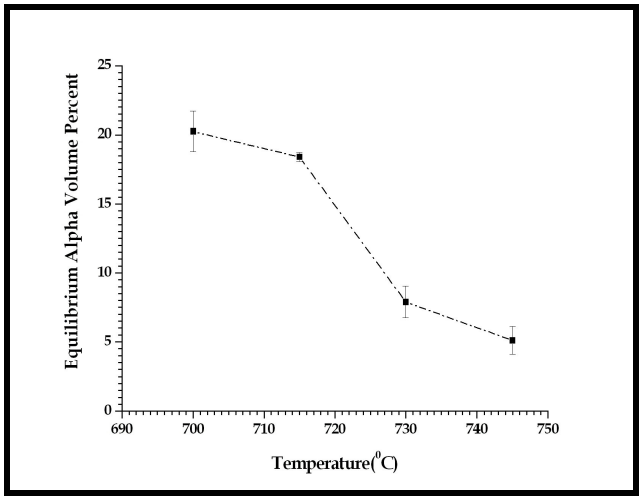

Figure 4.40. Equilibrium volume percent of α phase as a function of aging temperature.

boundary alpha (α_{GB}), side plates (α_{SP}) and intragranular alpha plates(α_{IG}). (Figures 4.41 a through d).As a result, the equilibrium α phase volume fraction $V_T^{\alpha,eqm}$ is the sum of volume fractions of each these transformation products present within the microstructure and can be expressed as:

$$V_T^{\alpha,eqm} = V_{GRB}^{\alpha,eqm} + V_{SP}^{\alpha,eqm} + V_{IG}^{\alpha,eqm} \qquad 4.3$$

where $V_{GRB}^{\alpha,eqm}$, $V_{SP}^{\alpha,eqm}$ and $V_{IG}^{\alpha,eqm}$ are the equilibrium volume fractions of grain boundary alpha, side plates and intragranular alpha plates, respectively. The volume fraction of these transformation products as a function of aging temperature were measured by systematic point counting and shown in Figure 4.42a-c. The immediate observations that can be withdrawn from these

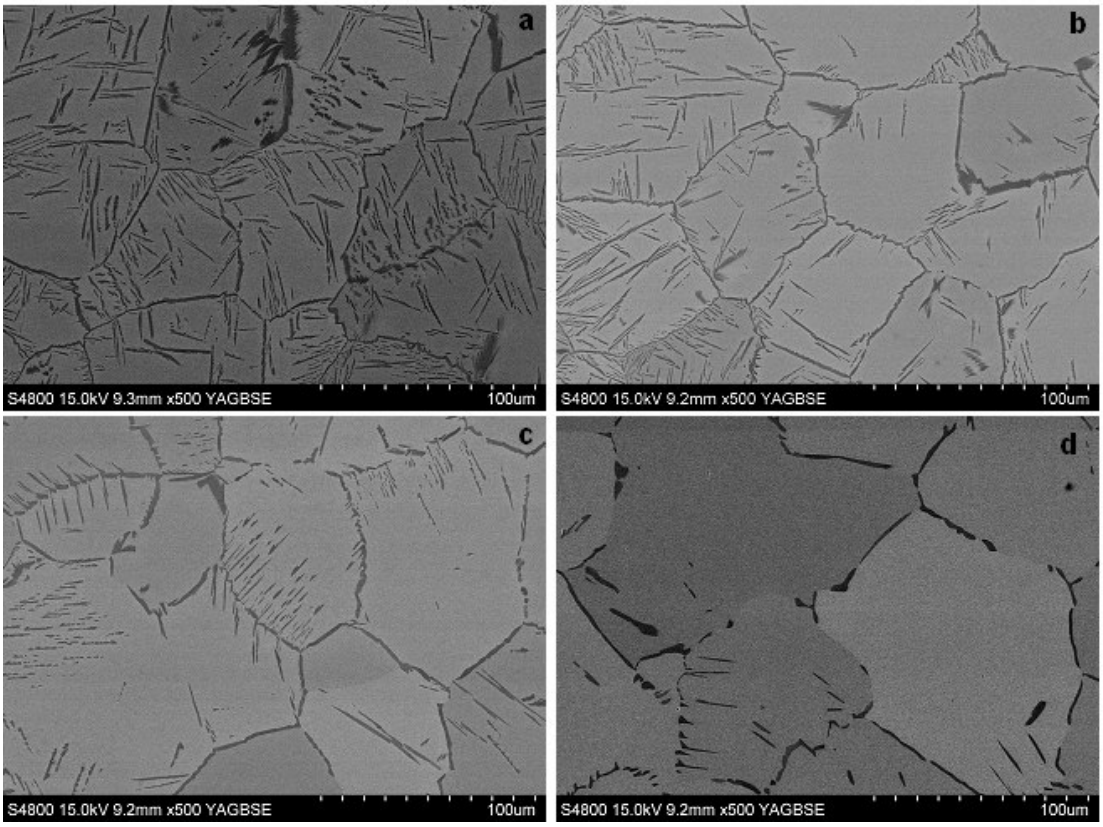

Figure 4.41. Equilibrium microstructures of TIMETAL LCB samples aged a) 700°C b)715°C c) 730°C and d)745°C.

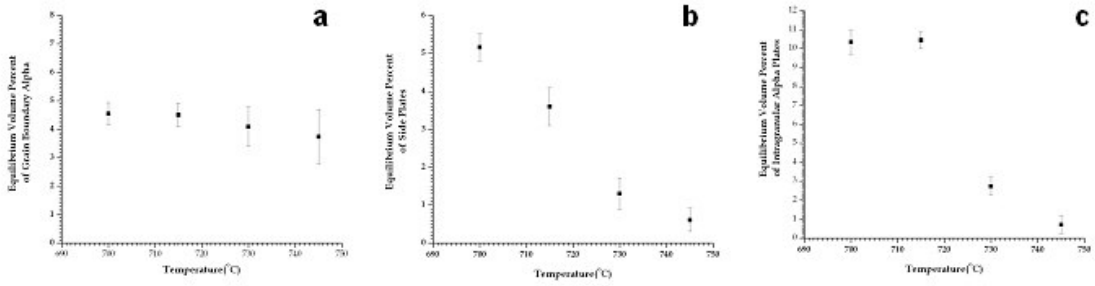

Figure 4.42. Equilibrium volume percent of a)Grain boundary α b) Side plates c) Intragranular α plate.

measurements are: 1) Grain boundary alpha volume fraction is relatively insensitive to variations in the aging temperature. 2) Side plate as well as the intragranular alpha volume fractions are functions of aging temperature, amount of both morphologies decreasing with increasing temperature.

4.4.2. Discussion of the Phase Transformation Kinetics

This investigation has shown that, microstructures that developed during the isothermal β→β+α transformation in TIMETAL LCB are sensitive to both transformation temperature and time. Furthermore, TIMETAL LCB follows the general trends of morphological classification system suggested by Dube [26] and extended by Aaronson [27] and the various shapes of alpha crystals develop in TIMETAL LCB during aging can be classified into a few distinctive and well defined morphologies.as:

- ***Grain boundary allotriomorphs***: Crystals which nucleate at grain boundaries in the matrix phase and grow more or less preferentially along these boundaries.
- ***Widmenstätten side plates***: These plates originate from alpha precipitates on the β/β grain boundaries and grow along well defined matrix planes.
- ***Intragranular Widmenstätten Plates***: These plates form within the matrix grains

Prior to precipitation, an incubation period was observed suggesting the presence of an activation energy barrier which is characteristic to diffusional phase transformations [28]. Upon exceeding this critical incubation period the first transformation product to occur, over the temperature range 700-745^{o}C, is α_{GRB}. Examination of the SEM micrographs of aged specimens have helped to demonstrate that, grain boundary precipitation does not occur simultaneously on

all boundaries upon quenching the sample to aging temperature and precipitation along 'select' boundaries occur earlier during the transformation. High angle boundaries were preferred over low angle boundaries during the early stages of the isothermal $\beta \rightarrow \beta+\alpha$ transformation, as well as at small undercoolings (T_{ST}-T), even at extended aging times.

These observation can be can be understood by considering the effect of grain boundary energy on the grain boundary nucleation rate [45].

Consider two hypothetical microstructures of similar grain sizes for this purpose. The first system consists of solely high angle grain boundaries and low angle grain boundaries are the only heterogeneous nucleation sites available with in the second system. Further, the energies of all the grain boundaries within a given system are assumed to be the same. Both systems are isothermally heat treated at a temperature such that phase transformations take place solely on the grain boundaries are, i.e transformation temperature is slightly below the T_{β}.

Next the classical form of Johnson-Mehl-Avrami equation [29-32] will be applied to bring an understanding the varying transformation kinetics on high angle and low angle grain boundaries. According to the JMA equation, the time corresponding to the start of transformations (f=0.01), irrespective of the grain boundary misorientation can be given as:

$$t_{0.01} = \frac{0.01}{k^{1/n}} \qquad 4.4$$

The values of rate and Avrami constants can be found from a plot of $\ln\ln(\frac{1}{1-f})$ versus $\ln$ time, where the intersection of this curve with the time axis gives the logarithm of rate constant, k and the slope corresponds to the Avrami constant, n. In general, n depends on the growth geometry and changes when this geometry alters. The value of k, however, is a function of both nucleation ($\dot{N}$) and growth ($\dot{G}$) rates [46].

At temperatures close to T_β, the nucleation rate is expected to be very slow, however very high growth rates can be expected if long range diffusion processes control the growth of alpha particles. As a result, the rate of transformation is controlled by the nucleation rate, *i.e.* the slower mechanism.

Re-writing equation 2.35. and assuming similar ϖ, ΔG_m, and C_{het} values at a given transformation temperature and grain size, the ratio of nucleation rate on the low angle boundaries to that on the high angle boundaries can be given as:

$$\frac{\dot{N}_{het}^{HAGB}}{\dot{N}_{het}^{LAGB}} \cong \exp\left(\frac{\Delta G^*_{LAGB} - \Delta G^*_{HAGB}}{kT}\right) \qquad 4.5$$

where ΔG^*_{LAGB} and ΔG^*_{HAGB} are the free energies of formation for the critical nuclei on low angle and high angle grain boundaries, respectively. It should be noted that, assuming similar concentration of nucleation sites for high and low angle boundaries is not a realistic approach, however, since the activation

energy is an exponential term in Equation 4.7, it is expected to have a more pronounced effect on the nucleation rate than the increase in the number of nucleation sites with varying grain boundary structure. Assuming a coherent interface structure for critical nuclei on both boundary types the ratio $\Delta G^*_{LAGB} \big/ \Delta G^*_{HAGB}$ may be expressed as:

$$\Delta G^*_{LAGB} \big/ \Delta G^*_{HAGB} \propto \frac{(2+\cos\theta_{LAGB})(1-\cos\theta_{LAGB})^2}{(2+\cos\theta_{HAGB})(1-\cos\theta_{HAGB})^2} \qquad 4.6$$

where $\cos\theta_{LAGB}$ and $\cos\theta_{HAGB}$ are contact angle between the precipitate and the low angle and high angle grain boundary, respectively. $\cos\theta$ depends on the energy of the boundary as well as on the orientation of the precipitate with respect to the adjoining grains. This will increase as the energy of the boundary decreases[45]. As ΔG^*_{LAGB} becomes larger than ΔG^*_{HAGB}, the exponential term in Equation 4.7 will be a large number and nucleation rate on high angle boundaries will be higher than on low angle boundaries. Since the rate constant of the JMA equation is directly proportional to the nucleation rate, decreasing nucleation rate will shift the nose of the start curve of the TTT diagram will towards longer times, for a microstructure consisting of low angle boundaries compared to one with high angle boundaries (Figure 4.43a).

As shown through EBSD analysis, transformation rate on low angle grain boundaries is also a function of aging temperature. At equilibrium, the un-

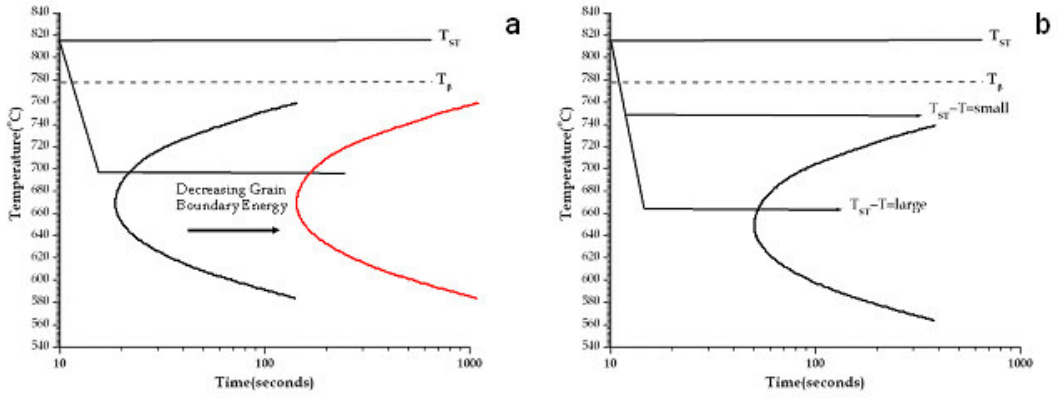

Figure 4.43 Effect of a) Grain boundary energy b) undercooling on α phase precipitation.

transformed grain boundary area at lower undercoolings was associated with low angle boundaries, whereas low angle boundaries successfully completed their at higher undercoolings. Slower transformation rates on low angle boundaries at higher aging temperatures can be understood by considering the effect of undercooling on the free energy of formation of the critical nucleus. Re-calling equation 3.23 gives:

$$\Delta G^{*} = \frac{16\pi\gamma_{\alpha\beta}^{3}}{3\Delta G_{V}}\left[\frac{1}{2}(2+\cos\theta)(1-\cos\theta)^{2}\right] \qquad 3.23$$

Since ΔG_V is directly proportional to the undercooling, the activation energy barrier to nucleation increases with increasing aging temperature. A hypothetical TTT diagram for a material consisting of only low angle boundaries is presented in Figure 4.43b and demonstrates that a larger undercooling will result in faster transformation kinetics.

Further, selection was made based on the orientation of two β grains with respect to each other. It was found that, the majority of the grain boundaries associated with alpha phase precipitation, tend to lie between two β grains sharing a common {110} pole. Alpha (α) precipitates forming on these boundaries have a Burgers OR with respect to one of the β grains. As a result of the common {110} direction, α precipitates maintain an orientation relationship close to the Burgers with respect to the adjacent beta grain. These observations are consisted with Furuhara et. al. who have shown that in a metastable β titanium alloy Ti-15-3 alpha precipitates tend to maintain coherency with respect to both of the matrix grains [47]. Bhattacharyya et. al.[48] suggested that an α particle will maintain good coherency in the c direction, if this particle precipitates on a boundary with a pure tilt character with the tilt axis being a common $<110>_{\beta}$ direction (Figure 4.46a). Since the interplanar spacings (d) of $\{0002\}_{\alpha}$ and $\{110\}_{\beta}$ planes are similar ($d\{0002\}_{\alpha} = 2.263\,\mathring{A}$ and $d\{110\}_{\beta} = 2.300\,\mathring{A}$) and the alpha phase has its $\{0001\}_{\alpha}$ pole parallel to the common $\{110\}_{\beta}$ pole, a good match is expected across the α/β interface. These authors also argued that good coherency may still be maintained even if the boundary deviates from pure tilt orientation (Figure 4.44 b). As a result, α/β interfacial energy ($\gamma_{\alpha\beta}$) will be reduced on both sides of the boundary and the activation energy barrier for

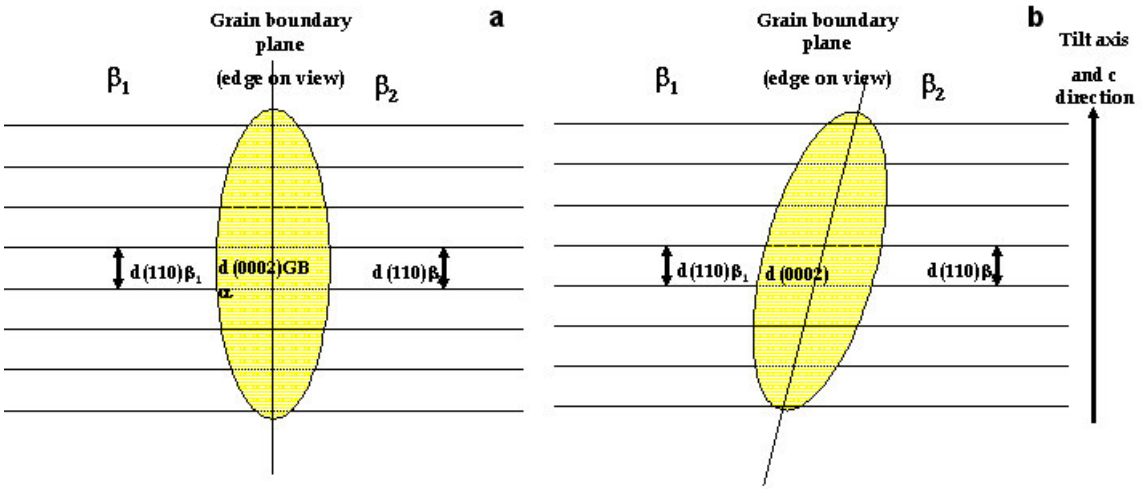

Figure 4. 44. Schematic representation of α phase precipitation on a) a pure tilt boundary b) a boundary deviating from pure tilt character [48].

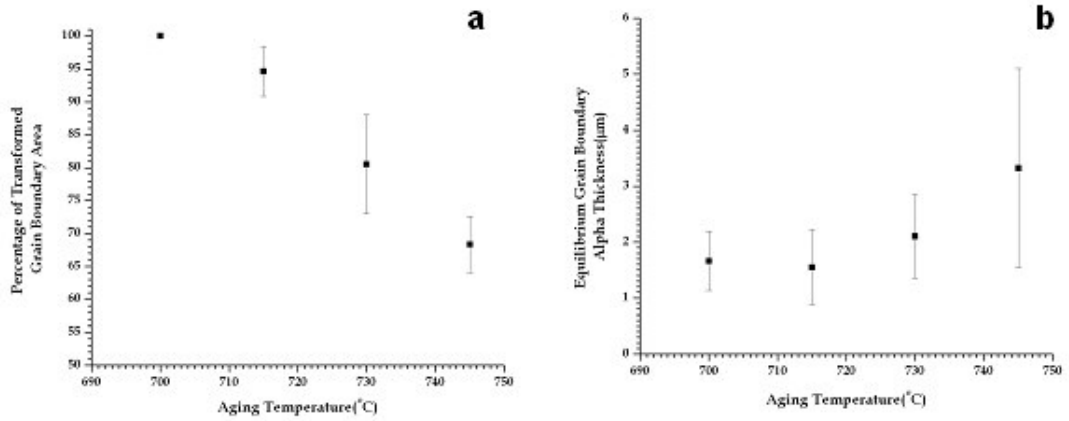

Figure 4.45. Variation in the a) percentage of transformed grain boundary area b) grain boundary alpha thickness with aging temperature.

nucleation decreases. It can be concluded that, α precipitation on boundaries favoring these conditions is promoted and the first α precipitates to form tend to destroy grain boundary area with a high $\gamma_{\beta\beta}$ while minimizing $\gamma_{\alpha\beta}$ as much as possible.

Furthermore, the volume fraction measurements have also helped to demonstrate that, equilibrium grain boundary α phase volume fraction is insensitive to variations in aging temperature. However, it was also found that both grain boundary α phase distribution and thickness are functions of temperature, Figures 4.45a and b. Distribution of grain boundary α particles was quantified as by measuring the fraction of the transformed grain boundary surface area per unit volume and it was found that, at any given transformation time, transformed grain boundary area increases with decreasing aging temperature. For example, 40% of the grain boundary area was still in an untransformed state after aging the TIMETAL LCB specimen at 745^{o}C for approximately 22 hours. As a result, grain boundary alpha phase distribution is not homogenous on the prior β grain boundaries as shown in Figure 4.46a. Even at these extended aging times, some grain boundaries exhibited a precipitate free structure, as shown with arrows in Figure 4.46a. In contrast, the entire grain boundary area have transformed after aging at 700^{o}C for approximately 3 hours as is shown in Figure 4.46b. Increasing grain boundary transformation with decreasing temperature can be associated with the rapid lengthening of α_{GRB} particles along the boundary with decreasing aging temperature. For example, Figure 4.47a and b shows transformation of three grain boundaries, first into disconnected α precipitates located on the triple point and on one of the grain

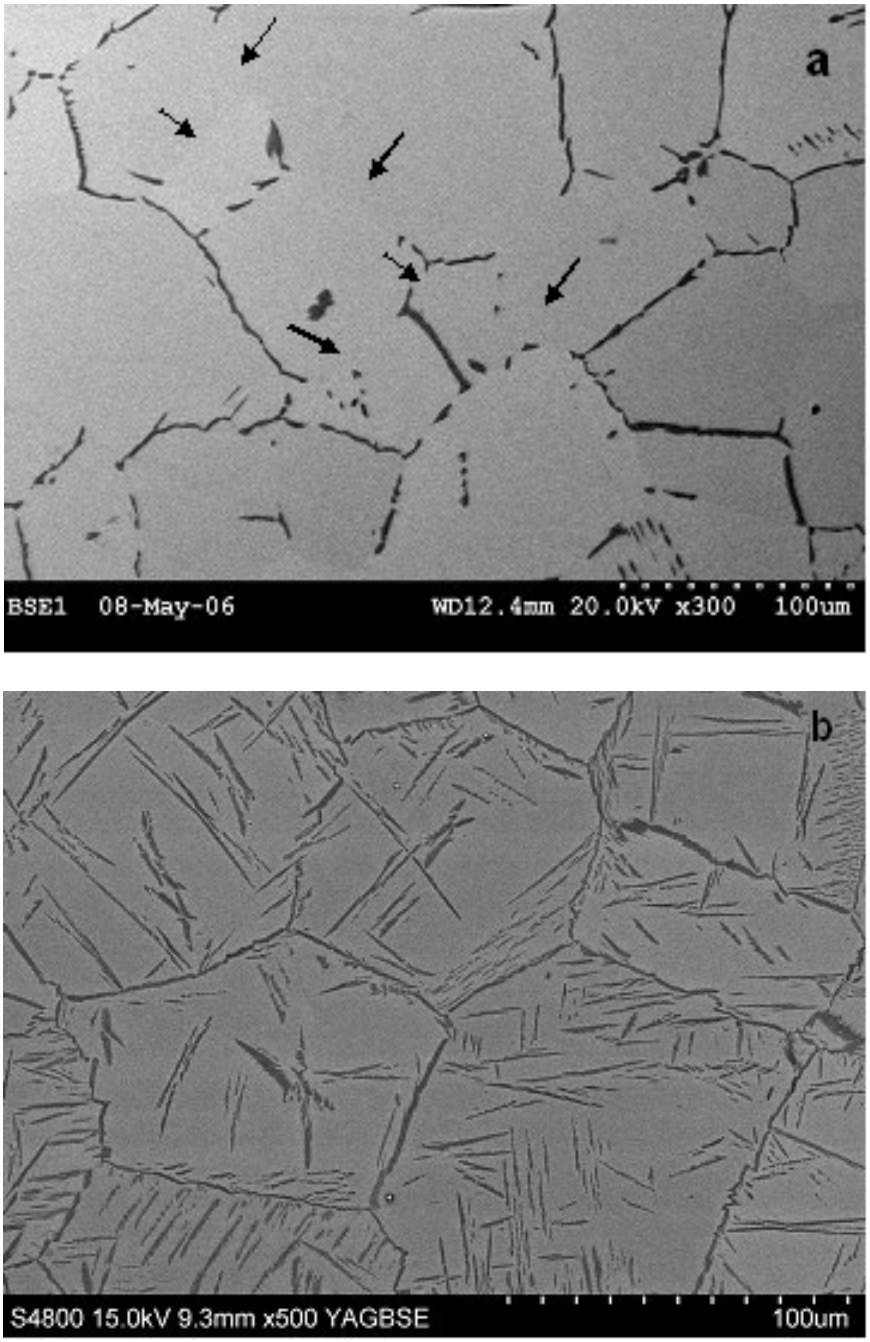

Figure 4.46.BSEI micrograph illustrating a)non uniform grain boundary α distribution in TIMETAL LCB aged at 745°C. Arrows indicate untransformed grain boundary area b) uniform grain boundary α distribution in TIMETAL LCB aged at 700°C.

boundary surfaces then, with increasing aging time, into grain boundary alpha thin film wetting the entire grain boundary area bounding the triple point junction. Investigating SEM microstructures of the specimens aged at 700^{o}C for three and ten minutes demonstrated that, upon forming on the prior β grain boundaries alpha phase precipitates rapidly grows along these boundaries and consume the untransformed grain boundary area.

The apparent thickness of the approximately one hundred grain boundary α precipitates were measured using BSEI micrographs of aged TIMETAL LCB specimens. Upon this analysis it was found that, the thickest grain boundary alpha particles were observed at the lowest undercooling and the thickness of grain boundary alpha precipitates decreased with decreasing aging temperature, Figure 4.45. As a result, the opposing effect of the aging temperature on the transformed grain boundary area and grain boundary α thickness the overall equilibrium volume fraction of grain boundary alpha phase remained insensitive to variations in aging temperature.

The second transformation product that was observed during aging TIMETAL LCB specimens was α_{WSP}. α_{WSP} precipitates emerges from grain boundary alpha precipitates located on faceted boundaries. These grain boundary facets are parts of a grain boundary that deviate from the main direction of the boundary and often lie along the low index crystal planes [49]. Figure 4.48 is a schematic representation of grain boundary structure before and after faceting.

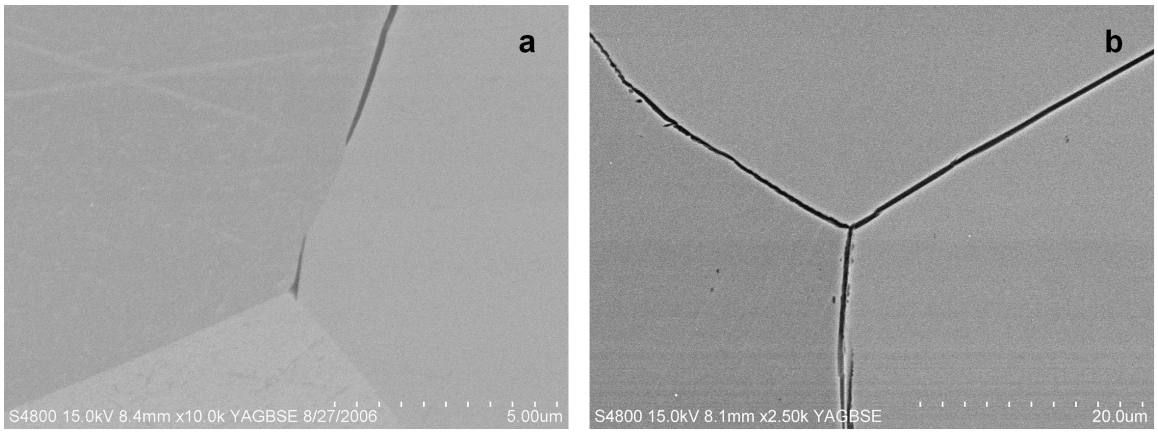

Figure 4.47. BSEI micrograph illustrating a) α phase precipitation at a triple point junction in TIMETAL LCB aged for 3 minutes b) rapid lengthening of alpha phase precipitates along the grain boundaries with increasing aging time to 10 minutes.

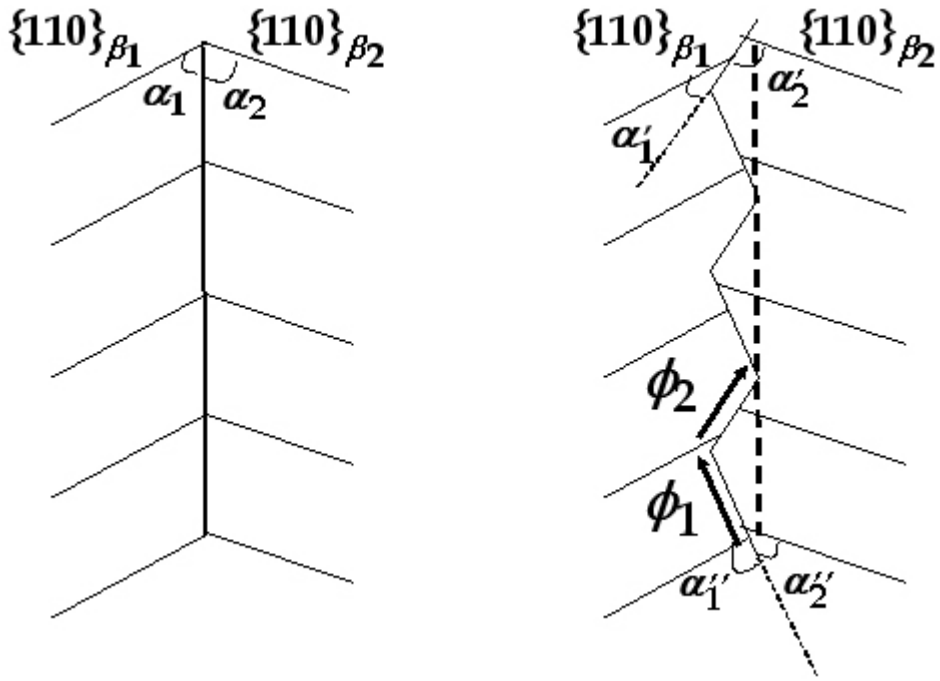

Figure 4.48 Schematic illustration of the relationship between the closed packed β planes and the grain boundary plane along a a) flat boundary b) faceted boundary.

In Figure 4.48a the original boundary structure is depicted with the $\{110\}_{\beta_1}$ and $\{110\}_{\beta_2}$ planes being inclined to the grain boundary plane at angles α_1 and α_2, respectively. Faceting introduces repetitive structural units to the grain boundary plane, with the boundary plane within each unit being parallel to two different crystallographic planes, shown as ϕ_1 and ϕ_2 where ϕ_1 lies parallel to the closed packed $\{110\}_{\beta_1}$ direction in the β_1 grain (Figure 4.48b).

Higher α_{WSP} volume percent measured at lower temperatures can be attributed to increasing $\%S_v$ of faceted boundaries with decreasing aging temperature, shown in Figure 4.49.

Segregation of impurities to the grain boundaries is one of the mechanisms that can cause faceting of grain boundaries. This phenomenon due to impurities has been reported to occur in Cu-Bi[36-41], Fe-(Sb, Te)[41] and Ni-(S, Te, Bi)[42] systems, and occurs most likely if there is a large difference between the host and impurity atoms. In a β titanium alloy, Ti-15-3, Del Prado et. al. has shown evidence of oxygen segregation to the grain boundaries [43]. Relatively large difference in the atomic radii of titanium ($r_{Ti} = 1.47\,\mathring{A}$) and oxygen ($r_{Ti} = 0.73\,\mathring{A}$) atoms imply that oxygen segregation to the grain boundaries may be one of the mechanisms controlling the faceting of β grain boundaries. The fact that faceting became more pronounced with decreasing aging temperature supports these view since the amount solution segregation to

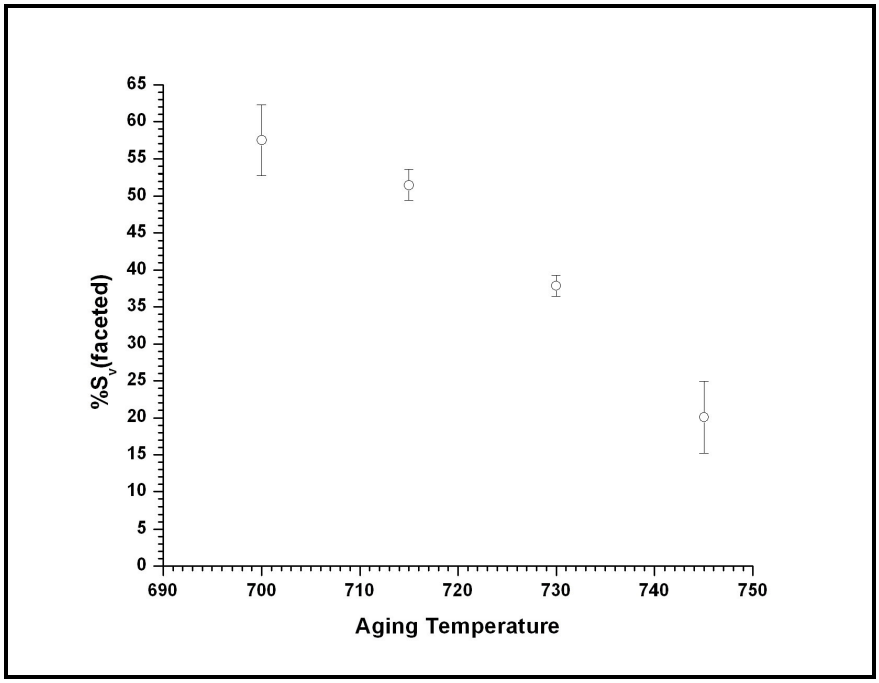

Figure4.49. Effect of aging temperature on the percentage of equilibrium faceted grain boundary area per unit volume $\%S_V(\text{faceted})$.

the grain boundaries increases with decreasing temperature and the equilibrium segregation of the solute can be described by the McLean's equation as [44]:

$$\frac{x^b}{1-x^b} = \frac{x^m}{1-x^m}\left(\frac{\Delta G}{RT}\right) \qquad 4.7.$$

Where x^b and x^m are the solute concentration at the grain boundary and in the matrix respectively and ΔG is the segregation free energy. It should also be noted that examination of approximately one hundred grain boundaries in solution treated microstructure via SEM confirmed that faceting was not present prior to aging and was induced with undercooling

Finally, α_{WI} formation, within the matrix grains was observed with increasing aging time. Upon systematic point counting, the volume fraction of these intragranular plates was found to increase with decreasing aging temperature. Intragranular plates form by homogenous nucleation, therefore, increasing amount of intragranular plates with decreasing aging temperature may be explained by considering the effect of undercooling on the driving force required for homogenous nucleation. Re-calling equation 3.23 gives:

$$\Delta G^{*} = \frac{16\pi\gamma^{3}}{3\Delta G_{V}} \qquad 3.23$$

This equation states that the activation energy required for critical nuclei formation by means of homogenous nucleation decreases with increasing ΔG_V. Since ΔG_V is directly proportional to the amount of undercooling, intragranular nucleation occurs more easily at lower temperatures.

The global transformation kinetics of titanium alloys are typically expressed by the classical form of Johhson-Mehl-Avrami (JMA) equation [29-30]. The volume fraction of second phase at any given transformation time is given as:

$$f^{\alpha} = \frac{V^{\alpha}}{V} = 1 - \exp(-kt^{n}) \qquad 4.7$$

where k and n being the rate and Avrami constants, respectively. $V^{\alpha}(t)$ is the volume fraction of alpha phase at a given reaction time and V is the equilibrium

volume fraction. Taking the natural logarithms of both sides of equation 4.7 twice gives the equation of a straight line as:

$$\ln\ln\left[\frac{1}{1-V^{\alpha}(t)}\right] = \ln k + n\ln t \qquad 4.8$$

The slope of this straight line is given by the Avrami constant, while its intercept with the y-axis is given by the rate constant.

The results of applying Equation 4.8 to the volume fraction data obtained at the aging temperatures considered in this study are plotted in Figures 4.50 a through d. It appears that transformation kinetics up to 745°C can be described by two stages which correspond to two straight lines on the plots. During the first stage, the slopes vary from 0.98 to 1.24 until the $\alpha_{GRB}+\alpha_{SP}$ transformation is completed (shown with arrows on Figure 4.30a through d) and in the second stage n values increase from 1.81to 2.19.

SEM examination has helped to verify that when α particles form on the grain boundaries they lengthen quite rapidly consuming the available nucleation sites. The elongated shape of grain boundary allotriomorphs results from the greater rate of lengthening along the boundary than the rate of thickening. Further evolution of grain boundary precipitates is seen to take place by growth of side plates into the matrix grains.

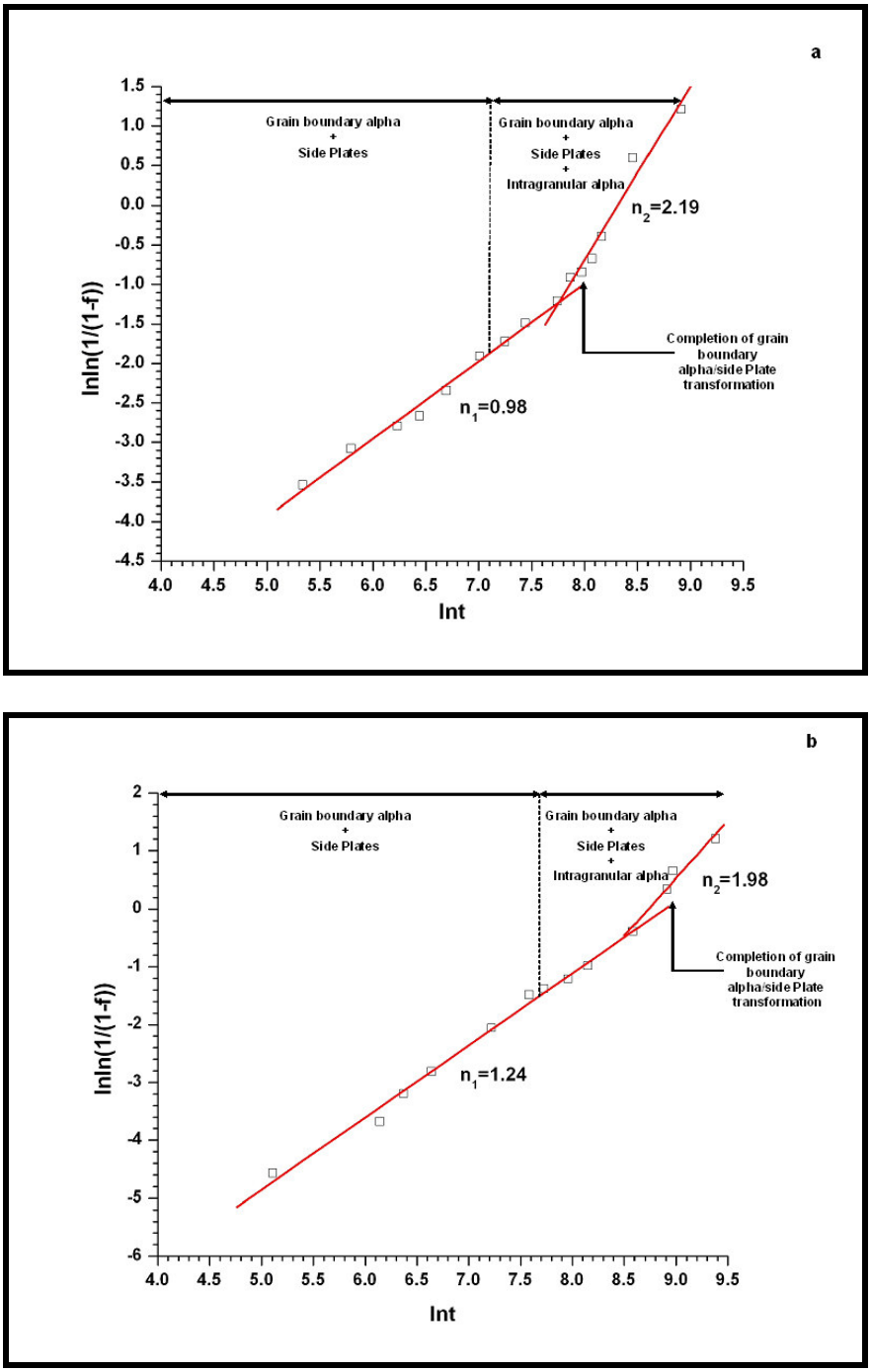

Figure 4.50. Application of JMA law to isothermal phase transformation kinetics at a)700^{o}C b)715^{o}C c)730^{o}C and d)745^{o}C.

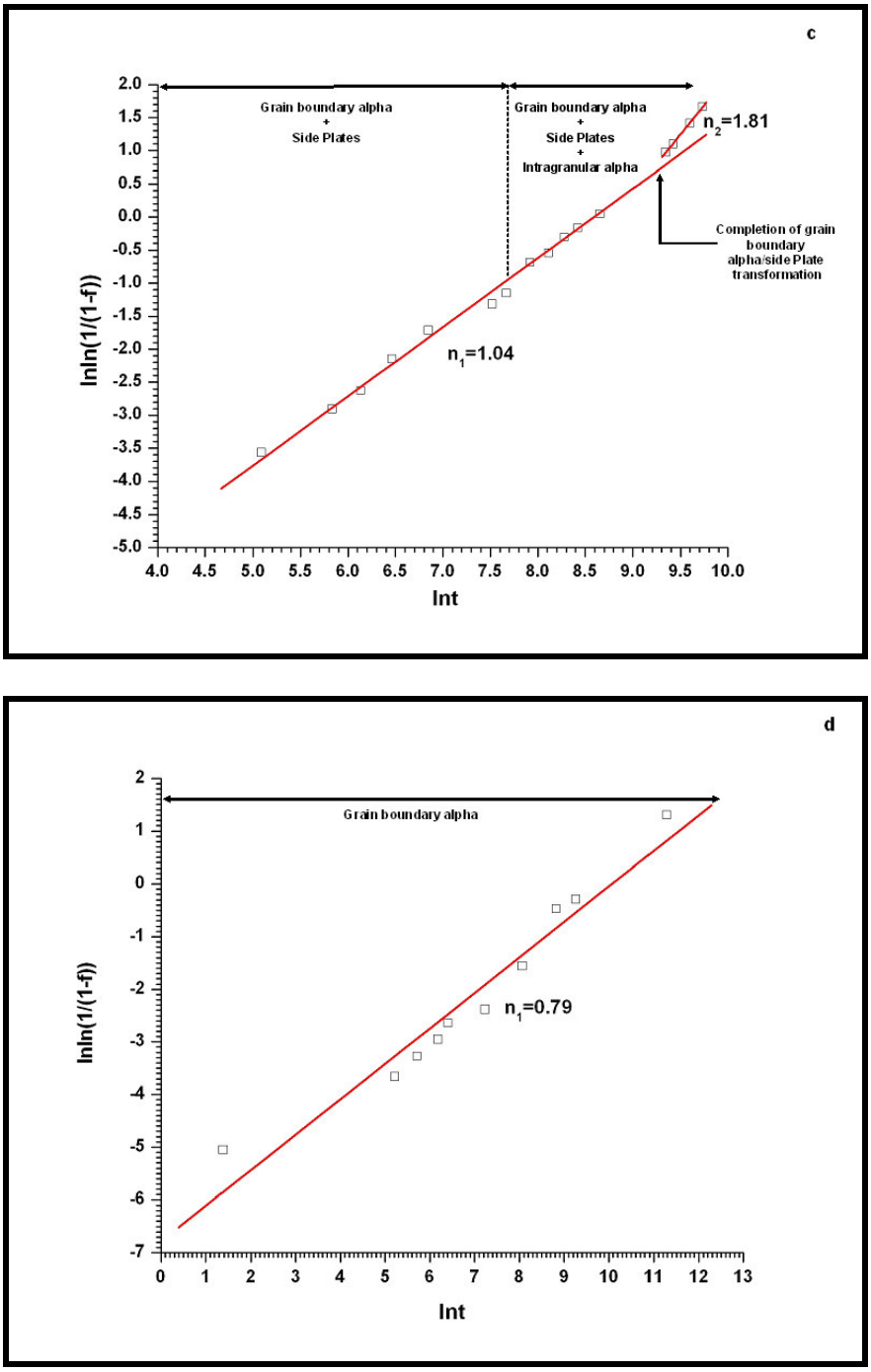

Figure 4.50. Continued.

As predicted by the theory governing the growth of second phase precipitates, both the lengthening rates of grain boundary alpha and plate-like particles are independent of reaction time [27]. This condition should result in an Avrami constant of n=1 if the transformation is controlled by early grain boundary saturation due to enhanced diffusion along the grain boundaries followed by one dimensional lengthening of the α_{SP} precipitates during the reaction.

Through volume fraction measurements it was found that, the aging time corresponding to the increase in the slope in the second stage of transformation, is related to the completion of $\alpha_{GB}+\alpha_{SP}$ transformation. As a result, the $\beta \rightarrow \beta+\alpha$ transformation in the second stage, continues by the growth of α_{WI} precipitates. As suggested by Darmkroger et. al. [33], the slopes of kinetic curves should approach n=2 if the transformation is taking place solely by two dimensional growth of intragranular plates.

At 745^{o}C a different phenomenon was observed in the JMA analysis. A single straight line was found, implying a single stage of transformation and SEM observations have shown that side plate and intragranular α formation is negligible at this stage, thus, the entire transformation can be associated with a single transformation product, i.e. grain boundary alpha. Under these conditions, experimental kinetics can be described by a single straight line with a slope of 0.79. At these high temperatures, the lattice diffusion is expected to dominate over the grain boundary diffusion [34] and the theory predicts that the thickness of plate like particles increases with the square root of time $(\text{time})^{1/2}$ [35]. As a

result of one dimensional thickening of grain boundary precipitates, through lattice diffusion the slopes of the kinetic curves should approach to 0.5. Thus value is slightly lower than the experimental value obtained in this study.

The observed phase transformation sequence, i.e. formation of α_{GRB} followed by α_{WSP} growth from α_{GRB} and finally intragranular α_{WIG} precipitation within the matrix grains, can be summarized on a Time-Temperature-Transformation (TTT) graph, shown in Figure 4.51 This graph is defined by the locus of points which represent the time to nucleate a detectable degree of transformation of different α phase morphologies at constant temperature. The incubation periods required for the precipitation of these alpha phase morphologies were determined by systematic point counting and examining the electron micrograph images of the aged TIMETAL LCB specimens and Upon comparing this graph, to that was previously reported by Azimzadeh, it was found that the TTT curve of TIMETAL LCB obtained during the present study has shifted towards shorter times which is indicative of faster transformation kinetics. A possible explanation for this discrepancy is the use of different techniques to detect the onset of α phase precipitation. In his study Azimzadeh[6]. has used X-ray diffraction and optical microscopy to detect α phase precipitation. He also noted, X-ray diffraction failed to detect α precipitation

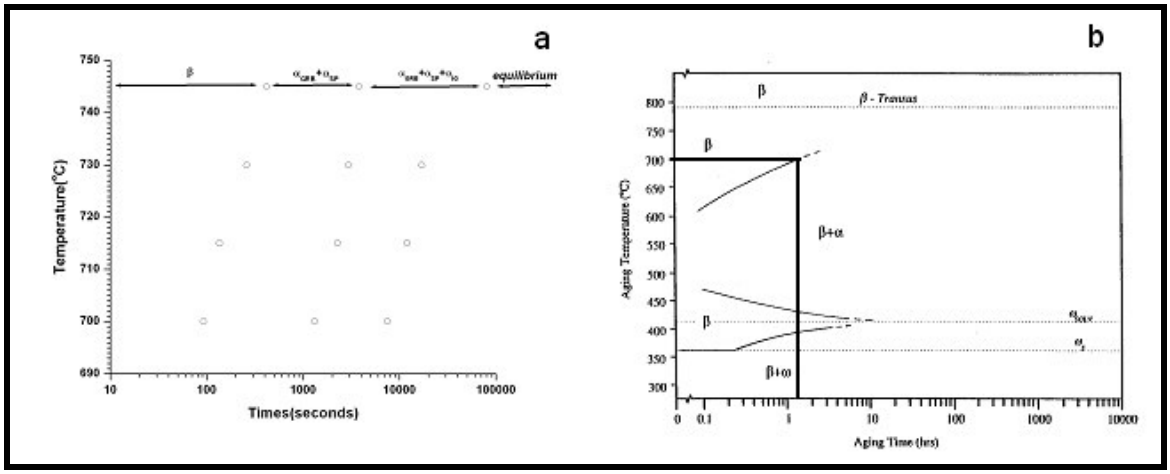

Figure 4.51 Time-Temperature-Transformation(TTT) curve of TIMETAL LCB obtained by a) Electron microscopy and image analysis b) Optical microscopy and –X-ray diffraction techniques as reported by Azimzadeh [5].

that occurred preferentially on the grain boundaries. In that study, optical microscopy was used, which has inferior resolution when compared to SEM. Comparing measurements in Figure 4.51 have shown that electron microscopy coupled with image analysis is more sensitive to small α phase precipitation amounts. As a result, α phase precipitation occurring at shorter aging times was successfully detected using the method found in this study.

4.4.3. Conclusions of the Phase Transformation Kinetics

In this investigation, the isothermal $\beta \rightarrow \beta+\alpha$ phase transformation kinetics were investigated. Upon SEM examination it was found that the metastable β phase can decompose into a variety of transformation products when aged below the β transus temperature. The sequence of transformation includes α_{GRB}, followed by α_{WSP} and finally α_{WI}

Precipitation α_{GRB} showed quantitative variations from boundary to boundary during the earlier stages of the reaction suggesting that activation energy barrier for α_{GRB} precipitation is lower along certain boundaries. It was shown through EBSD analysis that, grain boundary α precipitates tend to form initially on high energy high angle boundaries. and these boundaries tend to lie between β grains that share a common $<110>$ direction. The α precipitates are related to one of the adjacent β grains through Burger OR and show very small ($7\text{-}8^{o}$) deviation from Burgers OR with the opposite β grain As a result, the α/β interfacial energy is minimized on both side of the boundary.

Grain boundary surface area that has transformed into α phase increased with increasing aging time. At equilibrium grain boundary alpha phase volume fraction was found to be independent of aging temperature. However, distribution and thickness of grain boundary alpha phase were functions of temperature. More homogenous grain boundary alpha distribution can be obtained by decreasing aging temperature at the expense of decreasing average α_{GRB} thickness. By EBSD examination it was shown that, alpha(α) phase formation on

low angle grain boundaries does not occur at small undercoolings even at extended aging times. As a result, the amount of transformed grain boundary area of the equilibrium microstructure decreases with decreasing undercooling.

Both α_{WSP} and α_{WIG} volume fractions increased with decreasing aging temperature. SEM examination suggested that, side-plate formation is controlled by grain boundary structure, faceted boundaries promoting side plate growth.

The overall kinetics of $\beta \rightarrow \beta+\alpha$ transformation was quantified by image analysis measurements. The $\beta \rightarrow \beta+\alpha$ phase transformation kinetics was explained using the classical form of the Johnson-Mehl-Avrami (JMA) equation and different mechanisms governing progression of phase transformations were identified. The JMA analysis has aided to demonstrate that the mechanism of $\beta \rightarrow \beta+\alpha$ transformation depends on aging temperature. At lower aging temperatures, the phase transformation in TIMETAL LCB was found to be controlled by the rapid lengthening of the grain boundary α and side plates at the early stages of the transformation. Increased transformation included two dimensional growth of intragranular plates. At 745^{o}C the overall kinetics was controlled by thickening of grain boundary α precipitates.

An improved time-temperature –transformation (TTT) diagram for TIMETAL LCB was plotted, and contributions of different α morphologies on the overall phase transformation kinetics were identified.

References

1) B. Appolaire, L. Hericher, E. A. Gautier, “Modelling of phase transformation kinetics in Ti-alloys-Isothermal treatments”, Acta Materiala, 53, pp.3001-3011 (2005).

2) T. Furuhara, T. Maki and T. Makino “Microstructure control by thermomechanical processing in Ti-15-3 alloy”, Journal of Materials Processing Technology, 117, pp.318-323 (2001).

3) B. D. Cullity, “Elements of X-Ray Diffraction”, Addison Wesley Reading, MA, pp.369 (1978).

4) J. W. Martin, R. D. Doherty, B. Cantor, “Stability of Microstructure in Metallic Systems “ Cambridge Solid State Science Series, pp. 287-289 (1997).

5) F. H. Froes, J. M. Capenos and C. F. Yolton, “Decoration of Plastically Strained Regions in Metallic Systems”, Metallorgraphy, 9, pp.535-537 (1976).

6) S. Azimzadeh, “Phase Transformations in Metastable β Titanium Alloy TIMET LCB (Ti-6.8Mo-4.5Fe-1.5Al)”, Master of Science Thesis, Clemson University, Clemson, SC, December, 1995.

7) S. Toney and H. I. Aaronson, “Effects of Grain Boundary Structure on Precipitate Morphology in an Fe-1.55 Pct Si Alloy“ , Trans. metal. Soc. AIME, 221, pp.909 (1961).

8)H. I. Aaronson, in Decomposition of Austenite by Diffusional Processes, Zackay and H. I. Aaronson (eds.), Interscience, pp.387- (1962).

9) J. B. Clark, “Effects of Grain Boundary Structure on Precipitate Morphology in Al-18w/o Ag-an Application of High Temperature Electron Microscopy“ in High Temperature High Resolution Metallography, H. I. Aaronson and G. S. Ansell (eds.), Gordon and Breach, Science Publishers, New York, pp. 347-375 (1967).

10) D. Vaughan, “Grain boundary precipitation in an Al-Cu Alloy”, Acta Metall. 16, pp.563-577 (1968).

11) J. K. Park and A. J. Ardell, “Precipitation at Grain Boundaries in the Commercial Alloy Al 7075”, Acta metal., 34, pp.2399-2409 (1986)

12)P. N. T. Unwin and R. B. Nicholson, “Nucleation and Initial Stages of Growth of Grain Boundary Precipitates in Al-Zn-Mg and Al-Zn Alloys“ Acta Metall, 17., pp. 1379-1393 (1969).

13) E. P. Butler and P. R. Swann, “In-situ observation of the nucleation and initial growth of grain boundary precipitate in Al-Zn-Mg Alloys”, Acta Metall, 24, pp.343-352 (1976).

14) J. K. Park and A. J. Ardell, “Microstructures of Commercial 7075 Al Alloy in the T651 and T7 Tempers’, Metall. Trans. A, 14, pp.1957- 1965 (1983).

15) J. K. Park and A. J. Ardell, “Effect of Retroregression and Reaging Treatments on the Microstructure of Al-7075-T651”, Metall. Trans. A, 15, pp.1531- 1543 (1984).

16) V. Randle and O. Engler, Introduction to Texture Analysis: Macrotexture, Microtexture and Orientation Mapping”, CRC Press (2000).

17) T. W. Duerig and J. C. Williams, “ Overview: Microstructure and Properties of Beta Titanium Alloys”, in Beta Titanium Alloys in the 1980s, R.R. Boyer and H. W. Rosenberg (Eds.), The Minerals, Metals & Materials Society, Warrendale, PA, 1984, pp.16-67.

18) J.K. Mackenzie, “The distribution of rotation axes in a random aggregate of cubic crystals”, Acta Metallurgica, 12, pp.223 225(1964).

19) R. D. Doherty, D. A. Hughes, F. J. Humphreys, D. Juul Jensen, M. E. Kassner, W. E. King, T. R. McNelley, H. J. McQueen and A. D. Rollet, “Current Issues in Recrystallization: A review”, Materials Science and Engineering A, 238, pp.219-274 (1997).

20) Y. Hakawa, M. Muraki, J. A. Szpunar, “ The Changes of Grain Boundary Character Distribution During Secondary Recrystallozation of Electrical Steel”, Acta. Mater., 46, pp.1063-1073 (1998).

21) W. T. Read and W. Schokley, “ Dislocation Models of Crystal Boundaries”, Physical Rev. 78 (1950), 275-289.

22) H. Grimmer, W. Bollmann and D. H. Warrington, “Coincident site lattices and complete pattern shift lattices in cubic crystals”, Acta Cryst. 30, pp.197-207 (1974).

23) P. J. Goodhew, “ The Relationship Between Grain Boundary Structure and Energy”, in Grain Boundary Structure and Kinetics, ASM, Metals Park Ohio, pp.155-176 (1979).

24) D G. Brandon, “The Structure of High Angle Boundaries” Acta. Met. 14, pp.1479-1484(1966).

25) O. V. Mishin, V. Y. Gertsman and G. Gottstein, “Distributions of Orientations and Misorientation in Hot-Rolled Copper”, Mater. Char., 38, pp.39-48 (1997).

26)C. A. Dube, H. I. Aaronson and R. F. Mehl, “The Formation of Proeutectoid Ferrite in Plain Carbon Steels”, Rev. de met., 55, pp. 201 (1958)

27) H. I. Aaronson, Decomposition of Austenite by Diffusional Processes, p.387, Interscience, New York (1962).

28) J. D. Verhoeven, “ Fundamentals of Physical Metallurgy”, John Wiley and Sons, New York (1975).

29) W. A. Johnson and K. E. Mehl, Trans. Am. Inst. Min. Met. Eng., 195, pp.416- (1939).

30) M. Avrami, “Kinetics of Phase Change. I General Theory”, J. Chem. Phys., 7, pp.1103 (1939).

31) M. Avrami, “Kinetics of Phase Change. II Transformation Time Relations for Random Distribution of Nuclei”, J. Chem. Phys., 8, pp. 212 (1940).

32) M. Avrami, “Granulation, Phase Change and Microstructure Kinetics of Phase Chage. III”, J. Chem. Phys., 9, pp.177 (1941).

33) B. K. Darmkoger and G. R. Edwards, “ Continous cooling transformation kinetics in alpha-beta titanium alloys”, Simulation and theory of evolving microstrcutures, M. P. Anderson, A. D. Rollet (Eds.), The Minerals, Metals and Materials Society, pp.129-150 (1992).

34) R.W. Balluffi, S. M. Allen and W. Craig Carter, “ Kinetic Processes in Materils”, John Wiley and Sons, (1997).

35) C. J. Zener, “The Theory of Growth of Spherical Precipitates from Solid Solutions“, J. Appl. Phys., 20, pp.950-953 (1949).

36)A. M. Donald, L. M. Brown, “ Grain Boundary Faceting in Cu-Bi Alloys”, Acta Metall., 27, pp.59-66 (1979).

37) T. E. Hsieh, R. W. Balluffi, “Observations of roughening/de-faceting phase transitions in grain boundaries”, Acta Metall, 37, pp.2133 (1989)

38) D .E. Luzzi, “High Resolution Electronmicroscopy observations of faceted grain boundaries and twins in bismuth doped copper”, Ultramicroscopy, 37, pp.180-190 (1991).

39) T. G. Ference, R. W. Balluffi, “Observation of a reversible grain boundary faceting transition induced by changes of composition”, Scripta Metall, 22, pp.1929-1934 (1988).

40) M. Menyhard, B. Blurn, C. J. McMahon, “Grain boundary segregation and transformation in Bi-doped polycrystalline copper”, Acta Metall. Mater., 37, pp. 549-557 (1989).

41) J. R. Rellick, C. J. McMahon, H. L. Marcus, P. W. Palmberg, “Effect of Tellurium on Intergranular Cohesion of Iron”, Metall. Trans., 2, pp.1492 (1971).

42) C. Loier, J. Y. Boos, “Striation and Faceting of Grain Boundaries in Nickel due to Sulfur and Other Elements”, Metall. Trans. A, 12, pp.129-135(1981)

43) J. Del Prado, X. Song, D. Hu and X. Wu, “ The influence of oxygen and carbon content on aging Ti-15-3”, Journal of Materials Engineering and Performance, 14, pp. 728-734 (2005).

44) D. Mclean, Grain boundaries in Metals, Clarendon, Oxford, p. 116 (1957).

45) D. A. Porter and K. E. Easterling, “Phase Transformations in Metals and Alloys”, Nelson Thornes Ltd., UK (2001).

46) J. W.Christian, “The Theory of Transformations in Metals and Alloys”, Pergman Press, New York (1965)

47) T. Furuhara, S. Takagi, H. Watanabe and T. Maki, “ Crystallography of Grain boundary α Preciptiates in a β Titanium alloy”, Metallurgical and Materials Transactions A, 27, pp.1635-1646 (1996).

48) D. Bhattacharyya, G. B. Viswananthan, R. Denkenberger, D. Furrer, H. L. Fraser, “The role of crystallographic and geometrical relationships beteen α and β phases in an α/β titanium alloy”, Acta Materialia, 51, pp. 4679-4691 (2003).

49) P. Virtanen, T. Tiainen, T. Lepisto, “Precipitation at faceting grain boundaries of Cu-Ni-Sn alloys”, Materials Science and Engineering, 251, pp.269-275 (1998).

50) R. D. Towsend and J. S. Kirkaldy, “Widmenstätten Ferrite Formation in Fe-C Alloys”, Trans. ASM, 61, pp. 605-619 (1968).

CHAPTER V

SUMMARY AND CONCLUSIONS

The present investigation has examined the mechanisms controlling the precipitation of various alpha(α) phase morphologies which form during the elevated temperature beta(β)→beta(β)+alpha(α) phase transformations in TIMETAL LCB.

The β→β+α phase transformation starts after an incubation period, upon lowering the temperature below the β transus temperature (T_β) of the alloy. The first sites that transform, independent of the aging temperature, are the grain boundaries. During the early stages of the reaction, α_{GRB} precipitates are distributed non-uniformly and localized to specific boundaries. The specific choice of a boundary depends on the ability of a boundary minimizing the activation energy barrier required for α_{GRB} precipitation. At each instance, the α_{GRB} particles maintain a Burger's orientation relationship (OR) with one of the adjacent β grains and decrease the activation energy barrier required for their precipitation. Further reduction in the activation energy barrier is possible if the α_{GRB} particles maintain coherency with both of the adjacent β matrix grains, thereby have a low α/β interfacial free energy. A coherent α/β interface structure is possible if α_{GRB} particles maintain Burger's OR with one of the β grains and hold an orientation relationship close to Burger's (typically within 7-8^o) with the adjacent β grain. This criterion can be satisfied if two adjacent β matrixes share a common {110} direction.

The uniformity of α_{GRB} precipitates increases and the entire grain boundary area transforms into α_{GRB} precipitates with increasing aging time at high undercoolings. However, equilibrium microstructure of the aged specimens display untransformed grain boundary area at low undercoolings ($T\text{-}T\beta \approx 30^{o}C$). The untransformed grain boundary area at these undercoolings is associated with low angle boundaries because of the insufficient driving force required to overcome the activation energy barrier.

Once the orientation of α_{GRB} is established and Burger's OR is maintained with one of the adjacent β grains, α_{WSP} starts to grow from α_{GRB}. α_{WSP} particles have the same orientation with the α_{GRB} precipitates and emerge from α_{GRB} located on faceted grain boundaries. Grain boundaries dissociate into micron sized facets exclusively after quenching the specimen below T_{β} suggesting that, oxygen segregation to the grain boundaries may be responsible from faceting of the boundaries

The final morphology that forms during isothermal $\beta \rightarrow \alpha+\beta$ transformation is α_{WIG} particles which precipitate homogenously within the β matrix. The aging time required to initiate α_{WIG} precipitation increases with decreasing undercooling. The α_{WIG} volume fraction at equilibrium is a function of aging temperature, with the lower aging temperatures being associated with higher α_{WIG} amount. These observations suggest that, the driving force for α_{WIG} formation is the volume free energy change which is a direct function of the amount undercooling, $T_{\beta}\text{-}T$.

The Johnson-Mehl-Avrami (JMA) analysis of the global $\beta \rightarrow \beta+\alpha$ transformation kinetics suggests that, below 745°C, α_{GRB} particles rapidly lengthen along the β grain boundaries and consume the available nucleation sites. Upon grain boundary saturation, $\beta \rightarrow \beta+\alpha$ transformation progresses by the α_{WSP} growth from α_{GRB} into the β matrix. As a result, the early stages of the phase transformation kinetics are controlled by the one dimensional lengthening of α_{WSP}. Once $\alpha_{GRB}+\alpha_{SP}$ transformation is complete, further progression of the transformation takes place by the two dimensional growth of α_{WIG} particles. Phase transformation kinetics at 745°C is associated with a single stage, where $\beta \rightarrow \beta+\alpha$ transformation occur solely by one dimensional thickening of α_{GRB} particles. The contribution of different α morphologies on the phase transformation kinetics in TIMETAL LCB was identified and summarized on a time-temperature -transformation (TTT).

These findings imply that, it is possible to enhance the kinetics α_{GRB} precipitation by controlling the relative orientation of two β grains, with the grain boundaries between two β grains sharing a common {110} direction being preferential nucleation sites during aging. While this approach may reduce the thermo-mechanical processing times, further research is required to achieve a control over the orientation distribution of β grains in the single phase microstructure.

Furthermore, the distribution and density of α_{GRB}, α_{WSP} and α_{WIG} particles can be controlled by altering the solution treatment schedule, grain boundary

character distribution, aging time and temperature and alloy composition to achieve property variations for the specific needs of an application.

For example, under equivalent tensile properties, α phase volume fraction, and prior beta grain size the high cycle fatigue (HCF) behavior of metastable beta titanium alloys is controlled by the contiguity of α_{GRB}, a higher contiguity ratio being associated with a decreased crack initiation resistance. This study has demonstrated the possibility of controlling the continuity of α_{GRB} by varying low angle- to the high angle-boundary ratio within the single phase microstructure, through the proper choice of solution treatment condition. As a result, α_{GRB} precipitation can be promoted solely on high angle grain boundaries, while the untransformed low angle boundary area enhancing the discontinuity between α_{GRB} particles. Finally, it is possible to adjust the volume fraction of the α_{GRB} particles by varying the aging time and temperature.

Fracture toughness of metastable β titanium alloys is important where damage tolerance is required and promoted by precipitation of α_{WSP} particles. It is, hereby, suggested that at a given aging temperature it is possible to control the size, spacing, volume fraction and distribution of α_{WSP} particles by altering the alloy composition, such as the oxygen content, and promoting oxygen segregation to the grain boundaries. Higher oxygen segregation may be responsible for the enhanced grain boundary faceting and promote α_{WSP} precipitation during aging.

APPENDIX

VOLUME FRACTION DATA

The total volume fraction of alpha (α) phase, as well as volume fraction of grain boundary alpha (α_{GRB}), widmenstätten side plates and intragranular alpha (α_{WI}), at various aging treatment conditions employed during this study were determined through systematic point counting and tabulated in Tables A1 through 16.

Average volume percent (P_P), standard deviation ($\sigma(V_V)$) and accuracy of the measurements (%acc) are reported in Tables A17 through.A32.

Table A.1. Total Volume Percent Data of TIMETAL LCB Solution Treated at 820^0C for 30 minutes and aged at 745^0C for subsequently increasing times.

Image Number	0.5 m	1 m	7 m	10 m	12 m	15 m	17 m
1	0	0	0	0	0	0.52	0.26
2	0	0	0.52	0.26	0	0	0
3	0	0	0	0	0.52	0	0.26
4	0	0	0	0.52	0	0.52	0.52
5	0	0	0	0.26	0.52	0.26	1.3
6	0	0	0	0	0.52	0.52	0.26
7	0	0	0	0	0	0.26	0.78
8	0	0	0	0.26	0	0	0.26
9	0	0	0	0	0	0.78	0.52
10	0	0	0.26	0.26	1.04	0	0

Image Number	30 m	60 m	120 m	182 m	1333 m	1980 m
1	1.04	2.08	3.12	1.82	5.20	6.24
2	0.78	0.78	1.82	5.46	4.68	6.24
3	0.78	1.56	2.34	2.34	4.94	7.54
4	0.52	1.04	2.6	2.86	4.16	3.9
5	0.26	0.52	2.08	1.56	5.98	4.16
6	0.52	0.52	4.16	2.08	4.94	6.24
7	0.26	0.78	0.52	3.9	4.94	4.16
8	0.26	1.3	4.94	2.86	5.20	4.94
9	0	1.3	2.34	0.78	4.16	3.68
10	0.26	0	1.30	3.12	4.42	4.94

Table A.2. Total Volume Percent Data of TIMETAL LCB Solution Treated at 820^{0}C for 30 minutes and aged at 730^{0}C for subsequently increasing times.

Image Number	0.5 m	1 m	7 m	10 m	12 m	15 m	20 m	35 m	40 m	50 m	60 m
1	0	0	0.26	0.26	0.78	0.26	1.04	1.82	3.12	2.86	3.64
2	0	0	0.26	0.52	0	1.04	1.3	1.56	2.34	3.12	4.42
3	0	0	0	0.78	0.78	1.56	1.82	2.6	3.90	1.82	2.86
4	0	0	0.52	0.52	0.26	0.78	1.56	1.56	0.26	2.86	3.12
5	0	0	0	0.26	1.04	1.30	1.56	1.04	1.56	2.08	3.38
6	0	0	0.26	0.26	0.52	0.78	0	3.12	2.34	3.38	3.12
7	0	0	0.78	0.78	0.26	0.78	1.56	0.26	2.60	2.86	1.56
8	0	0	0.26	0.26	0.52	1.04	1.56	2.60	1.82	4.42	4.94
9	0	0	0	0.52	0.52	0.78	1.56	1.56	1.30	2.60	3.9
10	0	0	0.26	0	0.52	0.52	0.26	2.08	1.82	2.86	2.86

Image Number	70 m	80 m	100 m	195 m	210 m	220 m	250 m	285 m	315 m	330 m
1	4.42	5.46	6.50	9.36	7.54	5.72	8.84	7.28	8.58	8.58
2	2.60	4.94	5.46	10.57	8.58	7.54	6.50	7.02	8.84	9.10
3	2.86	3.64	5.20	7.8	10.40	7.54	6.76	8.58	8.58	7.28
4	3.9	4.16	2.60	9.36	7.285	8.32	9.10	11.70	7.02	7.28
5	4.42	6.76	4.68	6.50	6.50	8.58	6.50	10.92	7.28	5.72
6	3.90	3.34	4.16	5.72	8.84	8.32	12.48	7.02	5.98	8.84
7	5.72	5.20	7.28	4.84	6.76	8.065	7.54	8.06	8.32	7.54
8	4.94	4.16	4.68	5.46	5.20	10.92	8.325	7.02	10.145	7.02
9	4.68	4.16	5.72	7.54	7.54	6.24	7.02	9.10	6.25	8.84
10	3.90	5.20	5.46	7.02	7.02	8.32	8.06	10.14	9.92	9.88

Table A.3. Total Volume Percent Data of TIMETAL LCB Solution Treated at 820^{0}C for 30 minutes and aged at 715^{0}C for subsequently increasing times.

Image number	0.5 m	1 m	5 m	10 m	12 m	15 m	25 m	35 m
1	0	0	0	0.26	0.78	1.56	2.08	1.56
2	0	0	0.26	0.52	0.26	1.04	0.78	4.16
3	0	0	0.26	0.78	0.78	1.04	3.38	4.68
4	0	0	0.52	0.26	1.04	1.04	2.60	3.12
5	0	0	0	1.30	0.78	1.04	2.60	4.94
6	0	0	0.26	0	0.78	1.04	2.08	2.86
7	0	0	0	0.78	0.78	1.56	2.08	4.93
8	0	0	1.04	0.26	0.26	0.52	2.86	3.12
9	0	0	0.26	0.26	1.04	0.78	1.30	3.64
10	0	0	0	0.56	0.78	1.3	2.08	3.38

Image number	40 m	50 m	60 m	91 m	126 m	133 m	200 m	430 m
1	4.42	7.82	7.54	10.40	16.91	17.95	18.47	18.21
2	2.86	4.16	4.42	8.06	13.27	15.61	17.69	20.55
3	4.42	4.16	4.68	10.66	14.31	12.48	17.69	18.99
4	5.20	4.94	5.20	8.32	13.01	16.13	17.43	18.47
5	4.16	4.68	7.86	9.36	12.49	18.74	18.47	18.47
6	3.90	4.68	3.90	9.62	15.09	16.13	17.69	18.73
7	3.38	4.68	9.89	7.28	14.31	14.315	19.77	18.21
8	4.42	4.16	4.94	9.88	11.97	15.35	17.43	17.95
9	3.38	4.16	4.94	9.10	15.09	15.61	17.69	18.21
10	3.90	6.50	6.50	7.80	13.53	13.79	17.17	17.95

Table A.4. Total Volume Percent Data of TIMETAL LCB Solution Treated at 820^{0}C for 30 minutes and aged at 700^{0}C for subsequently increasing times.

Image Number	0.5 m	1 m	5 m	7 m	10 m	12 m	15 m	20 m	25 m	30 m
1	0	0	0.52	1.04	1.30	1.04	2.86	3.12	1.82	3.12
2	0	0	1.30	1.30	1.04	1.82	0.78	3.12	3.38	4.16
3	0	0	0.78	0.26	1.04	1.82	2.34	2.60	3.9	3.64
4	0	0	0.52	0.78	0.78	1.39	2.08	3.38	3.12	4.425
5	0	0	0.78	0.26	1.56	0.78	2.08	2.60	1.56	4.68
6	0	0	1.04	1.56	1.82	0.52	1.82	2.60	2.60	3.12
7	0	0	0.52	1.30	0.78	1.04	1.56	3.64	3.38	4.68
8	0	0	0.26	1.04	0.26	1.82	2.08	2.34	4.68	3.64
9	0	0	0.26	1.04	1.82	1.82	2.08	1.82	3.64	4.94
10	0	0	0.52	0.52	1.30	1.30	0.523	2.60	5.20	4.42

Image Number	40 m	45 m	50 m	55 m	60 m	80 m	125 m	200 m
1	4.425	6.76	7.545	9.36	12.22	18.99	20.03	23.68
2	4.945	9.1	4.945	7.8	10.145	22.64	19.78	26.54
3	5.2	8.32	10.925	8.06	10.145	16.91	20.03	19.77
4	4.42	7.02	7.8	8.32	6.24	17.17	21.07	20.55
5	7.02	6.76	7.03	11.96	9.62	16.91	20.55	20.03
6	4.94	5.72	3.4	9.62	8.325	16.91	17.17	19.25
7	6.24	4.68	5.98	5.46	8.32	15.615	15.615	19.25
8	4.42	4.945	7.28	5.465	10.4	14.57	20.29	19.25
9	6.76	6.24	7.02	8.845	11.44	16.39	19.25	20.29
10	4.94	7.8	8.32	7.285	11.18	16.91	19.25	18.99

Table A5. Grain Boundary Alpha Volume Percent Data of TIMETAL LCB Solution Treated at 820^0C for 30 minutes and aged at 745^0C for subsequently increasing times.

Image Number	0.5 m	1 m	7 m	10 m	12 m	15 m	17 m
1	0	0	0	0	0	0.52	0.26
2	0	0	0.52	0.26	0	0	0
3	0	0	0	0	0.52	0	0.26
4	0	0	0	0.52	0	0.52	0.52
5	0	0	0	0.26	0.52	0.26	1.30
6	0	0	0	0	0.52	0.52	0.26
7	0	0	0	0	0	0.26	0.78
8	0	0	0	0.26	0	0	0.26
9	0	0	0	0	0	0.78	0.52
10	0	0	0.26	0.26	1.04	0	0

Image Number	30 m	60 m	120 m	182 m	1333 m	1980 m
1	1.04	1.3	1.56	1.30	5.2	5.20
2	0.78	0.52	1.30	2.86	2.34	4.42
3	0.78	1.30	2.34	1.82	3.38	5.46
4	0.52	1.04	1.82	2.34	2.08	2.08
5	0	0.52	1.30	1.04	5.20	3.64
6	0.52	0.52	2.08	1.56	4.16	4.42
7	0.26	0.78	0.52	3.38	4.42	2.86
8	0.26	1.04	3.64	2.34	3.64	4.16
9	0	1.04	2.34	0.52	3.38	2.64
10	0	0	1.30	3.12	3.12	2.60

Table A6. Grain Boundary Alpha Volume Percent Data of TIMETAL LCB Solution Treated at 820^0C for 30 minutes and aged at 730^0C for subsequently increasing times.

Image number	0.5 m	1 m	7 m	10 m	12 m	15 m	20 m	35 m	40 m	50 m	60 m
1	0	0	0.26	0.26	0.78	0.26	1.04	1.04	2.34	2.60	2.86
2	0	0	0.26	0.52	0	1.04	1.3	1.56	2.08	2.34	2.60
3	0	0	0	0.78	0.78	1.56	1.82	2.08	3.64	1.56	2.34
4	0	0	0.52	0.52	0.26	0.78	1.56	1.56	0	2.86	2.60
5	0	0	0	0.26	1.04	1.30	1.56	1.04	1.30	1.56	2.86
6	0	0	0.26	0.26	0.52	0.78	0	3.125	1.82	2.60	2.34
7	0	0	0.78	0.78	0.26	0.78	1.56	0.26	2.08	2.60	1.56
8	0	0	0.26	0.26	0.52	1.04	1.56	1.82	1.82	3.125	3.64
9	0	0	0	0.52	0.52	0.78	1.56	1.56	1.30	2.08	2.86
10	0	0	0.26	0	0.52	0.52	0.26	1.82	1.56	2.60	2.34

Image number	70 m	80 m	100 m	195 m	210 m	220 m	250 m	285 m	315 m	330 m
1	3.12	2.86	3.38	4.42	4.42	2.60	4.16	2.34	3.38	4.16
2	2.34	3.38	3.64	5.72	4.16	3.64	4.42	3.64	5.72	3.90
3	2.34	2.86	3.9	4.16	4.94	3.90	3.90	5.46	5.20	2.60
4	1.30	2.86	1.82	4.16	4.16	4.16	3.12	3.90	3.90	3.64
5	2.86	3.9	2.6	4.42	3.90	4.16	2.08	5.98	4.68	3.64
6	3.38	2.04	2.86	3.90	5.46	5.98	5.72	4.94	2.08	4.42
7	3.90	3.38	4.68	2.76	2.34	3.38	4.42	4.16	3.64	5.46
8	4.42	3.64	2.60	4.16	3.90	4.42	3.64	3.38	4.16	3.12
9	2.86	3.12	3.12	3.9	3.90	3.90	4.42	5.20	3.12	4.16
10	2.6	3.12	3.64	3.38	3.125	4.16	4.16	4.68	4.42	5.98

Table A7. Grain Boundary Alpha Volume Percent Data of TIMETAL LCB Solution Treated at 820^{0}C for 30 minutes and aged at 715^{0}C for subsequently increasing times.

Image number	0.5 m	1 m	5 m	10 m	12 m	15 m	25 m	35 m
1	0	0	0	0.26	0.78	1.30	1.04	1.04
2	0	0	0.26	0.52	0.26	1.04	0.78	2.60
3	0	0	0.26	0.78	0.78	0.78	2.86	3.64
4	0	0	0.52	0.26	1.04	1.04	2.34	2.60
5	0	0	0	1.30	0.78	1.04	2.08	3.64
6	0	0	0.26	0	0.78	1.04	2.08	2.34
7	0	0	0	0.78	0.78	1.56	1.56	4.16
8	0	0	1.04	0.26	0.26	0.26	2.34	2.86
9	0	0	0.26	0.26	1.04	0.78	1.30	3.12
10	0	0	0	0.56	0.78	1.30	1.82	2.86

Image number	40 m	50 m	60 m	91 m	126 m	133 m	200 m	430 m
1	3.12	5.48	3.9	4.16	5.98	4.16	3.90	3.90
2	2.34	3.125	3.125	3.38	3.90	3.90	4.68	5.46
3	4.16	2.34	3.125	5.46	4.94	4.42	4.68	4.16
4	4.68	2.60	3.64	3.64	4.42	5.20	4.16	4.94
5	3.12	2.86	5.48	4.68	4.42	7.03	4.16	4.94
6	1.82	3.125	1.82	4.42	3.90	4.16	4.68	4.42
7	2.60	3.64	7.29	1.82	4.16	3.38	4.94	4.16
8	3.38	3.12	3.38	3.64	1.82	3.90	5.20	3.90
9	2.86	2.60	3.64	5.46	3.90	5.20	3.90	4.94
10	3.12	4.68	4.16	3.38	4.68	3.90	4.42	4.68

Table A8. Grain Boundary Alpha Volume Percent Data of TIMETAL LCB Solution Treated at 820^0C for 30 minutes and aged at 700^0C for subsequently increasing times.

Image number	0.5 m	1 m	5 m	7 m	10 m	12 m	15 m	20 m	25 m	30 m
1	0	0	0.52	1.04	1.3	1.04	2.60	2.86	1.56	2.08
2	0	0	1.30	1.30	1.04	1.82	0.78	2.60	2.86	3.12
3	0	0	0.78	0.26	1.04	1.82	1.56	2.60	3.38	3.12
4	0	0	0.52	0.78	0.78	1.04	1.82	2.60	2.86	3.12
5	0	0	0.78	0.26	1.56	0.78	1.82	2.60	0.78	3.90
6	0	0	1.04	1.56	1.82	0.26	1.82	2.34	2.34	2.34
7	0	0	0.52	1.30	0.78	1.04	1.56	3.64	2.86	3.12
8	0	0	0.26	1.04	0.26	1.82	2.08	2.08	4.42	3.12
9	0	0	0.26	1.04	1.82	1.82	2.08	1.82	2.34	3.12
10	0	0	0.52	0.52	1.3	1.04	0.52	2.08	3.64	3.64

Image number	40 m	45 m	50 m	55 m	60 m	80 m	125 m	200 m
1	3.12	4.16	2.60	4.94	4.16	4.94	4.68	4.94
2	3.12	3.90	3.12	2.86	2.86	4.94	4.16	5.72
3	3.90	5.72	5.20	4.94	4.68	4.16	3.90	4.42
4	2.60	3.90	3.90	3.90	3.38	4.68	4.94	3.90
5	4.16	2.86	4.43	5.98	5.46	4.16	4.42	4.94
6	2.60	3.64	1.06	4.42	3.38	3.90	5.46	4.68
7	1.82	1.82	3.38	2.86	4.42	4.68	4.42	3.38
8	3.64	3.12	4.94	3.12	3.90	4.16	4.94	4.94
9	5.72	2.60	4.16	3.90	4.68	3.64	4.16	4.42
10	3.64	4.16	4.16	2.08	3.64	3.38	4.16	4.16

Table A9. Side Plate Volume Percent Data of TIMETAL LCB Solution Treated at 820^{0}C for 30 minutes and aged at 745^{0}C for subsequently increasing times.

Image Number	0.5 m	1 m	7 m	10 m	12 m	15 m	17 m
1	0	0	0	0	0	0	0
2	0	0	0	0	0	0	0
3	0	0	0	0	0	0	0
4	0	0	0	0	0	0	0
5	0	0	0	0	0	0	0
6	0	0	0	0	0	0	0
7	0	0	0	0	0	0	0
8	0	0	0	0	0	0	0
9	0	0	0	0	0	0	0
10	0	0	0	0	0	0	0

Image Number	30 m	60 m	120 m	182 m	1333 m	1980 m
1	0	0.52	0.52	0.52	0	1.04
2	0	0.26	0.52	1.30	1.56	1.04
3	0	0.26	0	0.52	0.26	1.04
4	0	0	0.26	0	0.78	0.52
5	0.26	0	0.78	0	0	0.52
6	0	0	1.82	0.52	0.78	0.78
7	0	0	0	0.52	0	0.26
8	0	0.26	0.52	0.26	0.52	0.52
9	0	0.26	0	0	0.26	0.78
10	0.26	0	0	0	0.26	1.04

Table A10. Side Plate Volume Percent Data of TIMETAL LCB Solution Treated at 820^{0}C for 30 minutes and aged at 730^{0}C for subsequently increasing times.

Image number	0.5 m	1 m	7 m	10 m	12 m	15 m	20 m	35 m	40 m	50 m	60 m
1	0	0	0	0	0	0	0	0.52	0.52	0.26	0.52
2	0	0	0	0	0	0	0	0	0.26	0.78	1.04
3	0	0	0	0	0	0	0	0.52	0.26	0	0.52
4	0	0	0	0	0	0	0	0	0.26	0	0
5	0	0	0	0	0	0	0	0	0.26	0.52	0.26
6	0	0	0	0	0	0	0	0	0.52	0.78	0.78
7	0	0	0	0	0	0	0	0	0.52	0.26	0
8	0	0	0	0	0	0	0	0.78	0	0.78	0.78
9	0	0	0	0	0	0	0	0	0	0.52	0.52
10	0	0	0	0	0	0	0	0.26	0.26	0.26	0.52

Image number	70 m	80 m	100 m	195 m	210 m	220 m	250 m	285 m	315 m	330 m
1	1.04	1.04	1.56	1.56	1.04	1.04	1.30	1.82	1.56	1.82
2	0.26	0.78	0.26	1.56	1.56	2.34	0	0.78	1.04	1.82
3	0.26	0.78	1.30	1.56	1.30	1.04	1.82	1.04	1.04	0.78
4	1.30	1.30	0.78	1.82	0	1.30	2.08	4.94	0.52	0.78
5	0.52	1.56	1.04	0.26	1.30	1.56	1.56	1.56	1.04	0
6	0.52	0	0.52	0.52	1.30	1.04	3.90	0.52	1.56	1.30
7	0.78	0.78	1.30	0.52	2.34	1.56	0.78	1.3	1.82	1.04
8	0.52	0.52	1.30	1.04	0.52	1.3	1.56	0.78	3.12	1.30
9	1.30	0.52	1.04	1.30	1.56	0.26	0.78	1.82	0	1.56
10	0.78	1.04	1.56	2.08	1.30	1.30	1.30	1.30	1.82	1.82

Table A11. Side Plate Volume Percent Data of TIMETAL LCB Solution Treated at 820^{0}C for 30 minutes and aged at 715^{0}C for subsequently increasing times.

Image Number	0.5 m	1 m	5 m	10 m	12 m	15 m	25 m	35 m
1	0	0	0	0	0	0.26	0.52	0.52
2	0	0	0	0	0	0	0	1.04
3	0	0	0	0	0	0.26	0.52	1.04
4	0	0	0	0	0	0	0.26	0.52
5	0	0	0	0	0	0	0.52	1.30
6	0	0	0	0	0	0	0	0.52
7	0	0	0	0	0	0	0.52	0.52
8	0	0	0	0	0	0.26	0.52	0.26
9	0	0	0	0	0	0	0	0.26
10	0	0	0	0	0	0	0.26	0.52

Image Number	40 m	50 m	60 m	91 m	126 m	133 m	200 m	430 m
1	0.78	1.82	3.125	2.08	4.42	5.20	4.42	4.42
2	0.52	1.04	0.78	2.08	2.08	3.64	3.64	4.16
3	0.26	1.3	0.78	1.82	2.60	2.86	3.12	4.16
4	0.26	1.82	1.30	1.56	1.82	2.34	4.16	3.38
5	1.04	1.82	1.56	2.6	1.04	3.90	3.64	3.12
6	1.30	1.3	1.04	2.34	3.38	3.64	3.12	3.38
7	0.52	0	1.56	2.34	3.38	3.12	3.12	4.68
8	1.04	1.04	1.04	2.34	2.86	2.08	2.08	2.86
9	0.52	1.04	0.26	1.30	2.60	2.08	3.38	3.12
10	0.78	1.56	1.56	1.82	2.08	1.82	2.86	3.12

Table A12. Side Plate Volume Percent Data of TIMETAL LCB Solution Treated at 820^0C for 30 minutes and aged at 700^0C for subsequently increasing times.

Image Number	0.5 m	1 m	5 m	7 m	10 m	12 m	15 m	20 m	25 m	30 m
1	0	0	0	0	0	0	0.26	0.26	0.26	1.04
2	0	0	0	0	0	0	0	0.52	0.52	0.78
3	0	0	0	0	0	0	0.78	0	0.52	0.52
4	0	0	0	0	0	0.26	0.26	0.78	0	0.52
5	0	0	0	0	0	0	0.26	0	0.26	0.52
6	0	0	0	0	0	0.26	0	0.26	0.26	0.78
7	0	0	0	0	0	0	0	0	0.52	1.56
8	0	0	0	0	0	0	0	0.26	0.26	0
9	0	0	0	0	0	0	0	0	0	0.78
10	0	0	0	0	0	0.26	0	0.52	1.56	0.78

Image Number	40 m	45 m	50 m	55 m	60 m	80 m	125 m	200 m
1	1.04	1.82	1.82	2.60	4.16	4.68	4.16	8.85
2	1.04	2.34	1.04	1.56	3.12	6.77	6.25	5.46
3	0.52	1.82	3.12	1.56	3.12	4.16	4.68	5.46
4	1.04	1.30	2.86	2.6	1.30	4.16	5.46	4.94
5	1.82	2.6	1.56	3.38	1.56	3.90	5.20	5.46
6	1.56	1.56	1.04	1.56	1.82	4.42	4.94	4.68
7	2.34	2.08	0.78	0.78	1.30	3.12	3.125	5.20
8	0.52	1.04	1.30	0.78	3.64	3.38	5.20	4.16
9	0.26	1.82	2.08	1.82	2.60	3.90	5.20	5.46
10	1.30	2.08	1.82	3.12	3.64	5.20	4.94	4.68

Table A13. Intragranular Alpha Volume Percent Data of TIMETAL LCB Solution Treated at 820^{0}C for 30 minutes and aged at 745^{0}C for subsequently increasing times.

Image Number	0.5 m	1 m	7 m	10 m	12 m	15 m	17 m
1	0	0	0	0	0	0	0
2	0	0	0	0	0	0	0
3	0	0	0	0	0	0	0
4	0	0	0	0	0	0	0
5	0	0	0	0	0	0	0
6	0	0	0	0	0	0	0
7	0	0	0	0	0	0	0
8	0	0	0	0	0	0	0
9	0	0	0	0	0	0	0
10	0	0	0	0	0	0	0

Image Number	30 m	60 m	120 m	182 m	1333 m	1980 m
1	0	0.26	1.04	0	0	0
2	0	0	0	1.30	0.78	0.78
3	0	0	0	0	1.30	1.04
4	0	0	0.52	0.52	1.30	1.30
5	0	0	0	0.52	0.78	0
6	0	0	0.26	0	0	1.04
7	0	0	0	0	0.52	1.04
8	0	0	0.78	0.26	1.04	0.26
9	0	0	0	0.26	0.52	0.26
10	0	0	0	0	1.04	1.30

Table A14. Intragranular Alpha Volume Percent Data of TIMETAL LCB Solution Treated at 820^{0}C for 30 minutes and aged at 730^{0}C for subsequently increasing times.

Image number	0.5 m	1 m	7 m	10 m	12 m	15 m	20 m	35 m	40 m	50 m	60 m
1	0	0	0	0	0	0	0	0.26	0.26	0	0.26
2	0	0	0	0	0	0	0	0	0	0	0.78
3	0	0	0	0	0	0	0	0	0	0.26	0
4	0	0	0	0	0	0	0	0	0	0	0.52
5	0	0	0	0	0	0	0	0	0	0	0.26
6	0	0	0	0	0	0	0	0	0	0	0
7	0	0	0	0	0	0	0	0	0	0	0
8	0	0	0	0	0	0	0	0	0	0.52	0.52
9	0	0	0	0	0	0	0	0	0	0	0.52
10	0	0	0	0	0	0	0	0	0	0	0

Image number	70 m	80 m	100 m	195 m	210 m	220 m	250 m	285 m	315 m	330 m
1	0.26	1.56	1.56	3.38	2.08	2.08	3.38	3.12	3.64	2.60
2	0	0.78	1.56	3.29	2.86	1.56	2.08	2.60	2.08	3.38
3	0.26	0	0	2.08	4.16	2.6	1.04	2.08	2.34	3.90
4	1.30	0	0	3.38	3.125	2.86	3.9	2.86	2.60	2.86
5	1.04	1.30	1.04	1.82	1.30	2.86	2.86	3.38	1.56	2.08
6	0	1.30	0.78	1.30	2.08	1.30	2.86	1.56	2.34	3.12
7	1.04	1.04	1.30	1.56	2.08	3.125	2.34	2.60	2.86	1.04
8	0	0	0.78	0.26	0.78	5.2	3.12	2.86	2.86	2.60
9	0.52	0.52	1.56	2.34	2.08	2.08	1.82	2.08	3.12	3.12
10	0.52	1.04	0.26	1.56	2.6	2.86	2.6	4.16	3.68	2.08

Table A15. Intragranular Alpha Volume Percent Data of TIMETAL LCB Solution Treated at 820^0C for 30 minutes and aged at 715^0C for subsequently increasing times.

Image Number	0.5 m	1m	5 m	10 m	12 m	15 m	25 m	35 m
1	0	0	0	0	0	0	0.52	0
2	0	0	0	0	0	0	0	0.52
3	0	0	0	0	0	0	0	0
4	0	0	0	0	0	0	0	0
5	0	0	0	0	0	0	0	0
6	0	0	0	0	0	0	0	0
7	0	0	0	0	0	0	0	0.25
8	0	0	0	0	0	0	0	0
9	0	0	0	0	0	0	0	0.26
10	0	0	0	0	0	0	0	0

Image Number	40 m	50 m	60 m	91 m	126 m	133 m	200 m	430 m
1	0.52	0.52	0.52	4.16	6.51	8.59	10.15	9.89
2	0	0	0.52	2.60	7.29	8.07	9.37	10.93
3	0	0.52	0.78	3.38	6.77	5.20	9.89	10.67
4	0.26	0.52	0.26	3.12	6.77	8.59	9.11	10.15
5	0	0	1.30	2.08	7.03	7.81	10.67	10.41
6	0.78	0.26	1.04	2.86	7.81	8.33	9.89	10.93
7	0.26	1.04	1.04	3.12	6.77	7.81	11.71	9.37
8	0	0	0.52	3.90	7.29	9.37	10.15	11.19
9	0	0.52	1.04	2.34	8.59	8.33	10.41	10.15
10	0	0.26	0.78	2.60	6.77	8.07	9.89	10.15

Table A16. Intragranular Alpha Volume Percent Data of TIMETAL LCB Solution Treated at 820^{0}C for 30 minutes and aged at 700^{0}C for subsequently increasing times.

Image Number	0.5 m	1 m	5 m	7 m	10 m	12 m	15 m	20 m	25 m	30 m
1	0	0	0	0	0	0	0	0	0	0
2	0	0	0	0	0	0	0	0	0	0.26
3	0	0	0	0	0	0	0	0	0	0
4	0	0	0	0	0	0	0	0	0.26	0.78
5	0	0	0	0	0	0	0	0	0.52	0.26
6	0	0	0	0	0	0	0	0	0	0
7	0	0	0	0	0	0	0	0	0	0
8	0	0	0	0	0	0	0	0	0	0.52
9	0	0	0	0	0	0	0	0	1.30	1.04
10	0	0	0	0	0	0	0	0	0	0

Image Number	40 m	45 m	50 m	55 m	60 m	80 m	125 m	200 m
1	0.26	0.78	3.12	1.82	3.9	9.37	11.19	9.89
2	0.78	2.86	0.78	3.38	4.16	10.93	9.37	15.36
3	0.78	0.78	2.60	1.56	2.34	8.59	11.45	9.89
4	0.78	1.82	1.04	1.82	1.56	8.33	10.67	11.71
5	1.04	1.30	1.04	2.60	2.60	8.85	10.93	9.63
6	0.78	0.52	1.3	3.64	3.125	8.59	6.77	9.89
7	2.08	0.78	1.82	1.82	2.60	7.81	8.07	10.67
8	0.26	0.78	1.04	1.56	2.86	7.03	10.15	10.15
9	0.78	1.82	0.78	3.12	4.16	8.85	9.89	10.41
10	0	1.56	2.34	2.08	3.90	8.33	10.15	10.15

Table A177. Average Total Volume Percent (P_P), Standard Deviation ($\sigma(V_V)$) and Accuracy (acc(%)) of TIMETAL LCB Solution Treated at 820°C for 30 minutes and aged at 745°C for subsequently increasing times.

time(min)	P_P	$\sigma(V_v)$	acc(%)
0.5	0.00	--	--
1	0.00	--	--
7	0.07	0.17	9.94
10	0.15	0.18	5.47
12	0.26	0.36	6.31
15	0.28	0.28	4.56
17	0.41	0.39	4.34
30	0.46	0.32	3.17
60	0.98	0.59	2.74
120	2.52	1.29	2.33
182	2.67	1.31	2.23
1333	4.86	0.54	0.50
1980	5.20	1.29	1.13

Table A188. Average Total Volume Percent (P_P), Standard Deviation ($\sigma(V_V)$), and Accuracy (acc(%)) of TIMETAL LCB Solution Treated at 820°C for 30 minutes and aged at 730°C for subsequently increasing times.

time(min)	P_P	$\sigma(V_V)$	acc(%)
0.5	0.00	--	--
1	0.00	--	--
7	0.26	0.24	4.21
10	0.41	0.25	2.78
12	0.52	0.3	2.63
15	0.88	0.37	1.91
20	1.22	0.61	2.28
35	1.82	0.83	2.08
40	2.10	1.00	2.17
50	2.88	0.71	1.12
60	3.38	0.93	1.25
70	4.13	0.92	1.01
80	4.70	1.01	0.98
100	5.17	1.28	1.13
195	7.41	1.88	1.15
210	7.56	1.43	0.86
220	7.95	1.40	0.80
250	8.11	1.80	1.01
285	8.68	1.73	0.90
315	8.09	1.42	0.80
330	8.00	1.24	0.70

Table A19. Average Total Volume Percent (P_P), Standard Deviation ($\sigma(V_V)$), and Accuracy (acc(%)) of TIMETAL LCB Solution Treated at 820°C for 30 minutes and aged at 715°C for subsequently increasing times.

time(min)	P_P	$\sigma(V_V)$	acc(%)
0.5	0.00	--	--
1	0.00	--	--
5	0.26	0.32	5.61
10	0.49	0.37	3.44
12	0.72	0.26	1.64
15	1.09	0.31	1.29
25	2.18	0.74	1.54
35	3.63	1.06	1.33
40	4.00	0.67	0.76
50	4.99	1.21	1.10
60	5.98	1.90	1.45
91	9.04	1.14	0.57
126	13.99	1.45	0.47
133	15.61	1.84	0.53
200	17.95	0.76	0.19
430	18.57	0.76	0.18

Table A20. Average Total Volume Percent (P_P), Standard Deviation ($\sigma(V_V)$), and Accuracy (acc(%)) of TIMETAL LCB Solution Treated at 820°C for 30 minutes and aged at 700°C for subsequently increasing times.

time(min)	P_P	$\sigma(V_V)$	acc(%)
0.5	0.00	--	--
1	0.00	--	--
5	0.65	0.33	7.32
7	0.91	0.44	6.97
10	1.17	0.49	6.04
12	1.32	0.48	5.24
15	1.82	0.70	5.55
20	2.78	0.53	2.75
25	3.32	1.14	4.95
30	4.08	0.66	2.33
40	5.33	0.98	2.65
45	6.73	1.41	3.02
50	7.02	2.01	4.13
55	8.21	1.94	3.41
60	9.8	1.76	2.59
80	17.3	2.18	1.81882
125	19.3	1.66	1.24
200	20.76	2.44	1.69

Table A21. Average Grain Boundary Alpha Volume Percent (P_P), Standard Deviation ($\sigma(V_V)$) and Accuracy (acc(%)) of TIMETAL LCB Solution Treated at 820°C for 30 minutes and aged at 745°C for subsequently increasing times.

time(min)	P_P	$\sigma(V_V)$	acc(%)
0.5	0.00	--	--
1	0.00	--	--
7	0.078	0.17	9.94
10	0.15	0.18	5.47
12	0.26	0.36	6.31
15	0.28	0.28	4.56
17	0.41	0.39	4.34
30	0.42	0.37	4.02
60	0.80	0.41	2.33
120	1.82	0.84	2.10
182	2.02	0.94	2.12
1333	3.69	1.06	1.31
1980	3.74	1.16	1.41

Table A22. Average Grain Boundary Alpha Volume Percent (P_P), Standard Deviation ($\sigma(V_V)$) and Accuracy (acc(%)) of TIMETAL LCB Solution Treated at 820°C for 30 minutes and aged at 730°C for subsequently increasing times.

time(min)	P_P	$\sigma(V_V)$	acc(%)
0.5	0.00	--	--
1	0.00	--	--
7	0.26	0.24	13.32
10	0.41	0.25	8.80
12	0.52	0.30	8.32
15	0.88	0.37	6.06
20	1.22	0.61	7.21
35	1.58	0.75	6.85
40	1.79	0.92	7.41
50	2.38	0.51	3.09
60	2.6	0.53	2.94
70	2.91	0.87	4.31
80	3.11	0.51	2.36
100	3.22	0.80	3.58
195	4.09	0.76	2.68
210	4.03	0.86	3.08
220	4.03	0.86	3.08
250	4.00	0.95	3.42
285	4.36	1.08	3.57
315	4.03	1.05	3.76
330	4.1	1.00	3.52

Table A23. Average Grain Boundary Alpha Volume Percent (P_P), Standard Deviation ($\sigma(V_V)$) and Accuracy (acc(%)) of TIMETAL LCB Solution Treated at 820°C for 30 minutes and aged at 715°C for subsequently increasing times.

time(min)	P_P	$\sigma(V_V)$	acc(%)
0.5	0.00	--	--
1	0.00	--	--
5	0.26	0.32	17.76
10	0.49	0.37	10.89
12	0.72	0.26	5.21
15	1.01	0.35	5.00
25	1.82	0.64	5.07
35	2.88	0.86	4.31
40	3.12	0.83	3.83
50	3.35	0.99	4.26
60	3.9	1.44	5.32
91	4.00	1.09	3.93
126	4.21	1.05	3.59
133	4.52	1.05	3.35
200	4.47	0.43	1.38
430	4.55	0.52	1.64

Table A24. Average Grain Boundary Alpha Volume Percent (P_P), Standard Deviation ($\sigma(V_V)$) and Accuracy (acc(%)) of TIMETAL LCB Solution Treated at 820°C for 30 minutes and aged at 700°C for subsequently increasing times.

time(min)	P_P	$\sigma(V_V)$	acc(%)
0.5	0.00	-	--
1	0.00	-	--
5	0.65	0.33	7.32
7	0.91	0.44	6.97
10	1.17	0.49	6.04
12	1.24	0.54	6.28
15	1.66	0.61	5.30
20	2.52	0.50	2.86
25	2.70	1.03	5.50
30	3.07	0.53	2.49
40	3.43	1.06	4.46
45	3.58	1.06	4.27
50	3.69	1.22	4.77
55	3.90	1.19	4.40
60	4.05	0.77	2.74
80	4.26	0.53	1.79
125	4.52	0.47	1.50
200	4.55	0.65	2.06

Table A25. Average Side Plate Volume Percent (P_P), Standard Deviation ($\sigma(V_V)$) and Accuracy (acc(%)) of TIMETAL LCB Solution Treated at 820°C for 30 minutes and aged at 745°C for subsequently increasing times.

time(min)	P_P	$\sigma(V_V)$	Acc(%)
0.5	0.00	--	--
1	0.00	--	--
7	0.00	--	--
10	0.00	--	--
12	0.00	--	--
15	0.00	--	--
17	0.00	--	--
30	0.05	0.10	8.77
60	0.16	0.18	5.13
120	0.44	0.56	5.80
182	0.36	0.41	5.19
1333	0.44	0.49	5.08
1980	0.75	0.28	1.70

Table A26. Average Side Plate Volume Percent (P_P), Standard Deviation ($\sigma(V_V)$) and Accuracy (acc(%)) of TIMETAL LCB Solution Treated at 820°C for 30 minutes and aged at 730°C for subsequently increasing times.

time(min)	P_P	$\sigma(V_V)$	Acc(%)
0.5	0.00	--	--
1	0.00	--	--
7	0.00	--	--
10	0.00	--	--
12	0.00	--	--
15	0.00	--	--
20	0.00	--	--
35	0.20	0.29	20.92
40	0.28	0.19	9.79
50	0.42	0.3	10.30
60	0.49	0.33	9.72
70	0.71	0.38	7.72
80	0.83	0.43	7.47
100	1.06	0.43	5.85
195	1.22	0.61	7.21
210	1.22	0.62	7.33
220	1.27	0.52	5.90
250	1.50	1.03	9.91
285	1.58	1.25	11.41
315	1.35	0.84	8.98
330	1.22	0.58	6.86

Table A27. Average Side Plate Volume Percent (P_P), Standard Deviation ($\sigma(V_V)$) and Accuracy (acc(%)) of TIMETAL LCB Solution Treated at 820°C for 30 minutes and aged at 715°C for subsequently increasing times.

time(min)	P_P	$\sigma(V_V)$	Acc(%)
0.5	0.00	--	--
1	0.00	--	--
5	0.00	--	--
10	0.00	--	--
12	0.00	--	--
15	0.07	0.12	22.20
25	0.31	0.23	10.70
35	0.65	0.35	7.77
40	0.70	0.34	7.01
50	1.27	0.55	6.25
60	1.30	0.76	8.43
91	2.02	0.40	2.85
126	2.62	0.95	5.23
133	3.06	1.05	4.95
200	3.35	0.66	2.84
430	3.64	0.64	2.53

Table A28. Average Side Plate Volume Percent (P_P), Standard Deviation ($\sigma(V_V)$) and Accuracy (acc(%)) of TIMETAL LCB Solution Treated at 820°C for 30 minutes and aged at 700°C for subsequently increasing times.

time(min)	P_P	$\sigma(V_V)$	Acc(%)
0.5	0.00	--	--
1	0.00	--	--
5	0.65	0.33	7.32
7	0.91	0.44	6.97
10	1.17	0.49	6.04
12	1.24	0.54	6.28
15	1.66	0.61	5.30
20	2.52	0.5	2.86
25	2.70	1.03	5.50
30	3.07	0.53	2.49
40	3.43	1.06	4.46
45	3.58	1.06	4.27
50	3.69	1.22	4.77
55	3.90	1.19	4.40
60	4.05	0.77	2.74
80	4.26	0.53	1.79
125	4.52	0.47	1.50
200	4.55	0.65	2.06

Table A29. Average Intragranular Alpha Volume Percent (P_P), Standard Deviation ($\sigma(V_V)$) and Accuracy (acc(%)) of TIMETAL LCB Solution Treated at 820°C for 30 minutes and aged at 745°C for subsequently increasing times.

time(min)	P_P	$\sigma(V_V)$	Acc(%)
0.5	0.00	--	--
1	0.00	--	--
7	0.00	--	--
10	0.00	--	--
12	0.00	--	--
15	0.00	--	--
17	0.00	--	--
30	0.00	--	--
60	0.02	0.08	14.39
120	0.26	0.38	6.67
182	0.28	0.41	6.68
1333	0.73	0.47	2.93
1980	0.70	0.52	3.39

Table A30. Average Intragranular Alpha Volume Percent (P_P), Standard Deviation ($\sigma(V_V)$) and Accuracy (acc(%)) of TIMETAL LCB Solution Treated at 820°C for 30 minutes and aged at 730°C for subsequently increasing times.

time(min)	P_P	$\sigma(V_V)$	Acc(%)
0.5	0.00	--	--
1	0.00	--	--
7	0.00	--	--
10	0.00	--	--
12	0.00	--	--
15	0.00	--	--
20	0.00	--	--
35	0.02	0.08	14.39
40	0.02	0.08	14.39
50	0.07	0.17	9.94
60	0.28	0.28	4.56
70	0.49	0.48	4.47
80	0.75	0.59	3.59
100	0.88	0.61	3.16
195	2.09	1.02	2.22
210	2.31	0.94	1.85
220	2.65	1.08	1.86
250	2.60	0.82	1.43
285	2.73	0.73	1.22
315	2.70	0.66	1.11
330	2.67	0.80	1.36

Table A31. Average Intragranular Alpha Volume Percent (P_P), Standard Deviation ($\sigma(V_V)$) and Accuracy (acc(%)) of TIMETAL LCB Solution Treated at 820°C for 30 minutes and aged at 715°C for subsequently increasing times.

time(min)	P_P	$\sigma(V_V)$	Acc(%)
0.5	0.00	--	--
1	0.00	--	--
5	0.00	--	--
10	0.00	--	--
12	0.00	--	--
15	0.00	--	--
25	0.05	0.16	14.04
35	0.10	0.18	8.21
40	0.18	0.27	6.84
50	0.36	0.32	4.05
60	0.78	0.32	1.87
91	3.01	0.66	1.00
126	7.16	0.62	0.39
133	8.01	1.09	0.62
200	10.12	0.71	0.32
430	10.38	0.55	0.24

Table A32. Average Intragranular Alpha Volume Percent (P_P), Standard Deviation ($\sigma(V_V)$) and Accuracy (acc(%)) of TIMETAL LCB Solution Treated at 820°C for 30 minutes and aged at 700°C for subsequently increasing times.

time(min)	P_P	$\sigma(V_V)$	Acc(%)
0.5	0.00	--	--
1	0.00	--	--
5	0.00	--	--
7	0.00	--	--
10	0.00	--	--
12	0.00	--	--
15	0.00	--	--
20	0.00	--	--
25	0.20	0.42	30.31
30	0.28	0.37	19.07
40	0.75	0.56	10.77
45	1.30	0.72	7.99
50	1.58	0.83	7.58
55	2.34	0.78	4.81
60	3.12	0.88	4.07
80	8.66	1.01	1.68
125	9.86	1.46	2.13
200	10.77	1.71	2.29